Establishment of a Novel Patient hiPSC-derived *in vitro* Blood-Brain Barrier Model of Collagen IV Small Vessel Disease

Mary Anne Goodwin-Trotman

Gonville & Caius College

University of Cambridge

This thesis is submitted for the degree of Doctor of Philosophy

September 2020

Preface

<u>Contribution of Others</u>

Where others have contributed in whole or in part to a particular experiment, this is detailed within the relevant figure legend and associated text. Dr Alessandra Granata generated the COL4A2^{G702D} isogenic control line, performed all neural-crest smooth muscle cell differentiations and provided differentiated cells for use in co-culture experiments. Krushangi Patel completed all three germ-layer differentiation experiments for testing hiPSC pluripotency and some qRT-PCR for pluripotency markers. The MMP antibody array was performed with Dominika Krzyzanska.

Summary

Establishment of a Novel Patient hiPSC-derived *in vitro* Blood-Brain Barrier Model of Collagen IV Small Vessel Disease

Mary Goodwin-Trotman

Cerebral small vessel disease (SVD) is a prevalent cause of stroke (25-30%) and dementia (45%). Despite its frequency, little is known about the cause and disease progression of SVD. Matrisome alteration leading to blood-brain barrier (BBB) dysfunction is thought to play a role. Sporadic cases are exacerbated by age and vascular risk factors, predominantly affecting the elderly. However, mutations in Collagen IV α1/α2 (COL4A1/2), a highly abundant matrisome protein, cause monogenic SVD, which shares many clinical features with the sporadic form.

In order to better understand the pathomolecular mechanisms leading to SVD, human induced pluripotent stem cells (hiPSC) generated from patients with mutations in COL4A1/2 genes (COL4A1^{G755R} and COL4A2^{G702D}), isogenic controls and multiple wild-type (WT) control lines were used to establish a novel *in vitro* BBB model of Collagen IV SVD. Encompassing hiPSC-derived brain microvascular endothelial cells (BMEC), mural cells (MC) and astrocytes, the model was used to probe the phenotype of COL4A1/2 SVD.

Differentiation of hiPSC into BMEC was extensively optimised to overcome high variability between different hiPSC lines. Once established, hiPSC-BMEC were tested with functional assays including transendothelial electrical resistance (TEER), permeability assays (4kDa FITC-Dextran and Sodium Fluorescein), LDL-uptake and tube formation. hiPSC-BMEC were then combined with hiPSC-MC and hiPSC-astrocytes into a Transwell® co-culture model.

WT hiPSC-derived BMEC exhibit high TEER of ~3000-4000Ωxcm^2, which is increased and maintained over two weeks in co-culture with astrocytes. Limited, short-term increase in TEER is seen in co-culture with MC. Aspects of the COL4A1/2 SVD disease phenotype were reproduced *in vitro*. COL4A2^{G702D} BMEC exhibit lower tight junction protein expression; while COL4A1^{G755R} BMEC demonstrate discontinuous tight junctions. COL4A2^{G702D} BMEC also show defective P-glycoprotein (P-gp)-mediated Rhodamine123 efflux compared to the isogenic control, which is suggestive of a transport deficiency across the barrier. COL4A1^{G755R} and COL4A2^{G702D} BMEC and MC have increased levels of MMPs. Notably, these findings replicate what is seen in patients, strengthening the hypothesis that matrisome alterations are important in SVD.

Acknowledgements

I would like to extend my sincere thanks to my supervisor, Dr Alex Granata, for the unlimited help, advice, support and encouragement she has provided over the past three years. Throughout the course of my PhD, she has passed on a wealth of knowledge, from detailed experimental techniques, to scientific writing, project management and everything in between; and for that I am truly grateful.

Thank you to the past and present members of our laboratory group, Dominika Krzyzanska, Yiannis Kasioulis, Maha Al-Thani and especially Krushangi Patel, for all her assistance on the Collagen IV project. It has been a pleasure to have worked with you all.

Thank you to Prof. Hugh Markus for his guidance, support and enthusiasm for our work in the *in vitro* disease modelling group. Also, to the other members of the Stroke Research Group for their insightful discussions on SVD from a clinical perspective. Also, to Dr Helle Jørgensen, my PhD Adviser for her reassurance and encouragement.

Thanks to Dr Sanjay Sinha for his support and invaluable feedback on the progress of my research. Also, to members of his laboratory group, especially Dr Hongorzul Davaapil, Dr Maria Colzani, Dr Aishwarya Jacob and previous members Dr Will Bernard and Dr Felipe Serrano who have all taught me various experimental techniques over the years.

Thank you to Dr Magda Gerigk for her valuable input and time spent making and testing the engineered microfluidic system. I am grateful for all the bioengineering knowledge she has passed on to me. In addition, thank you to our collaborators in the Vascular Dementia programme, in particular, Dr Adam Mitchell and Prof. Tao Wang who hosted me in Manchester last year. My gratitude also goes to the funding bodies that have enabled this work to take place: Rosetrees Trust, British Heart Foundation, Alzheimer's Association and Stroke Association.

To my family, especially my parents, who have supported me so far and continue to encourage me. Finally, to my husband Christopher. Thank you for the many times you listened to my presentations, the countless weekends you waited for me to feed cells and for putting things on hold for this to be completed. Your infinite support has been essential for maintaining my motivation and mental health.

Abbreviations

BBB – Blood brain barrier

BM - Basement membrane

BMEC – Brain microvascular endothelial cell

CADASIL - Cerebral Autosomal Dominant Arteriopathy with Subcortical Infarcts and Leukoencephalopathy

CARASIL - Cerebral autosomal recessive arteriopathy with subcortical infarcts and leukoencephalopathy

CSF – Cerebral spinal fluid

CRISPR - clustered regularly interspaced short palindromic repeats

CT - Computed Tomography

ECM - Extracellular matrix

ER - Endoplasmic reticulum

FGF – Fibroblast growth factor

GFAP - Glial fibrillary acidic protein

GPCR - G-protein coupled receptor

gRNA – guide RNA

HANAC - Hereditary angiopathy with nephropathy, aneurysms, and muscle cramps syndrome

hiPSC – human induced pluripotent stem cell

HK – Housekeeping

HUVEC – Human umbilical vein endothelial cells

MACS – Magnetic activated cell sorting

MC – Mural cell

MEF – mouse embryonic fibroblast

MMP – Matrix metalloproteinase

MRI – Magnetic Resonance Imaging

mRNA – Messenger RNA

mtDNA – Mitochondrial DNA

NaFl – Sodium Fluorescein

NIM – Neural induction media

NMM – Neural maintenance media

NSC – Neural stem cell

NVU – Neurovascular unit

PAM - Protospacer Adjacent Motif

PDMS – Polydimethylsiloxane

P-gp – P-glycoprotein

qRT-PCR – Quantitative real-time PCR

R123 – Rhodamine123

RA - Retinoic Acid

sgRNA – Synthetic guide RNA

SHRSP - Spontaneously hypertensive stroke-prone rat

siRNA – short interfering RNA

SMC – Smooth muscle cell

SVD – Small vessel disease

TEER – Transendothelial electrical resistance

TNF – Tumour necrosis factor

tRNA – Transfer RNA

UTR – Untranslated region

VCI - Vascular cognitive impairment

VEGF - Vascular endothelial growth factor

WMH – White matter hyperintensity

WT - Wild type

Contents

List of Figures

List of Tables

Chapter 1: Introduction

1.1 Small Vessel Disease

Cerebral small vessel disease (SVD) is a broad all-encompassing term for pathology affecting the small vessels[1]. These include capillaries, arteries, venules and arterioles[1,2] which range in size from 50 to 400μm[2]. Clinical presentation of SVD is heterogeneous and can differ greatly between individuals[3]. SVD causes 25-30% of all strokes[1,4] and contributes to 45% of total dementia cases[5]. Vascular dementia, predominantly caused by SVD[6,7], is the second most common form of dementia after Alzheimer's disease[6]. Other clinical features of SVD include cognitive decline, mood disorder and pre-disposition to depression[1]. Gait problems, resulting from disruption of white matter integrity[8] have also been reported in SVD patients, with a shortening of stride length and reduced gait velocity[8]. Ultimately, SVD leads to morbidity earlier in life and increased mortality[9,10].

1.1.1 SVD pathology

Clinical features

Much of the initial SVD research studies relied on post-mortem analysis of affected individuals[11] to assess small vessel changes, since it is not possible to directly visualise microvasculature within the brain *in vivo*[11]. For this reason, little is known about the series of events preceding clinical decline and eventual mortality[12]. Thus, efforts to study and diagnose SVD depend heavily on neuroimaging. Although highly informative, this technology still does not offer detailed understanding at the macroscopic level of small vessel degeneration[11].

Neuroimaging tools employed in the research and diagnosis of SVD predominantly include Computed Tomography (CT) and Magnetic Resonance Imaging (MRI)[11]. SVD can present with a plethora of features (Figure 1.1), including white matter hyperintensities (WMH), which are classified as areas of hyperintensity on MRI correlating with increased risk of stroke and dementia[10]. Perivascular (Virchow-Robin) spaces, which are usually too small to be visible on neuroimaging, enlarge in SVD and become visible (usually 2mm)[13]. Lacunar infarcts are characterised by a 3-15mm rounded or oval fluid-filled cavity[14] caused by a sub-cortical infarct[15]. At the smaller end of the scale, cerebral microbleeds are visible 2-5mm hypointense regions[14].
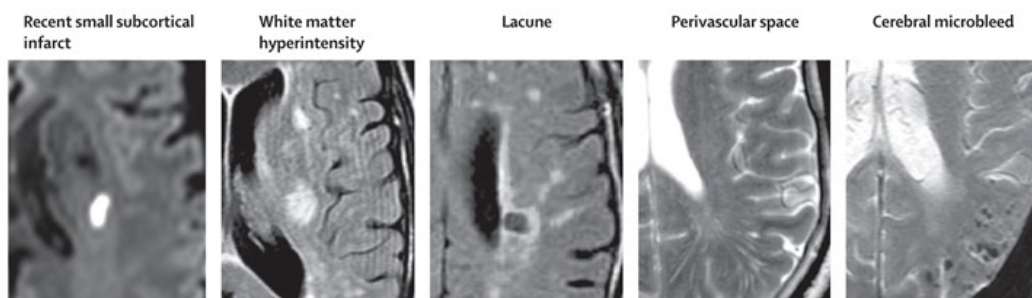
Figure 1.1 Neuroimaging features of SVD: including subcortical infarcts, WMH, lacunes, enlarged perivascular spaces and microbleeds; modified from[14]

Current treatments

Treatments for SVD currently centre around controlling risk factors with the aim of preventing a neurological event such as a stroke (reviewed by Bath and Wardlaw in 2015[16]). These include anticoagulants such as Warfarin or Aspirin, administered to reduce the risk of atrial fibrillation, but that convey no proven benefit specifically in SVD patients[16]. A common Alzheimer's Disease treatment, acetylcholinesterase inhibitors (AChEI), has been trialled in SVD patients, but also offers limited cognitive benefit for SVD patients[16]. One of the problems in treating SVD is that it is a chronic disease, and some treatments must be given acutely. For example, tissue plasminogen activator, used to treat ischaemic stroke, is only effective if administered within a few hours of the event[17]. Moreover, the lack of consensus on clinical sub-grouping of SVD cohorts, could complicate the interpretation of clinical trial data[18]. This lack of consensus is likely a result of the variation in neuroimaging capture method, analysis and agreement on SVD-specific features, between different groups[19]. Recently, in 2013, the authors of a review attempted to standardise the classification of SVD using neuroimaging features[19].

A staggering number of SVD patients go on to decline cognitively, despite interventions to reduce the risk of stroke[18]. Although, the authors of a recent review identify four drugs currently undergoing clinical trials, which may hold promise in the future, current treatments only treat symptoms, with little proven long-term benefit[18]. Hence, the requirement for understanding of the molecular changes in SVD is paramount[18] in order to generate new, disease modifying therapies to halt the debilitating effects of SVD. Multiple types of SVD have been identified, which complicates understanding of the molecular mechanisms.

1.1.2 Types of SVD

Sporadic

Sporadic SVD likely arises as a result of a myriad of environmental and genetic risk factors[1,20]. Age is a key contributor to sporadic SVD incidence, with around 80% of 65-year

olds displaying SVD pathology[21] and increasing lesions of white matter with advancing age[22]. Since age is a key contributor, incidence of sporadic SVD is on the increase, given the trend of an aging population[23]. Although, increased reporting could also serve as an explanation, resulting from advances in MRI and better detection of SVD[24]. Another non-modifiable contributor to SVD is genetic risk factors, including variants in *TREX1*[25], *COL4A1/2*[26], *HTRA1*[27] and *NOTCH3*[21]. Besides this, large studies have highlighted the inheritance of SVD traits, for example, heritability for WMH is in the region of 45-73%[24,28].

The main modifiable risk factor of sporadic SVD is hypertension, which, along with dietary salt intake, has been shown to correlate with SVD and WMH[29]. Other risk factors that can contribute include smoking, diabetes, atrial fibrillation, obesity and dyslipidaemia[30,31]. Concordantly, one of the main approaches to treating sporadic SVD is the control of these modifiable risk factors[2]. However, SVD caused by genetic factors is the main cause of stroke in young individuals (under 45 years old) and cannot be managed by controlling risk factors[32]. Moreover, the incidence of stroke in young people is not decreasing, and may even be increasing[33], which contributes to the need for identifying new therapies[18].

Monogenic

Besides sporadic SVD, a number of monogenic, or single-gene disorders causing SVD have been identified. These rare mutations are causal to around 1.5% of strokes in SVD[34], particularly affecting young people[32]. Increasing numbers of conditions are reported, with the progress of genetic testing and in conjunction with increased awareness of SVD as a potential cause of early-onset strokes. The most common form of monogenic SVD is cerebral autosomal dominant arteriopathy with subcortical infarcts and leukoencephalopathy (CADASIL)[11,35], which is caused by mutations in the *NOTCH3* gene[36]. These mutations, mostly affecting the extracellular domain, result in deposition of granular osmiophilic material (GOM)[35]. Migraine, memory impairment, ischaemic stroke, apathy and depression are all common features of CADASIL[11,37]. The recessive condition of the same name, cerebral autosomal recessive arteriopathy with subcortical infarcts and leukoencephalopathy (CARASIL) is caused by mutations in *HTRA1*, encoding a secreted enzyme HtrA Serine Peptidase 1[38]. *HTRA1* plays a role in TGFβ signalling[38] and missense mutations prevent *HTRA1* from repressing TGFβ signalling[38]. The final leukoencephalopathy is Cathepsin A-related arteriopathy with strokes and leukoencephalopathy (CARASAL), caused by mutations in *CTSA*[39], encoding cathepsin A.

Other monogenic SVDs include frame-shift C-terminal mutations in *TREX1,* a DNA exonuclease repair enzyme[40], which is causal to retinal vasculopathy with cerebral leukodystrophy (RVCL), presenting with loss of vision, stroke and dementia in middle age[40]. Mutations in *FOXC1* give rise to SVD presenting typical SVD neuroimaging features[41] with

WMH and lacunar infarcts[42] as well as glaucoma[43]. FOXC1 mutations also implicate the transcription *PITX2* in pathology of the disease[42]. Mutations in mitochondrial DNA (mtDNA) can also cause SVD. Mitochondrial encephalopathy with lactic acidosis and stroke-like episodes (MELAS) is caused by mutations in mtDNA transfer RNA (tRNA)*Leu(UUR)* [32] and presents with abnormal mitochondria in endothelial cells[44]. Sex chromosome mutations have also been associated with SVD. Fabry Disease is a an X-linked lysosomal storage disorder[20] caused by mutations in *GAL*[32] and occurs with changes in white matter that arise in adulthood[32,45].

Lastly, the focus of this work is on *COL4A1* and *COL4A2* mutations, which present with intracerebral haemorrhage[46] and porencephaly[47,48]. COL4A1/2 SVD differs in the age of onset, although is more prevalent in young patients[49]. COL4A1/2 SVD is discussed in detail in *part 1.4.*

Clinical overlap of sporadic and monogenic SVD

Sporadic and monogenic forms of SVD display much clinical overlap, including subcortical infarcts and white matter damage[1,50]. The two types of SVD are virtually indistinguishable, save for the earlier onset that is typically observed in monogenic forms[37,51]. The identification of genetic variants in stroke populations, some of which are in genes causal to monogenic SVD, further highlights the possibility of a shared mechanism in monogenic and sporadic SVD[51]. One of the main overlapping phenotypes in sporadic and monogenic SVD is blood-brain barrier (BBB) leakage[52].

Involvement of the BBB in SVD

BBB leakage increases with age[52] and is further exacerbated in SVD[53]. Animal models such as the spontaneously hypertensive stroke-prone rat (SHRSP) have shown that early endothelial cell damage can lead to red-blood cell accumulation and angiopathy[54]. The authors suggest that this early BBB leakage is causal to the observed SVD symptoms[54].

Methods used in SVD patients to demonstrate increased BBB permeability primarily involve measuring the level of albumin present in the cerebral spinal fluid (CSF) relative to the plasma[52]. MRI experiments using the tracer Gadolinium have also been employed, in which a diffuse increase of Gadolinium in white matter and CSF is observed in SVD, relative to controls[7]. One such experiment demonstrated that SVD patients with lacunar stroke had a more permeable BBB than those who suffered large artery stroke[7]. However, it is likely that these studies under represent the true extent of BBB breakdown, since tracers such as Gadolinium have limited sensitivity for lower levels of passage out of a vessel[55,56]. COL4A1/2 present similar disruption of the BBB comparable to sporadic forms[49,51,57]. Widespread BBB

disruption was demonstrated in the Col4a1[+/G498V] mouse with Evans Blue and FITC-Albumin leakage out of vessels[58].

In a 2016 review, the requirement for further research into the role of the BBB in SVD pathogenesis was highlighted[59]. Furthermore, BBB disruption has been reported in other neurological disorders, such as Alzheimer's disease[11], Multiple Sclerosis[60] and vascular dementia[5], thus we envisage wider implications of this study. The BBB is a complex, multifaceted system and thus far, there is a lack of comprehensive studies assessing the relationship between SVD and BBB leakage[61].

1.2 The blood-brain barrier

1.2.1 Structure and function

Seminal findings in the late 19th Century and the turn of the 20th Century by Ehrlich and Goldmann[62] introduced the concept of a barrier between the blood and the brain by demonstrating, for the first time, that injection of a dye into the brain did not pass into the CSF and *vice versa*[63]. Stern, in 1921, first used the term "blood-brain barrier" (BBB), to describe such a phenomenon[62]. In the intervening 100 years, great advances have been made towards understanding the role of the BBB.

The BBB contributes to the maintenance of the cerebral environment[64]. Contrary to earlier belief, it is more than a physical barrier, since it dynamically removes waste from, and delivers nutrients to, the neural tissue[65]. The interaction of multiple cells types of the BBB, primarily endothelia, astrocytes and pericytes (**Figure 1.2**), but also microglia and neurons, along with the surrounding basement membrane (BM), form the neurovascular unit (NVU)[66,67]. The collective result of this myriad of cell types and structural proteins, is the prevention of paracellular transport across the BBB[68], thereby forcing transcellular passage. Most small molecules of between 400-500Da will only pass through paracellularly if they are lipid soluble[69]. Although, gases and small lipids are able to transit[68]. In the brain vasculature, there is limited trans- and para-cellular transport, compared to endothelial barriers elsewhere in the body[63], regulated by the tight junctions of the BBB, which also interact dynamically with the actin cytoskeleton and adherens junctions[70].
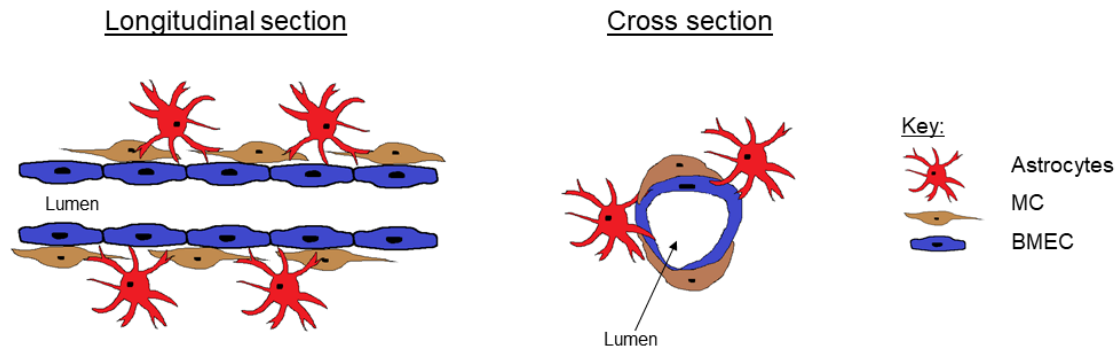
Figure 1.2 Schematic of the BBB: Longitudinal and cross-sections of a cerebral vessel with BMEC, astrocytes and MC

1.2.2 Cell types of the BBB

Brain microvascular endothelial cells

The prominent cell type forming the BBB is brain microvascular endothelial cells (BMEC). BMEC express many transmembrane and cell surface proteins that collectively contribute to the highly specialised function of the BBB. Especially, tight junctions between neighbouring cells are found at endothelial barriers throughout the body, but in the case of the BBB, they are especially restrictive, dramatically reducing the paracellular transport into the brain parenchyma[63,71]. This gives rise to the 'tightness' of the barrier, which can be measured experimentally using transendothelial resistance (TEER). TEER is used as readout for barrier tightness by using electrodes either side of a culture membrane to compute voltage into resistance[72,73]. *In vivo*, estimated values for the rat BBB are around $2000\Omega xcm^2$ [74,75], but could be as high as $8000\Omega xcm^2$ in humans[76,77].

Tight junctions are formed by transmembrane proteins that span the gaps between adjacent cells and include the claudins (1,3,5 and 12), occludin and Junctional Adhesion Molecules (JAMs)[71] (**Figure 1.3**). Of the claudins, claudin-5 plays a particularly important role at the BBB, demonstrated by loosening of the BBB in claudin-5 deficient mice[78]. The other cell-cell contact mediators include adherens junction proteins such as vascular endothelial (VE)-Cadherin and N-Cadherin[71]. CD31 (*PECAM1*), another adherens junction protein[79] (**Figure 1.3**), is important for stabilisation of the endothelial cells[80] with roles in mechanosensing and vascular remodelling[80,81]. Along with these tight junction and adherens junctions proteins, membranous transport proteins and receptors also contribute to BMEC function[71]. Sodium-independent transmembrane glucose transporters, such as GLUT1 (**Figure 1.3**), play a vital role in delivering nutrients to the neural tissue[82].

Efflux transporters, such as p-glycoprotein (*ABCB1;* **Figure 1.3**) are of particular importance for extruding waste products from the CNS[79,83]. P-glycoprotein is a transmembrane efflux transporter with two ATP-binding sites[84] and is part of the ATP-binding cassette (ABC) family[85]. Members of the ABC family are responsible for clearing non-natural compounds[86]. For this reason, their function has garnered much attention in the context of drug delivery across the BBB[87]. They are also heavily researched in the context of multi-drug resistant cancerous tumours, where P-glycoprotein (P-gp) is highly expressed on the surface (**Figure 1.3**), hence it also named multidrug resistance protein 1 (MDR1)[88]. A universal knockout mouse (mdr1a-/-) is substantially more sensitive to neurotoxic compounds, despite appearing unaffected in the resting state[89,90], highlighting the role of P-glycoprotein in neuroprotection. This is an alternate mechanism to paracellular leakage of the BBB caused by loosening of the tight junctions. P-gp extrudes toxic compounds, so when knocked out, the removal process does not occur and compounds can accumulate in the endothelial cells, causing failure[90]. However, little is known about the role of P-gp in stroke, with one report suggesting that P-gp increased in a rat model of cerebral ischaemia[91].

Other members of the family are breast cancer resistant protein (BCRP; named after the location of its original discovery)[87] and multidrug resistance associated protein (MRP)[92]. P-glycoprotein and BCRP are expressed on the luminal side of BMEC[71,87], whereas MRP is expressed on both the blood and brain sides[71,79,87] (**Figure 1.3**). As a result, BMEC are polarised in the apicobasal direction[93]. Although a feature of endothelial cells in other tissues, apicobasal polarisation is more pronounced in brain endothelial cells[93].

Cluster of differentiation (CD) proteins, in particular, CD34, are highly expressed at the cell surface[94]. They have roles in angiogenic processes, such as migration, in cerebral vessels[95]. Besides cell surface proteins, Zonula occludins such as ZO-1 are localised to the cytoplasm (**Figure 1.3**) and associate with the Claudins and occludin[96], acting as intermediaries to the cytoskeleton[64]. Together, this complex network of proteins is responsible for the restrictive function of BMEC.
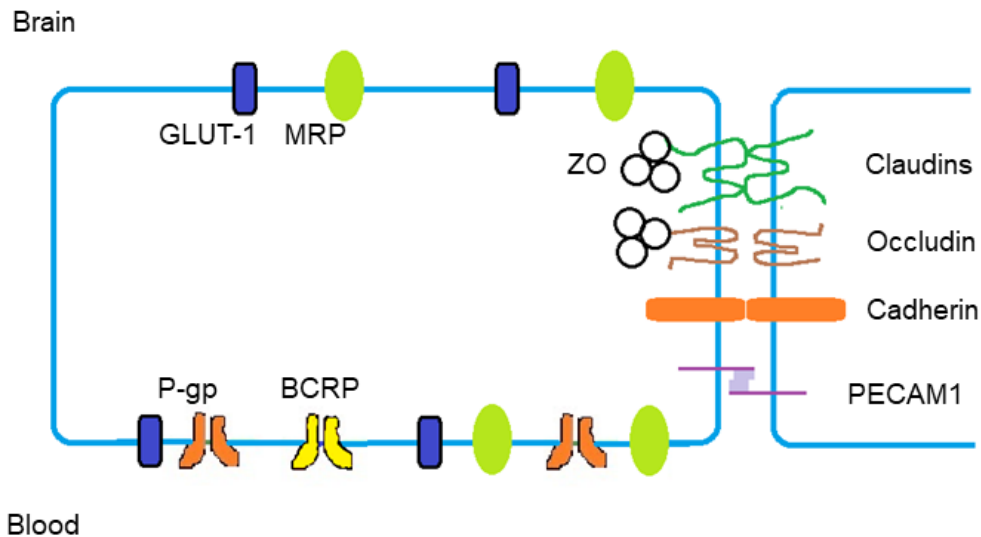
Figure 1.3 Tight junction and cell surface organisation of BMEC: displaying the location of transporters GLUT-1, MRP, P-gp and BCRP as well as tight junction proteins occludin, Claudins, Cadherins and PECAM-1 (modified from[71,79])

Astrocytes

Another key cell type of the BBB is astrocytes, which are part of a large family of glial cells that also includes oligodendrocytes and microglia[97]. Of the astrocyte group, eight out of 11 sub-types have been shown to directly associate with BMEC[68]. Astrocytes contribute to the function of the BBB in a number of ways. Firstly, they secrete matrix proteins, creating a layer of the BM[93]. Astrocytes also contact onto BMEC with end-feet processes[68], surrounding smaller capillaries[65,98], which promotes neurovascular coupling[99]. Astrocytic end-feet express high levels of the water channel Aquaporin 4 and potassium channel Kir4.1, contributing to ion exchange with BMEC[68]. Besides physically mediated effects, astrocytes release cytokines, such as fibroblast growth factor (FGF), angiopoetin-1 and glial-derived neurotrophic factor[65,68,100]. Astrocytes also release vascular endothelial growth factor (VEGF)[101], which is required for embryonic endothelial cell development[102]. It is by the release of cytokines that astrocytes elicit paracrine effects on BMEC, enhancing BBB properties[103]. Astrocyte conditioned media promotes BBB properties *in vitro*[104] and treating non-brain endothelial cells with astrocytic factors can induce the formation of tight junctions and the expression of P-gp[103,105].

Relatedly, astrocytes can also contribute to regulating blood flow in small vessels, since levels of intracellular Ca^{2+} at end-feet fluctuate in response to neural stimuli[65,106]. Hence, astrocytes play an important role in barrier maintenance[101]. Glial fibrillary acidic protein (GFAP) is a widely accepted marker of astrocytes[107], but Aldehyde dehydrogenase family 1

member L1 (ALDH1L1), the early marker S100β[108] and membranous marker Aquaporin 4[109] are also commonly used.

Unlike pericytes, astrocytes are not thought to contribute greatly to the embryonic development of the BBB and are more associated with maintenance[110]. Although, in harmony with pericytes, they release Wnt signalling molecules, suggesting there is a complex interplay of astrocyte and pericyte-mediated effects early in development[70].

Pericytes

Pericytes are contractile[111,112] vascular cells, located between astrocytes and BMEC[113] at the small vessels of the brain[114]. Together with smooth muscle cells (SMC), they are termed mural cells (MC), owing to their location within the BM[115]. Vascular SMC and pericytes originate from different embryonic lineages[116]. In the forebrain MC typically originate from the same embryonic lineage, the neuroectoderm[115], via neural crest [117]. Although, there are also mesoderm-derived pericytes in other regions of the brain[117,118]. SMC surround larger vessels, such as arterioles and arteries[65], whereas pericytes associate with small vessels such as capillaries.

Pericytes control blood flow[119], encase BMEC and stabilise the BBB[11,113]. They communicate with the endothelium, elicited through the production of platelet-derived growth factor B (PDGF-B) by BMEC, which acts as a ligand for the PDGFR-β receptor on pericytes[120,121]. Indeed, PDGF-B null mice (Pdgfrb$^{-/-}$) have improper BBB formation, demonstrating that pericytes are essential for neurovascular development[110]. Pericytes also control expression of tight junction markers and transport between adjoining BMEC[110,122].

A commonly used marker of pericytes *in vivo*, α-smooth muscle actin (αSMA)[111], is non-specific since it also expressed in SMC[115]. Other markers found across vascular cells include Desmin, Nestin and Vimentin[115], which are also shared between SMC and pericytes[115]. Along with the marker PDGFR-β, pericytes express cell surface proteins such as RGS5 and NG2[123,124]. However, none of these markers are exclusive to pericytes, so using a panel of multiple markers might help to distinguish pericytes from SMC[115].

Though limited, there are some distinguishing morphological features of pericytes, separating them from SMC. Pericytes have rounded nuclei, wrapping around small vessels longitudinally, whereas elongated SMC have flattened nuclei and extend their length in a perpendicular direction across vessels[115].

1.2.3 The matrisome

The non-cellular component of the BBB, collectively termed the 'matrisome', refers to the proteins comprising, and those associated with, the ECM[125]. In this case, since the ECM

resides in contact with BMEC and has a more specialised function, it is referred to as the BM[126]. Collectively, cells of the BBB, along with the BM, form the NVU. As previously mentioned, collagen IV forms half of the BM[127,128], interacting with other components[129] which include perlecan, fibronectin, nidogen and laminin[126] (**Figure 1.4**). These proteins are secreted by cell types of the BBB, including BMEC, pericytes and astrocytes[126]. Together BM proteins form a thin layer[65] between cells, which is around 100nm thick[130,131]. The ECM comprises approximately 300 proteins[132], whilst BM associated proteins contained within the all-encompassing term of 'matrisome', number as many as 800[129].
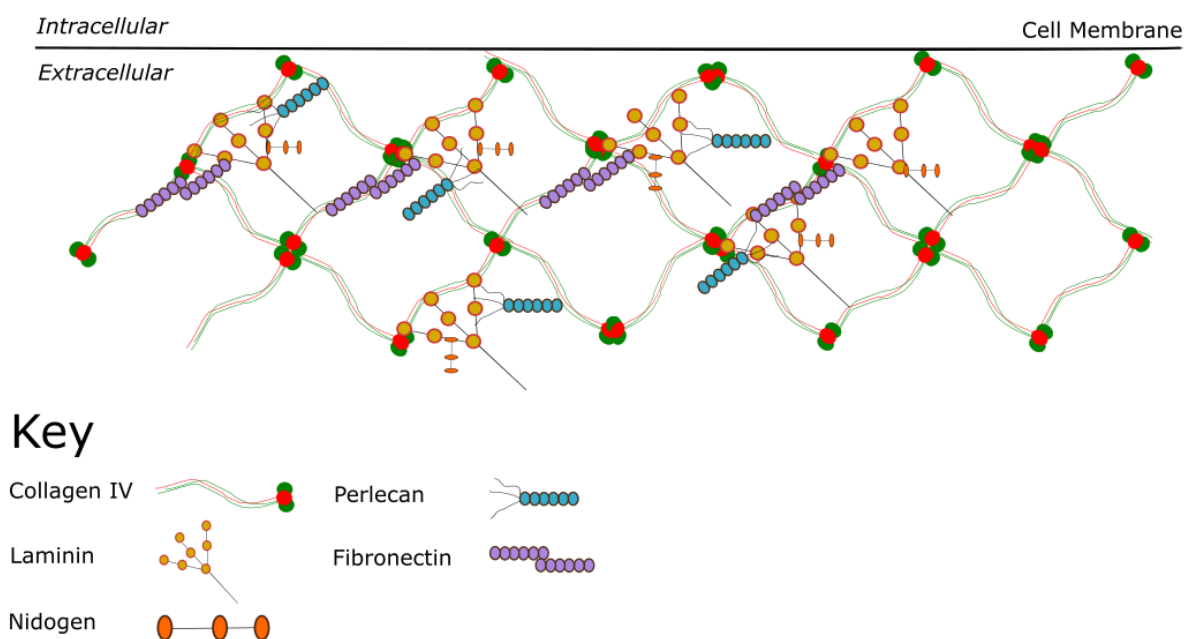
Figure 1.4 The core components of the BM: adapted from[127,133–135]

Other than its architecturally supportive role, the BM contains an array of proteins that mediate cell-cell communication[130] and cells of the BBB bind to BM components through integrins[136]. To illustrate, astrocyte-BMEC crosstalk is influenced by the BM proteoglycan agrin[64] that tethers astrocytic end feet to the BMEC, through its interaction with Aquaporin 4[137]. Evidenced by the debilitating effects of COL4A1/2 mutations, the matrisome plays a key role in cerebral vasculature, despite the little attention it has garnered compared to the cellular constituents of the BBB[126].

Matrisome proteins are continually degraded and replenished, maintaining homeostasis of the BM under a tightly controlled process[132,138]. Hence, disruption to this process and imperfect ECM remodelling is implicated in many disease[132] such as cancer and

fibrosis[132,139]. Matrisome malformation has also be postulated as a potential mechanism in SVD[129,140].

1.3 Matrisome defects as a shared mechanism in sporadic and monogenic SVD

1.3.1 The role of the matrisome in SVD

In monogenic SVD, a central hypothesis of matrisome alteration, either directly or indirectly could account for pathogenesis. Indirectly, in CADASIL, defected NOTCH3 extracellular domain (ECD) recruits ECM proteins and accumulates as GOM deposited in the BM[129,141] (**Figure 1.5**). Similarly, in CARASIL, the HTRA1 serine protease is an ECM regulator[132]. HTRA1 targets latent TGF-β binding protein 1 (LTBP1)[142], an extracellular matrix protein and key regulator of TGF-β bioavailability[129,143] (**Figure 1.5**). Furthermore, in the context of FOXC1 SVD, BM defects are present in a zebrafish Foxc1 knockdown which displays cerebral haemorrhages, suggesting an essential role for Foxc1 in the integrity of the BM[144]. Concurrently, matrix metalloproteinases (MMPs) which are regulators of the BM[145], are increased in a neural crest Foxc1$^{-/-}$ mouse model[146], suggesting an indirect role of matrisome alteration in patients with *FOXC1* mutations[129].

In contrast, COL4A1/2 mutations directly affect matrisome homeostasis, since COL4A1/2 contributes greatly to the BM[127,128]. In COL4A1 mutations, BM defects are prevalent manifestations of collagen IV SVD, evident in electron microscopy of kidney and skin biopsies[129,147]. Concordantly, COL4A2 mutations also give rise to BM aberrations[48] and these BM defects could explain the involvement of ocular and renal symptoms in COL4A1/2[46,129]. Thus, these manifestations highlight collagen IV as an ideal model to probe BM pathology in monogenic SVD.
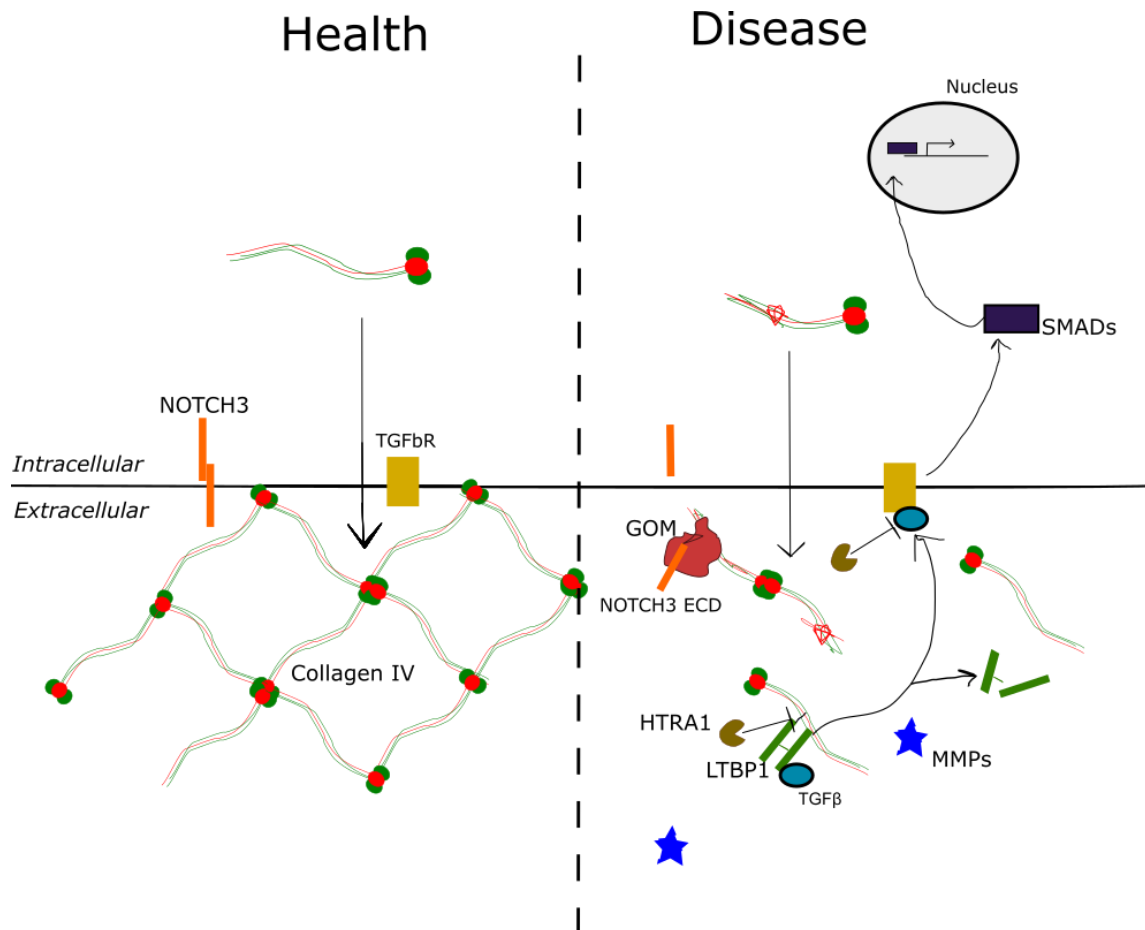
Figure 1.5 The convergent pathways of monogenic SVD: The pathogenesis of CADASIL, CARASIL and collagen IV with hypothesised convergent pathways of matrisome alteration, through interaction with TGFβ, MMPs and the SMAD pathway (Based on[11,46])

Concordantly, BM alterations are also evident in sporadic SVD[148]. These can manifest as thickening of the BM, changes to the elastic lamina and an increased deposition of collagen[149]. Moreover, a key risk factor of SVD, hypertension, causes narrowing of the vessel lumen, a process in which MMPs have been implicated[129,150]. Long-term effects of hypertension can result in remodelling of the ECM as well as aberrant elastic fibre formation[151]. ECM dysregulation has also been associated with aging[138], another risk factor for sporadic SVD[21].

This clinical overlap strengthens the argument that matrisome changes are involved in both forms of SVD[21]. Along with the knowledge that COL4A1/2 variants are associated with sporadic SVD[152]. In the context of cerebral SVD, matrisome defects could affect the integrity of the BBB[153]. Therefore, the BBB is a promising target to probe the hypothesis that matrisome alterations are causal to shared sporadic and monogenic SVD pathology[154]. Because of this overlapping pathology, findings in monogenic SVD could generate insight

into sporadic disease[1] and elucidate potential disease-causing mechanisms. As previously described, matrisome protein deposition and degradation is a tightly controlled process[132,138] which is in part maintained by MMPs[145]. Hence, the abnormal matrisome in SVD could suggest a role for MMPs in SVD[155–157]. Although, currently there is a lack of detailed understanding of this interaction[157].

1.3.2 The role of MMPs in stroke and SVD

MMPs

MMPs are zinc-dependent enzymes that break down ECM proteins[145] from their location on the cell surface[158]. MMPs are typically classified as gelatinases, stromelysins, matrilysins or collagenases, depending on their targets[145]. However, there are many MMPs that have multiple targets and some ECM proteins can be digested by more than one MMP[145,158]. collagen IV is a substrate for collagenases MMP2, 9 and MMP10[158,159]. The regulation of MMPs is in part controlled by tissue inhibitors of MMPs (TIMPs)[160]. MMPs and TIMPs can also have complementary functions and be recruited together to elicit matrisome degradation. For example, MMP14 works synergistically with TIMP2 to activate MMP2[161–163]. MMPs, in particular MMP1, play a role in fragmentation of collagen during aging[138,164] but are also involved in disease processes. For example, joint increase of MMP2 and MMP9 has been associated with reduced collagen IV in multiple disease states such as cancer[165] and reperfusion injury[166]. With relevance to stroke and SVD, MMP2 plays a particular role in the BM, degrading collagen IV[167,168], but MMP3 and MMP19 are also abundant in the BM[169,170].

MMPs in stroke and SVD

Along with ECM remodelling, MMPs can degrade tight junctions[171,172], therefore signifying their involvement in BBB breakdown[155,156]. MMPs have long been suggested as regulators of BBB opening in the context of stroke[173]. Concordant with this, occludin increases in the blood of patients after ischaemic stroke[156,174]. Specifically, occludin is a target of MMP2 and 9[175,176] and its reduction has been associated with increased MMP14[177], owing to the role of MMP14 in activating MMP2[161,163]. claudin-5 has also been implicated as a substrate for MMPs, with ischaemic stroke prompting re-distribution away from the cytoskeleton in the presence of secreted MMP2 and 9[175]. Additionally, on application of the inflammatory stimulus lipopolysaccharide (LPS), a mouse model of ischaemic stroke displayed tight junction disruption in concordance with raised MMP9[178].

More broadly, patients with vascular cognitive impairment (VCI) resulting from SVD exhibit increased MMPs in CSF[155]. In particular, MMP3 activity was significantly increased compared to controls and MMP9 non-significantly increased[155]. Interestingly, the albumin ratio, used as a measure of BBB leakage, correlated with decreasing levels of MMP2[155]. The

involvement of MMPs in stroke has also been heavily studied in the context of post-stroke administration of tissue plasminogen activator[179]. By activating MMPs[180], tissue plasminogen activator worsens BBB leakage[179]. MMPs are also increased in ischaemic stroke[17]. In particular, MMP2 is affected in the acute stages of ischaemic stroke[17,181] whereas MMP9 is thought to play a role in both the acute[182,183] and secondary phases of BBB leakage[17,184]. Specific to this work, supernatant collected from COL4A2^{G702D} fibroblasts[48] had increased levels of MMP14 (Dr Tom van Agtmael, *Unpublished*).

Of the MMP inhibitors, TIMP3 is elevated in CADASIL patients and accumulates in cerebral vessels[129]. TIMP3 is also increased in the CADASIL mouse model TgNotch3^{R169C} [129,141]. Similarly, TIMP4 is increased in SVD patients with ischaemic stroke that display brain atrophy[157] and TIMP1, has a demonstrable role in ischaemic stroke in patients[185] and in a mouse model[17,186]. Thus, given the knowledge from patients and mouse models, MMPs could play a role in matrisome alteration and hence, BBB disruption. This also reveals MMPs as a potential target for therapeutic intervention.

MMPs as a target for therapy

Doxycycline is a tetracycline antibiotic and pan-MMP inhibitor[187]. It has a proven ability to reduce collagen IV breakdown in skeletal muscle injury, even in the absence of overall improvement to tissue damage[166]. Moreover, Doxycycline has been shown to improve outcomes of a mouse model of traumatic brain injury[188]. With particular relevance to stroke, Doxycycline reduced vascular remodelling in the SHRSP model[187].

Besides Doxycycline, a number of small molecules and antibodies to MMPs have been trialled in cancer treatment, although these were all unsuccessful[189]. These failings highlight the complex interplay of MMPs in homeostasis and the consideration that must be given to the potential disruption of beneficial roles of MMPs[189]. In another context, MMP levels must be considered prior to application of certain treatments. For example, MMP9 level correlates with poorer outcome in patients treated with tissue plasminogen activator[190,191]. With rigorous understanding of the underlying cellular mechanisms, MMPs could offer a target for therapy and a reductionist monogenic model could serve as an ideal method in which to explore the complex interplay of MMPs and TIMPs.

1.4 Type IV Collagen and COL4A1/2 SVD

1.4.1 Collagen IV α1 α2 protein

The *COL4A1* gene (containing 52 exons[192]) and the *COL4A2* gene (containing 48 exons[46]) are located in the q34 region of chromosome 13 in humans[46] (**Figure 1.6**), with a shared promoter[193]. The sequences for human *COL4A1* and *COL4A2* are highly conserved across species[46] and are 45% the same[194].

Within the endoplasmic reticulum (ER), collagen IV α1 and collagen IV α2 form a heterotrimer, consisting of two chains of α1 and one chain of α2, (e.g. α1α1α2; **Figure 1.6**)[195,196].

The ER is an integral part of collagen formation, where a plethora of chaperones and enzymes modify procollagen into the final secreted form (extensively reviewed in[197]). Helical formation is initiated by the non-collagenous domain (NC1) at the carboxy terminus[198] and terminates at the 7S domain at the amino end[199] (**Figure 1.6**). The third and final component, the collagenous domain, accounts for 90% of the protein[200]. It encompasses Gly-Xaa-Yaa repeats, (whereby Xaa and Yaa could be any other amino acid)[201], essential components for folding of the triple helix[202]. Following heterotrimer formation, collagen IV is secreted into the BM, constituting around half of the total protein[127,128]. Out of all collagen IV subtypes, the α1α1α2 form is most prevalent [203,204].
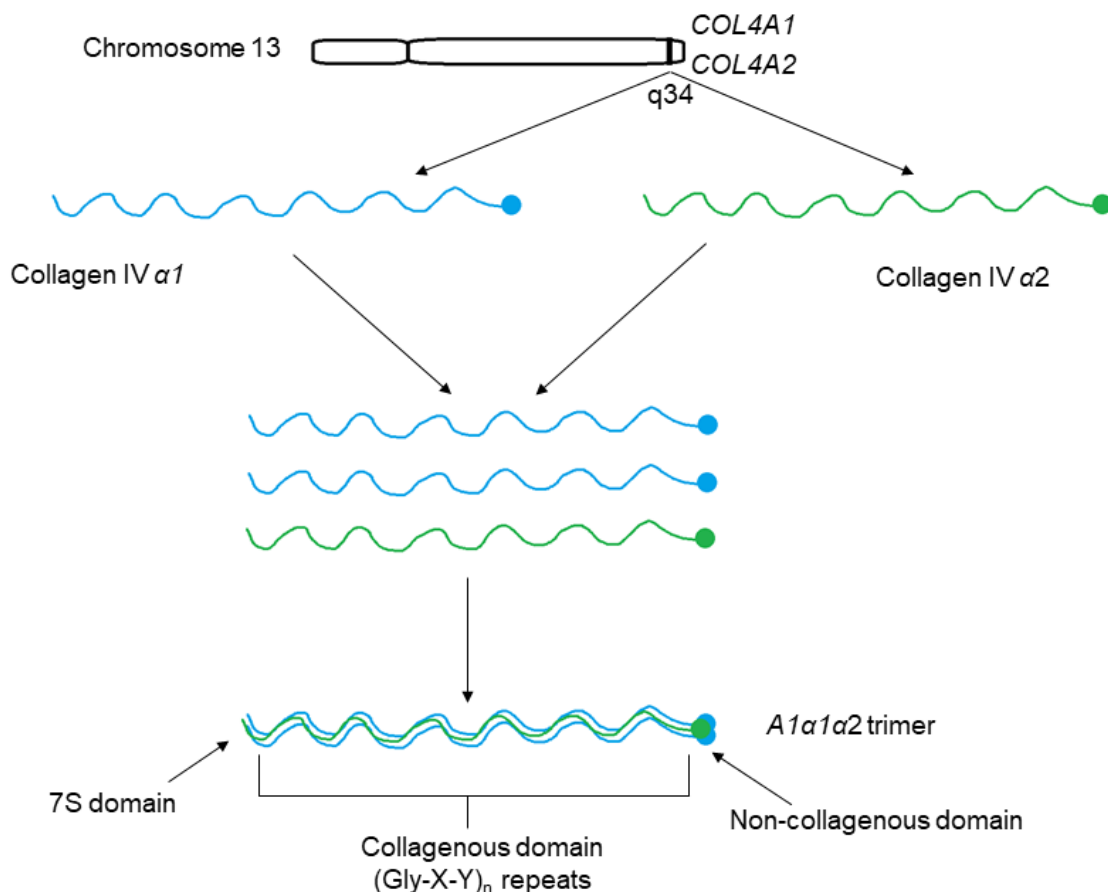
Figure 1.6 Collagen IV assembly: *COL4A1* and *COL4A2* genes are located on chromosome 13, giving rise to sub-chains α1 and α2, which form a triple helix. These chains contain a 7S domain, collagenous domain and non-collagenous domain[195,199,202]. Redrawn from[46].

1.4.2 COL4A1/2 SVD

COL4A1 and *COL4A2* mutations are penetrant and severe[51] and give rise to a plethora of clinical features, differing in the age of onset[49]. Besides broad SVD symptoms reported above, *COL4A1/2* mutations typically present with porencephaly (cerebral cavity)[47,48], perinatal stroke[205] and intracerebral haemorrhage[46]. COL4A1/2 SVD symptoms can occur in early age, even *in utero*, with haemorrhages visible neonatally[205]. However, others can present later in middle-age with only a single symptom [206] or even be asymptomatic[48].

Mutations in *COL4A1* can also lead to kidney, eye and muscle defects[207]. These features are collectively termed hereditary angiopathy with nephropathy, aneurysms and muscle cramps (HANAC) syndrome[147,208]. HANAC patients don't have reported neurological symptoms of small vessels[147,208,209], although the limits of neuroimaging mean that the absence of small vessel effects cannot be confirmed. Hence, it is currently unclear whether COL4A1 SVD and HANAC are distinct diseases with different causal mechanisms[207,210]. Typically, HANAC mutations are localised to the CB3(IV) region in *COL4A1*, a key integrin-binding site, leading some to speculate on a separate functional detriment in HANAC[147,208,209]. Alternatively, the apparently independent clinical syndromes of COL4A1 SVD and HANAC, could be the result of dosage-dependent effects in different tissues, owing to the varying collagen IV α-chain incorporation in different BMs[207]. For example, studies of COL4A1 myopathies suggest tissue-specific manifestations of COL4A1/2 mutations[207]. Although, in one family, the same missense mutation (COL4A1^{G1239R}) produced HANAC in the father but porencephaly in his daughter, which could highlight an important and often overlooked role of environmental influences in pathology[211].

Mutations in *COL4A1* and *COL4A2* were updated from a 2012 review[46] to include those published to present (**Tables 1.1** and **1.2**). For clarity, only those mutations with reported cerebrovascular presentation are included, e.g. not HANAC-causing mutations. There is a total of 66 reported mutations in *COL4A1* (**Table 1.1**) and 13 in *COL4A2* (**Table 1.2**) with SVD pathology. Misdiagnosis of SVD for other neurological conditions could prevent genetic testing, and thus underrepresent the incidence of monogenic SVD. For example, a medical history concordant with SVD in one family was originally misdiagnosed as multiple sclerosis[212].

One of the main features reported in neonates is schizencephaly (**Tables 1.1** and **1.2**). The COL4A1/2 mutation is likely to be causal to this phenotype[213] since vascular defects are a pathogenic cause of this neuroimaging feature[214]. Although, schizencephaly could also result from a past intracerebral haemorrhage during development[214], highlighting the difficulty of interpreting neonatal MRI findings captured long after the original insult. Similarly,

porencephaly is a prominent feature and could be the result of a haemorrhage during development[48]. Epilepsy or seizures have also been reported, which are suggested clinical presentations of COL4A1/2 SVD, in the absence of neuroimaging features[215].

Most mutations with cerebral SVD pathogenicity occur in a glycine (G) residue of the G-X-Y repeat[194]. Notably, often the neutrally-charged glycine residue[215,216] is replaced by aspartic acid (D) or glutamic acid (E), which are charged[194], or arginine (R) and valine (V) which are branched[194]. However, neutral amino acids, serine (S) and leucine (L) are also reported in place of glycine (**Table 1.1**), albeit less frequently[215,216]. In a recent review, it was suggested that glycine substitutions nearer the amino terminal end are less severe[194].

As an increasing number of mutations are reported, there are instances in which an amino acid at the same position is substituted with different amino acids, for example, COL4A1^{G882D} [217] and COL4A1^{G882E} [218] (**Table 1.1**). At position 498, two mutations are also reported, but in this case, one glycine becomes charged aspartic acid[208] and the other neutral valine[147,209]. Similarly, at the G1580 location, which is in the NC1 domain (**Figure 1.7**) three separate mutations are reported: arginine[205], serine[219] and alanine[220]. This corroborates the hypothesis that it is the disruption of a glycine that conveys pathogenicity, rather than the composition of its replacement[194].

Interestingly, two mutations that do not alter glycine residues (COL4A1^{M1016V} and COL4A1^{Q1316E}), but instead the 'Y' position in G-X-Y repeats, have not had SVD phenotype reported, but only eye and muscle presentations[200], which could be concordant with HANAC syndrome. In the same way, *COL4A2* mutations are also typically glycine substitutions but, thus far, there are no reported cases of substitution of a glycine for more than one alternate amino acid (**Table 1.2**). Of the frameshift mutations, both COL4A1^{G696fs} and COL4A2^{R1069fs} result in premature stop codons[47,221]. COL4A2^{R1069fs} causes a loss of COL4A2 chain synthesis from the affected allele[47] but the outcome has not been reported for COL4A1^{G696fs}. From the total reported (**Table 1.1** and **1.2**), frameshift mutations are less frequent than G-X-Y mutations. However, there is not enough evidence to suggest frameshift mutations cause a more severe phenotype.

COL4A2 mutations are more rare than *COL4A1* but present with a similar, albeit less severe phenotype[194]. The apparent reduced severity of *COL4A2* mutations could be explained by α1α1α2 chain stoichiometry, whereby heterozygous mutations in *COL4A1* account for 75% of erroneous collagen IV protein, but *COL4A2* only accounts for 50%[129]. In turn, this could illustrate why *COL4A2* mutations appear rarer, since their reduced severity could mean they convey sub-clinical small vessel changes[46].

Table 1.1 Reported mutations in *COL4A1* causing cerebrovascular symptoms: (correct as of May 2020; modified and updated from[46]). Fs = frameshift, dup = duplication, SS= splice site, UTR = untranslated region.

NO.	MUTATION	CLINICAL/NEUROIMAGING REPORT	REF.
1.	3' UTR *32G>A	Leukoencephalopathy, white matter lesions	222
2.	M1L	Leukoencephalopathy, intracerebral haemorrhage, porencephaly	223
3.	P352L	Intracerebral haemorrhage, microbleeds	224
4.	G417R	Leukoencephalopathy	225
5.	G498D	Leukoencephalopathy, intracerebral haemorrhage,	208
6.	G498V	Leukoencephalopathy, intracerebral haemorrhage, microbleeds	147,209
7.	G519R	Intracerebral haemorrhage, leukoencephalopathy	147,209
8.	G525L	Intracerebral haemorrhage, leukoencephalopathy	208
9.	G528D	Leukoencephalopathy, microbleeds	147,209
10.	R538G	Intracerebral haemorrhage	224
11.	K540R	Leukoencephalopathy	226
12.	G562E	Porencephaly, intracerebral haemorrhage, microbleeds, leukoencephalopathy	227,228
13.	G655E	Intraventricular haemorrhage, porencephaly, schizencephaly	220
14.	G658D	Leukoencephalopathy	229
15.	G670R	Leukoencephalopathy, porencephaly	220
16.	G688D	Intracerebral haemorrhage	206
17.	G693E	Porencephaly	229
18.	G696S	WMH, porencephaly, microbleeds, intracranial haemorrhage	230,231
19.	G696 (fs)	WMH, hemiparesis	221
20.	c.2194-1G>A (SS)	Porencephaly, microhaemorrhages	221
21.	G708V	Schizencephaly, epilepsy	232
22.	G720D	Microbleeds, porencephaly, leukoencephalopathy	233,234
23.	G749S	Porencephaly, intracerebral haemorrhage	235–237
24.	G755R	Leukoencephalopathy, intracerebral haemorrhage	212
25.	G758E	Schizencephaly	238
26.	G773R	Porencephaly	217
27.	G785E	Intrauterine stroke	239
28.	G805R	Intracerebral haemorrhage, hemiparesis, WMH, microbleeds	240
29.	G808V	Intracererbral haemorrhage, porencephaly	241
30.	G832R	WMH, haemorrhagic stroke	242
31.	G861S	Porencephaly, hemiparesis	220
32.	G879E	Cerebellar atrophy	220
33.	G882D	WMH	217
34.	G882E	Porencephaly, schizencephaly	218
35.	G888R	Leukoencephalopathy, porencephaly	220,225
36.	c.2716+1 G>A	Intracererbral haemorrhage, porencephaly	241

37.	G966E	Epilepsy	[243]
38.	G990E	Porencephaly, leukoencephalopathy	[229]
39.	G990V	Porencephaly, microhaemorrhages	[244,245]
40.	G1008R	Porencephaly, intracerebral haemorrhage	[241]
41.	G1035V	Schizencephaly	[246]
42.	G1044R	Porencephaly, intracerebral haemorrhage	[241]
43.	G1064S	Porencephaly	[244]
44.	G1067A	Hemiparesis	[220]
45.	G1082E	Porencephaly, epilepsy	[247]
46.	G1094R	Porencephaly	[220]
47.	G1103R	Porencephaly, intracerebral haemorrhage	[213]
48.	G1130D	Porencephaly and leukoencephalopathy	[223]
49.	G1236R	Porencephaly, intracerebral haemorrhage and microbleeds	[248,249]
50.	G1239R	Porencephaly,	[211,250]
51.	G1257E	Porencephaly, leukoencephalopathy	[220]
52.	G1266R	Porencephaly, leukoencephalopathy, microbleeds	[217]
53.	G1278S	Leukoencephalopathy, seizures	[216]
54.	G1314V	Porencephaly, leukoencephalopathy	[229]
55.	G1326R	Intracerebral haemorrhage, schizencephaly	[251,252]
56.	G1344A	Porencephaly, hemiparesis, seizures	[253]
57.	G1378D	Porencephaly, leukoencephalopathy	[229]
58.	G1384S	Porencephaly, intracerebral haemorrhage	[237]
59.	G1423R	Porencephaly, leukoencephalopathy	[223]
60.	P1530_M1531dup	Intracerebral haemorrhage	[254]
61.	M1556V	microbleeds, intracranial haemorrhage	[255]
62.	G1580R	Porencephaly, leukoencephalopathy, intracerebral haemorrhage	[205]
63.	G1580S	Porencephaly, epilepsy	[219]
64.	G1580A	Porencephaly, leukoencephalopathy, seizures	[220]
65.	N1627K	Cerebral haemorrhages	[203]

Table 1.2 Reported mutations in *COL4A2* causing cerebrovascular symptoms: (correct as of May 2020; modified and updated from[46]). Fs = frameshift.

NO.	MUTATION	CLINICAL/NEUROIMAGING REPORT	REF.
1.	3206delC	Porencephaly, hemiparesis, learning disability	47
2.	G702D	Porencephaly, epilepsy	48,256
3.	G800E	Porencephaly, epilepsy	257
4.	G941R	Hemiparesis, intracerebral haemorrhage	258
5.	G1037E	Intracerebral haemorrhage, porencephaly	259
6.	R1069fs	Porencephaly	47
7.	E1123G	Schizencephaly	260,261
8.	Q1150K	Intracerebral haemorrhage	262
9.	G1152D	Porencephaly	259
10.	G1164R	Porencephaly and hemiplegia	263
11.	G1377R	Schizencephaly	250
12.	G1389R	Porencephaly, hemiparesis	47
13.	A1690T	Intracerebral haemorrhage	262

The spatial location of glycine mutations in *COL4A1* and *COL4A2* are highlighted along with those associated with binding sites (**Figure 1.7**), as extensively reported by Parkin *et al*[264]. In *COL4A1*, G519R is located in binding sites for ECM components laminin, heparan sulfate proteoglycan (HSPG) and fibronectin[264], while G562E is located in a ligand-binding site of von Hippel Lindau (VHL), a tumour suppressor that binds to collagen IVα1 and 2[265]. G1580R, is in a laminin binding site and is also the location of three reported missense mutations, suggesting the key role this interaction may play in ECM composition[46]. In *COL4A2*, G1037E is in a binding site for the serine protease factor IX[264]. Moreover, G1152 is in the region for binding of laminin, nidogen and HSPG[264].
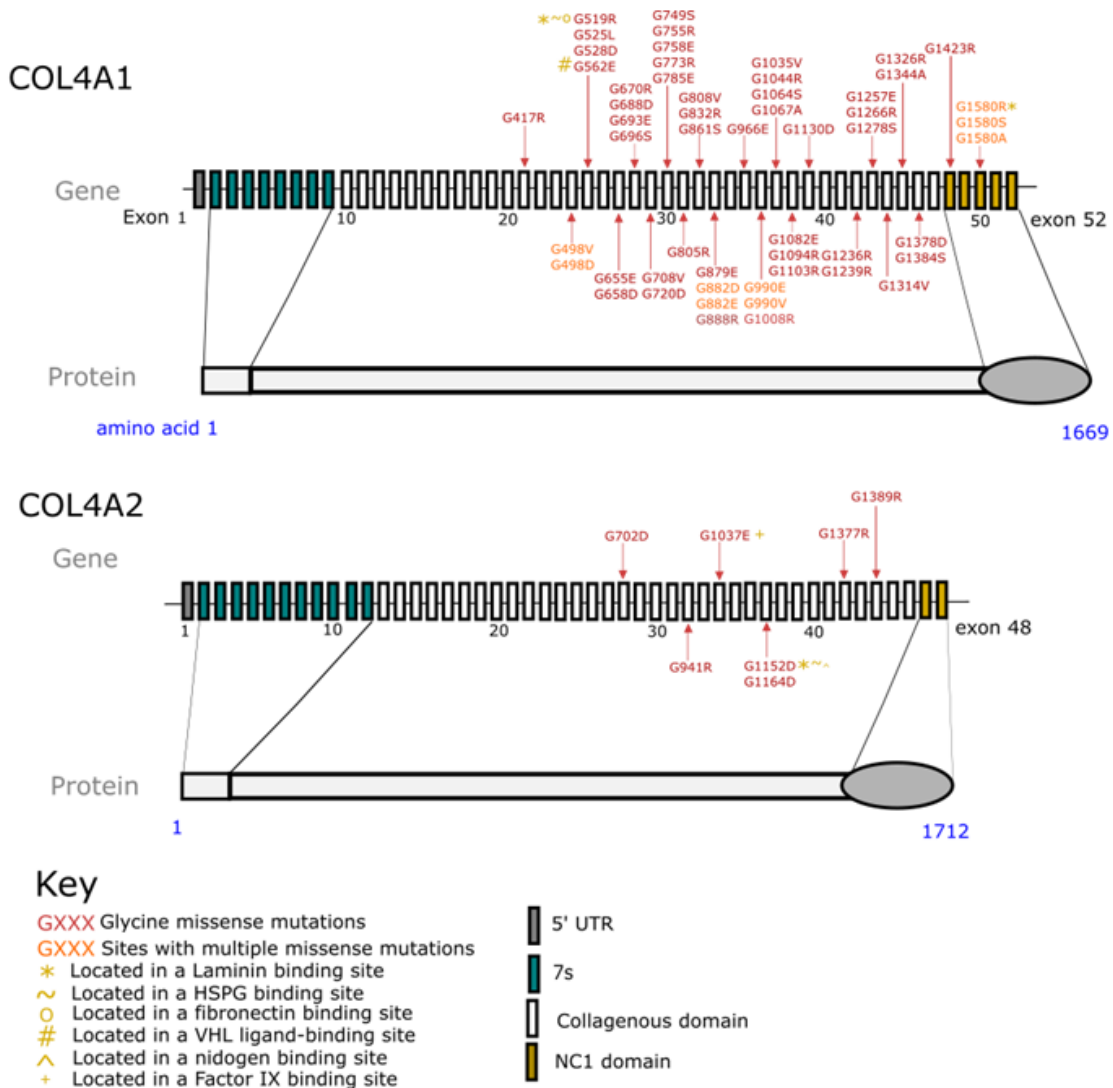
Figure 1.7 The location of glycine missense mutations and their proximity to binding sites: Glycine missense mutations in the collagen α-1 (IV) chain isoform 1 preprotein (52 exons, 1669 amino acids) and collagen α-2 (IV) chain preprotein (48 exons, 1712 amino acids), all exons are drawn the same size for simplification. Information collated from [46,215,220] and binding site information from[264].

Since collagen IV, mainly formed of collagen IV α1/2[195,196], contributes to such a vast proportion of the extracellular matrix (ECM)[202], it is unsurprising that alteration in the formation and deposition of collagen IV can have devastating consequences. Collagen IV interacts with the other main components of the BM (laminin, nidogen and perlecan)[129], but, it's specific role in the BM of cerebral vessels is largely unknown[129]. However, studies in another major BM component, laminin, have shed some light on potential results of aberrant

BM composition[129]. That is, ablating laminin in the astrocytes of mice results in BBB disruption and stroke[266].

However, it is currently unclear how COL4A1/2 mutations cause SVD[46]. A suggested mechanism is that secretion of IV into the BM is impaired[262]. This is evidenced by less secretion of both collagen IV chains (α1 and α2) in patients with either COL4A1 or COL4A2 mutations[46,129]. Moreover, nonsense-mediated decay of the COL4A1 mRNA transcript in the fibroblasts of patients with COL4A1 mutations obliterates mRNA expression, subsequently reducing protein levels[129,221]. An alternate hypothesis is that secretion does take place, but of a mutant form of protein[46]. In turn, the secreted COL4A1/2 mutant protein could act in a dominant-negative way over BM components in the extracellular space[129]. For example, in mice lacking Col4a1 and Col4a2, protein levels of nidogen and laminin are affected[267]. Conversely, another hypothesis is intracellular retention[207] whereby mis-folded collagen IV accumulates in the ER, causing toxic ER stress that triggers the unfolded protein response[46,262]. Intriguingly, COL4A2^{G702D} patient fibroblasts showed reduced intracellular accumulation of COL4A2 on treatment with the chemical chaperone, sodium phenylbutyrate (PBA)[48]. A similar improvement was also demonstrated in the Col4a1$^{+/\Delta41}$ whereby treatment with PBA reduced haemorrhages[201], suggesting this is a tangible target for therapy. Importantly, all of these suggested mechanisms conclude in a central hypothesis of reduced collagen IV in the BM[129].

1.4.3 Mutations used in this work

In this work, two representative glycine substitutions, one in *COL4A1* and one in *COL4A2* were acquired to model SVD.

COL4A1^{G755R}

The first is a heterozygous mutation that is characterised by the substitution of a guanine for an adenine at position c.2263, in exon 30 of *COL4A1*, which results in an amino acid change from a glycine to an arginine at position 755[212]. The male patient presented at age 14, having suffered from two strokes. A family history of SVD symptoms was reported, spanning three generations[212]. The mother had migraine and the grandmother, who had suffered two strokes, was diagnosed as having Multiple Sclerosis[212]. On MRI, there is a similar presentation of periventricular abnormalities in white matter of the index case, the mother and grandmother (**Figure 1.8A-C**)[212]. Moreover, the mother was shown to have leukoencephalopthy[212] and both her and her son, the index case, were found to have the COL4A1^{G755R} mutation. It is the mother from whom dermal fibroblasts were obtained, under the care of Professor Hugh Markus in the Stroke Research Group at the University of Cambridge.
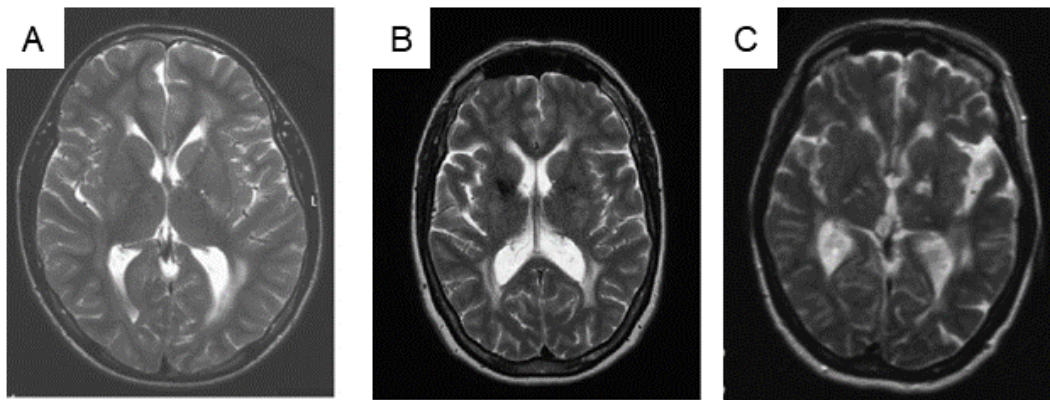
Figure 1.8 MRI images of COL4A1^{G755R} **family cases:** T2 MRI axial view of **(A)** index case **(B)** the index case's mother and **(C)** the index case's grandmother; modified from[268]

COL4A2^{G702D}

The second mutation, COL4A2^{G702D} is also heterozygous and is characterised by a replacement of a guanine for an adenine at position c.2105, resulting in a change from a glycine to aspartic acid at position 702, (G702D) (**Figure 1.9A**). The reported patient and his asymptomatic father both carry the mutation[48]. Analysis of dermal biopsies demonstrated ER stress in the patient but not the father, however, BM defects were present in both (**Figure 1.9B**)[48]. hiPSC from the unaffected father, harbouring the COL4A2^{G702D} mutation, were provided by Dr Tom Van Agtmael[48]. Since this report, the same mutation has been published to have occurred *de novo* in an unrelated patient presenting at age 17 with migraine and WMH on MRI[256].
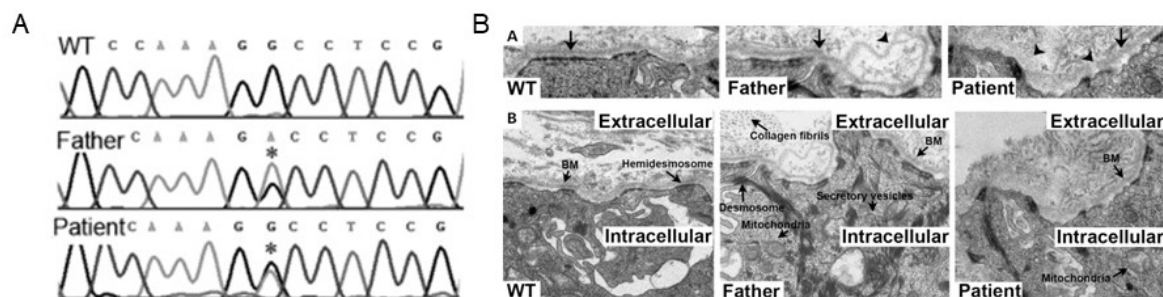
Figure 1.9 COL4A2^{G702D} **mutation and BM pathology: (A)** COL4A2 c.2105 G>A mutation in patient and father **(B)** BM defects in patient and father (arrowhead denotes BM defects and the arrow shows intact BM; modified from[48])

1.4.4 Mouse models of Col4a1/2 SVD

Collagen IV deficiency is embryonic lethal in mouse[267,269] demonstrated by no viable homozygotes beyond the second trimester of gestation[46,270]. Post-mortem analysis of these offspring revealed incomplete formation of the vasculature and extensive BM disruption[270]. COL4A1/2 heterozygous mouse mutants display eye, kidney and widespread vessel defects, alongside cerebral pathology such as porencephaly and haemorrhages[270]. In particular, a heterozygous Col4a1$^{+/G498V}$ mouse[58] carrying a mutation that has also been reported in a patient[147,209], displayed microbleeds within one month of birth. These mice also displayed thinning of the BM with reduced collagen IV α1 and α2, but no intracellular accumulation of collagen IV[58].

Twelve mutations reported in Col4a1 (9) and Col4a2 (2), display very heterogenous features, attributed in part, by the authors to environmental effects[270]. Of these, the heterozygote Col4a2^{ENU415}, which denotes a Col4a2^{V31F} mutation caused by the mutagen N-ethyl-N-nitrosourea (ENU), displayed varying patterns of haemorrhage between different pups[270]. Overall the authors do not report defects of the BM, either thickening or thinning, in these offspring[270].

Three different mouse mutants (Col4a1^{G627W}, Col4a1^{G1064D}, Col4a1^{K950E}) have different tissue-specific BM defects[271]. Col4a1^{K950E}, in which the 'Y' position of the G-X-Y repeat changes from a lysine (K) to a glutamic acid (E), causes less severe kidney defects than the glycine mutation (Col4a1^{G1046D}), which is in the same genetic background[194,271]. Similarly, BM aberrations in Col4a1^{G627W}, appeared to be worse than Col4a1^{K950E}, which fits with knowledge gained from human mutations, in which Glycine mutations in the G-X-Y repeat convey greater pathogenicity[194]

Moreover, a Col4a1$^{+/\Delta ex40}$ mouse model (recently[46] correctly re-identified as $^{\Delta ex41}$), created using random mutagenesis, leading to skipping of exon 41, demonstrated porencephaly and haemorrhages[235]. The homozygous Col4a1$^{\Delta ex41}$ offspring displayed little incorporation of collagen into the BM[129,235]. The authors demonstrated that surgical delivery of Col4a1$^{\Delta ex41}$ mice was able to prevent cerebral haemorrhage[235], with all mice born naturally displaying haemorrhage. It was later suggested that caesarean section should be adopted in human patients with known *COL4A1* mutations[205], demonstrating clinical relevance of this mouse model. Moreover, mouse models display shared pathology with human COL4A1/2 mutations[270].

However, the mouse models currently in use do not fully replicate human disease, because they fail to recapitulate the genetic diversity that drives human pathology[272]. For example, in

one study, vascular tortuosity was only present in mice from a single strain (C57BL/6J)[192,227]. Moreover, although a prevalent symptom in humans, porencephaly was present in less than 20% of Col4a1 mutant mice originating from a homogeneous genetic background[248], suggesting that interaction with the environment is not reflected in mouse models[192]. Thus, one animal model is unlikely to describe all human features, limiting its utility in uncovering the pathomolecular mechanisms underlying COL4A1/2 SVD[129]. Hence, an *in vitro* BBB model of COL4A1/2 SVD could contribute human-relevant results to existing mouse models, enabling better understanding of SVD pathophysiology.

1.5 *In vitro* models of the BBB

In vitro models of the BBB are numerous. Their design and successful implementation centres on two requirements: identification of a suitable cell type and appropriate selection of a physical scaffold in which to house these cells.

1.5.1 Primary and immortalised cells

The first consideration for developing an *in vitro* BBB model is what cell type to use. Cellular combinations used thus far include primary brain capillary murine or porcine cells, as well as a mix of human and murine primary cells[273]. Multiple immortalised cell lines are also available commercially, both murine (bEND3[274] and RBE4[275]) and human (such as HMEC-1[276] and HCMEC/D3[277]). Of late, the most heavily favoured are HCMEC/D3, which have been applied to drug transport studies[277]. However, as seen in mouse bEND.3 cells, these immortalised cells can lack tight junctions[274]. Other groups have used non-brain specific cells such as human umbilical vein endothelial cells (HUVEC)[278], which display much lower TEER (less than $30\Omega \times cm^2$)[279].

However, both primary and immortalised cells have drawbacks. Primary cells are difficult to isolate and in the case of human cells, it remains a challenge to obtain healthy brain tissue for isolation[273]. Even if they can be acquired commercially, they are costly and limited as they reach senescence within 5-6 passages[273]. Hence, the use of human induced pluripotent stem cells (hiPSC) has revolutionised the BBB disease modelling field.

1.5.2 hiPSC

Induced pluripotent stem cells (iPSC) were first reported in 2006, by Yamanaka and his colleagues[280]. In this seminal work, the authors demonstrated that by treating somatic cells (mouse adult or embryonic fibroblasts) with transcription factors Oct3/4, Sox2 and tumour-related factors C-Myc and Klf4, they could artificially produce a population of pluripotent cells, akin to embryonic stem cells[280]. Thus, the term 'induced pluripotent stem cells' was born[280]. These cells self-renew indefinitely and have the ability to become almost all cell types of the body, whilst retaining the genetic background of the original individual[280]. The

following year, in 2007, Yamanaka and his team, presented the first case of generating iPSC from human dermal fibroblasts[281] (hiPSC), paving the way for their use in patient-specific personalised therapy. Their discovery revolutionised the world of disease modelling, earning Yamanaka the Nobel Prize for Medicine in 2012.

In the intervening 13 years since this first report, key steps have been taken towards advancing the use of hiPSC for disease modelling. Firstly, the delivery method of Yamanaka factors was improved, moving from retrovirus, which can insert into the genome[282] to non-integrating Sendai Virus[283]. Along with this, advances in clustered regularly interspaced short palindromic repeats (CRISPR)/Cas9 technology now enable the creation of isogenic control lines, which serve as a better comparison than unrelated WT lines with a different genetic background[284].

hiPSCs offer many benefits in terms of disease modelling. Firstly, they overcome inter-species differences, for example, human astrocytes are much large and have many more processes than mouse astrocytes[98]. This makes results more relevant to pharmacological testing[273], with a direct route to preclinical testing. They remove not only inter-species differences but also inter-person differences in genetic background, since an hiPSC line maintains the background from the person from which it was derived[281]. Moreover, they are relatively inexpensive and can be used for rapid and scalable assays compared to *in vivo* animal models or isolated primary cells[273]. They circumvent the technical challenge of isolating primary human cells, which is complicated and time-consuming[273]. Importantly, they can be used to generate all cell types of the BBB, from the same hiPSC line, therefore creating an isogenic model[285]. hiPSCs are also beneficial since they can be used to generate intermediate populations, such as neural stem cells [286] or neural crest[287], which are highly proliferative and reproducible cryopreserved, meaning that these intermediate populations can be terminally differentiated when required, shortening the differentiation time while maintaining equal performance.

hiPSC disease models have so far been successfully implemented in other vascular disorders such as Marfan Syndrome[288] and another monogenic form of SVD, CADASIL[289,290]. A report on the neurological disorder Huntingdon's Disease, using hiPSC-BMEC from patients, revealed phenotypic abnormalities akin to clinical presentation, such as BBB defects[291]. Moreover, Prion disease modelled with an iPSC-derived organoid system revealed tau pathology *in vitro*[292–294].

1.5.3 BBB model systems

Having selected a cell type of choice, there are multiple platforms that can be used to generate an *in vitro* BBB model. The classical choice is the semipermeable, porous
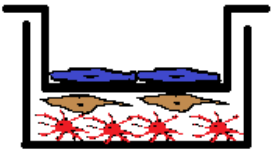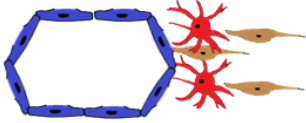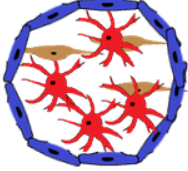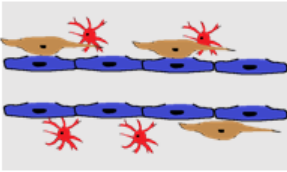
Transswell® insert. These offer an easily manipulated system[273], in which complexity can easily be built up. Reconfigurable cellular arrangements are easily realised, but, most typically, BMEC are positioned on the apical side, pericytes on the basolateral side and astrocytes in the bottom of the well[65] (**Table 1.3**).

However, 2D Transwell® systems have limitations. For example, the physical separation of cells into two chambers mean that they do not recapitulate *in vivo* structure[65]. Flow, mimicking the blood in vessels, exerts shear stress, and is a key component to include in BBB models[295]. This is lacking in most Transwell® models which are maintained in static conditions[273]. Hence, some groups have moved to utilise 3D microfluidic structures [273,296] (**Table 1.3**), that allow high-resolution imaging and enable migration studies[273]. However, these require specialised set ups[297], often needing specialised equipment and bioengineering experience.

In efforts to overcome these limitations, others have utilised techniques of organoid culture (**Table 1.3**). This juvenile technology uses the spontaneous formation of multiple cell types in suspension, producing a miniature organ-like structure that mimics the complex tissue microenvironment[298,299]. BBB Organoids can be produced with BMEC, astrocytes and pericytes[300]. Moreover, using primary human cells, BBB organoids form spontaneously under the correct conditions[301] and express P-glycoprotein on the outer surface, mimicking its typical luminal location[297]. However, necrosis in the core after prolonged culture *in vitro* is a limitation of these complex systems[302].

To circumvent the difficulties of 3D organoid culture, other groups have proposed mimicking the BBB with gel-embedded vasculature (**Table 1.3**)[273]. Here, ECM scaffolds self-polymerise[273] and are used to provide paracellular factors present *in vivo*[298], supporting the formation of 3D vessels. However, this technique requires understanding of the specific *in vivo* BBB matrix, which is still lacking[298].

Table 1.3 A comparison of the main BBB *in vitro* model approaches: advantages and disadvantages.

Model	Schematic	Advantages	Disadvantages
Transwell® Insert		✓ Simple to set up ✓ Enable different cellular combinations	✗ No cell-cell contact ✗ Static
3D microfluidic vessel		✓ 3D vessels ✓ Cell-cell contact ✓ Flow	✗ Technically challenging ✗ Inability to perform TEER
Organoid		✓ Cell-cell contact ✓ Self-organised	✗ Inability to perform permeability/TEER studies ✗ Lack of vasculature to supply the core ✗ High failure rate
Gel-embedded vasculature		✓ 3D vessels ✓ Cell-cell contact ✓ *in vivo*-like cytokines in the matrix	✗ Technically challenging ✗ Static

1.5.4 Functional assays

Once designed, BBB models must be thoroughly tested to demonstrate their relevance to the *in vivo* BBB. Functional assays are employed as key determinants of equating artificial *in vitro* performance to *in vivo* function[298]. The most widely used functional test of BMEC function is TEER. *In vitro,* this is recorded with an epithelial voltohmmeter which uses two pairs of electrodes[72], one applying current and one measuring the output, on each side of a monolayer, for example a Transwell® membrane[73]. Using Ohm's law, the ratio of voltage to current is computed, before subtraction of a blank measurement and multiplication by the surface area[73], to arrive at $\Omega \times cm^2$.

There is still some debate concerning appropriate TEER values *in vitro*[73] as well as scepticism regarding the overreliance on resistance data, which can be affected by

temperature, position of the electrode, media composition, type of electrodes used as well as user interpretation[303,304]. Thus, a barrier test such as permeability to known size compounds could be more reliable. The gold standard barrier test is mass spectrometry to quantify drug compounds passing across a monolayer[305]. Although, permeability assays with fluorescent compounds such as FITC-Dextran (4KDa, 10kDa, 40kDa) or small hydrophilic molecules including Sodium Fluorescein (376 Da), Lucifer Yellow (444Da) or Sucrose (342Da) are easier and cheaper to use[306]. Consideration should be given to the size exclusion expected *in vitro*, as many groups have relied on large sized molecules that would not pass the BBB *in vivo* anyway[55]. Since both TEER and permeability assays have limitations, studies that utilise multiple methods are favoured[306].

1.5.5 hiPSC-derived *in vitro* BBB models

The infinite resource and opportunities of hiPSCs were exploited in this work, to create an *in vitro* SVD disease model of the BBB. This was achieved by generating the three main cells types of the BBB (BMEC, astrocytes and MC) from hiPSCs and combining them into the 2D Transwell® system previously described (**Table 1.3**). First, to generate the cells of interest, the following protocols were adopted.

hiPSC-BMEC

The first report of hiPSC-BMEC was from the group of Eric Shusta in 2012[307] (**Figure 1.10**). In this original protocol, Shusta, Lippmann and colleagues reported the use of co-differentiation of endothelial and neural cells, with unconditioned media, to yield BMEC with TEER of 1450Ωxcm^2 [307]. Most protocols follow a similar premise, starting from single-cell seeding and proceeding through an endothelial induction phase before selection, either by sorting or attachment to a specific matrix, to yield BMEC (**Figure 1.10**).

However, another approach used hiPSC-derived arterial and venus endothelial precursors[308], to produce brain-like cells[309]. The production of more than one terminal cell type from the same intermediate population is also possible, for example a CD34+ population was differentiated to both endothelia and SMC[310]. This highlights the flexibility and scope of experimental design that can be achieved with hiPSCs. Of late, hiPSC-BMEC have been reported to consistently achieve values of 2000-8000Ωxcm^2[311].

Importantly, the success of using hiPSC-derived cells relies on methods to determine correct function of BMEC *in vitro*, especially in light of persistent criticism regarding their fetal-like characteristics[312]. Recently, hiPSC-BBB models have been able to acquire *in vivo*-like properties owing to their realistic drug transport capabilities[305].
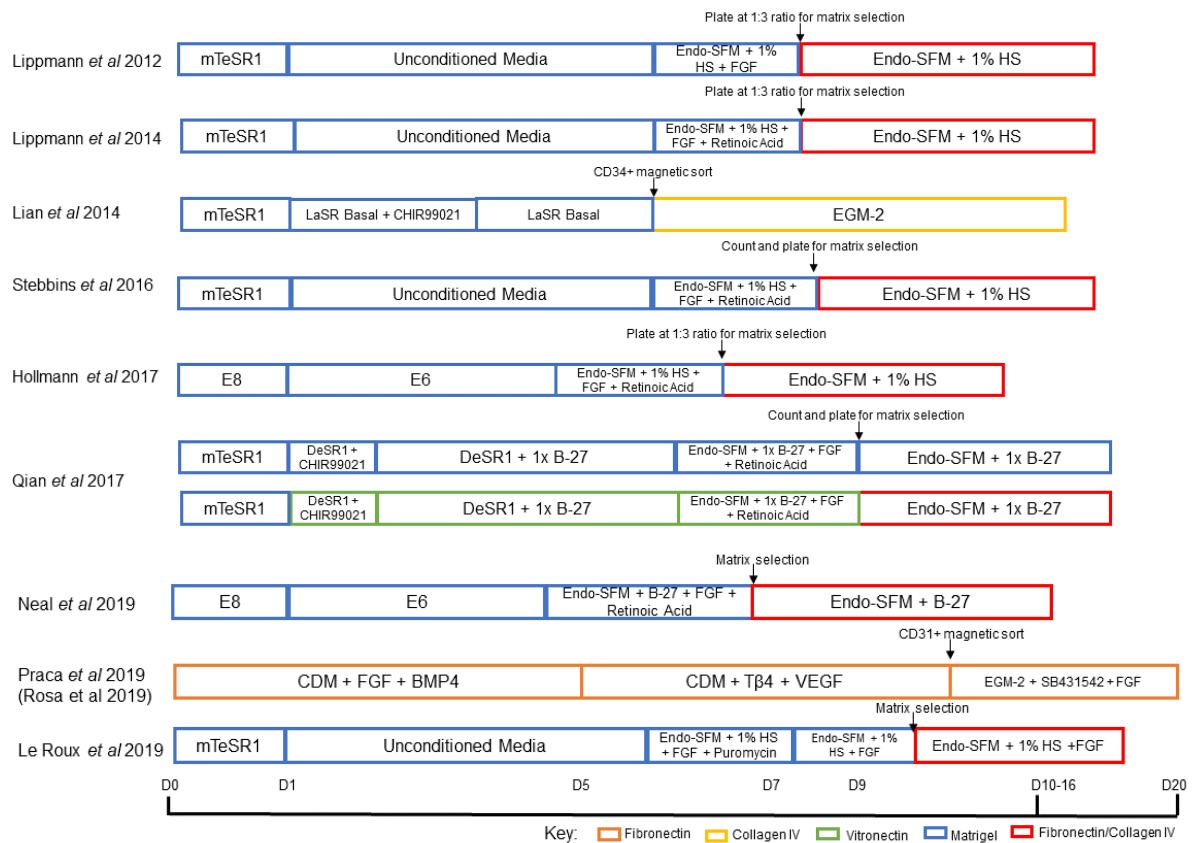
Figure 1.10 Published hiPSC-BMEC protocols: a comparison of hiPSC-BMEC protocols, arrows indicate method of purification [77,305,307–311,313–315] (EGM: endothelial cell growth medium)

Whilst hiPSC differentiation allows for non-invasive *in vitro* studies on hiPSC-BBB models[273], it is difficult to determine if hiPSC-derived endothelial cells, or BMEC, behave in the same way as human *in vivo* cells and if so, that they can be reproduced consistently[316]. Recent single-cell RNA sequencing has revealed that populations of hiPSC endothelial cells are heterogeneous, revealing only one cluster of cells that represent *in vivo* endothelial cells [316]. Ideally, vigorous phenotyping should not only include confirmation of endothelial markers and function, but the exclusion of a neuroepithelial phenotype.

It is difficult to differentiate bona fide hiPSC-derived endothelial cells because of the limitations of hiPSCs. hiPSC differentiation protocols often produce immature cells that are more fetal-like than adult-like[312]. Also, it still remains unclear whether hiPSC reprogramming resets the cellular age of the original cells, removing the epigenetic signature of the patient[298,317]. Although, one group demonstrated that donor epigenetics was maintained in hiPSCs[285,318]. Moreover, modelling complex chronic disorders with hiPSCs, does not take in

to consideration the contribution of environmental factors[285]. This is of particular relevance, since the COL4A2^{G702D} hiPSC line used in this work is from an asymptomatic individual[48].

hiPSC-astrocytes

There are multiple approaches to generate hiPSC-astrocytes and most rely on the production of a proliferative, intermediate population. The nomenclature used to describe these cells is debated. A ubiquitous population of neural stem cells (NSC)[319] gives rise to so-called neural progenitor cells, which are more specialised and have reduced replicative capacity[320]. The term neural precursor cell (NPC), which will be used here, refers to a non-specific, mixed population of neural stem and progenitor cells[321]. NPCs are derived through a neuroectoderm lineage, displaying positivity for PAX6[322], SOX1[286] NESTIN and SOX2[323].

Thus far, a variety of methods have been employed to generate NPCs from hiPSC in adherence culture (**Figure 1.11**). Embryoid body (EB) suspension methods predicated on spontaneous differentiation[324] also yield PAX/NESTIN+ NPCs[325], but will not be discussed here. Embryonic stem cell (ESC) derived protocols, such as the first report of *in vitro* NPC generation in 2001[326], are also not included, given the focus of this work is on hiPSC.

Dual-SMAD inhibition with SB431542 and Noggin are readily used[286,325,327–329], with the exception of two protocols, one of which used a non-specified commercial media[330] of unknown composition and the other that used the ALK2 inhibitor DMH1 in place of Noggin[331] (**Figure 1.11**). The duration ranges from around 10 days to one month (**Figure 1.11**). Common features between these protocols is the aim of generating neural rosettes. These are polarised structures that are suggested to equate to the neural tube that forms early in development[332].
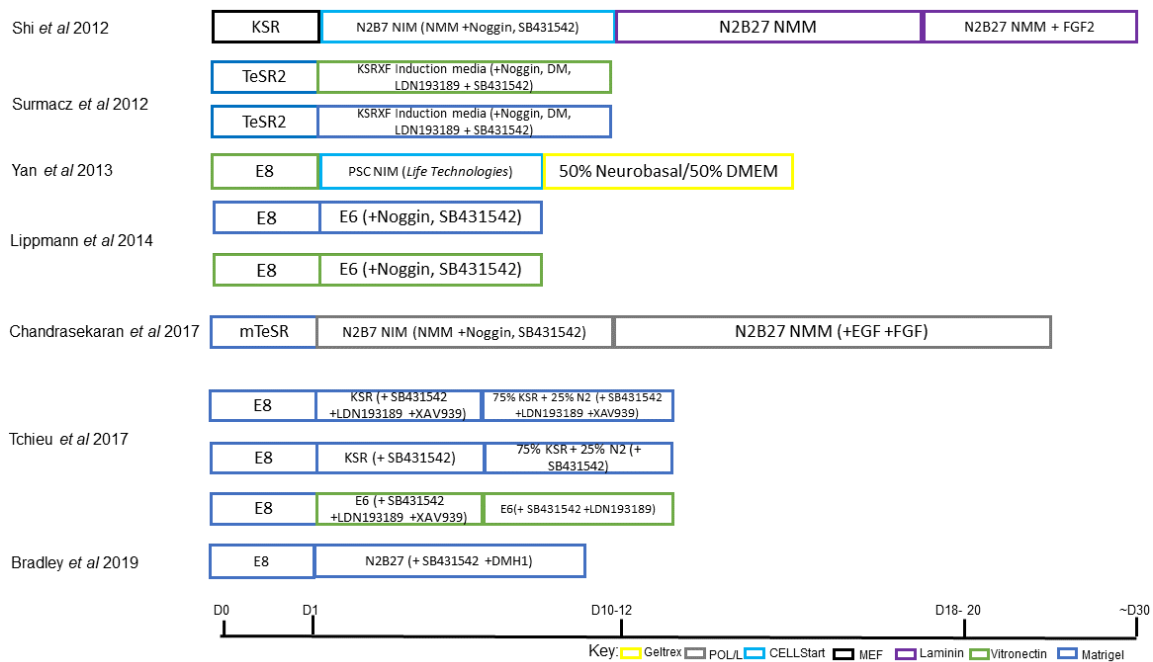
Figure 1.11 Published hiPSC-NPC protocols: a comparison of adherent hiPSC-NPC protocols[286,325,327–329,331,333] (KSR: KnockOut serum replacement; DM: dorsomorphin; PSC: pluripotent stem cell)

In vivo, adult NSCs resident in the subventricular zone of the brain give rise to astrocytes[334,335]. This little understood *in vivo* phenomenon is reproduced *in vitro* with a cocktail of astrocyte induction factors, for example, CNTF, BMP2 and FGF[336]. Again, to reduce complexity, only adherent protocols are presented (**Figure 1.12**), but a comprehensive review in 2016 details the 18 protocols available that include EBs[107]. Characteristically, these protocols maintain NPCs in N2B27 neural maintenance media (NMM), before inducing astrocytic specialisation (**Figure 1.12**). Typically these protocols take several weeks to yield astrocytes from NPCs, but there is one accelerated simplified protocol takes hiPSC directly to Astrocytes in just four weeks (**Figure 1.12B**)[328].
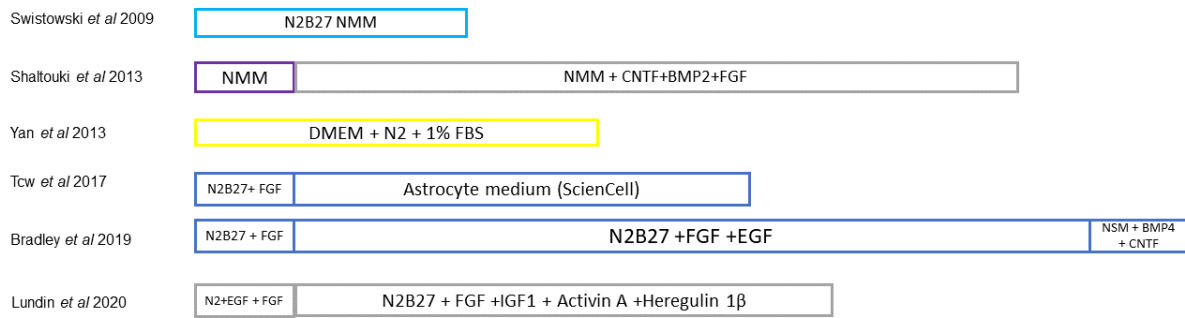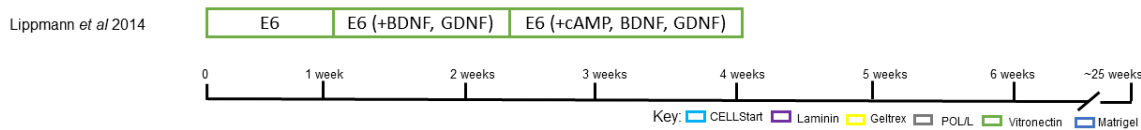
Figure 1.12 Published NPC-astrocyte and hiPSC-astrocyte protocols: a comparison of adherent **(A)** NPC-Astrocyte protocols and **(B)** hiPSC-Astrocyte[331,333,336–339] (EGF: epidermal growth factor, BDNF: brain-derived neurotrophic factor; GDNF: glial cell-line derived neurotrophic factor)

hiPSC-pericytes

As mentioned above, brain pericytes are an elusive cell type to characterise with confidence[115]. Generation of hiPSC into pericytes has thus far been controversial, since it remains a challenge to determine the difference *in vitro* between pericytes and vascular SMCs[340]. Most of this confusion results from the absence of specific markers that distinguish pericytes and SMCs[340]. Lineage specificity of hiPSC protocols is paramount, since it is well known that different germ layers give rise to vascular cells in different regions[116]. As previously mentioned, forebrain pericytes arise from neural crest[117] and cells in other regions are derived from mesoderm[117,118].

For clarity, only those protocols naming 'pericytes' or pericyte-like[118] cells or that display markers for pericytes are discussed here (**Figure 1.13**). Most protocols use a neural crest intermediate population, positive for P75[341], but mesoderm protocols, through the generation of mesenchymal cells, have also been shown to give rise to cells with transcriptional and functional relevance to human primary pericytes[342]. Terminal pericytes are commonly characterised for the expression of NG2, CD44 and CD146[340,342,343]. Of the reported approaches, one protocol transits through a more generic progenitor population, called early vascular cells (EVCs), in which both endothelial and pericytes can be generated[344]. Most of these differentiation protocols start from single cell seeding, others from colonies[343]. Matrix

selection and repeated passage are the most common form of specification (**Figure 1.13**). One approach reports that an intermediate population of neural crest stem cell (NCSC) can be separated with MACS beads before plating with PDGFBB and TGFβ1 for pericyte specification[345]. Many protocols employ commercially available media, such as from ScienCell, PromoCell or StemCell Technologies, highlighting how little is known about the specifics of pericyte generation from hiPSC.

In this project, the protocol established in the laboratory of Dr Sinha[346,347] will be used, since these MC demonstrate a plastic phenotype, with cells readily able to be directed towards a more pericyte-like or SMC-like phenotype by altering the media or matrix composition (Dr Alex Granata, *Unpublished work*).
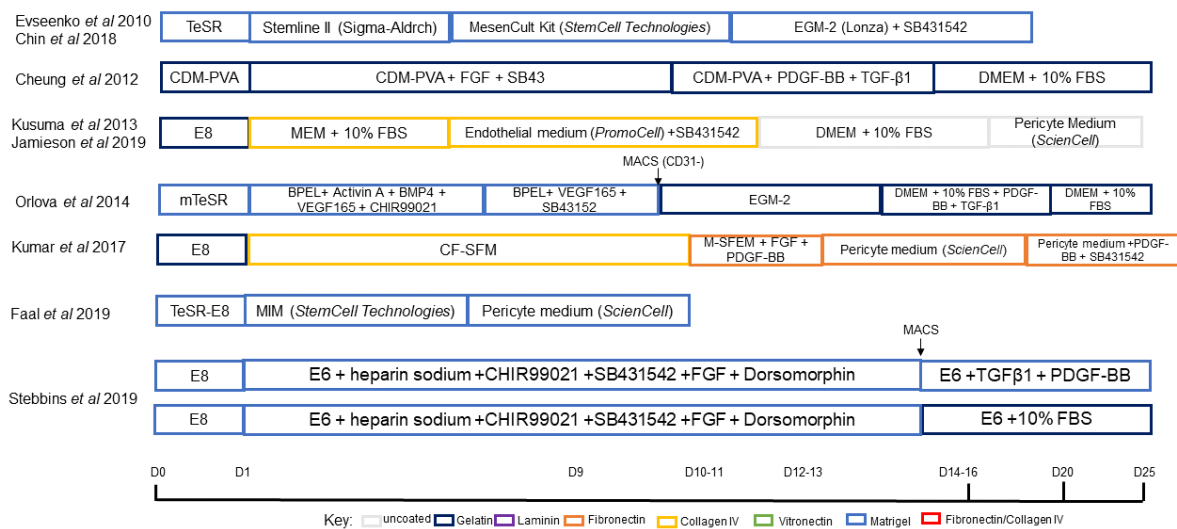
Figure 1.13 Published hiPSC-pericyte protocols: a comparison of hiPSC-pericyte protocols[118,342–345,347–350] (BPEL: BSA, PVA and essential lipids; CF-SFM: colony-forming serum-free medium; M-SFEM: mesenchymal serum-free expansion medium; MIM: mesoderm induction medium)

1.6 Rationale for this work

There is an unmet need for new, disease-modifying therapies for SVD (*Section 1.1.3*), yet little is known about the underlying mechanisms of SVD (*Section 1.3*). Pre-clinical mouse models don't recapitulate all aspects of human disease[298,351], so there is a requirement for a human-relevant model. hiPSC from patients provide a relevant system in which to study SVD and formulate disease insights (*Section 1.5.2*). Thus, the findings emerging from the *in vitro* model developed here will complement *in vivo* studies, such as the well-characterised

Col4a1^{G1064D} mouse[271] and taken together, will advance our understanding of COL4A1/2 SVD.

The BBB is a suitable system to unravel the underlying cause of matrisome-associated disruption. In this work, hiPSC-derived cells will be used to model the BBB, meaning our model will be isogenic and patient-specific, a feat achieved by only a handful of groups[352–354]. Of the discussed BBB models, the Transwell® system was chosen as the most appropriate for this work, since it readily allows build-up from one, two or three cell types and enables the ability to use mixed co-culture of COL4A patient and WT/control cells, to tease out the disease mechanisms (*Section 1.5.3*).

In order to generate this model, hiPSC harbouring mutations in *COL4A1* and *COL4A2* (*Section 1.2.3*) and control lines, were differentiated into BMEC, astrocytes and MC. The main focus of this thesis is on the generation and optimisation of hiPSC-BMEC, to build up a novel BBB model. MC and isogenic controls (provided by Dr Alex Granata) will be added to advance the *in vitro* BBB system and complete the control and disease models. Although most of the studies were performed in a 2D Transwell® system, key aspects such as flow, to exert shear stress as well as cell-cell contact, were later introduced into the model. Using this strategy, we aim to develop the first *in vitro* model of SVD using hiPSC with collagen IV mutations.

1.7 Previous work leading to this project

hiPSC harbouring a COL4A2^{G702D} mutation[48], were provided by Dr Tom Van Agtmael. COL4A1^{G755R} dermal fibroblasts were obtained with consent from the patient (under the care of Professor Hugh Markus), cultured and sequenced by Dr Alex Granata before reprogramming by the hiPSC Core Facility in Cambridge. The following initial experiments were conducted before the commencement of this project.

1.7.1 CRISPR/Cas9 correction of COL4A2^{G702D} hiPSC

CRISPR/Cas9 was performed using synthetic guide RNA and ribonucleoprotein Cas9. The heterozygous G>A mutation at position c.2105 in the *COL4A2* gene (**Figure 1.14A**) was correct by replacement, using donor DNA, of adenine for the wild-type guanine. Two separate clones, 14 and 17 were generated (**Figure 1.14B-C**). A silent, Protospacer Adjacent Motif (PAM) site mutation of C>T, that did not alter the amino acid was used to select clones with donor DNA integration from the initial mixed pool (**Figure 1.14B-C**).

Figure 1.14 COL4A2^{G702D}
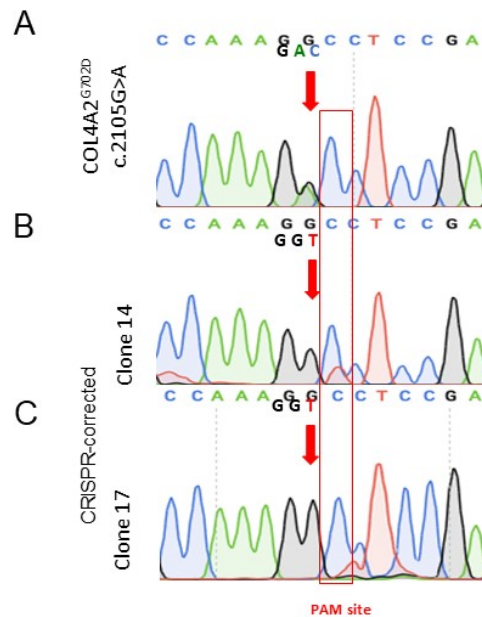
Figure 1.14 COL4A2^{G702D} CRISPR correction: Generation of CRISPR/Cas9 gene edited COL4A2^{G702D} hiPSC lines (Asp>Gly) **(A)** COL4A2^{G702D} mutation **(B)** corrected clone 14 and **(C)** corrected clone 17. Conducted by Dr Alex Granata.

1.7.2 Differentiation of hiPSC to neural crest derived MC

Wild-type (WT), COL4A1^{G755R}, COL4A2^{G702D} and iCOL4A2 cl14, were differentiated to neural crest derived SMC as previously described[287] (performed by Dr Alex Granata). These cells are positive in immunocytochemistry for SMC markers Calponin and SM-α-Actin (**Figure 1.15A**) and in qRT-PCR for *CNN1*, *ACTA2* and *SM22* (**Figure 1.15B**).

They were assessed for expression of pericyte markers, which were confirmed in immunocytochemistry for NG2 (**Figure 1.15A**) and qRT-PCR for *NG2* and *PDGFR-BB* (**Figure 1.15C**). Hence, these cells are named indiscriminately as MC, as they have mixed SMC and pericyte characteristics. MC contract, demonstrated by cycling of calcium-indicator Fluo4AM upon treatment with Carbachol (**Figure 1.15D**).
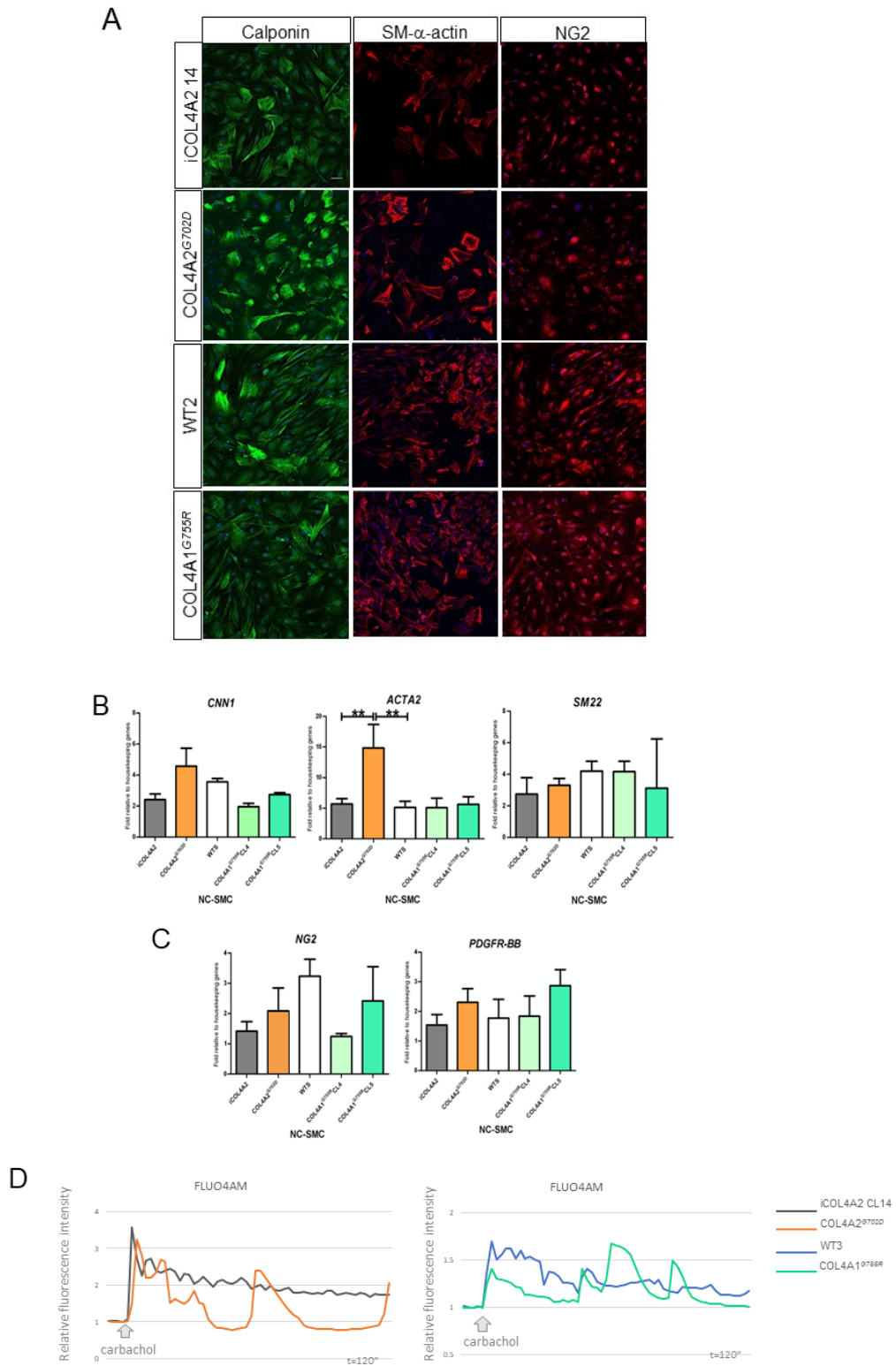
Figure 1.15 Differentiation of hiPSC into functional MC (A) immunocytochemistry for MC (SMC/pericyte) markers **(B)** qRT-PCR for SMC markers n=3 **(C)** qRT-PCR for pericyte markers n=3 **(D)** Fluo-4AM-Ca^{2+} contraction single cell analysis; n=3. Conducted by Dr Alex Granata.

1.7.3 COL4A1/2 hiPSC-MC display phenotypic abnormalities

Proliferation

COL4A2^{G702D} MC have significantly reduced proliferation compared to WT, demonstrated by lower positivity for Ki67 (**Figure 1.16**). Conversely, COL4A1^{G755R} display a non-significant trend of reduced proliferation (**Figure 1.16**).
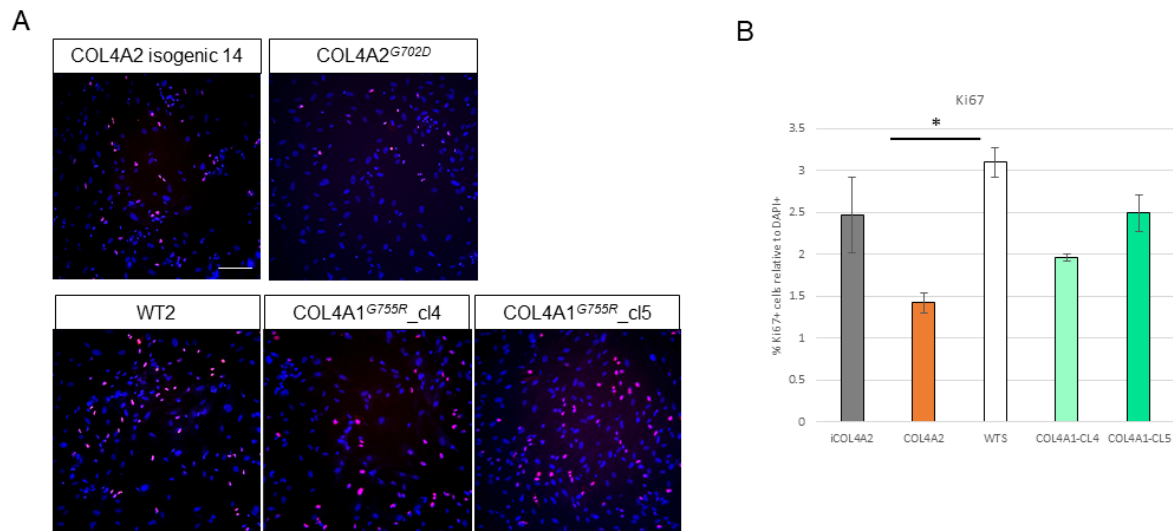
Figure 1.16 MC proliferation assay: Ki67 proliferation **(A)** Immunocytochemistry of Ki67 in MC **(B)** % Ki67 positive cells relative to DAPI positive. 5 images per well were quantified. (WTs=2) N=3. Scale bars are mean +/-SD. Conducted by Dr Alex Granata.

Collagen IV and MMPs

COL4A2^{G702D} MC display significantly reduced collagen IV compared to WT (**Figure 1.17A**). Concordantly, MMPs 1,2 and 9 are significantly increased in COL4A2^{G702D} relative to the isogenic control (**Figure 1.17B**), but only MMP1 is significantly increased in COL4A1^{G755R}_cl4 and 5. TIMPs 1,2 and 3 are also significantly increased in both COL4A2^{G702D} and COL4A1^{G755R}.
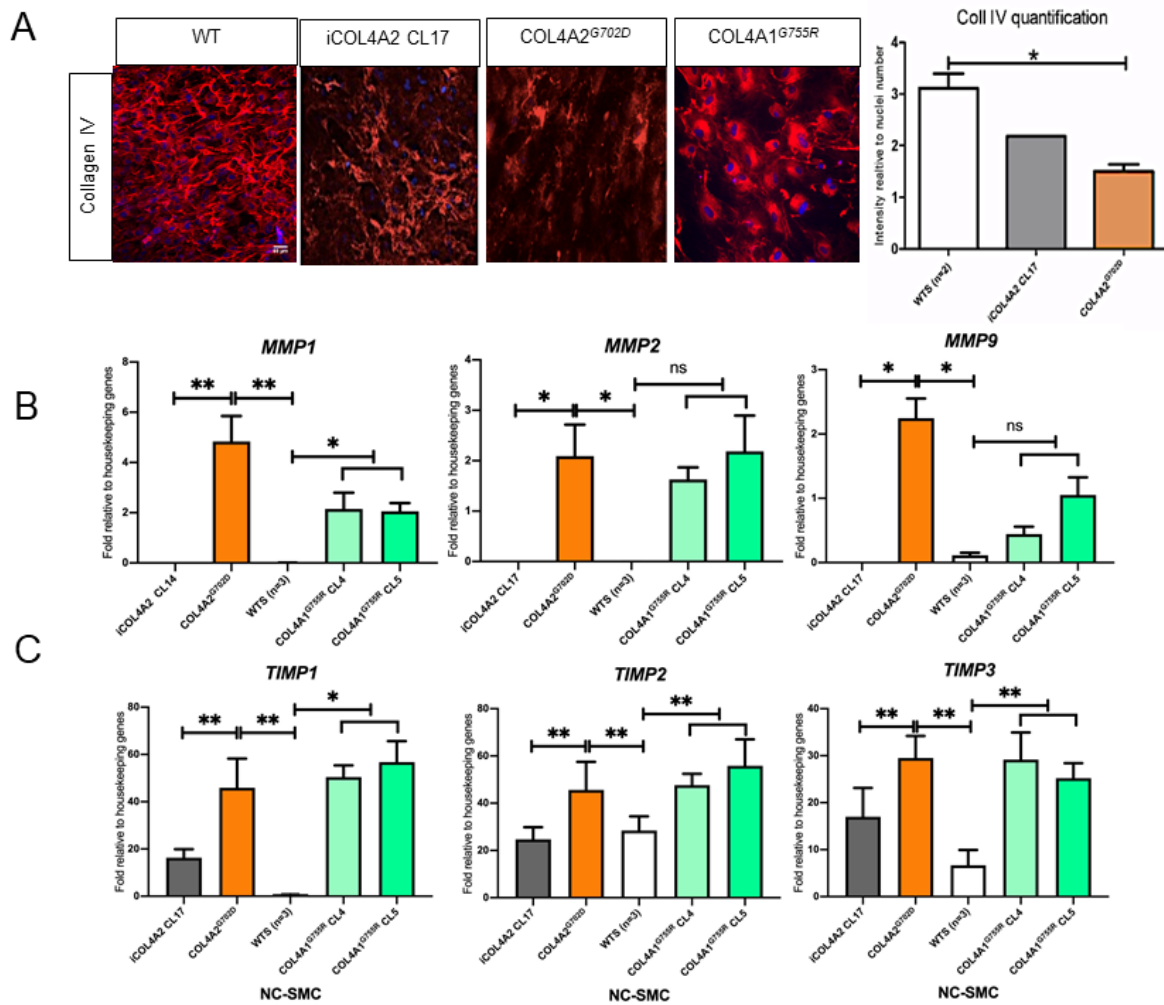
Figure 1.17 Collagen IV and MMPs in MC: **(A)** Immunocytochemistry for collagen IV in MC and relative quantification, **(B)** *MMP1, 2, 9* qRT-PCR and **(C)** *TIMP1,2* and *3* qRT-PCR, relative to HK average, n=3. Conducted by Dr Alex Granata.

1.8 Hypothesis and Aims of this project

1.8.1 Hypothesis

COL4A1/2 SVD pathophysiology is caused by NVU dysfunction, which leads to increased permeability of the BBB.

1.8.2 Aims

1. To develop a physiologically relevant *in vitro* co-culture model of the BBB, with control and COL4A1/2 SVD hiPSC-derived BMEC, MC and astrocytes.

2. To elucidate the disease-causing mechanism of COL4A1/2-SVD, resulting in impaired BBB structure and function.

Chapter 2: Materials and Methods

2.1 Cell Culture

All cells were maintained in antibiotic-free media in a humidified 5% CO_2 incubator at 37ºC. Cells were routinely tested for the presence of Mycoplasma using the Venor®GeM Classic Mycoplasma PCR Detection kit (Minerva Biolabs).

2.1.1 hiPSC cell line information

In total, eleven hiPSC lines were used in this work: four WT hiPSC lines, two clones of patient line COL4A1^{G755R}, one clone of patient line COL4A2^{G702D} and two CRISPR-corrected isogenic controls for COL4A1^{G755R} and COL4A2^{G702D}. (**Table 2.1**).

Table 2.1 hiPSC line information

Assigned Name	Original name	Individual	Age	Gender	hiPSC source	Reprogramming method	Reference
WT1	A1ATD	A1ATD (corrected)	65	M	iPS Core Facility, Cambridge	Retrovirus	355,356
WT2	BBHX	Healthy Control	55	M	iPS Core Facility, Cambridge	Unknown	N/A
WT3	HPSI031 4i-sojd_3	Healthy Control	45-49	F	HIPSCI Consortium	Sendai virus	N/A
WT4	HPSI021 4i-wibj_2	Healthy Control	55-59	F	HIPSCI Consortium	Sendai Virus	N/A
COL4A1^{G755R} Clone 4	N/A	SVD patient	65	F	iPS Core Facility, Cambridge	Sendai Virus	N/A
COL4A1^{G755R} Clone 5	N/A	SVD patient	65	F	iPS Core Facility, Cambridge	Sendai Virus	N/A
COL4A2^{G702D}	N/A	Father of SVD patient	75	M	Dr Tom Van Agtmael	Unknown	48
COL4A2^{G702D} isogenic 14	N/A	CRISPR-corrected	75	M	Dr Alex Granata	Unknown	N/A
COL4A2^{G702D} isogenic 17	N/A	CRISPR-corrected	75	M	Dr Alex Granata	Unknown	N/A
COL4A1^{G755R} isogenic 6	N/A	CRISPR-corrected	65	F	Mary Goodwin-Trotman	Sendai Virus	N/A
COL4A1^{G755R} isogenic 11	N/A	CRISPR-corrected	65	F	Mary Goodwin-Trotman	Sendai Virus	N/A

2.1.2 Feeder-free hiPSC thawing

A vial of hiPSC was thawed until only a small pellet of ice remained. 1ml of E8 media (**Table 2.2**), was added to the vial and the contents transferred to 3ml of E8 in a 15ml centrifugation tube (BIOFIL). Cells were centrifuged at 120g for 2 minutes before the supernatant was

aspirated. The pellet was gently re-suspended in 1ml of E8 with Rho Kinase Inhibitor (ROCK inhibitor; Y-27632, Stem Cell Technologies) and plated into a 6-well plate pre-coated at room temperature for 1 hour with Vitronectin (1:25 dilution, VxF, Stem Cell Technologies).

Table 2.2 Essential 8 (E8) medium components

Components	Volume (250ml)	Supplier Information
DMEM/F-12	250ml	Thermo Fisher, 31330038
Insulin Transferrin Selenium	5ml	Thermo Fisher, 41400045
Sodium Bicarbonate (7.5%)	1.8ml	Thermo Fisher, 25080094
L-ascorbic acid (6.4mg/ml)	2.5ml	Sigma-Aldrich, A8960
FGF-2 (4µg/ml)	1.56ml (25ng/ml)	Biochemistry Department, University of Cambridge
TGFβ (1.74ug/ml)	250µl (1.74ng/ml)	R&D Systems, 240-B/CF

2.1.3 Feeder-free hiPSC maintenance

Cells were maintained with daily E8 medium changes on VxF and passaged every 3-5 days. In brief, cells were washed with 1X PBS (Corning®), before incubating at room temperature with ReLeSR™ (Stem Cell Technologies) for 1 minute. ReLeSR™ was removed and the cells were left at room temperature for 5 minutes. After this, 500µl of E8 was added and the plate was tapped 4-5 times to dislodge the colonies, before re-plating at a ratio of between 1:2 and 1:8 dependent on the cell line.

2.1.4 Feeder-free hiPSC freezing

Cells were collected using ReLeSR™ (described above) and centrifuged at 120g for 2 minutes. The pellet was gently re-suspended in 1ml of freeze medium (**Table 2.3**) containing KnockOut™ Serum Replacement (KOSR), and 10% DMSO. The cells were transferred to a 2ml Nalgene® cryogenic vial (Sigma Aldrich) and gradually cooled (1ºC/minute) in an Isopropyl alcohol freezing container (Mr. Frosty, Nalgene®, Thermo Fisher) in a -70ºC freezer, before transferal to Liquid Nitrogen for long-term storage.

Table 2.3 hiPSC freezing medium components

Components	Volume (10ml)	Supplier Information
E8 medium	5ml (50%)	See above
KOSR	4ml (40%)	Thermo Fisher, A31815-02
Dimethyl sulfoxide (DMSO)	1ml (10%)	Sigma Aldrich, D2650

2.1.5 HUVEC thawing and maintenance

HUVEC were acquired commercially (Gibco™ C0035C, Thermo Fisher). The vial was thawed until only a small pellet of ice remained, before 1ml of Medium 200 with Low Serum Growth Supplement (LSGS, **Table 2.4**) was added and transferred to 3ml of media in a 15ml centrifuge tube. Cells were centrifuged at 300g for 3 minutes and the supernatant was aspirated. Cells were re-suspended and plated at a density of $2.5 \times 10^3/cm^3$ in a T75 canted neck, vented cap culture flask (Corning®, Thermo Fisher) pre-coated overnight with collagen I (0.1% Type 1 collagen from calf skin, Sigma Aldrich). Medium was changed daily and cells were passaged every 4-7 days using TrypLE express (Gibco™ Thermo Fisher). Briefly, cells in a T75 were washed with 1X PBS and incubated with 7ml of TrypLE Express at room temperature for 5 minutes. Cells were collected in a 15ml centrifuge tube and centrifuged at 300g for 3 minutes before being counted with a Neubauer improved Haemocytometer (Heinz Herenz Hamburg) and plated at $2.5 \times 10^3/cm^3$ in HUVEC culture medium.

Table 2.4 HUVEC culture medium components

Components	Volume (500ml)	Supplier Information
Medium 200	500ml	Thermo Fisher, M200500
LSGS (50x)	10ml	Thermo Fisher, S00310

2.2 hiPSC Genotyping

2.2.1 Genomic DNA extraction

Confluent hiPSC colonies were collected with ReLeSR™ and pelleted in a 1.5ml Eppendorf tube. DNA was extracted by re-suspending the pellet in 25µl of Quick Extract™ DNA Extraction Solution (Lucigen, CamBio) and incubating at 65ºC for 6 minutes, before vortexing for 15 seconds (Vortex Genie 2, Scientific Industries) and incubating at 98ºC for 2 minutes. DNA was quantified using a Nanodrop 2000 Spectrophotometer (Thermo Fisher).

2.2.2 Polymerase Chain Reaction

Specific primers (see Appendix) were designed to give a 200-2000bp product, spanning the nucleotide of interest. The region of interest was amplified using Q5 High-Fidelity DNA Polymerase (New England Biolabs). Reaction requirements are detailed in **Table 2.5**. The PCR reaction was performed in a T100 Thermal Cycler (BioRad). The reaction profile can be found in **Table 2.6**.

Table 2.5 Q5 High-Fidelity DNA components per reaction

Components	Volume	Supplier Information
5x Q5 Reaction Buffer	5µl	New England Biolabs, M0493S
10mM dNTPs	0.5µl	Thermo Fisher, 10610851
10µM Forward Primer	1.25µl	Sigma-Aldrich, bespoke design
10µM Reverse Primer	1.25µl	Sigma-Aldrich, bespoke design
Q5 High-Fidelity DNA Polymerase	0.25µl	New England Biolabs, M0493S
DNA (50-100ng)	1-4µl	N/A
Nuclease-free H_2O	To 25µl	Thermo Fisher, AM9937

Table 2.6 Q5 PCR reaction programme: *temperature depends on primers

Temperature		Time
98ºC		30 seconds
98ºC	Repeat 35 cycles	10 seconds
60-75ºC*		30 seconds
72ºC		30 seconds
72ºC		7 minutes
4ºC		∞

2.2.3 Agarose Gel Electrophoresis and Sequencing

1.0g of UltraPure Agarose (Invitrogen) was added to 100ml of 1xTBE buffer (UltraPure™ 10X TBE, Invitrogen diluted 1:10 with MilliQ H_2O) in a 250ml conical flask and swirled to mix. The mixture was microwaved on 50% power and regularly agitated until the contents of the flask were transparent. 4µl of SYBR™ Safe DNA Gel Stain (Thermo Fisher Scientific) was added to the flask and mixed, before pouring into gel apparatus with a 12-well comb. After the gel had set, it was placed into an electrophoresis chamber (Hybaid, Thermo Fisher Scientfic) and the chamber was filled with 1X TBE buffer. 2.5µl of 1Kb DNA Hyperladder (Bioline) was added to the first well of the gel and 2.5µl of each sample was combined with 0.5µl of 5x DNA Loading Dye (Bioline) and added to subsequent wells. The gel was run using a power supply (E863, 600v-250mA, Consort) for 20-30 minutes at 100V before imaging on a Gel Doc™ XR+ system (Bio-Rad) with ImageLab™ Software (v5.2, BioRad).

The PCR product was purified using a NucleoSpin Gel and PCR Clean-up kit (Machery-Nagel) and sequenced by Source Bioscience (Nottingham, UK) with 10ng/µl PCR product

and 3.2pmol/µl primer. Sequences were visualised in SnapGene Viewer (v4.2.9, SnapGene, GSL Biotech LLC).

2.3 hiPSC differentiation

2.3.1 Directed differentiation of hiPSCs into the three germ layers (Endoderm, Mesoderm and Ectoderm)

Performed by Krushangi Patel

All hiPSC lines were differentiated into the three germ layers to demonstrate pluripotency. For all three lineages, hiPSCs were dissociated with Accutase and seeded into 24 well plates (Corning Co-Star) onto 0.1% Gelatin (from porcine skin, Sigma Aldrich) at $2.63 \times 10^4/cm^2$ (for endoderm and mesoderm) or $1.84 \times 10^4/cm^2$ (ectoderm) in E8 (**Table 2.2**) and ROCK inhibitor (1:1000, Y-27632, Stem Cell Technologies). The following day, medium was refreshed to E8 without ROCK inhibitor. Differentiation was started 48hrs post-seeding and differentiation medium was changed daily.

For endoderm, cells were cultured for three days in CDM-PVA (**Table 2.7**) with 10µM SB431542, 10ng/ml BMP-4, 20ng/ml FGF-2 and 10µM LY294002 (**Table 2.8**). For mesoderm, cells were cultured for two days CDM-PVA with 20ng/ml FGF-2, 10µM LY294002 and 10ng/ml BMP-4 (**Table 2.9**) was used. Finally, for ectoderm, cells were cultured for four days in 1µM all trans Retinoic Acid (RA) and 25ng/ml BMP-4 (**Table 2.10**). Cells were fixed in 4% Paraformaldehyde (PFA, Boster) and stained using GATA-4 (Endoderm), Brachury (Mesoderm) and PAX6 (Ectoderm) imaged on a Leica CTR4000 microscope (Leica Microsystems) using a DFC 3000 with Leica Application Suite software (v4.0.0.11706, Leica Microsystems). See Appendix for list of antibodies.

Table 2.7 CDM-PVA components

Components	Volume (250ml)	Supplier Information
IMDM	125ml	Thermo Fisher, 21980-032
F-12 Nut Mix + GlutaMAX-I	125ml	Thermo Fisher, 31765-027
Concentrated Lipids	2.5ml	Thermo Fisher, 11905-031
1-Thioglycerol	10µl	Sigma-Aldrich, M1753
Insulin	175µl	Sigma-Aldrich, 11376497001
Transferrin	125µl	Sigma-Aldrich, T1147
Poly vinyl alcohol (PVA)	5ml	Sigma-Aldrich, P8136

Table 2.8 Endoderm differentiation medium components

Components	Volume (9ml)	Supplier Information
CDM-PVA	10ml	See **Table 7**
10ng/ml BMP-4	10µl	Bio-Techne, 314-BP-500/CF
20ng/ml FGF-2	50µl	Biochemistry Department, University of Cambridge
10µM LY294002	10µl	Promega, V1201
100 ng/mL Activin	1ml	Biochemistry Department, University of Cambridge

Table 2.9 Mesoderm differentiation medium components

Components	Volume (10ml)	Supplier Information
CDM-PVA	10ml	See **Table 7**
10ng/ml BMP-4	10µl	Bio-Techne, 314-BP-500/CF
20ng/ml FGF-2	50µl	Biochemistry Department, University of Cambridge
10µM LY294002	10µl	Promega, V1201

Table 2.10 Ectoderm differentiation medium components

Components	Volume (10ml)	Supplier Information
CDM-PVA	10ml	See **Table 7**
25 ng/ml BMP4	25µl	Bio-Techne, 314-BP-500/CF
1 µM RA	0.5µl	Sigma-Aldrich, R2625

2.3.2 Differentiation of hiPSC into NC-SMCs

Performed by Dr Alex Granata

hiPSC were differentiated into neural crest smooth muscle cells (NC-SMCs) as previously described [288,346,347]. In brief, hiPSC were passaged with ReLeSR™ (Stem Cell Technologies) and plated onto 0.1% Gelatin (from porcine skin, Sigma Aldrich) in CDM-PVA (**Table 2.7**). 24 hours after plating, cells were washed once with PBS and media was changed to CDM-PVA with 12ng/mL FGF-2 and 10µM SB431542 (Tocris Bioscience) and refreshed daily for 5 days. On day 5, cells were passaged with TrypLE (Thermo Fisher) and thereafter passaged when confluent, until passage 10-12. NCs were assessed for the marker P75 in qRT-PCR

and were further differentiated into SMCs by culturing in CDM-PVA with 10ng/ml PDGF-BB and 2ng/ml TGFβ-1 (PT). Cells were media changed every other day for 12 days (PTd12) and passaged when confluent, before assessing at PTd12 for Calponin, PDGFRb, MCAM, NG2 and RGS5. Cells were then maintained long-term in DMEM/F12 (Thermo Fisher) supplemented with 10% fetal bovine serum (FBS; Sigma-Aldrich). qRT-PCR was performed to assess SMC phenotype at day 14 (SMC S14) for Calponin, PDGFRβ, MCAM, NG2 and RGS5 and day 30 (SMC S30) for Calponin, as well as in immunocytochemistry concurrently.

2.3.3 Differentiation of hiPSC into BMECs

hiPSC were differentiated into BMECs using a previously reported protocol [77,311]. One day before seeding, 6-well plates were coated with 0.5% Matrigel® (Corning®) in DMEM/F12 (ThermoFisher) and stored at 37ºC overnight. The next day, 70-80% confluent hiPSC were washed once with 1X PBS and then incubated with StemPro™ Accutase™ Cell Dissociation Reagent (Thermo Fisher Scientific) at 37°C for 4 minutes and dislodged, diluted 1:4 with E8 (described above) and centrifuged, before being re-suspended, counted and plated at a density of $1.56 \times 10^4/cm^2$ with ROCK inhibitor. 24 hours later, media was changed to TeSR™-E6 (Stem Cell Technologies, **Table 2.11**) and refreshed daily for 4 days. After this, cells were cultured in Endothelial medium (**Table 2.12**) composed of Endothelial serum-free media (SFM) and B-27, with 10ng/ml FGF-2 and 10µM RA for 2 days. Meanwhile, culture plates were coated with collagen IV (from human placenta, 1mg/ml, Bornstein and Traub Type IV; C5533, Sigma Aldrich) and fibronectin (from bovine plasma, 1mg/ml, F1141, Sigma Aldrich) according to a 4:1:5 ratio (**Table 2.13**). This mixture was used directly on 12-well (CLS3460, Corning®) or 24-well Transwells® (CLS3470, Corning®) or further diluted 1:5 in 1X PBS for cell culture plates (6-,12-, or 24-well, Corning®, Thermo Fisher) [314] using a set coating volume (**Table 2.14**) and incubated at 37ºC from 4 hours to overnight.

Following two days of Endothelial medium treatment, cells were washed once with 1X PBS and disassociated with Accutase into single cells before counting and plating at a set density (**Table 2.15**) into Endothelial medium onto collagen IV/fibronectin coated plates. 24 hours after plating, media was refreshed to Endothelial medium without FGF-2 or RA. Subsequent media changes were performed every 48hours for 5-7 days. BMEC phenotype was assessed using immunocytochemistry for VE-Cadherin, claudin-5, occludin and GLUT-1 (antibodies can be found in the Appendix) and qRT-PCR for CD34, PECAM-1, VE-Cadherin, occludin, claudin-5 and OCT4. Intermediate neuroectoderm-like populations at day 4 and 6 of differentiation were assessed for P75, PAX6 and NESTIN by qRT-PCR.

Table 2.11 TeSR™-E6 medium components

Components	Volume (50ml)	Supplier Information
TeSR™-E6	47.5ml	Stem Cell Technologies, 05946
TeSR™-E6 Supplement (20X)	2.5ml	Stem Cell Technologies, 05946

Table 2.12 Endothelial medium components

Components	Volume (50ml)	Supplier Information
Human Endothelial Serum-Free Medium	49.5ml	Thermo Fisher, 11111044
B-27	250µl	Thermo Fisher, 1704044
FGF-2 (4µg/ml)	250µl (20ng/ml)	Biochemistry Department, University of Cambridge
Retinoic Acid (20mM)	25µl (10µM)	Sigma-Aldrich, R2625

Table 2.13 Collagen IV/Fibronectin dilutions

Collagen IV	Fibronectin	1X PBS	Total Volume
400ul	100ul	500ul	1ml
480ul	120ul	600ul	1.2ml
600ul	150ul	750ul	1.5ml
800ul	200ul	1000ul	2ml

Table 2.14 Collagen IV/Fibronectin coating volume

Vessel	Coating volume
12wp Transwell® (4:1:5)	200µl
24wp Transwell® (4:1:5)	100µl
12 well plate (4:1:5 then 1:5)	500µl
24 well plate (4:1:5 then 1:5)	250µl
6 well plate (4:1:5 then 1:5)	1ml

Table 2.15 Sub-culturing seeding density: acquired from[314]

Vessel	Cell Seeding Number
6-well	1.0×10^6/well
12-well	5.0×10^5/well
24-well	2.5×10^5/well
12-well Transwell®	1.1×10^6/filter
24-well Transwell®	3.3×10^5/filter

2.3.4 Differentiation of hiPSCs into astrocytes

hiPSC differentiation into NSCs

hiPSCs were differentiated into NSCs using an available protocol, but modified so the initial stage begins with E6 medium (Adapted from [286]). hiPSCs were passaged with Accutase and counted before plating in E8 medium with ROCK inhibitor as single cells at a density of 2.0×10^5/cm^2 on VTN-N (Thermo Fisher, 1 hour coating at room temperature). 24 hours later, media was changed to a neural induction media (NIM) consisting of TeSR™-E6 with three cytokines: SB431542, XAV939 and LDN193189 (**Table 2.16**). Media was refreshed every 24 hours for 10 to 12 days before passaging with Accutase 1:1 onto VTN-N into N2B27 neural maintenance media (NMM; Neurobasal, DMEM/F-12, N-2, B-27, GlutaMAX, NEAA, Sodium Pyruvate, 2-mercaptoethanol, Insulin and FGF-2, **Table 2.17**). After approximately 3-5 days (until 100% confluent), cells were passaged with Accutase, counted and plated at 5.0×10^4/cm^2 onto Laminin (L2020, Sigma-Aldrich) and once confluent, disassociated to single cells and cryopreserved in NMM + 10% DMSO. On thawing, samples were harvested for qRT-PCR and immunocytochemistry performed, with markers for PAX6, OCT4, NESTIN and FOXG1 to confirm NSC phenotype.

Table 2.16 NIM components

Components	Volume (50ml)	Supplier Information
TeSR™-E6	47.5ml	Stem Cell Technologies, 05946
TeSR™-E6 Supplement (20X)	2.5ml	Stem Cell Technologies, 05946
SB431542 (20mM)	25µl (10µM)	Sigma-Aldrich, S4317
LDN193189 (10mM)	5µl (1µM)	Sigma-Aldrich, SML0559
XAV939 (10mM)	10µl (2µM)	Sigma-Aldrich, X3004

Table 2.17 NMM components

Components	Volume (250ml)	Supplier Information
Neurobasal	125ml	Thermo Fisher, 12348017
DMEM:F12+Glutamax	125ml	Thermo Fisher, 10565018
N-2 Supplement	1.25ml	Thermo Fisher, 17502048
B-27 Supplement	2.5ml	Thermo Fisher, 1704044
GlutaMAX	1.25ml	Thermo Fisher, 35050061
Non-essential amino acids (NEAA)	1.25ml	Thermo Fisher, 11140035
Sodium Pyruvate (100mM)	1.25ml	Thermo Fisher, 11360070
2-mercaptoethanol (50mM)	250µl	Thermo Fisher, 31350010
Insulin (10mg/ml)	62.5µl	Sigma-Aldrich, 10516

NSC differentiation into astrocytes

hiPSC-derived NSCs were further differentiated into astrocytes using a previously published protocol [336]. Culture plates were coated with Poly-L-ornithine (PLO; Sigma-Aldrich) for 1 hour at room temperature before washing with 1X PBS and coating overnight with 1:300 Laminin L2020 (Sigma-Aldrich). The following day, NSCs were plated at a density of 50-60% on PLO-Laminin in NMM (described above). 24hrs after plating, media was changed to astrocyte differentiation media (NMM with CNTF and BMP2 and FGF-2, **Table 2.18**). Media was changed every 48hrs for 5-6 passages. Cells were assessed for astrocyte phenotype using qRT-PCR (with primers for PAX6, NESTIN, OCT4, FOXG1, GFAP and CHD5) and immunocytochemistry for GFAP.

Table 2.18 Astrocyte differentiation medium components

Components	Volume (50ml)	Supplier Information
Neural Maintenance medium (above)	50ml	See above
CNTF (5mg/ml)	5µl (5ng/ml)	PeproTech, 450-13-5
BMP-2 (5mg/ml)	5µl (5ng/ml)	PeproTech, 120-02
FGF-2 (4µg/ml)	10µl	Biochemistry Department, University of Cambridge

2.3.5 siRNA gene silencing

hiPSC-BMEC were plated into 6 well plates at the sub-culture stage (described above). At 4-5 days post sub-culture, 40-100nm of stock concentration 20µM MMP14 (Ambion™ Silencer™ Select 4390824) or scrambled siRNA (Dharmacon, SI03650318) was combined

with 96µl of Opti-MEM™ (ThermoFisher Scientific). Separately, 2.5µl of DharmaFECT (Dharmacon, T-2001-01) was added to 97.5µl of Opti-MEM™. After 5 minutes at room temperature, the two were mixed and incubated at room temperature for a further 20 minutes. The 200µl was made up to 1ml per 6 well. After 24hrs, media was changed to Endothelial medium. The following day, a 12-well of each condition was lysed with RLT buffer for RNA extraction (see '2.4.2 RNA Extraction' below). 6 well plates were treated for a second time, as described, before being collected on the 5th day for protein analysis (see '2.4.12 Protein Extraction from Whole Cell Lysate' below).

2.4 Assays

2.4.1 Transendothelial Electrical Resistance (TEER)

One day after plating BMECs onto Transwells® (as above), TEER measurements using STX2 electrodes and an EVOM2 Voltohmmeter (World Precision Instruments) were acquired, as described previously [77]. Measurements were taken every 24 hours, after equilibration to room temperature. The STX2 electrode was positioned within the well (**Figure 2.1**) and the resistance (Ω) was recorded once equilibrated, before repeating in two more locations in the Transwell®, to calculate the mean resistance. All values are given as Ωxcm^2 after subtracting the resistance of an empty, coated Transwell® filter maintained in the same culture media, and multiplying by the surface area (12-well Transwell® 1.12cm^2, 24-well Transwell® 0.33cm^2) as described previously [77]
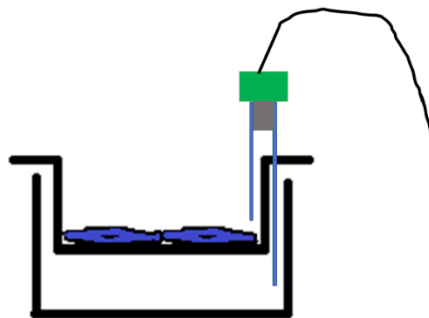
Figure 2.1 TEER assay electrode set-up: STX2 electrode placement in a Transwell®

2.4.2 RNA Extraction

Confluent, adherent hiPSC colonies or differentiated cells were lysed directly in the culture well with 350µl of RLT buffer from the RNAEasy Kit (Qiagen). RNA was extracted following the manufacturer's instructions.

2.4.3 Reverse transcription of RNA to cDNA

RNA concentration was quantified using a NanoDrop 2000 (Thermo Fisher). 250ng of RNA was used to synthesise cDNA with the Maxima First Strand cDNA Synthesis Kit (**Table 2.19**)

Table 2.19 Maxima first strand cDNA synthesis components

Components	Volume	Supplier Information
Maxima Enzyme Mix	1µl	Thermo Fisher, K1671
5x Reaction Mix	2µl	Thermo Fisher, K1671
RNA	250ng	N/A
Nuclease-free H_2O	To 10µl	Thermo Fisher, AM9937

The cDNA synthesis reaction (**Table 2.20**) was performed in a T100 Thermal Cycler (Bio-Rad) before diluting 1:40 in nuclease-free H_2O, in preparation for qRT-PCR.

Table 2.20 Thermocycler programme for cDNA synthesis

Temperature	Time
25ºC	10 minutes
50ºC	15 minutes
85ºC	5 minutes
4ºC	∞

2.4.4 Quantitative Real Time PCR (qRT-PCR)

Primers were designed or acquired from the literature (full sequences can be found in the Appendix). qRT-PCR was carried out with Fast SYBR Green Master Mix (**Table 2.21**) in a MicroAmp optical 384-well reaction plate using the 384W ΔΔCT SYBR Green programme on a QuantStudio 7 Flex qRT-PCR machine (Applied Biosystems, Thermo Fisher). Programme information can be found in **Table 2.22**.

Table 2.21 SYBR Green components per single reaction

Components	Volume (10µl)	Supplier Information
Fast SYBR Green MasterMix	4.69µl	Thermo Fisher, 4385616
10µM Forward Primer	0.094µl	Sigma-Aldrich, bespoke design
10µM Reverse Primer	0.094µl	Sigma-Aldrich, bespoke design
H_2O	2.63µl	Thermo Fisher, AM9937
cDNA	2.5µl	(As above)

Table 2.22 384W ΔΔCT SYBR thermocycler programme for qRT-PCR

Temperature		Time
50ºC		2 minutes
95ºC		10 minutes
95ºC	Repeat 40 cycles	15 seconds
60ºC		1 Minute
95ºC		15 seconds
60ºC		1 minute
95ºC		15 seconds

Cycle Threshold data were analysed with QuantStudio Software V1.3 (Applied Biosystems, Thermo Fisher). Data are given as fold change (ΔΔCT) relative to the mean of GAPDH and PBGD housekeeping genes and to the level in hiPSCs of the same cell line, unless otherwise stated.

2.4.5 Immunocytochemistry

Cells in culture dishes were fixed with 4% PFA (Boster) for 20 minutes at 4°C or 100% ice cold Methanol for 15 minutes at -20°C and then washed 3 times with 1X PBS containing Calcium and Magnesium (+/+, Oxoid) for 3 minutes each time. Cells were permeabilised with 0.05% Triton-X-100 in 10% FBS before being incubated with primary antibodies (see Appendix) overnight at 4°C. The cells were then washed with PBS (+/+) 3 times for 3 minutes. Secondary Alexa Fluor antibodies (see Appendix) as well as DAPI (Sigma-Aldrich) were incubated for 1 hour at room temperature before a final 3 washes with PBS (+/+). Image acquisition was performed on a Zeiss confocal microscope or Leica Sp5 (Leica Microsystems) and analysis performed in FIJI/ImageJ. Quantification of fluorescence intensity was performed by taking the mean pixel intensity (Integrated Density, threshold 75-170) relative to the number of DAPI-positive cells, from an average of 3-5 fields of view from the same well. All images are representative images.

2.4.6 Fluorescein isothiocyanate–dextran permeability

Fluorescein isothiocyanate–dextran (FITC-Dextran) experiments were conducted 2 days post-subculture onto fibronectin/collagen IV coated 24 well Transwells®. An empty, coated Transwell® was included as a control. Spent media was removed from the upper chamber of the Transwell® and replaced with 600µl of 40KDa, 10KDa (both 25mg/ml) or 4KDa FITC-Dextran (50mg/ml) diluted 1:100 in endothelial serum-free media with B-27. Samples of 100µl were taken from the basolateral side every two hours for eight hours (**Figure 2.2**). Dextran compounds are listed in **Table 2.23**.
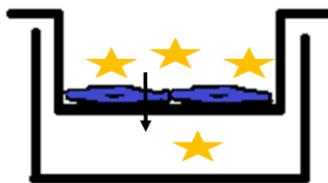
Figure 2.2 Fluorescent permeability assay: FITC-Dextran experimental strategy in a Transwell®

Raw fluorescence was measured on a TECAN Infinite M200 Pro plate reader with Magellan™ software (v7.2, TECAN) in a 96 well flat black plate (Thermo Fisher Scientific), with an excitation wavelength of 490nm and emission 520nm with a gain of 50, 25 flashes and z-position of 20000.

Table 2.23 FITC-Dextran compounds

Compound and Size	Supplier Information
40kDa	Sigma FD40S
10kDa	Sigma FD10S
4kDa	Sigma 46944

2.4.7 Sodium fluorescein

Sodium Fluorescein experiments were conducted 2 days post-subculture onto fibronectin/collagen IV coated 24 well Transwells®. An empty, coated Transwell® was included as a control. Spent media was removed from the upper chamber of the Transwell® and replaced with 600µl of Sodium Fluorescein (F6377, Sigma-Aldrich 1mg/ml) diluted 1:100 in endothelial serum-free media with B-27. Samples of 100µl were taken from the basolateral side every two hours for eight hours. Raw fluorescence was measured on a TECAN Infinite M200 Pro plate reader in a 96 well flat black plate (Thermo Fisher Scientific), with an excitation wavelength of 460nm and emission 515nm with a gain of 50, 25 flashes and z-position of 20000.

2.4.8 Tube Formation

Previously described methodology was adapted (Lippmann *et al* 2012). 24-well tissue culture plates were coated with 500µl of 40% Matrigel® (Corning®) for 1hr at 37ºC. Collagen/fibronectin-purified hiPSC-BMEC were dissociated using Accutase. Cells were counted (as described above) and 100,000 cells were plated into each Matrigel-coated well in Endothelial serum-free media with B-27, supplemented with 40 ng/mL VEGF (100-20-100,

PeproTech). Phase images were acquired after 12/24/48 hours until tubes were formed. Thereafter, cells were fixed in 100% ice-cold Methanol and stained for BMEC markers (as above).

2.4.9 Low Density Lipoprotein-Uptake

Previously described methodology was used (Lippmann *et al* 2012). Low density lipoprotein (LDL)-uptake experiments were conducted 2-6 days post-subculture onto fibronectin/collagen IV coated 12 well plates. Spent media was removed and cells were washed twice with 1X PBS. Cells were incubated with Alexa Fluor 488 conjugated Acetylated LDL (ThermoFisher Scientific 1:100) for four hours at 37ºC. Cells were washed twice with 1X PBS and immediately imaged on a Leica CTR4000 microscope (Leica Microsystems) using a DFC 3000 with Leica Application Suite software (v4.0.0.11706, Leica Microsystems) and overlaid with a phase contrast image to determine cell number and percentage uptake of LDL.

2.4.10 Rhodamine123 Accumulation

Previously described methodology was used (Lippmann *et al* 2012). Briefly, hiPSC-BMEC were plated into a fibronectin/collagen IV 24 well plate as above. Spent media was removed and cells were washed twice with PBS. Cells were incubated with or without 5µM Cyclosporin A (C1832, Sigma-Aldrich) for 30 minutes at 37ºC. Following this, cells were washed twice with PBS and incubated with 10µM Rhodamine123 (R123; R8004, Sigma-Aldrich) for 60 minutes at 37ºC. Cells were washed with PBS twice before permeabilisation with 300µl of 5% Triton-X 100 (Sigma-Aldrich) in 1X PBS for 10 minutes at 37ºC. Triplicate wells of 100µl were plated into a 96 well flat black plate (Thermo Fisher Scientific). Raw fluorescence was detected on a TECAN Infinite M200 Pro plate reader with an excitation wavelength of 488nm and emission 535nm with a gain of 50, 25 flashes and z-position of 20000. Data was reported as mean of 3 technical replicates minus a blank (5% Triton-X 100) relative to the cell number of a sister well which was acquired by Accutase and counting the total number of cells (described previously).

2.4.11 Flow Cytometry

Flow Cytometry experiments were performed 4-6 days post-subculture of hiPSC-BMEC onto 12 well plates of fibronectin/collagen IV. Confluent wells were disassociated using Accutase and filtered to a single cell solution through a 40µm cell strainer (Corning®, Fisher Scientific). The cell suspension was fixed at 4ºC for 10 minutes using Fixation/Permeabilisation solution (BD Biosciences) and washed twice in PBS + 10% FBS. Cells were re-suspended in PBS + 10% FBS and incubated with primary antibodies or pre-conjugated antibodies for 30 minutes at 4ºC. An unstained sample was generated by

combining equal volumes of each cell suspension. Cells were washed twice in PBS + 10% FBS and re-suspended in 300µl of PBS + 10% FBS in preparation for analysis. If antibodies were not conjugated and a secondary antibody was used, cells were incubated for a further 30 minutes for 4ºC before washing and preparing for analysis the same manner. Cells were analysed using a Canto II Flow Cytometer (BD Bioscience). FACSDiva™ Software (BD Bioscience) was used for data capture and results were post-processed with FCSalyzer (v0.9.16)

2.4.12 Protein Extraction from Whole Cell Lysate

Cell samples for protein extraction were collected by first washing with 1X PBS, before replacing with a fresh 200µl of PBS. A 1.8cm cell scraper (Corning®) was used to collect all cells and matrix from the well of a 12 well plate before pelleting in a Microfuge (SciSpin). The collected sample was immediately placed onto ice before direct processing or placed into a -70ºC freezer for processing later.

Proteinase (Sigma-Aldrich, P8340) and Phosphatase inhibitors (Simga-Aldrich, P5726) were added at 1:100 dilution to Abcam Cell Lysis Buffer (ab134004, Abcam; sodium pyrophosphate decahydrate, sodium chloride, sodium EDTA, Tris HCL, Triton-X-100, EGTA, Leupeptin, sodium orthovanadate and β-glycerophosphate, pH 7.5) or RIPA buffer (Cayman Chemical; Tris HCL, sodium chloride, sodium deoxycholate and SDS, pH 7.6). 15-30µl of this solution was added to the cell sample and it was agitated at low speed for 5 minutes on a vortex before incubation on ice for 20 minutes. The sample was centrifuged at full speed for 2 minutes and the supernatant was recovered.

2.4.13 Quantification of Protein Concentration

Protein concentration of the whole cell lysate was quantified using the Pierce™ Bicinchoninic acid (BCA) Protein Assay Kit (Thermo Fisher). In brief, BCA buffer B was added to buffer A (1:50) and 98ul of A:B was added to each well of a 96-well flat-bottomed clear plate (Corning® CoStar). To this, 2µl of sample in duplicate (whole cell supernatant from the above lysis) or standards of BSA of known concentration (0, 2, 4, 6 and 8µg) were added and the plate was placed on an orbital shaker (ROTAMAX 120 Heidolph) at ~0.5 to 1 cycles per second for 15-20 minutes. The absorption at 570nm was measured on a TECAN Infinite M200 Pro plate reader. Absorption of known standards was plotted in MS Excel on an XY graph and the equation **y=mx+B** was used to determine the concentration as follows:

Concentration (µg/µl) = ((Mean absorption – X-intercept (**B**))/slope (**m**))/2

2.4.14 Western Blot

Preparation of Samples

Following quantification of protein concentration, 20-40µg of cell lysate sample was combined with 4x Dual Colour Protein Loading buffer (Boster) and 1:200 β-mercaptoethanol (Sigma Aldrich) and the volume adjusted to 10µl with nuclease-free H_2O, before being heated at 98ºC for 3-5 minutes.

Gel Running

A 10-well 4–15% Mini-PROTEAN® TGX™ Precast Protein Gel (Bio-Rad) was positioned inside a Mini-PROTEAN Tetra Cell (Bio-Rad). 1X Running buffer (10X Tris/Glycine/SDS (Bio-Rad) diluted 1:10 in MilliQ H_2O) was used to fill the chamber. Protein ladder (Precision Plus Protein™ All Blue Standard, BioRad) was loaded into the first well, followed by 20µg of each sample before running on a PS250 Electrophoresis Power Supply (Hybaid) at 100V for 10 minutes and then 175V for a further 45 minutes.

Gel Transfer

Two sheets of Mini Trans-Blot® Filter Paper (BioRad) were submerged in 1X Transfer Buffer (10X Tris/Glycine (Bio-Rad) diluted in MilliQ H_2O, with 20% Methanol (99.9%, for HPLC, Thermo Fisher Chemical) and placed onto a sponge on one side of the cassette. Immobilon-P PVDF paper (Merck Millipore) was activated by submerging in 100% Methanol and placed on top of the Mini Trans-Blot® Filter Paper. Following this, the gel was removed from the cast and placed onto the PVDF paper. Two more sheets of Mini Trans-Blot® Filter Paper were submerged in 1X Transfer Buffer and placed on top of the gel before rolling the paper thoroughly, to remove all bubbles between the gel and the PVDF paper. Another sponge was placed on top of the sandwich and sealed inside the apparatus, before placing inside a Mini Trans-Blot® Electrophoretic Transfer Cell (Bio-Rad). 1X Transfer Buffer was added to fill the chamber, along with an ice-block, before the whole apparatus was submerged in an ice bucket. The transfer was performed at 100V for 90 minutes.

Membrane Blotting

All incubations and washes were performed in a 50ml tube on a MX-T6-S tube roller (Scilogex) at 50% speed, in a volume of 3-5ml.

The PVDF membrane was removed from the cassette and washed in 1X TBST (10X TBST (175.2g NaCl, 24.2g TRIS) and 0.1% TWEEN® 20 (Sigma Aldrich) diluted 1:10 in MilliQ H_2O). Following this, the membrane was incubated with 3ml of 5.0% BSA (Sigma-Aldrich, A3059) at room temperature for 1 hour. Blocking buffer was removed and replaced with primary antibody (all antibodies can be found in the Appendix) in 5.0% BSA and incubated overnight at 4ºC.

The following day, primary antibody was removed, and the membrane was washed in 1X TBST three times for 5 minutes. The membrane was incubated with HRP secondary antibody in 1x TBST for 1 hour at room temperature, before 3 more TBST 1X washes. Residual liquid was removed with blotting paper and the membrane placed onto a plastic sheet. ECL Plus Western Blotting Substrate (Thermo Fisher) was made by mixing solution A and solution B (1:40). 500µl was added to the membrane and another plastic sheet was placed on top, to evenly distribute the solution. Following 1 minute of incubation, the membrane was placed in a Gel Doc™ XR+ system (BioRad). The ImageLab™ Software (v5.2, BioRad) High Resolution programme with Signal Accumulation Mode was used to capture images at incremental exposure times.

Blot Stripping

When probing for another protein of interest where the expected band size and/or species in which the antibody was raised overlapped, the blot was stripped, re-blocked and re-probed (up to a maximum of three times). To do this, 3ml of mild stripping buffer (**Table 2.24**) was applied to the membrane and incubated at room temperature for 10 minutes. Spent buffer was removed and replaced with fresh stripping buffer for a further 10 minutes. The second incubation was discarded, and the membrane was washed twice for 10 minutes with 1X PBS and twice with 1X TBST for 5 minutes. Following stripping, the membrane was blocked with blocking buffer (described above) for 30 minutes before incubation with antibodies (as described above).

Table 2.24 Mild stripping buffer composition

Components	Volume (50ml)	Supplier Information
Glycine	0.75g	Sigma-Aldrich, 50046
SDS	0.05g	Sigma-Aldrich, 75746
TWEEN® 20	500µl	Sigma-Aldrich, P7949
Ultrapure Water	To 50ml	N/A

Quantification of Band Intensity

Image intensity was quantified in FIJI (ImageJ) by first selecting a region of interest (ROI) encompassing the band of interest. The total intensity was measured by taking the Mean Gray Value of the band and an area immediately adjacent to the band, as the background value. Intensity was normalised to β-Actin for the same sample. The following calculation was used to calculate the relative intensity of the band of interest:

$$\text{Relative intensity} = \frac{(255\text{-Mean Gray Value of band of interest}) - (255\text{-Mean Gray Value of background})}{(255\text{-Mean Gray Value of }\beta\text{-Actin band}) - (255\text{-Mean Gray Value of }\beta\text{-Actin background})} \div \text{Smallest value}$$

2.4.15 Human MMP Antibody Array

A commercial antibody array was acquired (ab134004, Abcam) that targeted MMP1, MMP2, MMP3, MMP8, MMP9, MMP10, MMP13, TIMP1, TIMP2 and TIMP4 and completed following the manufacturer's instructions. All washes and incubations were performed on an orbital shaker at ~0.5 to 1 cycles per second.

Firstly, the membrane was placed into an 8-well tray and incubated with 2ml of 1X Blocking Buffer at room temperature for 30 minutes before being removed and replaced with 250µg of protein (lysed in 2X Cell Lysis Buffer (diluted 1:1 in nuclease-free H_2O) and quantified using the BCA assay as above) diluted to 1ml in 1X Blocking Buffer; overnight at 4ºC. The following day, a Large Volume Wash was performed whereby 30ml of Wash Buffer I was applied to the membrane for 30-45 minutes at room temperature. Three more washes of 2ml of Wash Buffer I were performed in the 8-well tray, for 5 minutes at room temperature. Following this, two washes using 2ml of Wash Buffer II were performed. After the last wash, membranes were incubated with 1ml of 1X Biotin-Conjugated Anti-Cytokines overnight at 4ºC. The following day washes with Wash Buffer I and Wash Buffer II were performed (as described above), before addition of 2ml of 1X HRP-Conjugated Streptavidin overnight at 4ºC. Washes were performed as described and membranes were prepared for chemiluminescence detection by placing onto blotting paper to remove any residual liquid and then onto the provided plastic sheet. 500µl of 1:1 Detection Buffer C and Detection Buffer D was added to the membrane and gently distributed evenly across the surface and incubated at room temperature for 2 minutes. A second plastic sheet was placed on top, before being placed in a Gel Doc™ XR+ system. ImageLab™ Software was used to serially acquire images at known exposure times until signal was saturated. Images were quantified using the same methodology for the Western Blot, except the 'positive' dots were averaged (instead of β-Actin), before being subtracted from the dot of interest.

2.5 *In vitro* co-culture BBB models

2.5.1 Transwell®

Either 12-well or 24-well Transwells® (Corning® 0.4 µm pore; Sigma Aldrich) were coated on the apical and basolateral side with collagen IV/fibronectin (as above). For triple co-culture experiments, following coating, Transwells® were turned upside down onto the lid of the culture plate. hiPSC-mural cells (provided by Dr Alex Granata) were dissociated with TrypLE (described above) and seeded onto the basolateral side of the Transwell® coated

with 0.1% Gelatin. After incubation for 1 hour, Transwells® were returned upright to culture plates and hiPSC-BMECs were dissociated and the seeded onto the apical side. For triple co-culture experiments, hiPSC-astrocytes were plated (as described above) into a separate 12-well or 24-well plate as required. The next day, Transwells® with BMEC with(out) mural cells were placed into the well with hiPSC-astrocytes. Transwells® were maintained without any further medium changes for up to 14 days. TEER measurements were performed daily (as described above).

2.5.2 Quasi Vivo®

Model set-up

A bespoke Quasi Vivo® chamber (QV1100) was provided by Kirkstall that is compatible with Corning® 24-well Transwells®. The set-up comprises of a polydimethylsiloxane (PDMS) chamber with a diameter of 10mm. The chambers were connected to a polypropylene reservoir bottle with Tygon tubing and Luer lock connectors. Tubing was passed through a peristaltic pump (PF22X0103, Parker) that was first calibrated (see below) and set to a speed of 100µl/min. Tubing was arranged so that only flow was applied to the apical side of the chamber, with stop locks used to maintain the basolateral side under static conditions. Transwells® were removed from the chamber with forceps and placed into a culture plate to enable daily TEER measurements to be taken.

Calibration

A single empty Quasi Vivo® 1100 chamber was arranged in the system. Water was added to the reservoir bottle and the Parker pump was run at a known speed (0,1,3,5 or 7) for 5 minutes. The volume of water in the chamber was measured by weighing. This was repeated twice more and the mean of 3 measurements was plotted relative to the pump setting (**Figure 2.3**).
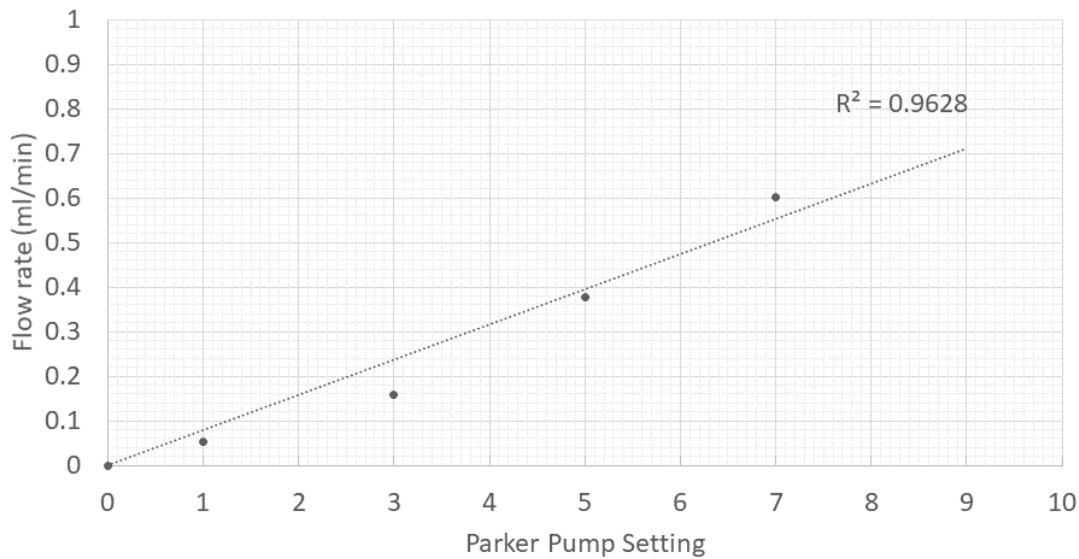
Figure 2.3 Calibration of the Parker peristaltic pump: calibration when one QV1100 chamber and one reservoir bottle is present.

2.5.3 BBB-on-a-chip

Device preparation

PDMS microvessel devices were manufactured as previously described[357] by Dr Gerigk (Dr Huang's laboratory, Engineering Department, University of Cambridge). One day prior to cell seeding, devices were prepared by injecting a collagen I gel and coating the outermost channels with collagen IV/fibronectin. In brief, collagen I gel was prepared by using a wide-orifice pipette tip (Sigma-Aldrich) to transfer 27.2µl of collagen I (Thermo Fisher, A1048301) into a 0.5ml Eppendorf. In a separate tube, 5µl of PBS (10x, containing phenol red), was combined with 3µl of NaOH and mixed thoroughly. On observation of a uniformly pink solution (indicative of a pH above 8.2), 5.4µl of distilled H_2O was carefully added down the side of the tube wall, before mixing thoroughly. This mixture was slowly added to the collagen I, so as not to generate bubbles. Using a 10µl pipette, 10µl of the complete solution was added to the gel-trap compartment of the microfluidic chip, using one of the innermost channels. The device was incubated at room temperature for 10 minutes before addition of Endothelial medium (described above) to the inlets on top of the device. The device was incubated at 37ºC for 1 hour.

After this incubation, fibronectin and collagen IV were combined as described above. Using a 10µl pipette, the matrix was added to the outermost channels by putting drops onto the inlet and using a gel-loading pipette tip (Thermo Fisher) in the outlet to slowly remove the mixture, allowing it to coat the complete channel. The device was incubated overnight at 37ºC.

Cell seeding

The outermost channels of the device were washed to remove residual collagen IV/fibronectin by adding drops of Endothelial medium to the inlet and using a gel-loading pipette tip at the outlet to remove the medium. hiPSC-BMECs were disassociated (as described above) at the point of sub-culture and resuspended in 1ml of Endothelial medium. Cells were added to the outermost channel by taking 10µl up with a pipette and then manually winding down the pipette volume, so that 3µl of cell suspension was added slowly, allowing it to fill the channel. The device was placed in an incubator at 37ºC for 45-60 minutes before a further addition of cells using the same method. The device was then turned upside down to yield a complete vessel formation in the outermost channel. After a further 45-60 minute incubation, the device was returned to the upright position and endothelial medium was added. The device was incubated overnight at 37ºC.

The following day, residual cells that had not adhered were removed using the washing process described above. Devices were maintained for 3-5 days before fixing with ice-cold methanol and immunostaining for BMEC markers (as described above).

2.6 Statistical Analysis

Unless otherwise stated within the text, all experiments were performed in biological triplicate (e.g. separate hiPSC differentiations). Statistical analysis was performed in GraphPad Prism (v8.2.0, GraphPad). Firstly, data sets containing two comparisons were tested for normality with a Shapiro-Wilk test, before performing a Kolmogorov-Smirnov (non-parametric) or an unpaired t-test (parametric). If the standard deviations were not equal, Welch's correction was used in place of an unpaired t-test.

For multiple comparisons, a one-way ANOVA or its non-parametric equivalent (Kruskal-Wallis) was used. Significance is denoted as follows: P>0.05 (ns), P≤0.05 (*), P≤0.01 (**), P≤0.001 (***) or P≤0.0001 (****). Results are reported as the mean ± Standard Deviation unless otherwise stated.

2.7 CRISPR-Cas9 gene editing

2.7.1 Design of guide RNAs (gRNAs)

The target DNA sequence for *COL4A1* was acquired from NCBI Gene (available at: https://www.ncbi.nlm.nih.gov/gene) and the nucleotide of interest was identified from the published literature[268], before being located in the gene sequence. One of the following two software packages was used to design gRNAs targeting the nucleotide of interest: CRISPR MIT (available at: http://crispr.mit.edu/) or Benchling (available at: https://benchling.com/). In general, gRNAs were selected according to the following criteria: close proximity to the

nucleotide of interest, low off-target effects in protein-coding regions, a PAM site that is easily mutated to introduce a silent mutation and 20 nucleotides in length.

For the vector integration, gRNA oligonucleotides (~20nt) were synthesised (Sigma-Aldrich) in 5'-3' format. Overhangs that were complementary to the vector site were added to the forward gRNA (*CACCG*~20nt*)* and the reverse gRNA (*AAAC)*~20nt *C)*. For the ribonucleoprotein approach, bespoke modified synthetic guide RNAs (sgRNA) were purchased from Synthego (CRISPRevolution Synthetic sgRNA kit). Sequences for gRNAs can be found in the Appendix.

2.7.2 Design of Donor DNA

Homology directed repair (HDR) donor DNA template was designed such that the nucleotide of interest (corrected to WT sequence) was positioned centrally, with a total length of 90 nucleotides. A silent mutation was introduced into the PAM site. Bespoke modified forward and reverse HDR templates were acquired from Integrated DNA Technologies (4nm Ultramer® DNA Oligonucleotides, IDT). Sequences for donor DNA can be found in the Appendix.

2.7.3 Vector-mediated CRISPR-Cas9 gene editing

CRISPR-Cas9 vector-mediated gene editing was carried out as described previously[358].

Cloning of gRNAs into the bacterial vector

In brief, forward and reverse gRNA oligonucleotides were annealed together (**Table 2.25**) using T4 Ligase Buffer and T4 Polynucleotide Kinase (New England Biolabs) using a T100 Thermal Cycler (**Table 2.26**).

Table 2.25 T4 ligase annealing reaction components

Components	Volume (10µl)	Supplier Information
T4 Ligase Buffer (10x)	1µl	New England Biolabs, M0202S
T4 Polynucleotide Kinase	1µl	New England Biolabs, M0201
Forward gRNA (100µm)	1µl	Sigma-Aldrich, bespoke design
Reverse gRNA (100µm)	1µl	Sigma-Aldrich, bespoke design
Nuclease-free H_2O	6µl	Thermo Fisher, AM9937

Table 2.26 Annealing of oligonucleotides reaction profile

Temperature	Time
37ºC	30 minutes
95ºC	5 minutes
95-25ºC	ramping at 5ºC/minute
4ºC	∞

The annealed oligos were diluted 1:200 (1µL of annealed oligo in 199µL of nuclease free water). Then, gRNAs were cloned into a WT pSpCas9n(BB) (pX460) vector (Addgene plasmid #48873) (**Tables 2.27** and **2.28**).

Table 2.27 Cloning into the vector reaction components

Components	Volume (20µl)	Supplier Information
Vector (100ng/ml)	1µl (100ng)	Addgene plasmid #48873
Diluted oligos	2µl	As above
Tango Buffer (10x)	2µl	Thermo Fisher, BY5
DTT (10mM)	1µl	Thermo Fisher, SSII kit
ATP (10mM)	1µl	New England Biolabs, 9804S
Fast Digest BbsI (BPiI)	1µl	Thermo Fisher, FD1014
T4 ligase	1µl	New England Biolabs, M0202S
Nuclease-free H_2O	to 20µl	Thermo Fisher, AM9937

Table 2.28 Cloning into the vector reaction profile

Temperature		Time
37ºC	6 cycles	5 minutes
21ºC		5 minutes
4ºC		∞

Linearised DNA was removed using Plasmid Safe Buffer and Exonuclease with ATP (**Tables 2.29** and **2.30**).

Table 2.29 Linearised DNA removal reaction components

Components	Volume (15μl)	Supplier Information
Ligation reaction from previous step	11μl	N/A
PlasmidSafe Buffer (10x)	1.5μl	CamBio, E3101K
ATP (10mM)	1.5μl	New England Biolabs, 9804S
PlasmidSafe exonuclease	1μl	CamBio, E3101K

Table 2.30 Linearised DNA removal reaction profile

Temperature	Time
37ºC	30 minutes
70ºC	30 minutes
4ºC	∞

Transformation of bacteria with the vector

Agar (Oxoid) was added to LB Broth culture media (Sigma-Aldrich) to make a 1% solution. Ampicllin was added to this solution, before plating onto 10cm plates and left to dry. Meanwhile, Alpha-Select Gold Efficiency bacteria (Bioline) were thawed on ice. The bacteria were supplemented with the vector incorporating the gRNA, before heatshock at 42°C for 40 seconds. The bacteria were then spread onto the agar plates and incubated overnight at 37°C. Approximately 14 hours later, colonies were picked and cultured overnight in loose-lid tubes (Falcon, BD Bioscience) in LB broth, in a shaking incubator at 37°C, 220-250rpm.

Plasmid extraction, vector sequencing and expansion

Bacterial cultures were then collected and centrifuged at 4,000rpm for 10 minutes. Plasmid DNA was extracted using a GenElute Plasmid Miniprep Kit (Sigma-Aldrich), following the manufacturer's instructions. 100μg/ml of Plasmid dsDNA was sequenced by Source BioScience and assessed for insertion of the gRNA sequence using SnapGene Viewer. The plasmids that were positive for the gRNA were expanded overnight in LB broth before extraction of plasmid DNA using a Qiagen Plasmid Midiprep Kit (Qiagen).

Maintenance and transfection of HEK293T cells

Human embryonic kidney cells (HEK293T) were maintained in mouse embryonic fibroblast (MEF) medium (**Table 2.31**) containing Advanced DMEM/F-12, 10% fetal bovine serum (FBS), 2mM L-Glutamine, and β-Mercaptoethanol. Cells were passaged with TrypLE every 2-3 days or when 70-80% confluent. 48hours before transfection, cells were plated at a density of 5.0×10^5 per well of a 6 well plate. For transfection, media was substituted for Opti-

MEM (ThermoFisher). Lipofectamine 2000 (Invitrogen) and 4μg of plasmid were incubated for 20 minutes at room temperature (15-25°C) in OptiMEM, before adding to the cells. One well was transfected with Pmax GFP (Lonza) as a transfection control, to assess the transfection efficiency and another well was left untreated, as a control sample. The next morning, media was changed to the above maintenance media and after a further 24hrs, media was supplemented with puromycin at a final concentration of 1μg/ml for 48-72 hours, before replacing with puromycin-free media. Cells were harvested for DNA extraction 48-72 hours after recovery from puromycin treatment.

Table 2.31 MEF medium components

Components	Volume (250ml)	Supplier Information
Advanced DMEM/F-12	225ml	Thermo Fisher, 12634010
FBS (100%)	25ml (10%)	Thermo Fisher, 10500-064
L-Glutamine	2.5ml (2mM)	Sigma-Aldrich, G3126
β-Mercaptoethanol	1.75μl	Sigma-Aldrich, M-7522

PCR and Agarose Gel Electrophoresis

Genomic DNA was extracted from transfected and untransfected (control) HEK293T cells using a GenElute Mammalian Genomic DNA Miniprep Kit (Sigma-Aldrich), following the manufacturer's instructions. Specific primers (see Appendix) were designed to give a 2Kb product surrounding the nucleotide of interest for each gRNA and two clearly distinguishable bands following heteroduplex formation and digestion with endonuclease. The region of interest was amplified as previously described.

T7 Endonuclease Assay

On observation of a single band of 2kb, the PCR product was purified using a NucleoSpin Gel and PCR Clean-up kit (Machery-Nagel), following the manufacturer's instructions. Next, 100ng un-transfected and 100ng transfected HEK293 purified genomic DNA was annealed (**Table 2.32**) using NEBuffer 2 (New England Biolabs) for heteroduplex formation. A control reaction, using 200ng of un-transfected DNA was also performed.

Table 2.32 Annealing un-transfected and transfected DNA

Temperature	Time
95ºC	5 minutes
95ºC-85ºC (-2ºC/second)	
85ºC-25ºC (-1ºC/second)	
4ºC	∞

Following this, 19µl of the resulting reaction was treated with 1µl of T7 Endonuclease I (New England Biolabs) for 30 minutes at 37°C before separation on a 1% Agarose gel. The Cas9 was confirmed to cut at the region of interest when 2 clear bands at the expected size were observed on the gel.

2.7.4 Ribonucleoprotein-mediated CRISPR-Cas9 gene editing

Transfection of hiPSC

P3 supplement was added to P3 solution, to yield 100µl (for five nucleofection reactions) following the manufacturer's instructions (P3 Primary Cell 4D Nucleofector™ X Kit S, Lonza). 2.25µl of Bespoke sgRNA (100µM, Synthego) was combined with 20µg of recombinant SpCas9 protein (4.8mg/ml, Biochemistry Department, University of Cambridge) and incubated at room temperature for 10 minutes. To this, 5µl HDR donor DNA template (bespoke design, 100µM, Integrated DNA Technologies, IDT) was added. Donor DNA and Cas9/sgRNA solutions were then combined with the complete P3 solution and maintained on ice during cell preparation.

hiPSCs were dissociated to single cells with Accutase and counted to obtain 1.0×10^6 cells, before centrifugation. The cell pellet was re-suspended in P3 solution containing Cas9, guide RNA and donor plasmid DNA and 20µl was transferred to a each well of a 16-well Nucelocuvette™ strip (P3 Primary Cell 4D Nucleofector™ X Kit S, Lonza). Cells were electroporated using a 4D Nucleofecor (Lonza) before addition of TeSR-E8 media (Stem Cell Technologies) with ROCK inhibitor and CloneR (Stem Cell Technologies) and incubation at 37°C for 10 minutes, to aid cell recovery. Cells were then plated onto a Vitronectin 1:25 coated 12-well plate.

The following day, spent media was collected containing a pool of nucleofected dead cells and centrifuged to obtain a cell pellet. DNA was extracted, Q5 PCR-amplified and sequenced as described above. Synthego ICE analysis (Available at: https://www.synthego.com/products/bioinformatics/crispr-analysis) or Tracking of Indels by decomposition (TIDE, available at: https://tide.deskgen.com/) was performed, comparing

control and nucleofected samples to obtain a percentage efficiency of cutting. On obtaining a positive nucleofection result, cells were grown to 70-80% confluency before being passaged with Accutase to single cells and plating at 1×10^3 cells/ml in a Vitronectin 1:25 coated 10cm dish (Thermo Fisher). After colonies emerged, they were picked and plated into 24 well plates for expansion, before Q5 PCR and sequencing (as described above).

Chapter 3: Optimisation of hiPSC-derived BMEC differentiation

3.1 Aims of this chapter

This chapter describes the optimisation and application of protocols to differentiate hiPSC into BMEC. For hiPSC-BMEC generation, a protocol that yields hiPSC-BMEC in a short time scale (about 10 days) was utilised[77]. However, qRT-PCR of separate differentiations of the same line yielded high variability between these replicates. Moreover, initial work with two WT hiPSC lines also revealed a high degree of variability between the two lines. Thus, the protocol was refined, taking on methods from other publications[314] as well as a recently published update from the authors of the original 2017 paper[311].

3.2 hiPSC-BMEC differentiation

A published protocol (**Figure 3.1**), was initially used to generate BMEC from hiPSC[77].The 10-15 day protocol begins by utilising the indiscriminate differentiation afforded by a basal, simplified medium, E6 (**Figure 3.2**). Cells are plated as single cells onto Matrigel® and grow into small colonies during four days of treatment with E6. On day five, cells are treated for two days with EC media, containing endothelial serum-free media (Endo-SFM), B-27, FGF-2 and RA for 2 days. Cells undergo rapid proliferation and by the end of the EC phase on day 7, areas of overgrowth form networks. At this point, sub-culture takes place whereby cells are disassociated to single cells and plated onto fibronectin/collagen IV in EC media. They undergo matrix selection, since fibronectin/collagen IV favours attachment of BMEC. After this, on day 8, cells display endothelial morphology and media is replaced with Endo-SFM and B-27 (i.e. no FGF-2 and RA; **Figure 3.2**).
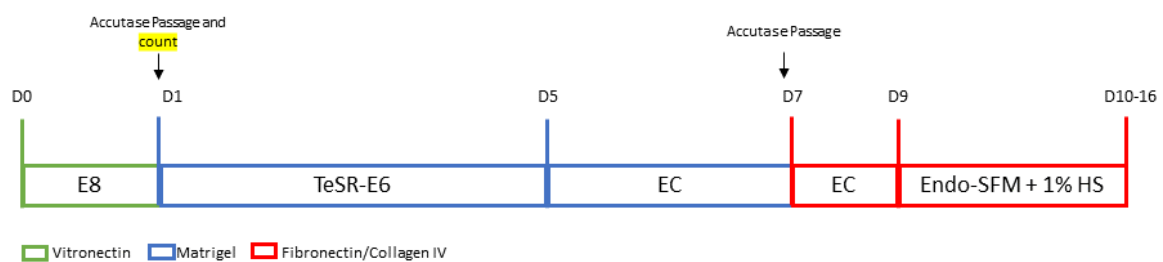
Figure 3.1 Differentiation timeline of hiPSC-BMEC: Cells are plated on Vitronectin XF in E8 media. On day 1, media is replenished to TeSR-E6 for 4 days, before treatment for 2 days with EC media. Following this, cells are single cell passaged with Accutase and plated onto collagen IV/fibronectin
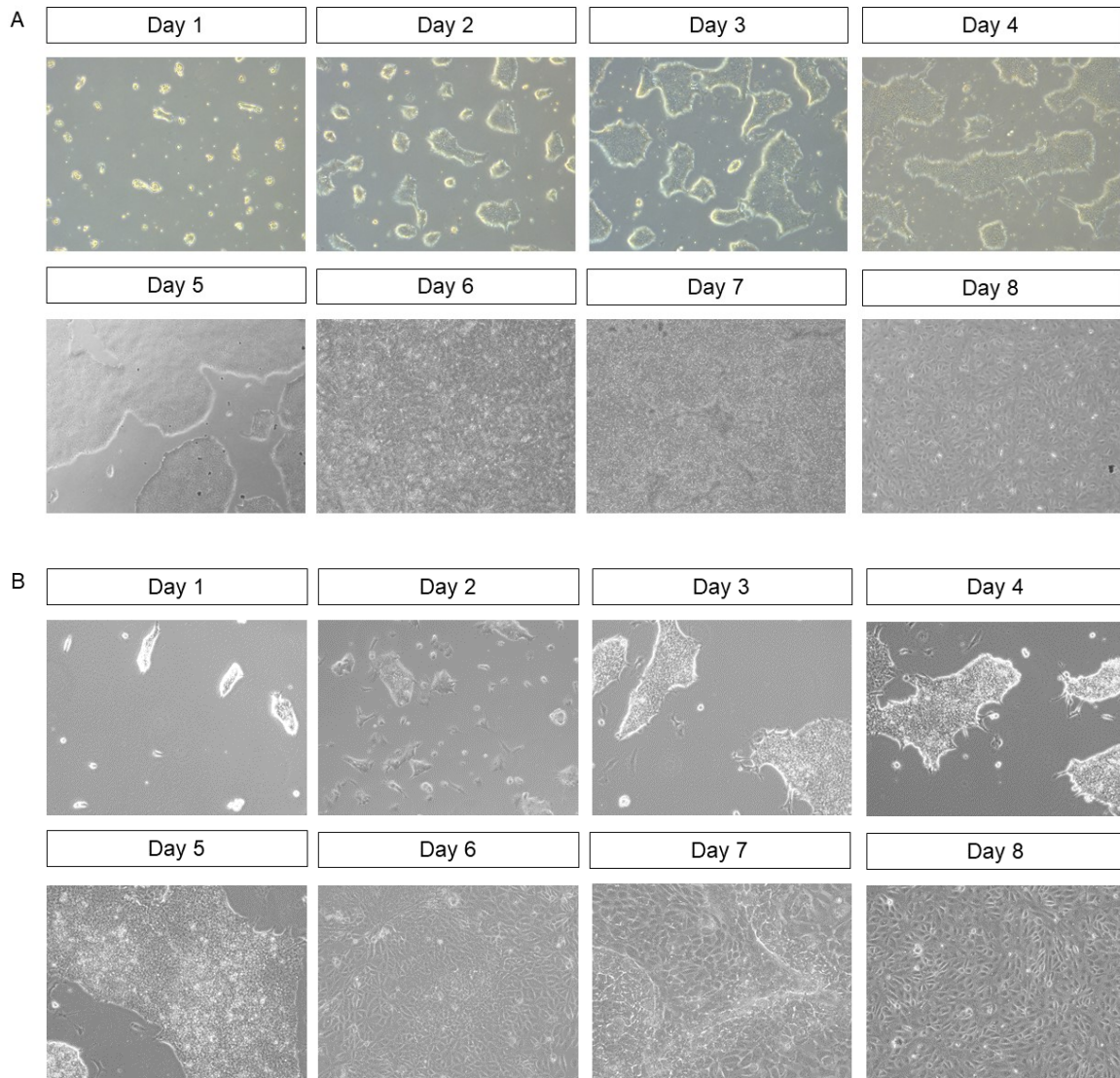
Figure 3.2 Representative phase contrast images of the hiPSC-BMEC differentiation: differentiation morphology from day 1 to 8, **(A)** 4x objective and **(B)** 10x objective. 10x images were provided by Dominika Krzyzanska.

3.2.1 hiPSC-BMEC transition through a neuroectoderm-like PAX6+ state

The initial 4-day period of E6 treatment is not well defined, but previous work from the Lippmann group[307,313], showed that the cells transitioned through a NESTIN+/βIII-tubulin neuroectoderm state.

There is a linear trend of increasing *PECAM1*, *CDH5* (VE-Cadherin) and *CLDN5* (claudin-5) during the time-course (**Figure 3.3A**). Pluripotency marker *POU5F1* (OCT4) shows immediate and continued decline in expression from day 4 to P1 of the differentiation (**Figure 3.3B**).

Although there is high variability between the replicates of WT1, there is no overall trend in either *PAX6* or *NES* (NESTIN) increasing across the time-course (**Figure 3.3C**). However, this high variation between experiments could be explained by the spontaneous differentiation caused by E6 treatment, which may promote variability in the cell population during the early phases of the differentiation. The reduction in *P75* (a neural crest marker, **Figure 3.3C**) suggests that these cells pass through a neuro-ectoderm like state, rather than a neural crest intermediate.
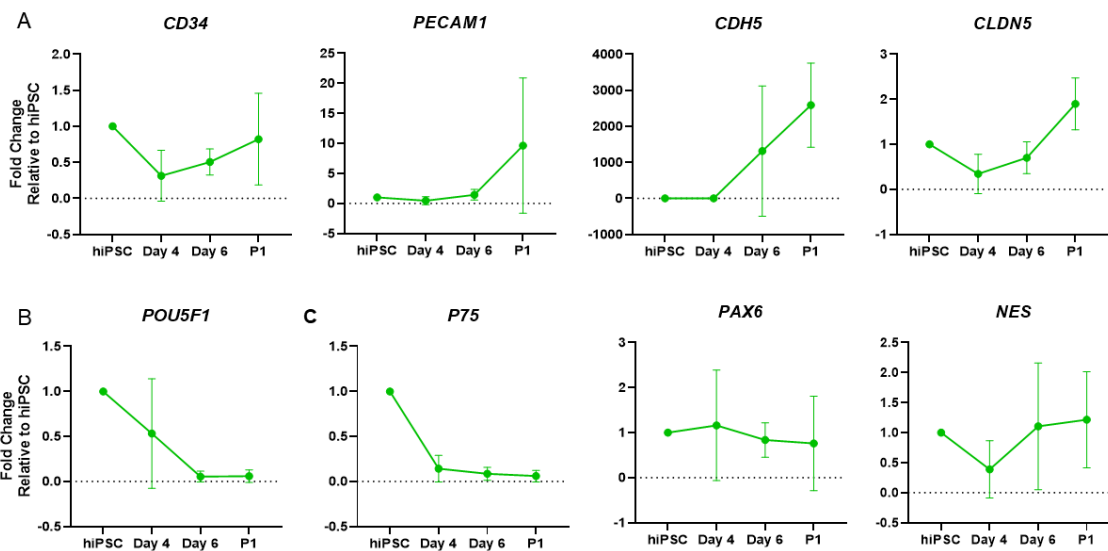
Figure 3.3 qRT-PCR of hiPSC, Day 4, Day 6 and Passage 1 hiPSC-BMEC: Time-course of WT1 hiPSC-BMEC differentiation qRT-PCR of **(A)** BMEC markers **(B)** *POU5F1*, and **(C)** intermediate markers *P75*, *PAX6* and *NES*; WT1 n=2 differentiations (abbreviation, P=passage).

3.2.2 hiPSC-BMEC differentiation revels inter-line variability in RNA expression and heterogenous culture

Subsequent experiments with two WT lines revealed high inter-line variability (**Figure 3.4; Table 2.1**). All markers show higher expression in WT1 compared to WT2. In particular, *CDH5* levels for WT1 are significantly (over 730-fold) higher than WT2. However, this could suggest that WT2 does not have the same differentiation capacity as WT1. To address this, more WT lines were later included.

Since initial hiPSC differentiations into BMEC yielded highly variable qPCR results and a heterogeneous culture; a number of optimisation steps were attempted, to harmonise differentiations between multiple cells lines and differentiations of the same cell line.
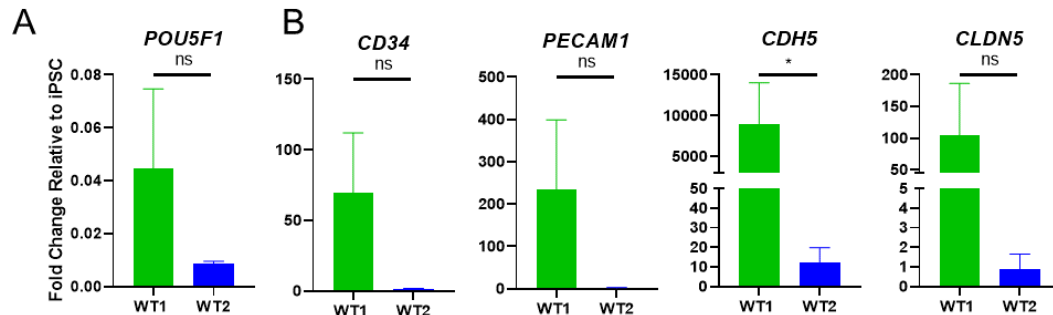
Figure 3.4 qRT-PCR at passage 1 for WT1 and WT1 hiPSC-BMEC: (A) pluripotency marker *POU5F1* P=0.1087 and **(B)** BMEC markers, *CD34* p=0.0501, *PECAM1*, P=0.0715, *CDH5* P=0.0357, *CLDN5* P=0.0965; WT1 and WT2 lines, N=3 separate differentiations, error bars are Mean +/- SD; unpaired t-test.

3.3 hiPSC-BMEC differentiation optimisation

To reduce the inter-line and inter-differentiation variation observed with the original protocol, a number of optimisation steps were attempted. Firstly, taking insight from the literature, cells were counted and plated at the sub-culturing stage at a density of $1.11 \times 10^5/cm^2$ in well plates and $1.1 \times 10^6/cm^2$ in Transwells®[314]. This varies from the original protocol which uses a ratio to sub-culture, which does not take into consideration differences between lines or differentiations[77]. Next, optimisations of plating density, media components and selection method were conducted.

3.3.1 Varying the plating density affects the end-point population of hiPSC-BMEC

Since different hiPSC lines proliferate at different rates, various plating densities were tested to determine the suitable density for individual lines, with the aim of harmonising results at the end-stage. The initial protocol[77] presents a seeding density range of 10,000-15,600/cm²[77]. Six seeding densities were tested, covering the reported range and above, up to $20,000/cm^2$.

The difference following the first 4 days of E6 differentiation is visually apparent between two WT lines (**Figure 3.5**). WT1 (**Figure 3.5A**), proliferates more than WT2 (**Figure 3.5B**), with almost a complete monolayer at the highest density of $20,000/cm^2$, whereas WT2 is only ~60% confluent. This highlights the variation between independent hiPSC lines, which could explain gene expression differences in the end-point population.
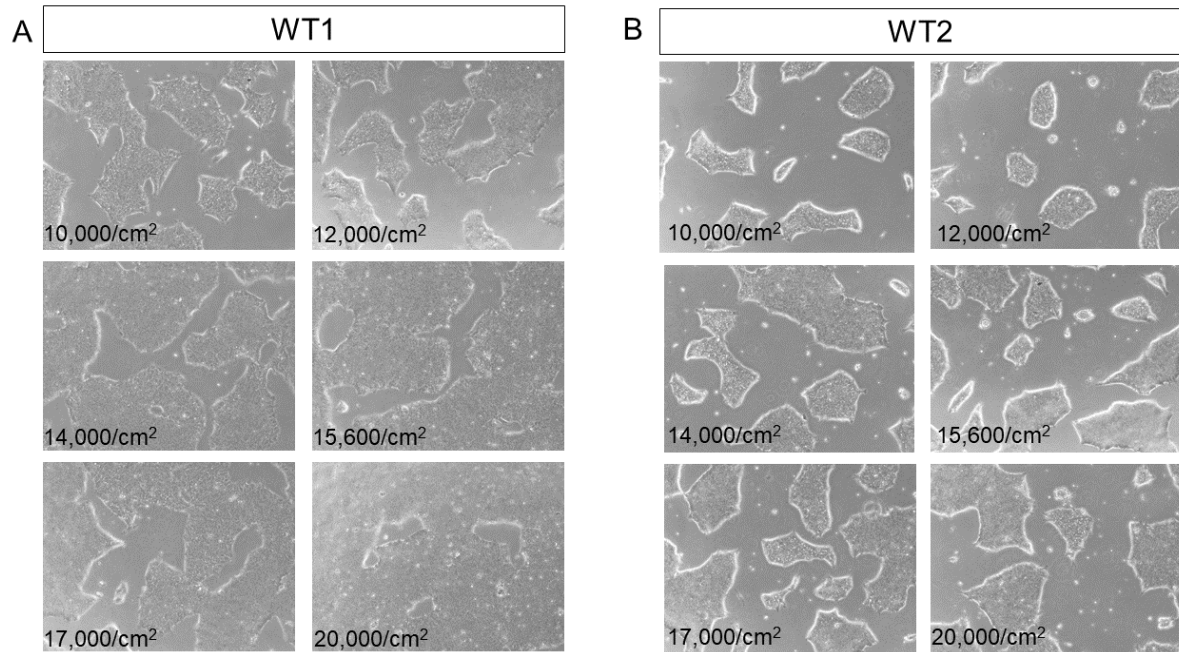
Figure 3.5 Plating density comparison of WT1 and WT2 at day 4 of E6: Two WT lines display differences in proliferation **(A)** WT1 and **(B)** WT2, images are 4x objective.

Moreover, qRT-PCR gene expression analysis reveals a trend in WT1 at the intermediate stage (day 7) whereby higher starting density (20,000/cm^2) increases marker expression compared to lower (15,600/cm^2) (**Figure 3.6A**). This trend continues to be evident after sub-culturing (**Figure 3.6C**). However, WT2 does not show this similar trend (**Figure 3.6B,D**).
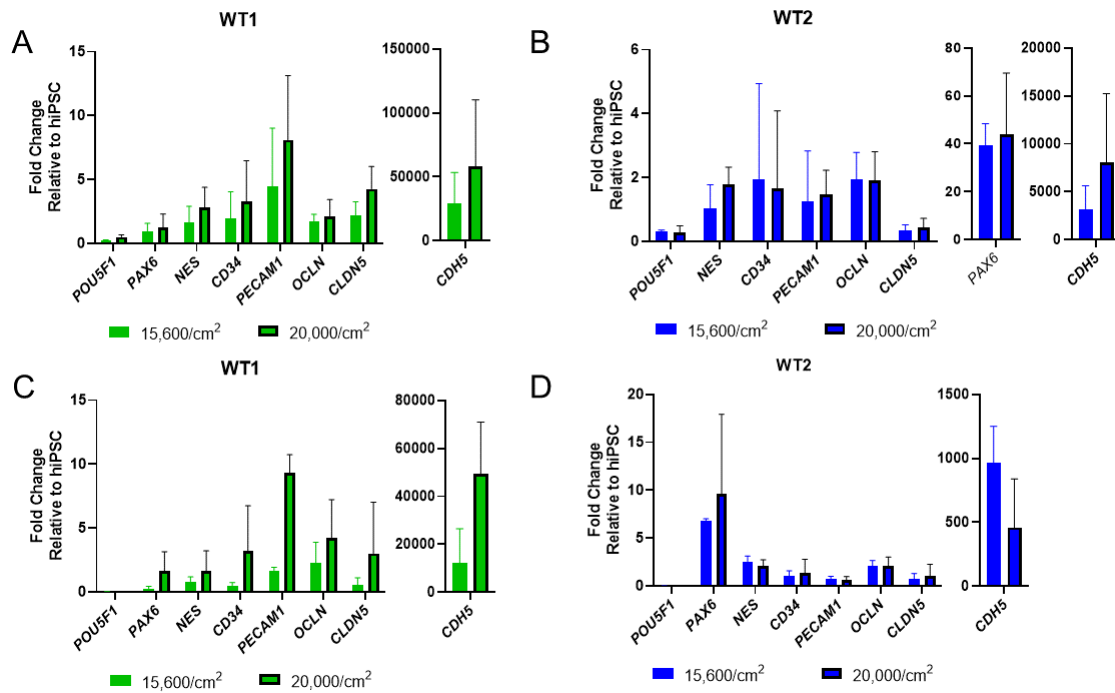
Figure 3.6 Plating density comparison for WT1 and WT2 hiPSC-BMEC at day 7 and passage 1: Starting density gene expression at Intermediate stage (day 7) for **(A)** WT1 and **(B)** WT2 and end-stage (P1) for **(C)** WT1 and **(D)** WT2. Both WT1 and WT2, intermediate n=3 differentiations, end-stage n=2 differentiations, error bars are mean +/- SD.

Following these initial experiments, two new WT lines derived with current reprogramming methods (Sendai Virus, Cytotune 2.0) and characterised with Array CGH information were introduced. Using these new lines, WT3 and WT4 (**Table 2.1**), experiments were conducted to determine if, other than gene expression, altering the seeding density affects the functional capacity of hiPSC-BMEC. In this case, WT3 and WT4 were tested at two disparate densities: 10,000/cm^2 and 20,000/cm^2 (**Figure 3.7A**). WT3 has increased TEER from cells that started at a lower seeding density (**Figure 3.7B**), however for WT4, the higher starting density TEER peaks at day 1 post sub-culture but is then not dissimilar to the lower density (**Figure 3.7B**).
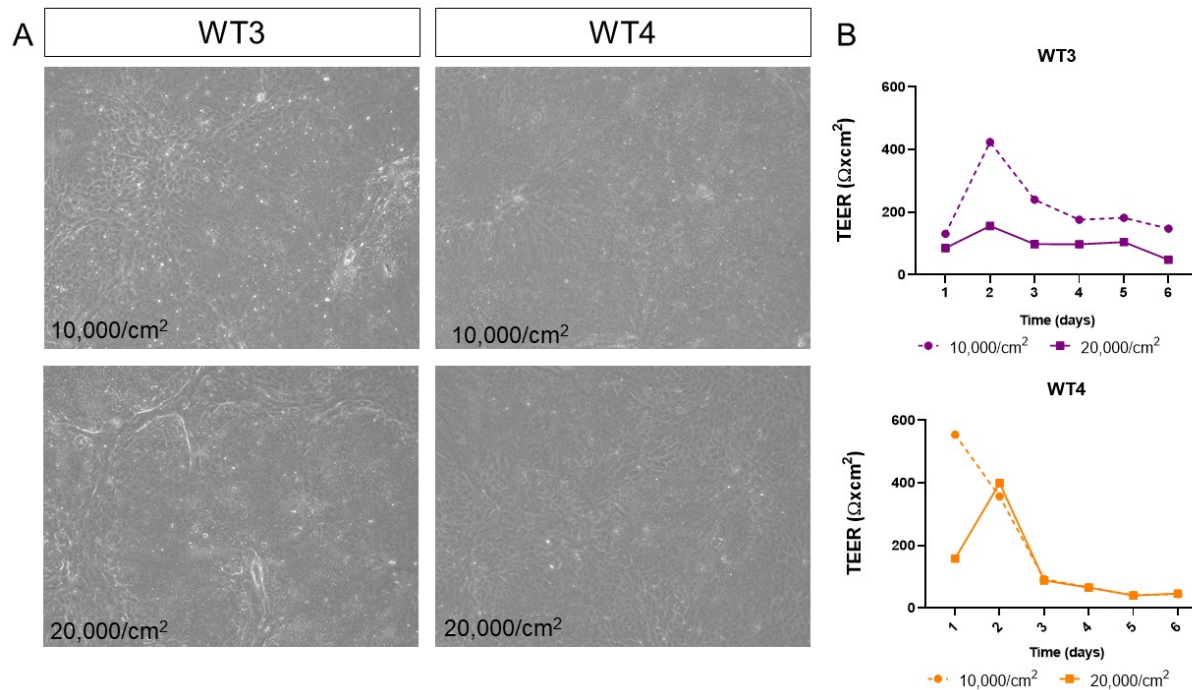
Figure 3.7 Plating density comparison of WT3 and WT4 hiPSC-BMEC: Two WT lines display differences between seeding densities **(A)** WT3 and WT4 after 6 days of differentiation. **(B)** WT3 and WT4 TEER. Images are 4x objective.

3.3.2 Replacing 1% Human Serum with fully defined B-27 supplement reduces the variation between lines

Using undefined 1% human serum may be contributing to uncontrollable variation between cell lines as well as potentially introducing batch-effects, as reported in an updated protocol from the Lippmann group[311]. The protocol was adapted by replacing 1%HS with B-27 media in the EC phase and post-subculture (**Figure 3.8A**).
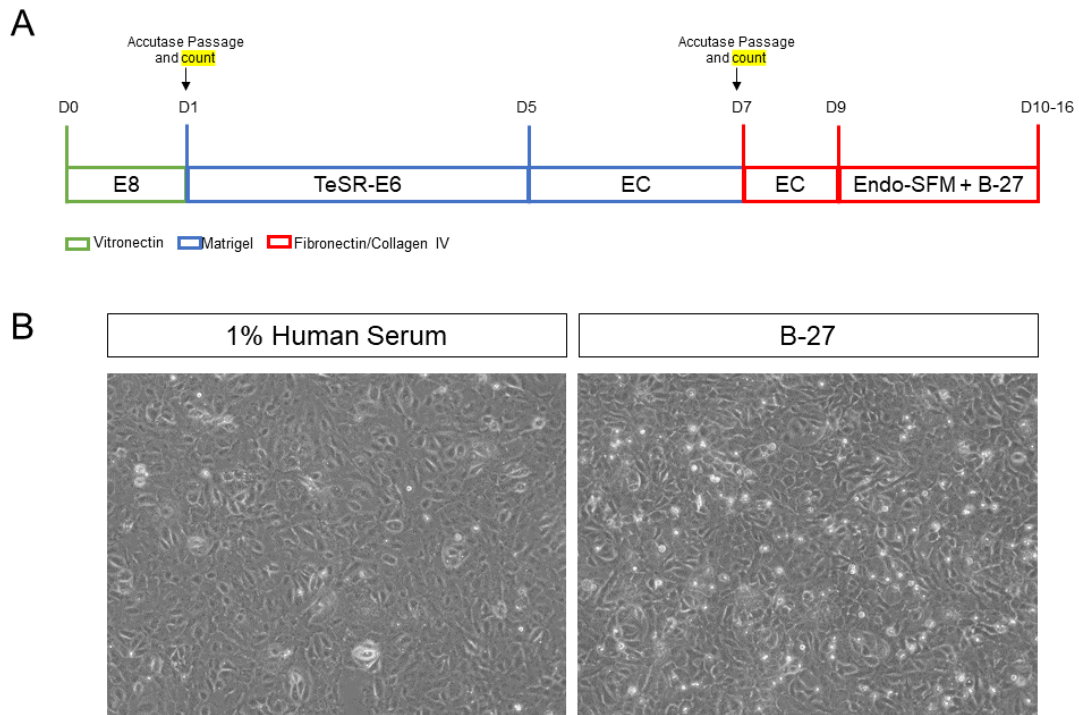
Figure 3.8 Improved hiPSC-BMEC differentiation protocol: New strategy for hiPSC-BMEC differentiation, replacing 1% human serum with B-27 **(A)** and **(B)** Phase images of WT3 P1 BMEC (10x objective).

Results show that hiPSC are able to differentiate into BMEC using B-27, with correct morphology comparable to 1% HS (**Figure 3.8B**) as well as displaying positivity for claudin-5 by immunostaining (**Figure 3.9A**). B-27 does not reduce the variation between differentiations (**Figure 3.9B**), although this is only 2 differentiations. Overall, the level of expression of BMEC markers is comparable between 1% HS and B-27 samples, indicating that B-27 does not reduce differentiation capacity compared to 1% HS (**Figure 3.9B**). However, across 3 technical replicate Transwells® from one experiment, B-27 differentiated cells have reduced TEER, compared to 1% HS (**Figure 3.9C**). The maximum TEER reached here ($225\Omega xcm^2$) is lower than the expected range ($1000\text{-}3000\Omega xcm^2$), which could suggest that the differentiation was sub-optimal for both 1%HS and B-27.
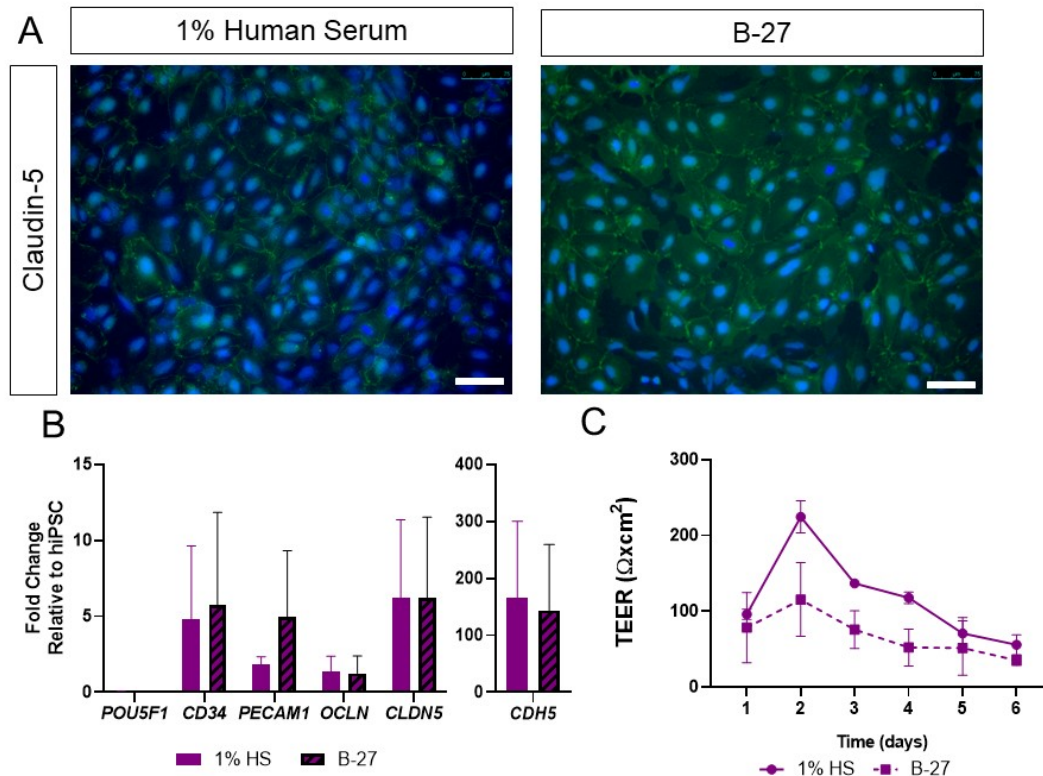
Figure 3.9 Comparison of 1%HS and B-27 hiPSC-BMEC differentiation capacity: Characterisation of 1%HS and B-27 WT3 BMEC **(A)** immunocytochemistry for claudin-5 and **(B)** end-stage qRT-PCR for key BMEC markers, n=2 differentiations **(C)** TEER n=3 separate Transwells® from the same experiment. Scale bar is 75µM.

3.3.3 Removing collagen IV from the selection matrix does not impair hiPSC-BMEC survival

The protocol[77] uses collagen IV and fibronectin at the sub-culture stage. Based on previous observations, the sub-culture stage could be contributing to differences in the end population, since plating density experiments did not reveal any improvement (**Figures 3.6 and 3.7**). Therefore, the requirement to use both collagen IV and fibronectin for matrix selection was investigated. Moreover, this project utilises patient hiPSC with COL4 mutations, which highlights the importance of testing if collagen IV can be removed from the matrix coating, so that it does not interfere with any phenotypic changes observed in COL4 mutant hiPSC lines, by masking or exacerbating the phenotype.

For fibronectin alone, attachment is comparable to that achieved with fibronectin and collagen IV together (**Figure 3.10**). However, without fibronectin, collagen IV is not sufficient to enable attachment of hiPSC-BMEC as a proliferative monolayer (**Figure 3.10**). Ultimately,

collagen IV was maintained as part of the matrix selection, as this experiment suggests it should not contribute to COL4 hiPSC-BMEC phenotype.
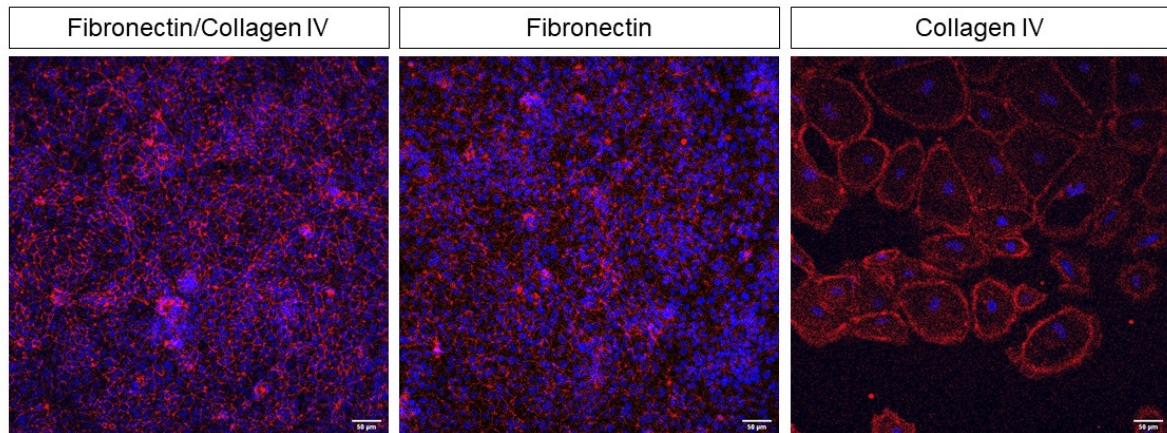
Figure 3.10 A comparison of subculture matrix composition: Immunocytochemistry WT1 BMEC for occludin (red) co-stained with DAPI (blue) plated on fibronectin/collagen IV, fibronectin alone and collagen IV alone, images are representative, scale bar is 50µm.

3.3.4 Pre-selection with puromycin increases the purity of BMECs plated onto Collagen IV/Fibronectin

Given that plating onto collagen IV/fibronectin yields a heterogeneous population, the antibiotic Puromycin, an agonist for the P-gp efflux receptor[359], has been presented as a selective agent for mature BMEC during differentiation from hiPSC[305]. Firstly, qRT-PCR was performed to determine the level of P-gp expression across WT lines. Relative to hiPSC, *ABCB1* (P-gp) increased between 7 and 40-fold higher in three WT lines at P1, 4-7 days post sub-culture (**Figure 3.11A**). This suggests that P1 BMEC do have expression of P-gp, although this may not translate to protein level, which needs to be expressed on the cell surface to be functional.

To test the efficacy of Puromycin as a selection agent, WT1 hiPSC-BMEC were treated with Puromycin at P1, following sub-culture onto collagen IV/fibronectin with either a high (1ng/ml) or low (0.5ng/ml) concentration. Both concentrations result in large amounts of cell death and loss of cell-cell contact (**Figure 3.11C-D**) when compared to un-treated WT1 BMEC (**Figure 3.11B**).
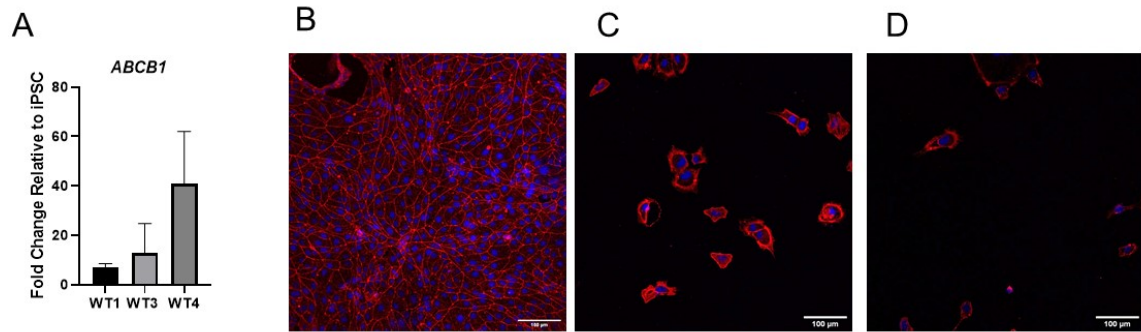
Figure 3.11 The effect of puromycin treatment on passage 1 of WT1 hiPSC-BMEC: (A) *ABCB1* (P-glycoprotein) expression in WT1, WT3 and WT4 BMEC n=3, **(B)** WT1 P1 untreated BMEC stained for occludin, WT1 P1 BMEC treated with **(C)** 0.5ng/ml puromycin and **(D)** 1.0ng/ml puromycin. Scale bar is 100µm.

The large cell death seen at P1 (**Figure 3.11C-D**), suggests the timing of puromycin addition is critical. Therefore, in the following experiments, puromycin was added at an earlier stage in the differentiation, to act as a pre-selection mechanism to remove un- or partially-differentiated cells before sub-culture, according to the recent protocol published by the Mabondzo group[305].

Treatment with 1ng/ml during the EC stage (day 5) results in large amounts of cell death at day 6, following 1 day of treatment (**Figure 3.12**). Puromycin removes residual hiPSC colonies visible at day 6 in un-treated differentiation (**Figure 3.12**) which in turn reduces the overgrowth that is seen by day 7. The resulting population after sub-culture (Day 8, **Figure 3.12**), demonstrates correct endothelial morphology.
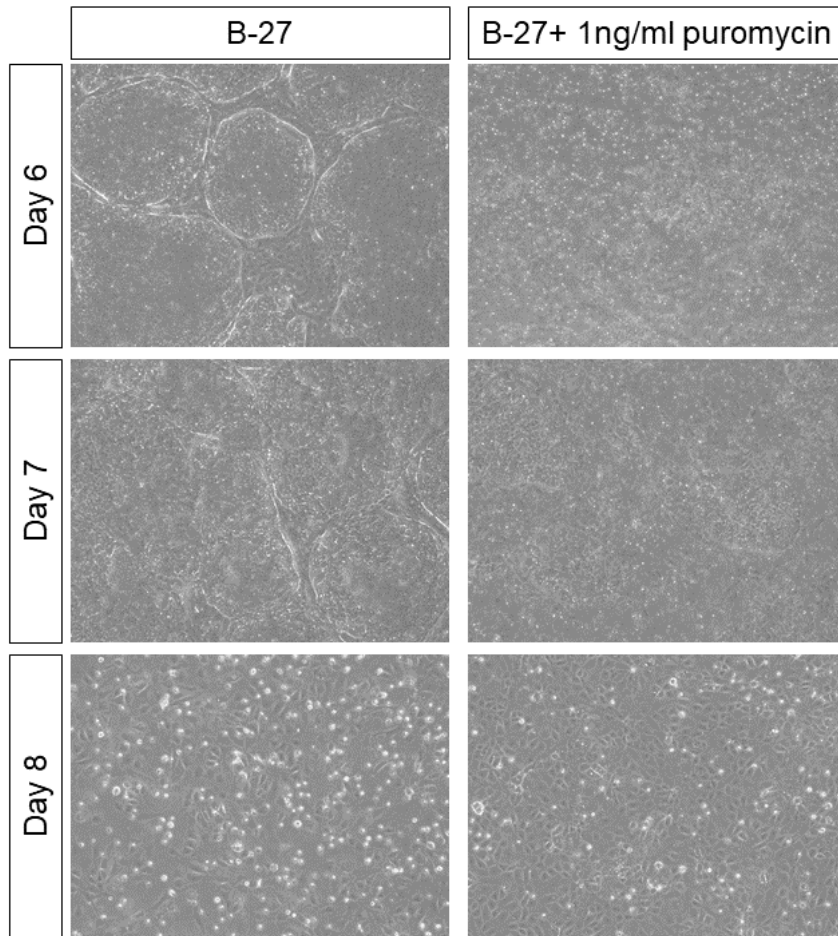
Figure 3.12 The effect of puromycin treatment on day 6 of WT3 hiPSC-BMEC: Phase images of Day 6,7 and 8 of WT3 differentiation. 4x objective.

However, routine adoption of puromycin requires further optimisation given that the seeding density currently used is designed to account for the selection process of plating onto fibronectin/collagen IV, thus resulting in large cell death and low cell attachment. In the case of puromycin-treated cells, less cell death occurred and more cells attached (**Figure 3.13A**), resulting in overgrown, dense monolayers immediately post sub-culture. Puromycin treatment shows a trend of increasing expression by qRT-PCR of *CD34*, *PECAM1* and *OCLN*, whilst *CDH5* and *CLDN5* decrease upon treatment (**Figure 3.13B**). However, this trend would need to be confirmed through repeated experiments. The optimisation steps and their outcomes are summarised in **Table 3.1**.
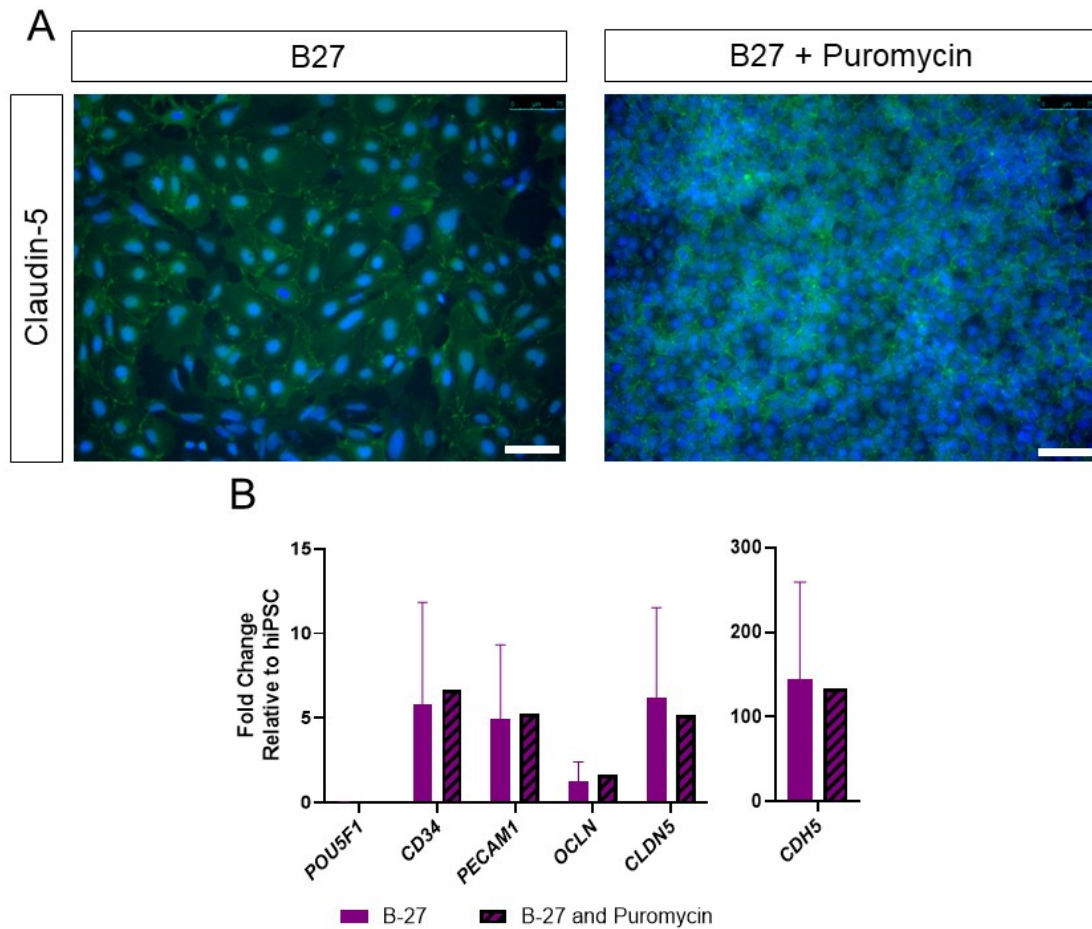
Figure 3.13 The end-stage effect of puromycin treatment on day 6 of WT3 hiPSC-BMEC: Characterisation of and B-27 and B-27 puromycin-treated WT3 BMEC **(A)** immunocytochemistry for claudin-5 and **(B)** end-stage gene expression for key BMEC markers, B-27 N=2 differentiations, B-27+ Puromycin n=1 differentiation, error bars are mean +/- SD of technical triplicates. Scale bar is 75µM.

Table 3.1 Summary of BMEC protocol optimisation

Optimisation Approach	Experiment Results	Outcome
Count cells at the sub-culturing stage	• Improves TEER reproducibility and removes line-to-line monoculture density	• Adopted recommended seeding density in all experiments[314]
Optimise plating density for each different line	• Some correlation (1 line) of increased density increasing BMEC markers (**Figure 3.6**) • Some correlation (1 line) or decreasing density increases TEER (**Figure 3.7**) • Inconsistent data between WT lines • Does not improve line-to-line or differentiation-to-differentiation variability (**Figure 3.6**)	• Not progressed for each line, standard density (15,600/cm^2) used for all lines.
Replace 1% human serum with B-27[311]	• Reported to reduce variation between differentiations[311] • Limited experimental replicates demonstrate comparable qPCR and TEER to 1% HS (**Figures 3.8, 3.9**)	• 1% HS replaced with B-27 for all experiments
Puromycin treatment to pre-select BMECs before matrix selection[305]	• Timing of the treatment is crucial (**Figures 3.11, 3.12**) • Pre-selection before sub-culture reduces heterogeneity of BMEC and yields similar gene expression to un-treated (**Figure 3.13**)	• Needs further optimisation of sub-culturing density

3.4 hiPSC-BMEC characterisation

Following optimisation of the protocol, thorough characterisation experiments were carried out with WT lines to test for BMEC phenotype and functionality. Firstly, hiPSC-BMEC were tested for expression of markers in immunocytochemistry that are abundant in the *in vivo* neurovasculature. These include tight junction proteins claudin-5, which plays an important role in BBB stabilisation[78] and occludin. The glucose transporter GLUT-1 was also explored since it plays an important role in delivery nutrients across the BBB[82]. Finally, the adherens junction protein, VE-Cadherin[71] was analysed. These markers were also tested in qRT-PCR, along with *CD34* and *PECAM1* (CD31), which stabilises endothelial cells[80]. Finally, *POU5F1* (OCT4) to demonstrate reduction compared to the starting hiPSC population.

Phenotypic characterisation assays were performed on P1 BMEC, 2-3 days post sub-culture for immunocytochemistry, tube formation and qRT-PCR and 5-7 days post sub-culture for LDL, Ki67 and R123.

Also, hiPSC-BMEC were compared to HUVEC, to demonstrate the brain-like phenotype of BMEC compared to large-vessel primary endothelial cells. hiPSC-BMEC should display higher TEER, lower passage of fluorescent compounds and increased marker expression of tight junction-associated proteins such as claudin-5[78].

3.4.1 hiPSC-BMEC are positive for key markers, assessed with ICC, qPCR and Flow Cytometry

WT1,2,3 and 4 display BMEC cobblestone morphology (**Figure 3.14**) similar to that seen with primary HUVEC (**Figure 3.28A**). hiPSC-BMEC are positive to markers occludin, GLUT-1, VE-cadherin and claudin-5 (**Figure 3.15**) in immunocytochemistry.
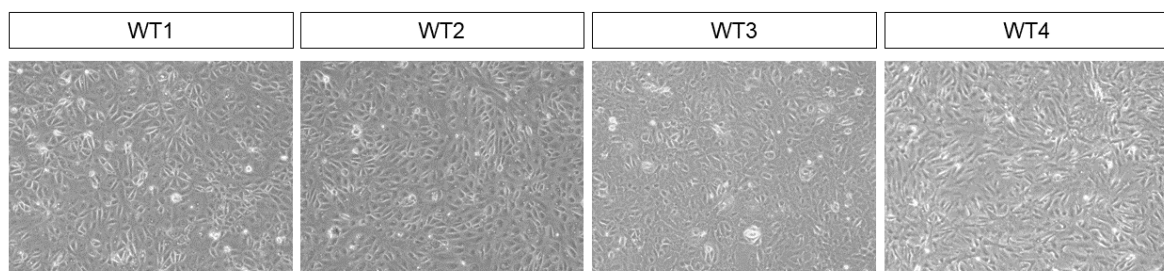
Figure 3.14 Morphology of WT1-4 passage 1 hiPSC-BMEC: hiPSC-BMEC Passage 1 morphology images of WT1, WT2, WT3 and WT4 (10x objective).
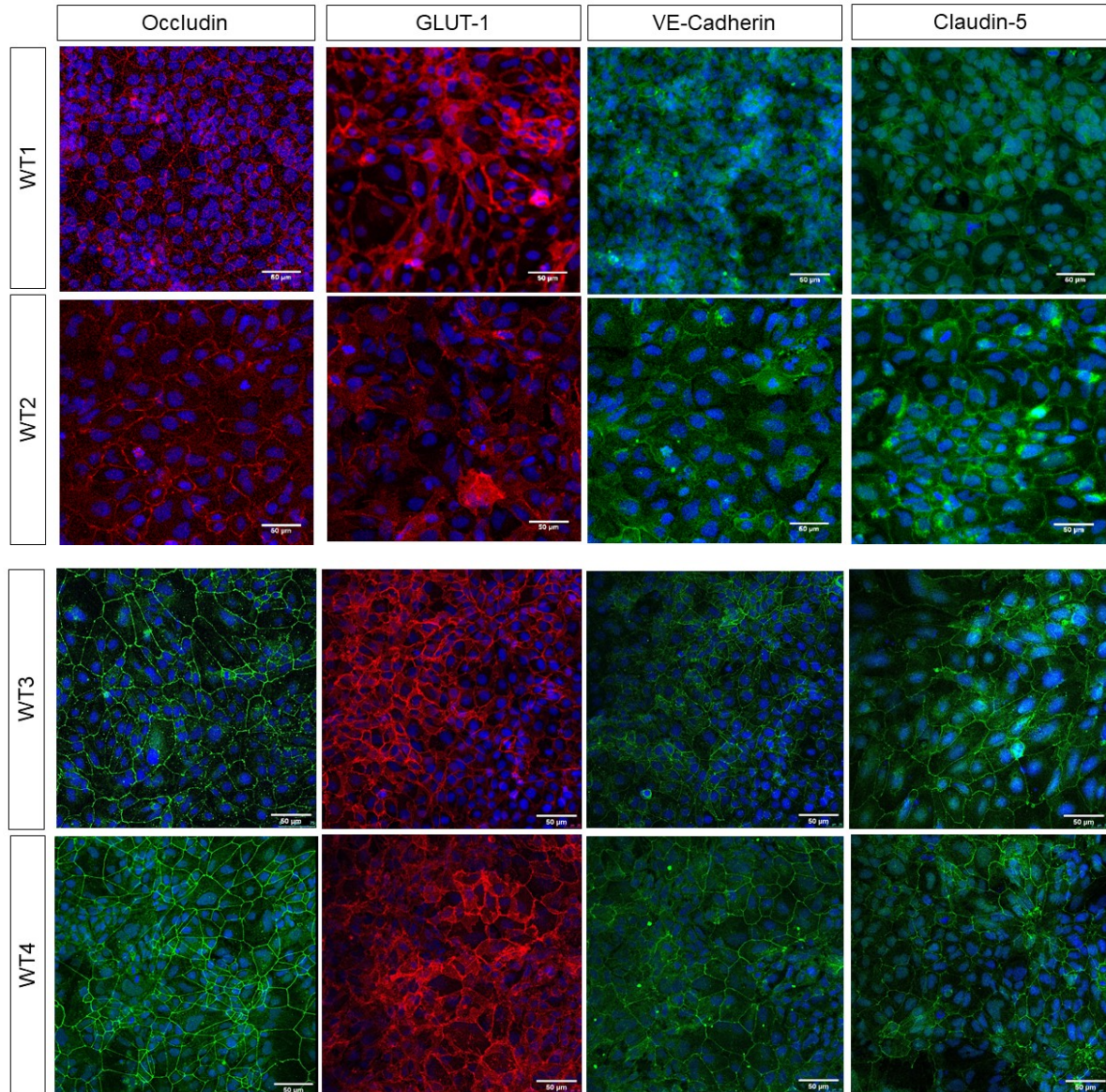
Figure 3.15 Immunocytochemistry of passage 1 WT1-4 hiPSC-BMEC:

Immunocytochemistry for occludin, GLUT-1, VE-Cadherin and claudin-5. Scale bar is 50µm.

The modified B-27 protocol produced comparable qPCR results between two WT lines, WT3 and WT4 (**Figure 3.16**). *CDH5* is significantly lower expressed in WT4 compared to WT3 (**Figure 3.16B**) but all other markers are not significantly different between WT3 and WT4. Crucially, compared to the previous qRT-PCR data obtained with the original differentiation protocol (**Figure 3.4**), this data is more comparable between lines.
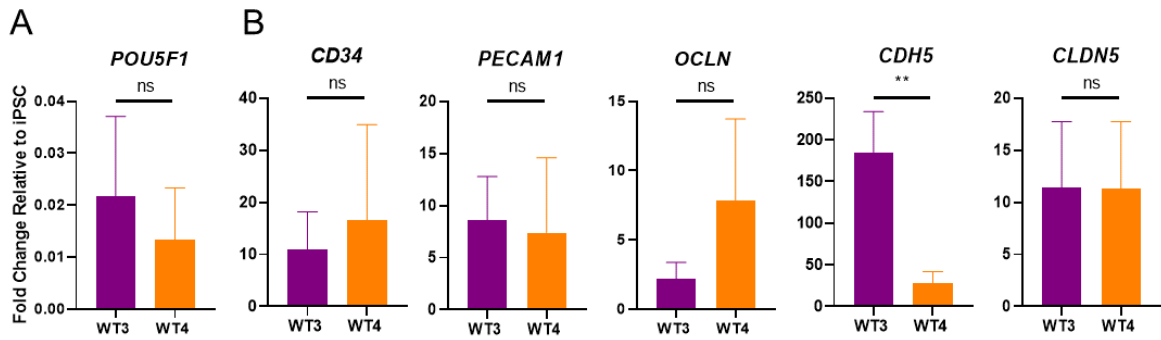
Figure 3.16 qRT-PCR of passage 1 WT3 and WT4 hiPSC-BMEC: qRT-PCR for **(A)** pluripotency marker *POU5F1* P=0.4755 and **(B)** BMEC markers, *CD34* p=0.6489, *PECAM1*, P=0.8169, *OCLN* P=0.1758, *CDH5* P=0.005835, *CLDN5* P=0.9809. WT3 and WT4 lines, n=3 separate differentiations, error bars are mean +/- SD.

claudin-5 is particularly important for the BBB, since claudin-5 deficient mice exhibit loosening of the BBB[78]. Flow cytometry was used to confirm qRT-PCR expression as well as quantify the protein expression seen qualitatively in immunocytochemistry. By flow cytometry, WT3 and WT4 demonstrate over 95% positivity for claudin-5 compared to an unstained population (**Figure 3.17**).
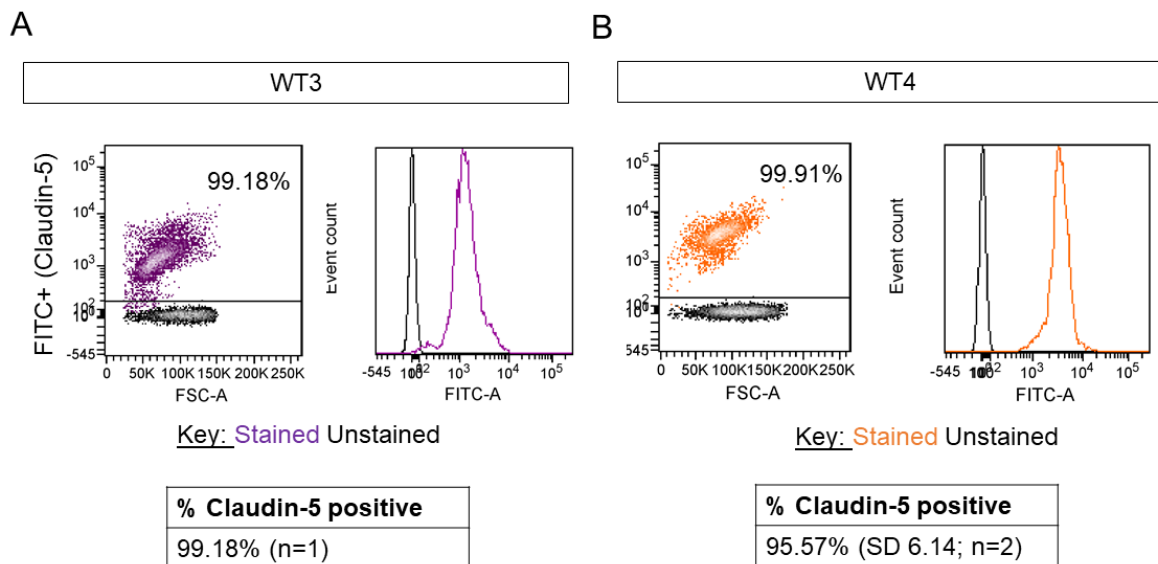
Figure 3.17 Flow cytometry of passage 1 WT3 and WT4 hiPSC-BMEC: claudin-5 positivity of hiPSC-BMEC for WT3 and WT4. WT3 n=1, WT4 n=2.

3.4.2 hiPSC-BMEC display barrier properties

To assess functional barrier properties, hiPSC-BMEC were plated onto Transwells® at the sub-culture stage and several assays were performed to test their BBB-like properties. TEER is used as a proxy measure for the 'tightness' of the barrier. An epithelial voltohmmeter using two pairs of electrodes, one to apply current and one to measure the output[72] is used to compute resistance using Ohm's Law[73]. *In vivo*, TEER is estimated to be around 2000Ωxcm^2 in the rat[74,75] and 8000Ωxcm^2 in humans[76,77]. Paracellular transport was tested using fluorescent molecules of known size such as FITC-Dextran (40kDa, 10kDa and 4kDa) and sodium fluorescein. Taken together, the results of these assays test the hiPSC-BMEC with relevance to the BBB.

3.4.2.1 hiPSC BMEC on Transwells® display increased marker expression

WT1 and WT2 BMEC form a monolayer on Transwells®, with continuous occludin tight junction expression seen by immunocytochemistry (**Figure 3.18A,B**). WT2 hiPSC-BMEC plated on Transwells® have higher expression of *OCLN* and *CLDN5* than in 12 well plates (**Figure 3.18C**). For WT3, with the exception of *OCLN* and *CDH5*, WT3 hiPSC-BMEC plated on Transwells® exhibit higher marker expression than cells from the same differentiation plated in a 12 well plate (**Figure 3.18D**). Both WT2 and WT3 display reduced expression of VE-Cadherin on Transwells® compared to 12 well plates (**Figure 3.18C,D**).
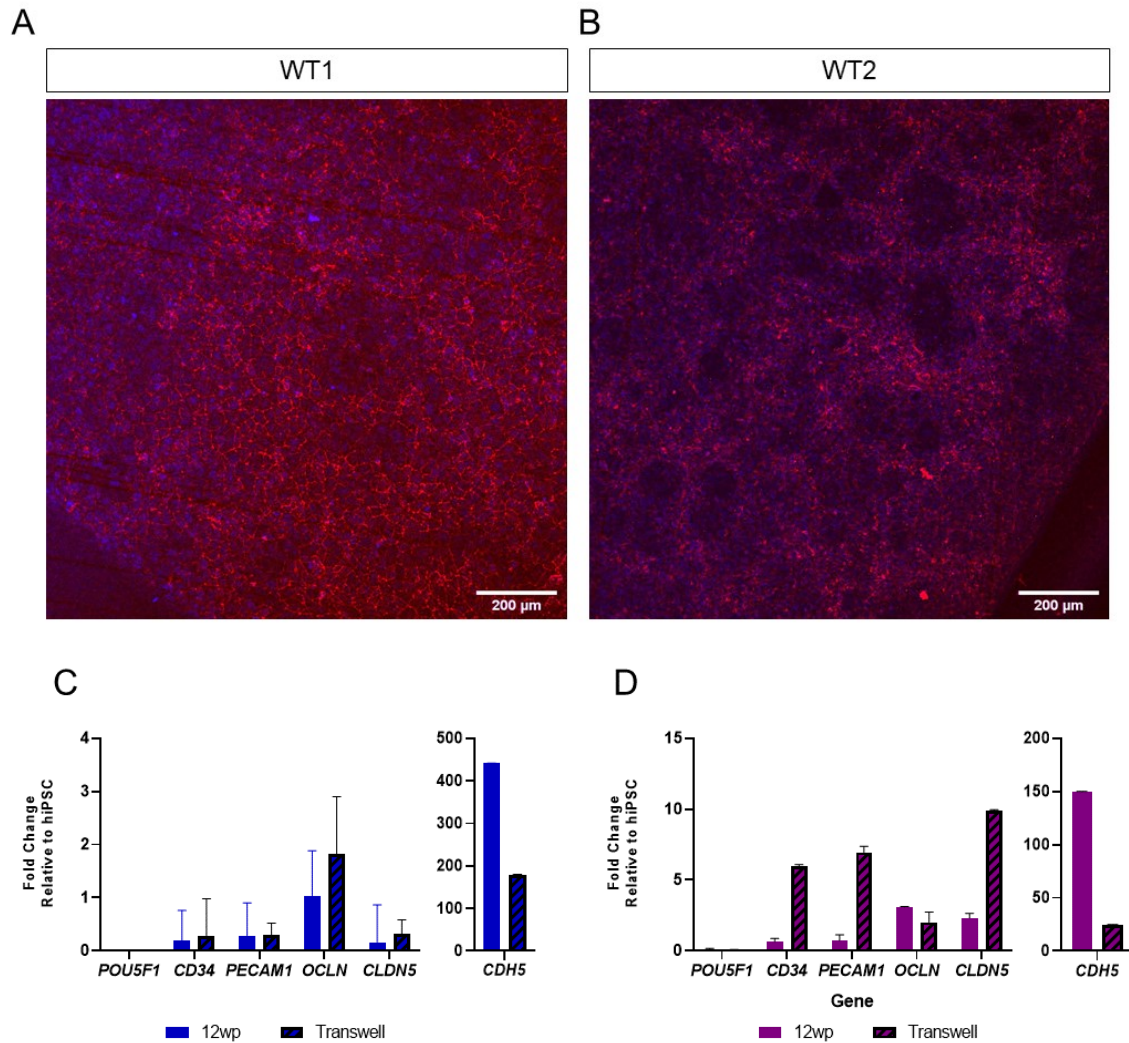
Figure 3.18 Comparison of WT hiPSC-BMEC on Transwells® or culture plates:
Transwell® immunocytochemistry for occludin, co-stained with DAPI **(A)** WT1 **(B)** WT2 and
(C) qRT-PCR of WT2 BMEC and **(D)** WT3 BMEC on 12 well plates and Transwells®, n=1
differentiation, error bars are technical triplicates.

3.4.2.1 Transendothelial Electrical Resistance

TEER is an important measure of the barrier, with the aim to reach values similar to the ones
reported *in vivo* using an *in vitro* system. Moreover, TEER is measured over time to
understand the longevity of the barrier properties of the hiPSC-BMEC monolayer and to
pinpoint the peak value reached. TEER values were recorded from day 1 post sub-culture,
continuing until values were near to or equal to the blank Transwell® (without cells) in order
to understand the complete behaviour of the monolayer in each experiment. Values are
reported by subtracting the value from a blank Transwell® and multiplying by the surface
area ($\Omega \times cm^2$).

TEER values typically peak between 1000-2000Ωxcm^2 but they can reach over 3000Ωxcm^2 (3195Ωxcm^2, WT4, **Figure 3.19C**). Comparatively, HUVEC TEER is maintained at around 25-35Ωxcm^2 for 3 days (**Figure 3.28C**). There is variation in the duration of TEER values, with some Transwells® maintaining TEER for 10 days, and others losing TEER by 5 days (**Figure 3.19**). Mostly, recordings follow a similar pattern, in which values peak at 2-3 days post sub-culture before declining. But in some cases, values increase again after this initial decrease (**Figure 3.19 A,B**).
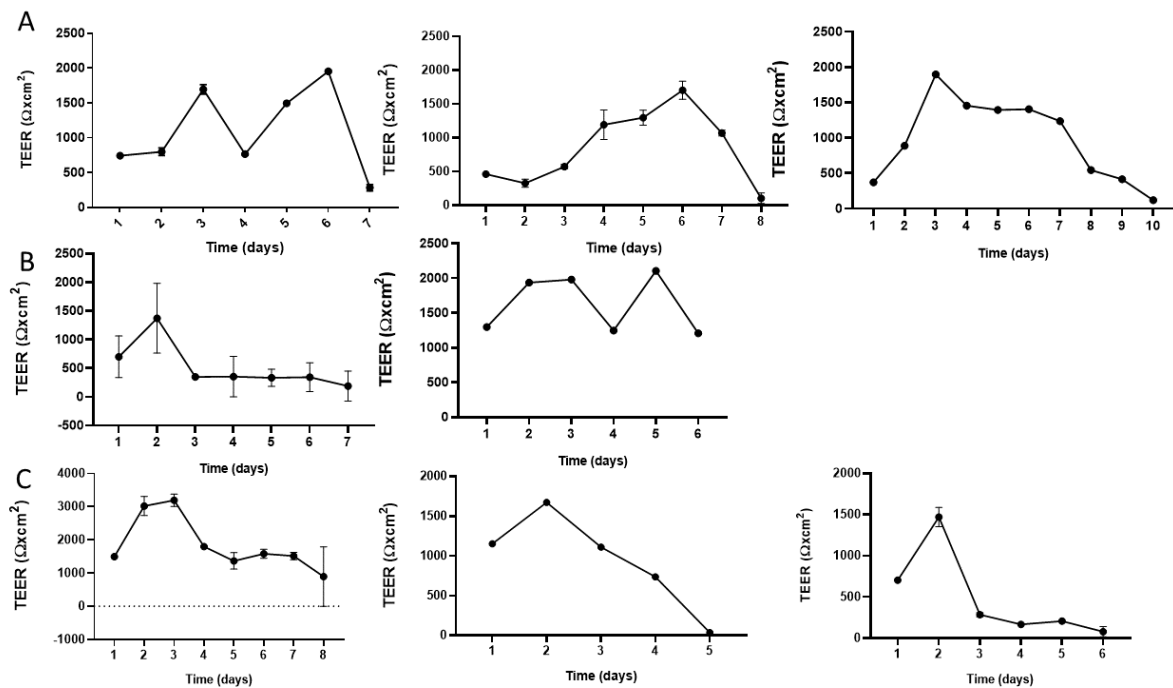
Figure 3.19 TEER of WT hiPSC-BMEC: TEER for **(A)** WT1 **(B)** WT3 and **(C)** WT4. Each graph indicates a separate biological replicate, error bars are mean +/- SD of separate Transwells® from the same experiment (2-4 Transwells®).

3.4.2.2 FITC-Dextran size exclusion

FITC-Dextran was used as a measure of the paracellular permeability of the hiPSC-BMEC monolayer, e.g. the readiness by which a fluorescent compound of known size passes between cells. The aim was to identify an assay that is sensitive enough to determine differences in paracellular permeability between different hiPSC-BMEC samples, especially going forward with the COL4A1/2 disease model.

Before conducting FITC-Dextran experiments, TEER was recorded to ensure comparable values across separate Transwells®. Samples were collected from the underside of the

Transswell® every 2 hours and reported as a percentage of the fluorescence that passes through a blank Transwell® (100%) over 2-8hours. Experiments from different differentiations are reported on separate line graphs with values summarised as the mean fluorescence reading relative to the blank over the total 2-8 hour time period in bar graphs.

In initial experiments, 40KDa FITC-Dextran was tested (**Figure 3.20**) across 4 independent experiments with WT1 and 2 experiments with WT2. As a percentage of the blank over 2-8hours, results are comparable between WT1 (18.57%) and WT2 (16.41%) but display high standard deviations (**Figure 3.20C**). Noticeably the independent Transwells® from the same differentiation, plated in parallel, do not always follow the same trend, evidenced by the large standard deviation (**Figure 3.20**). This could suggest that not all Transwells® have a monolayer and barrier properties are lost within 8 hours, or that there is variability in plating density between different Transwells®. However, the large size of the FITC-Dextran used (40kDa) was not sensitive enough to detect these discrepancies.
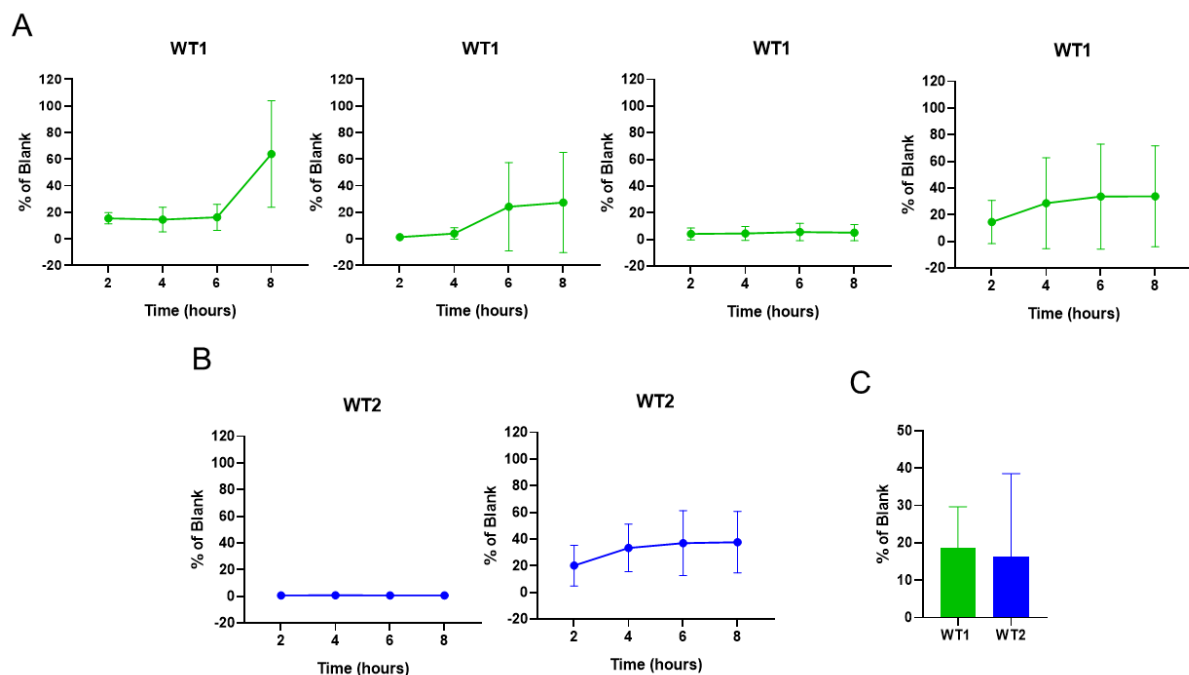
Figure 3.20 40KDa FITC-Dextran permeability assay for WT1 and WT2 hiPSC-BMEC: 40KDa FITC dextran for the 2-8hour time course of **(A)** WT1 (n=4), **(B)** WT2 (n=2) and **(C)** all data as % of blank. Error bars are mean +/-SD of separate Transwells® of the same experiment (n=2)

Hence, in order to develop a more robust test of barrier properties, a smaller sized fluorescent compound was needed. To this end, incrementally smaller sizes of FITC-Dextran were used to identify a compound that attains better separation between disparate lines and differentiations. Initially 10kDa FITC-Dextran was compared to the existing 40kDa.

Two WT lines (WT1 and WT2) from the same differentiation, were used to compare 10KDa and 40KDa (**Figure 3.21A,B**). For both lines, 10KDa was more sensitive than 40KDa, as predicted. For WT1, 2.07% of 10KDa Dextran passed through, compared to 1.13% of 40KDa (**Figure 3.21C**) and for WT2 it was 2.49% of 10KDa compared to 0.97% of 40KDa (**Figure 3.21C**).
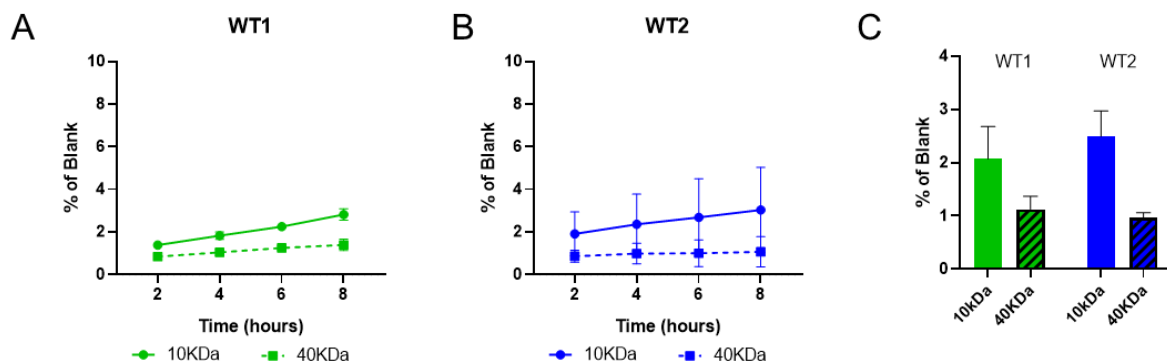
Figure 3.21 Comparison of 40KDa and 10KDa FITC-Dextran on WT1 and WT2 hiPSC-BMEC: **(A)** WT1, **(B)** WT2 and **(C)** percentage of the respective blank value across 2-8hrs for both sizes. Each graph is one differentiation, with 40kD n=2 Transwells® and 10kD n=3 separate Transwells®. Error bars are mean +/- SD of technical triplicates

The assay was further refined by the use of 4kDa FITC-Dextran (**Figure 3.22A**). By the end of the 8-hour time course, similar values were obtained (4kDa 0.57%, 10kD 0.55%, **Figure 3.22A**). But, when averaged across the 2-8 hour time period, the mean percentage passage of 10KDa relative to the blank, was greater than 4kDa (1.14% and 0.52%, respectively; **Figure 3.22B**). This suggests that 4kDa FITC-Dextran, which is 2.5 times smaller than 10KDa, gives similar results for measurements of barrier properties. Comparatively, for HUVEC 13.8% of 4kDa dextran passes through, relative to the blank (**Figure 3.28F,G**). This suggests that, as predicted, hiPSC-BMEC display more BBB-like barrier properties than large vessel HUVEC, since more 4kDa Dextran passes through a monolayer of HUVEC.
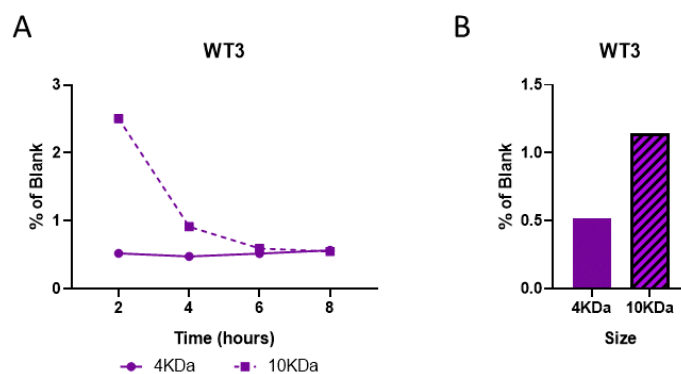
Figure 3.22 Comparison of 10KDa and 4KDa FITC-Dextran on WT3 hiPSC-BMEC: (A) FITC-Dextran 40kDa and 10KDa time course and **(B)** percentage of the respective blank value over 2-8hrs for both sizes

3.4.2.3 Sodium Fluorescein

Following improvements in sensitivity moving from 40kDa to 10kDa and 4kDa FITC-Dextran, sodium fluorescein (NaFl) was adopted to further test the paracellular barrier properties. Going forward, it is imperative to be confident in extrapolating differences between control and disease hiPSC-BMEC.

Compared to 4kDa (4000 Daltons), NaFl is around ten times smaller (376.27 Daltons). In a side-by-side comparison of Transwells® from the same experiment (**Figure 3.23A**), NaFl mean value over 2-8 hours is 10.90%, whereas 4KD FITC-Dextran is 2.05% (**Figure 3.23B**), suggesting that NaFl is a more sensitive assay than 4kD FITC-Dextran. Since NaFl yields lower fluorescence (blank peak of 1682 RFU, compared to 8947 RFU for 4kD Dextran), this also suggests that there is less likelihood of saturation of the fluorescence detection.
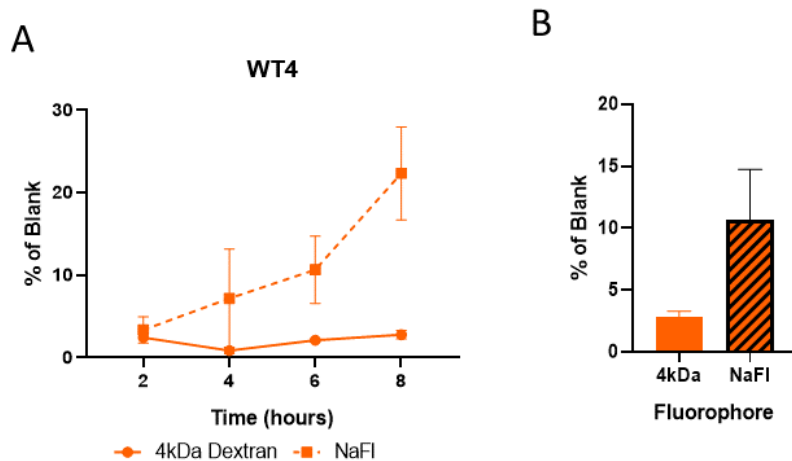
Figure 3.23 Comparison of 4KDa FITC-Dextran and NaFl: (A) WT4 4kD FITC-Dextran and NaFl time course and **(B)** % blank over 2-8hrs. N=1 differentiation, with 2 technical replicate Transwells®. Error bars are mean +/- SD of technical triplicates

Moreover, NaFl yields reproducible results between two WT lines, WT3 and WT4 (2.91% and 6.69% of blank respectively), across two separate differentiations (**Figure 3.24**). When tested on HUVEC, 69.5% of NaFl passes through, relative to the blank (**Figure 3.28E,G**). Thus, NaFl was adopted as the primary method for assessing barrier properties for hiPSC-BMEC.
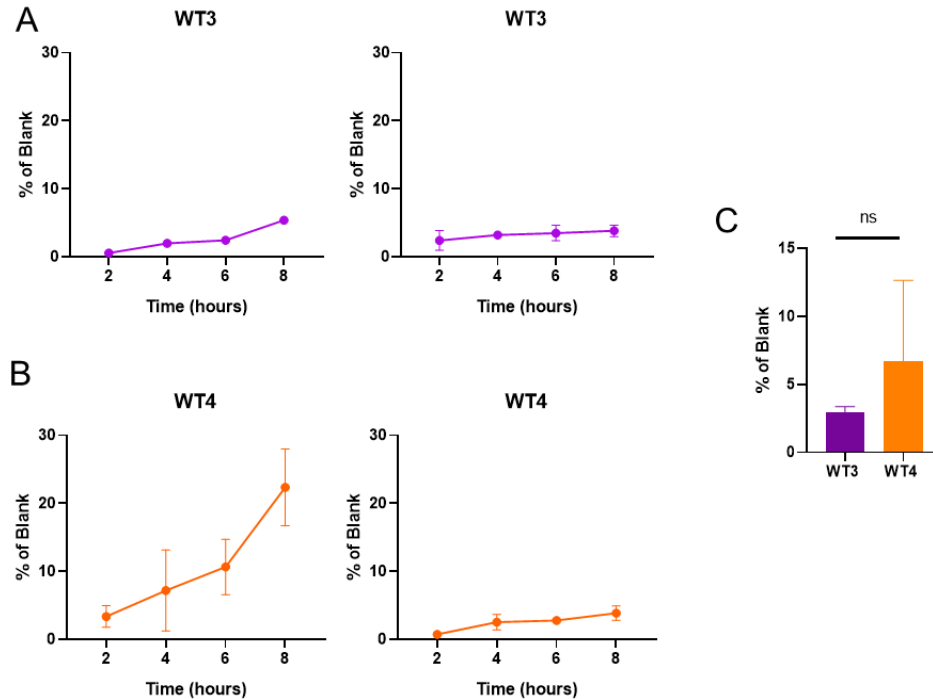
Figure 3.24 NaFl permeability assay in WT3 and WT4 hiPSC-BMEC: NaFl from two separate experiments of **(A)** WT3 **(B)** WT4 **(C)** % of blank over 2-8hrs (n=2). Each graph is 1 differentiation, with 1-3 technical replicate Transwells®. Error bars are mean +/- SD

3.4.3 hiPSC-BMEC are able to take up Low Density Lipoprotein

In the body, endothelial cells play a role in the metabolism of low-density lipoprotein (LDL), removing it from the bloodstream by direct uptake into the cell[360]. Although endothelial cells are not the only cell type capable of sequestering LDL, previous groups have implemented LDL uptake to differentiate endothelial cells from other contaminating isolated cells in bovine cultures[361]. Hence, applying acetylated LDL to hiPSC-BMEC, we expect to see uptake in concordance with the predicted endothelial phenotype. Since this is an active process, AF488-LDL was applied to live cells, in keeping with other hiPSC-BMEC studies[307]. AF488-LDL was applied to P1 BMEC 4-7 days post-subculture and removed after 4 hours, before co-staining with Hoechst. Both WT3 and WT4 uptake LDL, visible as a peri-nuclear stain (**Figure 3.25**). Further investigation is required to quantify the differences between the images and to determine if this is a line- or differentiation-specific outcome.
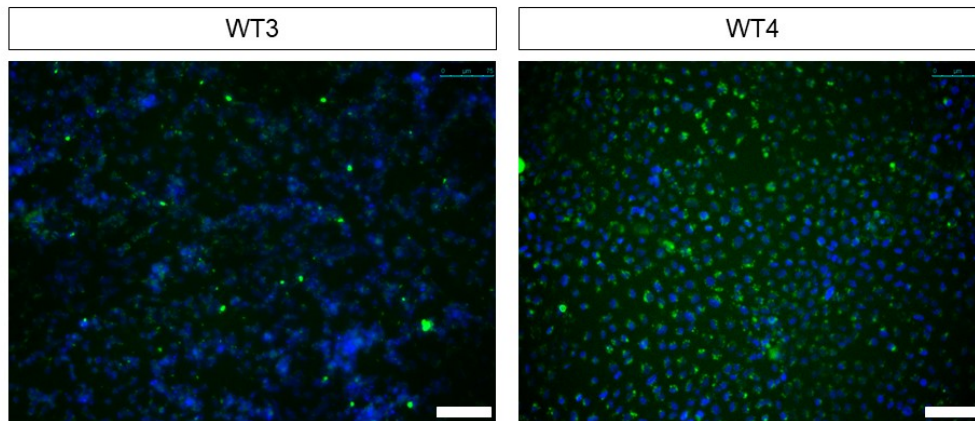
Figure 3.25 LDL-uptake in WT3 and WT4 hiPSC-BMEC: WT3 and WT4 BMEC AF488 LDL uptake (green) co-stained with Hoechst. Scale bar is 75μm.

3.4.4 hiSPC-BMEC uptake Rhodamine123 and show impaired efflux transport on treatment with cyclosporin A

P-gp, which is highly expressed on BMEC, plays an important role in extruding toxic products from the neural tissue[79,83]. Assessing its function complements the resistance measured with TEER and the paracellular transport tested with fluorescent compounds. Moreover, ischaemic stroke has been shown to temporarily increase P-gp at the BBB[91], suggesting a role in disease that could be relevant to SVD.

The Rhodamine123 (R123) assay is used as a proxy indication of P-gp function and utilises an inhibitor to test uptake and efflux[307]. Cyclosporin A (CsA) is an inhibitor of the ABC transporter p-gp[362]. Therefore, the inhibited sample should result in higher fluorescence, representing an intracellular accumulation of R123; since efflux through P-gp is impaired. Fluorescence is calculated relative to the cell number from a sister well.

Reported in each graph is the mean fluorescence of 3 triplicate wells plated from the same experiment, relative to the cell number (**Figure 3.26A-C**). Data are also reported as the ratio of CsA inhibited fluorescence (+CsA) divided by uninhibited samples (-CsA; **Figure 3.26D**). A value >1.0, where fluorescence is higher in the inhibited sample relative to the uninhibited, is the expected result for functional P-gp efflux transport.

Results are variable between WT3 and WT4 in the three representative independent experiments (**Figure 3.26A-C**), but the mean ratio of +CsA/-CsA is above 1.0 for both WT3 (1.44 ± 0.28) and WT4 (1.22 ± 0.26).
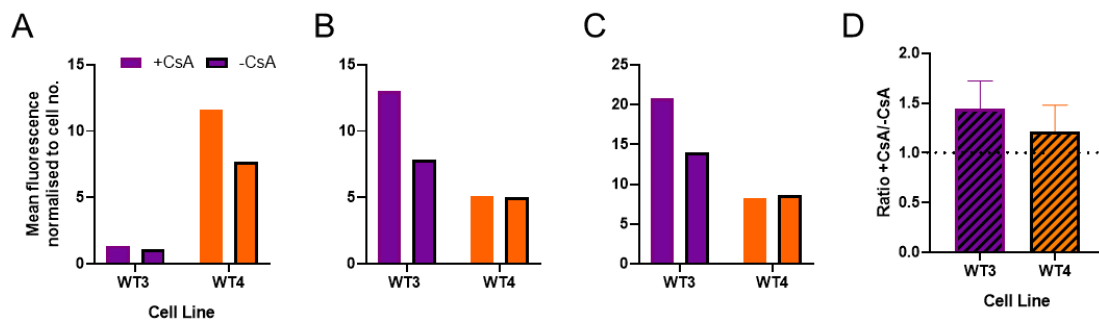
Figure 3.26 R123 assay in WT3 and WT4 hiPSC-BMEC: Three independent representative R123 assays from separate differentiations **(A)**, **(B)** and **(C)** for WT3 and WT4, relative to cell number, **(D)** the mean ratio of +CsA/-CsA, WT3 n=6 and WT4 n=4.

3.4.5 hiPSC-BMEC are capable of undergoing tube formation, promoted by VEGF

To test the functional capacity of the hiPSC-BMEC to undergo angiogenesis, akin to that *in vivo*, P1 BMEC sub-cultured onto fibronectin/collagen IV were disassociated to single cells and plated into Matrigel as described. WT1 BMEC are able to form tubular networks (**Figure 3.27**) and network formation is promoted by VEGF.
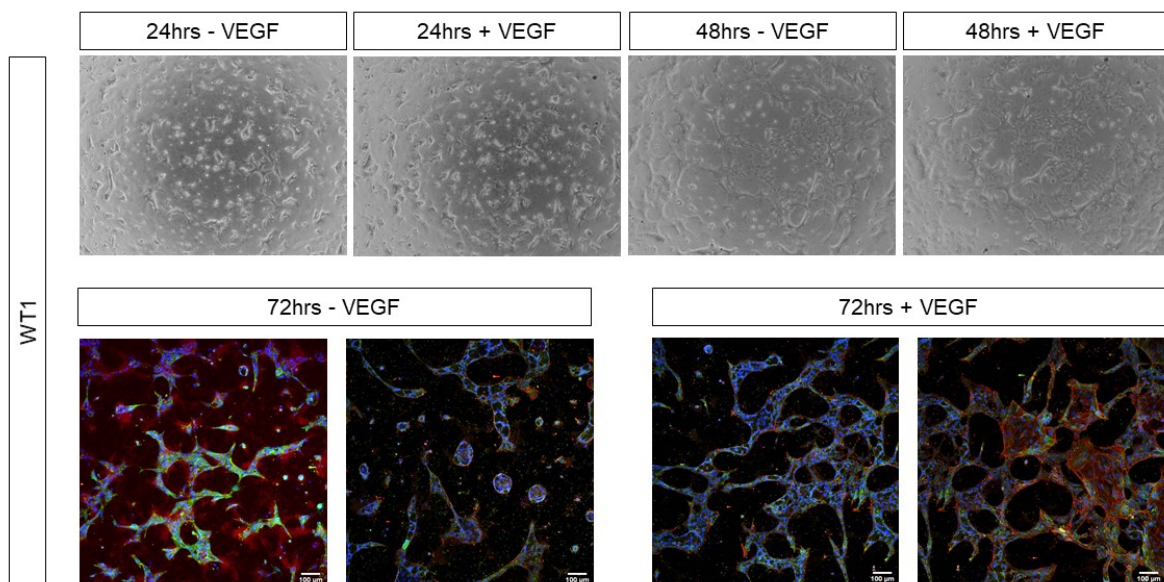
Figure 3.27 Tube formation in WT1 hiPSC-BMEC: WT1 tube formation with and without VEGF over 24-72hrs. Phase images are 4x objective. Immunocytochemistry for occludin (red), VE-Cadherin (green), co-stained with DAPI; Scale bar is 100µm.

3.5 hiPSC-BMEC display more brain-like endothelial properties than large vessel HUVEC

HUVEC were used as a control to demonstrate the brain-like properties of hiPSC-BMEC, which exceed that of large vessel primary endothelial cells. BMEC allow limited trans- and para-cellular transport when compared to other endothelial barriers in the body, owing to 'tighter' tight junctions[63]. Hence, HUVEC were tested in hiPSC-BMEC assays, to determine the comparative barrier properties between the two cell types. HUVEC display homogeneous cobblestone morphology (**Figure 3.28A**), and cells are positive for VE-Cadherin (**Figure 3.28B**). TEER for HUVEC is maintained around 30Ωxcm^2 over three days (**Figure 3.28C**), around 100-times lower than maximal values reached by hiPSC-BMEC (**Figure 3.19**). Gene expression using qRT-PCR, demonstrates high expression of *PECAM1* and *CDH5* (VE-Cadherin) relative to HK genes (**Figure 3.28D**), but low expression of *OCLN* and *CLDN5*. However these values are in keeping with hiPSC-BMEC expression relative to HK (**Figure 4.29**). A mean of 13.8% of 4kDa dextran passes through the HUVEC monolayer, relative to the blank (**Figure 3.28F,G**). This is higher than for hiPSC-BMEC (0.52%; **Figure 3.22B**). Mean NaFl leakage is also high in HUVEC (69.5%; **Figure 3.28E,G**) when compared to WT3 and WT4 hiPSC-BMEC (2.91% and 6.69% of blank respectively; **Figure 3.24**).
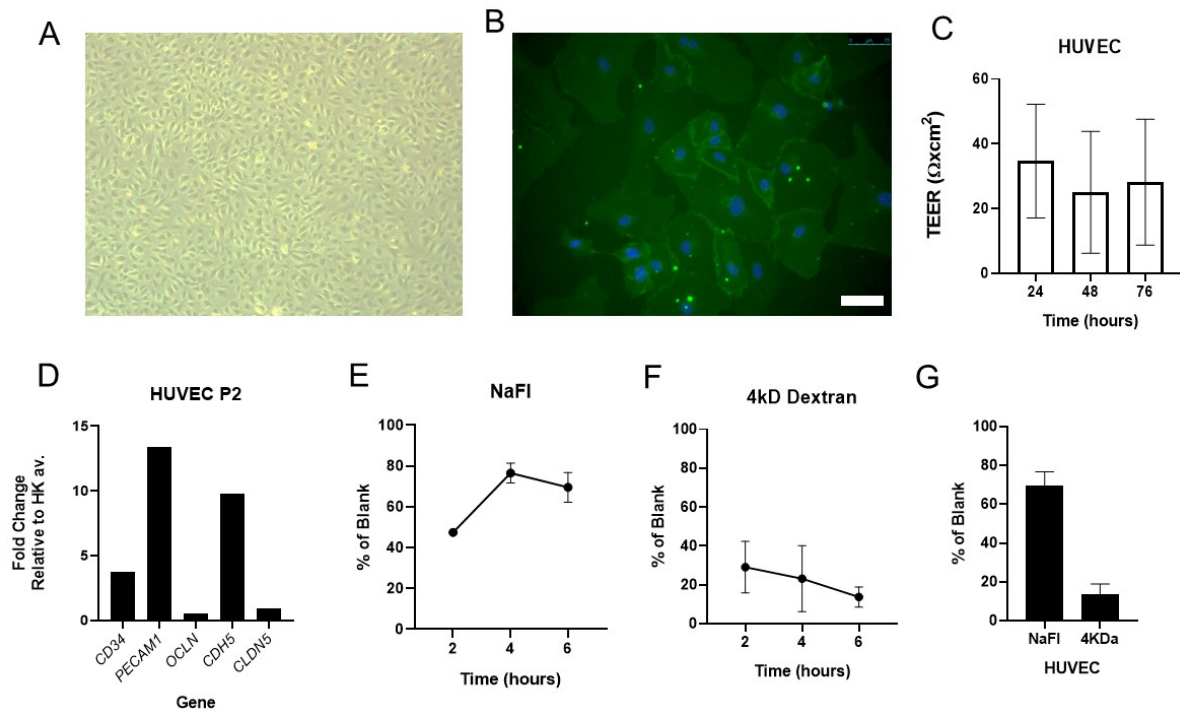
Figure 3.28 HUVEC characterisation: (A) phase image 4x objective **(B)** VE-Cadherin staining, scale bar is 75µm **(C)** TEER n=5 separate experiments **(D)** HUVEC qRT-PCR at P2, relative to HK average **(E)** NaFl n=2 separate Transwells® from the same experiment **(F)** 4KDa FITC-Dextran n=2 separate Transwells® from the same experiment **(G)** barrier experiments displayed as a % of blank. Images are representative, error bars are mean +/- SD

3.6 Troubleshooting hiPSC-BMEC differentiation

Some key experimental insights into hiPSC-BMEC generation are listed in **Table 3.2.**

Table 3.2 Troubleshooting the hiPSC-BMEC protocol and the potential solutions

Problem	Potential solution
No/low TEER	• Increase Accutase time between 45minutes and 1 hour to ensure single cells are plated
Inconsistent TEER between parallel Transwells® from the same differentiation	• Plate the total number of cells required directly onto the Transwell® and shake to distribute, before topping up with media
Plated hiPSC lift off as EBs in E6 period	• When coating plates, thaw Matrigel completely on ice and use DMEM/F12 at 4ºC • Coat Matrigel overnight and either use the next day or replace with DMEM/F12 and use within 3 days
Poor cell attachment at sub-culture stage	• Coat overnight with collagen IV/fibronectin/PBS at the correct ratio (4:1:5) for Transwells® and dilute 1:5 for plates

3.7 Chapter summary

This chapter has demonstrated adaptation and optimisation of an existing protocol to differentiate hiPSC into BMEC to produce consistent results between different WT lines and separate differentiations of the same line. hiPSC-BMEC exhibit barrier properties shown with TEER, Dextran and NaFl assays as well as endothelial behaviour such as tube formation and LDL-uptake. In the next chapter, the optimised protocol was utilised to differentiate COL4A1/2 hiPSC into BMEC, as an *in vitro* model of collagen IV SVD.

Chapter 4: Phenotypic abnormalities of COL4A2^{G702D} and COL4A1^{G755R} hiPSC-BMEC: a role for MMPs

4.1 Aims of this chapter

Two patient-derived hiPSC lines (COL4A2^{G702D} and COL4A1^{G755R}) were used to study collagen IV SVD *in vitro*. Both of these mutations occur in glycine residues of the G-X-Y repeats that characterise the collagenous domain, which cause the majority of COL4A1/2 SVD[194].

Three hiPSC clones (3,4 and 5) were derived from COL4A1^{G755R} fibroblasts, however, clone 3 exhibited poor growth so experiments were performed with Clone 4 and 5. Only one clone of COL4A2^{G702D} was available and two isogenic clones (14 and 17) were provided by Dr Alex Granata. The COL4A1^{G755R} isogenic was not initially available, hence WT lines were used for comparison.

Initially, hiPSC were differentiated to BMEC and tested for correct phenotype and barrier properties with assays reported in Chapter 3. Observed phenotypic differences compared to WT/isogenic controls as well as insight from the literature, was used to further interrogate the model and determine possible mechanisms.

4.2 Characterisation of disease lines COL4A1^{G755R} and COL4A2^{G702D}

hiPSC characterisation (pluripotency qRT-PCR and immunocytochemistry analysis and three germ layer differentiation) of individual lines can be found in the appendix.

4.2.1 Sequencing

COL4A1^{G755R} is characterised by substitution of a Guanine for an Adenine at position c.2263 in COL4A1 on chromosome 13. This results in an amino acid change from a Glycine to an Arginine at position 755 **(Figure 4.1A)**. COL4A2^{G702D} is characterised by the replacement of a Guanine for an Adenine at position c.2105, resulting in a change from a Glycine to Aspartic Acid at position 702 **(Figure 4.1B)**. COL4A2^{G702D} has been CRISPR-corrected to produce two clones (cl 14 and 17), whereby the Adenine at position c.2105 has been substituted for the wild-type Guanine.
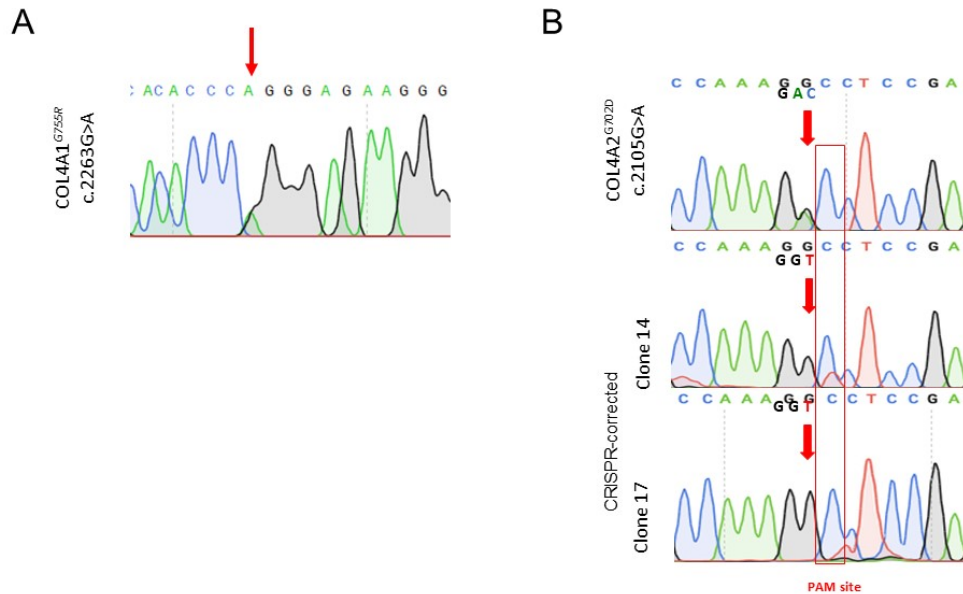
Figure 4.1 Sequencing of COL4A1^{G755R} and COL4A2^{G702D}: Sequencing of **(A)** COL4A1^{G755R} and **(B)** COL4A2^{G702D} with CRISPR-Correction of COL4A2^{G702D} (CRISPR/Cas9 was performed by Dr Alex Granata).

4.3 CRISPR/Cas9 mediated correction of COL4A1^{G755R} hiPSC to generate an isogenic control

Given the high variation that can be seen between WT lines with different genetic backgrounds (evidenced by the four WT lines used in Chapter 3), two approaches were taken to gene edit COL4A1^{G755R} hiPSC to generate an isogenic control line, to serve as a more comparable control. Full guide RNA sequences, primers and donor DNA can be found in the Appendix.

4.3.1 Vector-mediated CRISPR-Cas9 gene editing

Initially, gRNAs were designed as described in the Materials and Methods for incorporation into the pSpCas9(BB)-2A-Puro (PX459) V2.0 plasmid (**Figure 4.2A**; Source: Addgene).
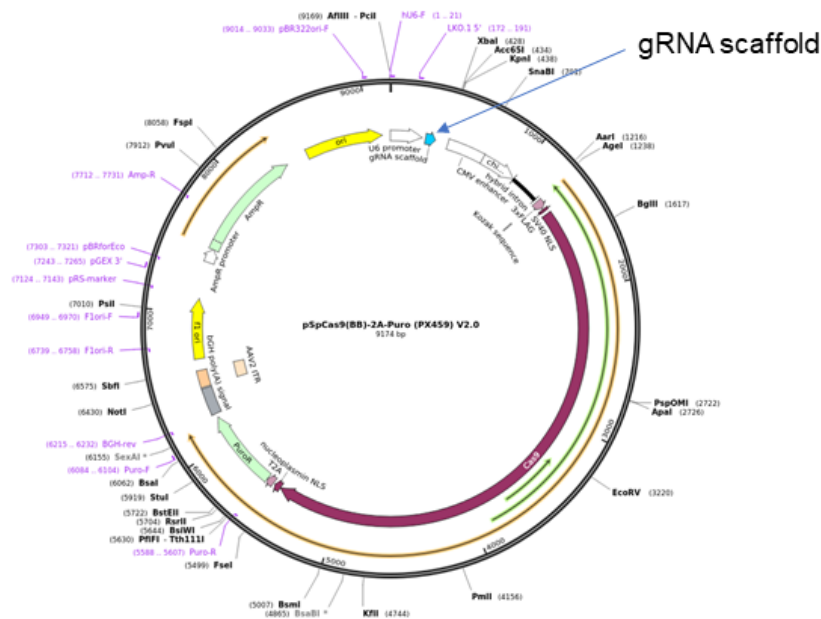
Figure 4.2 Cas9 plasmid structure: pSpCas9(BB)-2A-Puro (PX459) V2.0 plasmid (Source: Addgene)

gRNAs were designed with overhangs that are complementary to the gRNA scaffold within the SpCas9 (**Figure 4.2A**): <u>CACCG</u>(~20nt)<u>G</u>. A gRNA was selected based on two criteria: 1) close proximity to the mutation; 2) low off-target region effects. Three gRNAs (**Table 4.1**) were incorporated into the vector as described.

Table 4.1 gRNA plasmid Cas9 sequences

gRNA	Sequence
1	<u>CACCG</u>AGTCCCGGTAGACCAACTCC<u>G</u>
2	<u>CACCG</u>TAGGTGTCGCTCCTGGTGGG<u>G</u>
3	<u>CACCG</u>CGGCATTCCTGGCACACCC<u>G</u>

In order to determine optimal transfection reaction conditions prior to targeting hiPSC, a fast-growing and easy to manipulate cell type, HEK293 was used. Different HEK293 plating densities were tested to determine the highest efficiency of vector integration. A GFP plasmid was transfected with Lipofectamine 2000 into HEK293 cells at four different densities (**Figure 4.3A**). The highest percentage transfection efficiency was achieved with the lowest density of 2.5×10^5 cells per 6-well plate (**Figure 4.3A**). However, in order to have sufficient cellular material for subsequent steps, the higher density of 5.0×10^5 cells was selected.

HEK293 cells transfected with gRNA Cas9 plasmid were collected 24 hours later and DNA was extracted and amplified. After heteroduplex formation of WT un-transfected and transfected DNA, followed by treatment with T7 endonuclease, the PCR product was run on a gel to determine that the Cas9 plasmid cut. In this case, only gRNA 3 (**Table 4.1**) was successful in cutting (**Figure 4.3B**). Using band sizes predicted by the primer proximity to the PAM site, the expected sizes were observed (**Figure 4.3B**). However, the efficiency was very low, with a high failure rate of the T7 assay and faint observable bands resulting from the cut (1189bp and 737bp, **Figure 4.3B**). Therefore, a new approach was taken to obtain higher efficiency and to avoid laborious and time-consuming bacterial cloning and HEK293 optimisation steps.
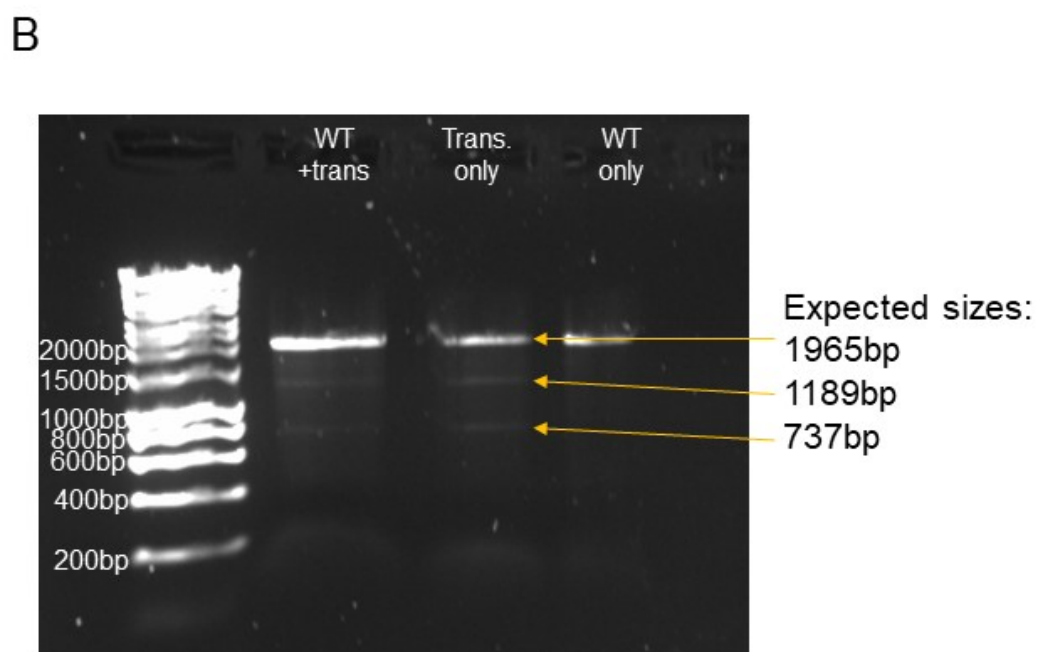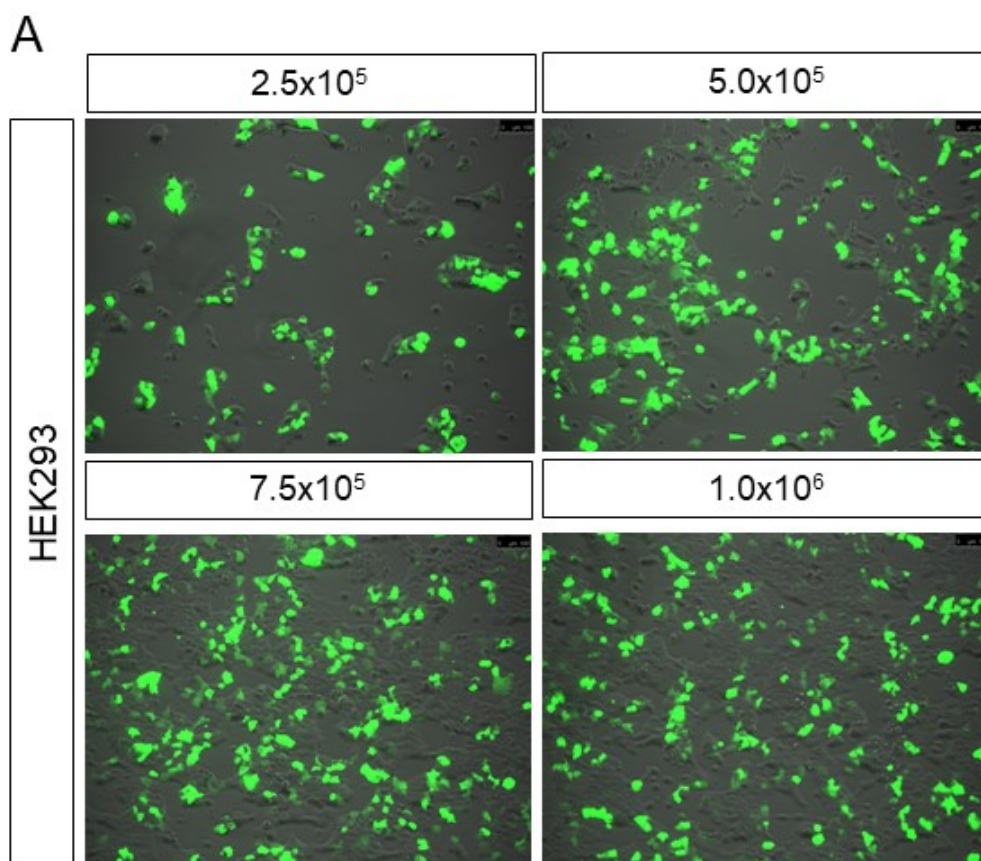
Figure 4.3 HEK293 transfection and T7 assay: **(A)** HEK293 GFP plasmid efficiency **(B)** T7 assay: Lane 1 WT DNA and transfected DNA, Lane 2 transfected only, Lane 3 WT only

4.3.2 Ribonucleoprotein-mediated CRISPR/Cas9 gene editing

To overcome the low efficiency of vector-mediated CRISPR/Cas9, a new approach was taken, by using recombinant spCas9 protein and synthetic gRNAs. Two new gRNAs were designed using Benchling, as described in the Materials and Methods (**Table 4.2**).

Table 4.2 Synthetic gRNA sequences

gRNA	Sequence
1	CTGGCACACCCAGGGAGAAG
2	CGGCATTCCTGGCACACCCA
3	CCGGCATTCCTGGCACACCC

Prior to testing these gRNAs with unknown editing efficiencies, a positive control guide which targets the RELA gene, was acquired from Synthego to validate nucleofection reaction conditions in hiPSC. Synthego report efficiency of between 80-97% in HEK293, Jurkat and U2OS cells (CRISPRevolution Controls Kit (Human) User Manual) for the RELA gRNA.

Five programmes on a Lonza 4D nucleofector were tested, as recommended by the manufacturer (CA-137, CB-150, CD-118, CM-113, DN-100). COL4A1^{G755R}_cl4 hiPSC were used to ensure relevance to the proposed CRIPSR/Cas9 mediated correction in this line. Dead cells were collected 24hrs after nucleofection and PCR-amplified before Sanger Sequencing. Editing efficiency was assessed using Tracking of Indels by Decomposition (TIDE[363]; www.tide.deskgen.com) software, an *in silico* replacement of the T7 Endonuclease assay.

Three of the programmes did not yield a cut (CB-150, CD-118 and CM-113; **Table 4.3**). Programme CA-137, as recommended by Synthego, the sgRNA supplier, resulted in 7.5% efficiency.

Table 4.3 Lonza 4D nucleofector programme efficiencies in COL4A1^{G755R}_cl4 hiPSC

Programme	Efficiency (determined by TIDE)
CA-137	7.5%
CB-150	0%
CD-118	0%
CM-113	0%
DN-100	12.3%

The highest efficiency, 12.3%, was achieved with programme DN-100 (**Table 4.3; Figure 4.4**). The cut was confirmed by observable discrepancy between control (black) and test sample sequences (green) at the predicted cut site (**Figure 4.4**).
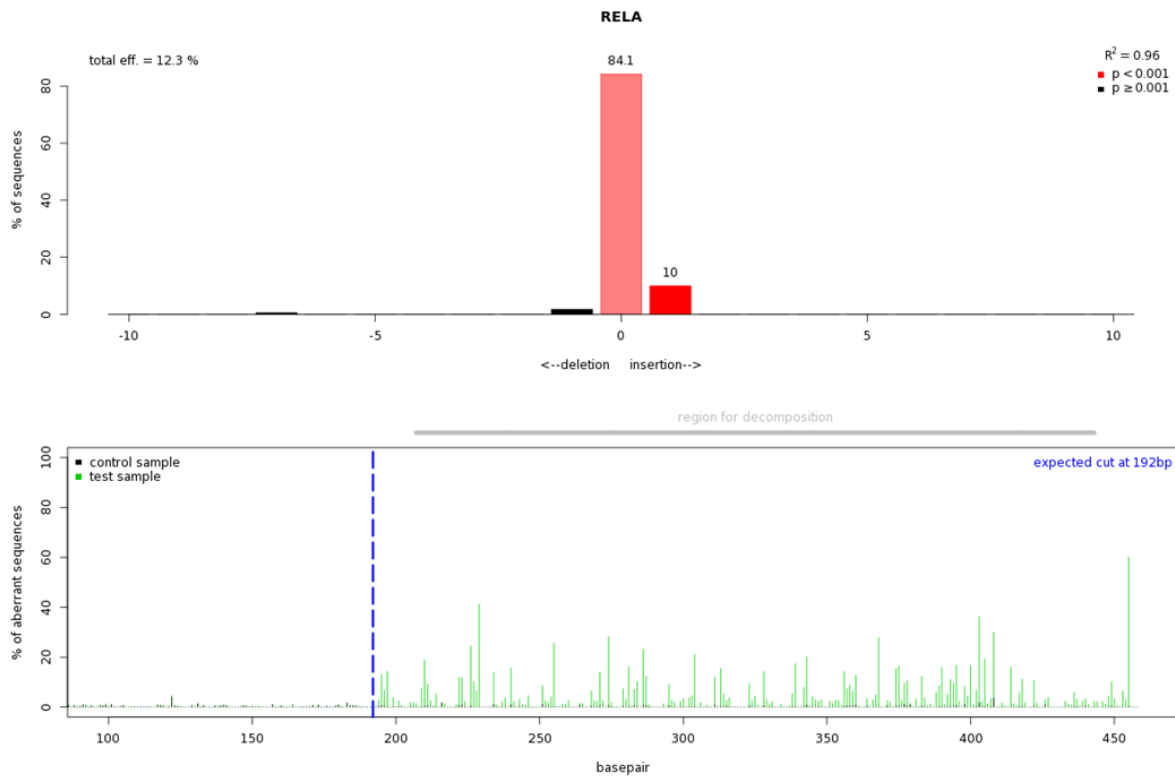
Figure 4.4 Cutting efficiency of the RELA sgRNA: TIDE result for RELA positive control. Screenshot from TIDE[363]

Once the highest efficiency programme, DN-100, had been identified, sgRNA targeting the COL4A1^{G755R} mutation were used in COL4A1^{G755R} _cl4 hiPSC. Dead cells collected 24hrs after nucleofection yielded an editing efficiency of only 3.1%. Cells were cultured for a further seven days and sequencing was repeated. At this stage, the efficiency was 14.4%, confirming the sgRNA had cut (**Figure 4.5A**). PAM site mutation indicated that the donor DNA had been incorporated (**Figure 4.5B**).
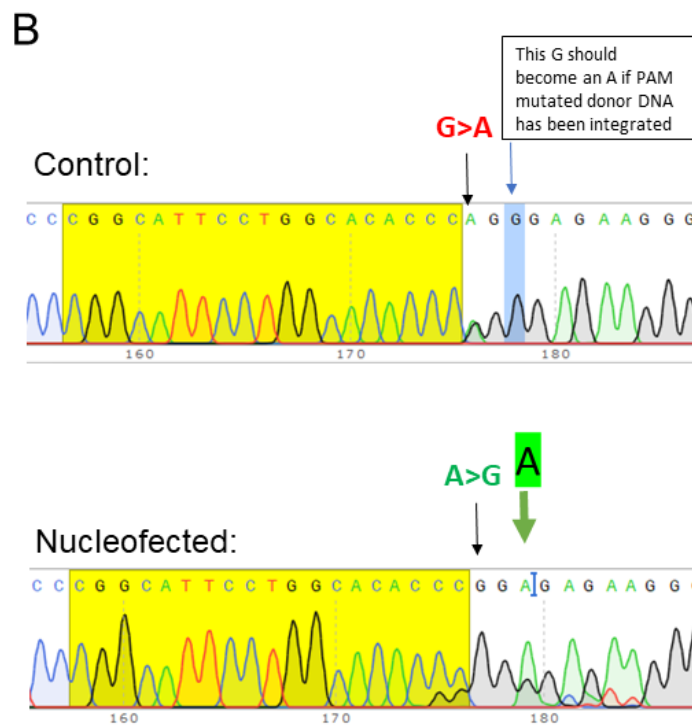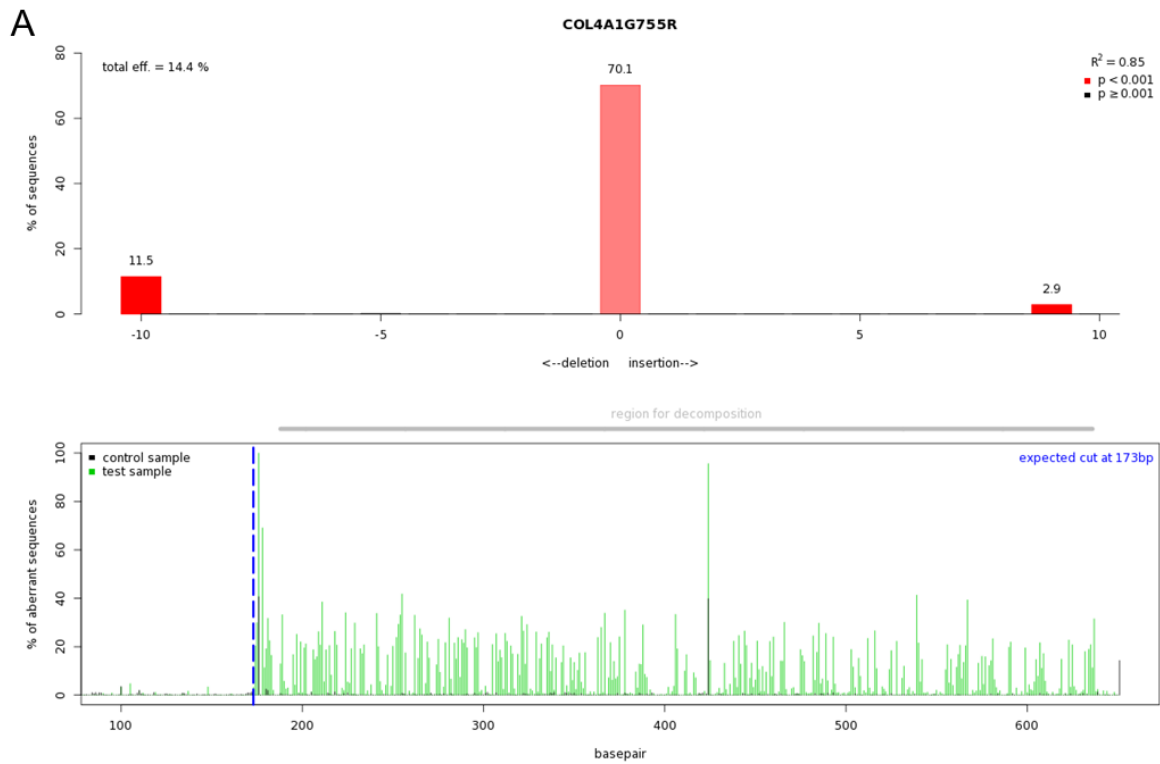
Figure 4.5 Cutting efficiency of COL4A1G755R sgRNA and sequencing of the pool: (A) TIDE for COL4A1^{G755R} gRNA editing efficiency using TIDE[363] and **(B)** control and nucleofected sequencing results with PAM site mutation indicated.

COL4A1_cl4 colonies were picked and sequenced to identify corrected clones **(Figure 4.6)**. A complete figure of all sequenced clones can be found in the Appendix.
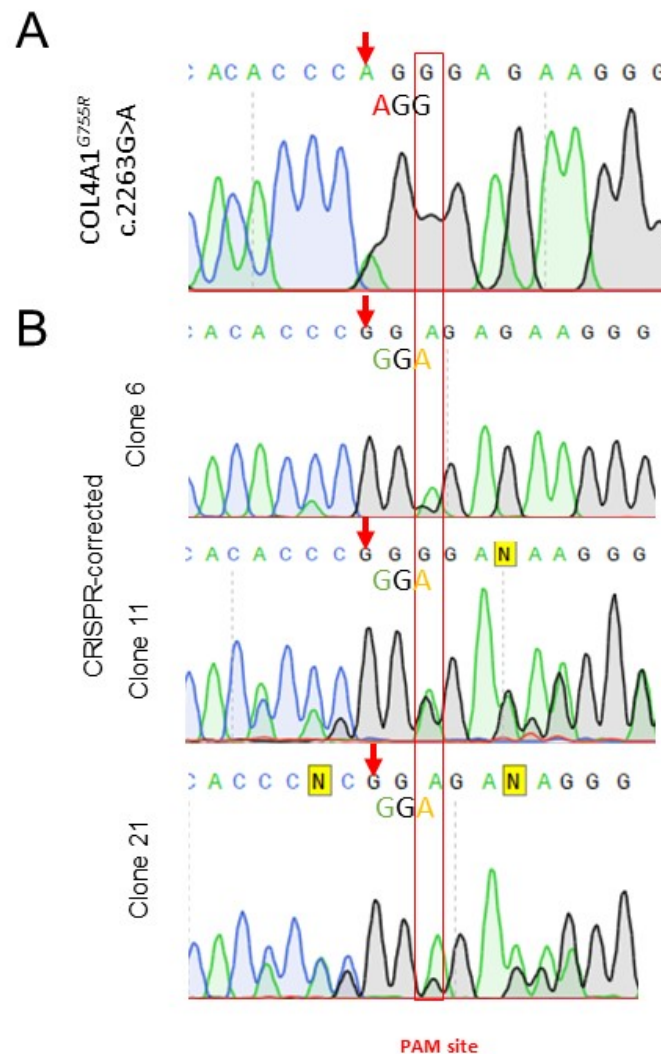
Figure 4.6 Sequencing of COL4A1^{G755R} and the CRISPR-corrected clones: (A) COL4A1^{G755R} and **(B)** CRISPR-corrected clones 6,11 and 21. The red arrows indicate the mutated nucleotide (A) and corrected nucleotide (B).

4.3.3 Characterisation of COL4A1 isogenic hiPSC

Corrected clones 6 and11 were expanded and assessed for pluripotency markers by qRT-PCR and immunocytochemistry (**Figure 4.7**). Both clones are positive for OCT4 by immunocytochemistry and qRT-PCR (*POU5F1;* **Figure 4.7B and C**) but display lower expression of SOX2 (**Figure 4.7B and C**). SOX2 was expressed in the parent line, COL4A1_cl4 (Appendix, **Figure 7.7**). Three germ layer differentiation can be found in the Appendix.
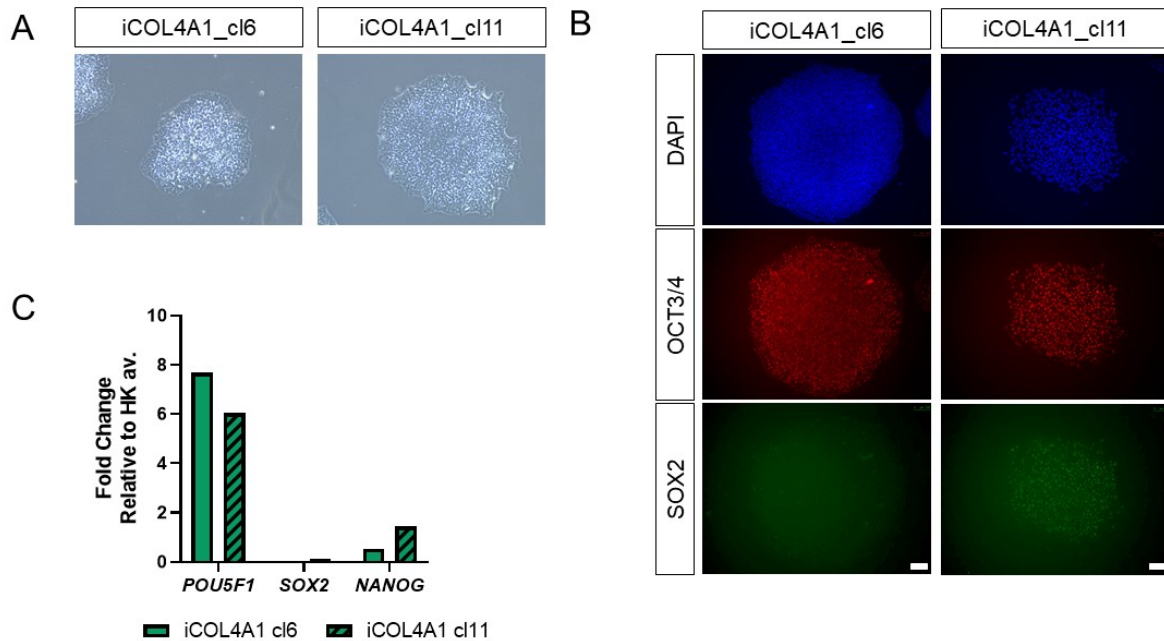
Figure 4.7 Pluripotency characterisation of iCOL4A1 lines: isogenic clone 6 and 11 pluripotency assays **(A)** hiPSC morphology (10x objective) **(B)** immunocytochemistry for OCT3/4 and SOX2 and **(C)** qRT-PCR for *POU5F1*, *SOX2* and *NANOG*, scale bar is 100µm.

4.4 hiPSC-BMEC phenotype of diseased lines

COL4A1/2 hiPSC were differentiated to BMEC and tested in the assays described in chapter 3. These include qRT-PCR, immunocytochemistry, LDL-uptake, TEER, FITC-Dextran and NaFl. The COL4A2^{G702D} line is compared to the isogenic control (clones 14 and 17) which was provided by Dr Alex Granata. The COL4A1^{G755R} isogenic was not initially available, hence WT lines were used for comparison. As with WT lines in Chapter 3, phenotypic characterisation assays were performed on P1 BMEC, 2-3 days post sub-culture for immunocytochemistry, tube formation and qRT-PCR and 5-7 days post sub-culture for LDL, Ki67 and R123.

4.4.1 qRT-PCR

BMEC markers were quantified as ΔΔCt, with BMEC expression relative to the hiPSC line from which the BMEC were derived e.g. fold change relative to hiPSC.
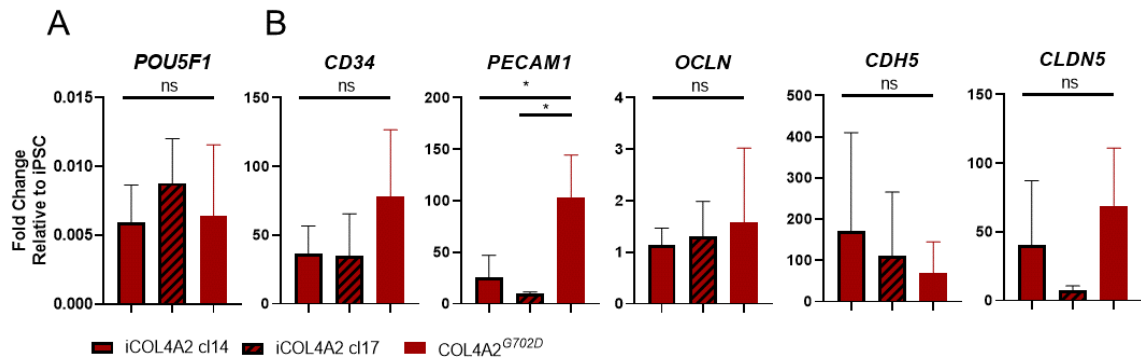
Figure 4.8 qRT-PCR for BMEC markers in iCOL4A2 and COL4A2^{G702D}: qRT-PCR for **(A)** pluripotency marker *POU5F1* (OCT3/4) and **(B)** BMEC markers, *CD34, PECAM1, OCLN, CDH5* and *CLDN5*; N=3 separate differentiations; error bars are Mean +/- SD; one-Way ANOVA.

PECAM1 was significantly increased in COL4A2^{G702D} relative to iCOL4A2 cl14 (P= 0.0295; **Figure 4.8B**) and iCOL4A2 cl17 (P=0.0134; **Figure 4.8B**). PECAM1 plays a role in mechanosensing and the stabilisation of endothelial cells[80,81]. However, when expressed relative to the housekeeping average (**Figure 4.29A**), there is no significant difference in COL4A2^{G702D} relative to iCOL4A2 cl14 and cl17, suggesting this could be a difference in the ability of the lines to differentiate from hiPSC or different basal hiPSC expression of *PECAM1* between the lines.

All other markers were non-significantly different between COL4A2^{G702D} and isogenic controls. VE-Cadherin (*CDH5*), was significantly increased in WT3 compared to WT4 (P= 0.0005; **Figure 4.9B**), COL4A1^{G755R}_cl4 (P= 0.0003; **Figure 4.9B**) and COL4A1^{G755R}_cl5 (P= 0.0002; **Figure 4.9B**). This discrepancy remains when expressed relative to the housekeeping average (**Figure 4.29B**). All other markers were non-significantly different between COL4A1^{G755R} and WTs.
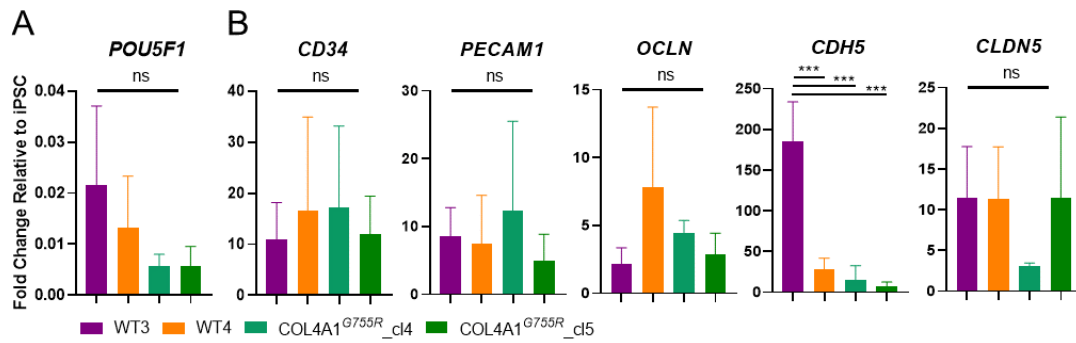
Figure 4.9 qRT-PCR for BMEC markers in WT3, WT4 and COL4A1^{G755R}: qRT-PCR for **(A)** pluripotency marker *POU5F1* (OCT3/4) and **(B)** BMEC markers, *CD34, PECAM1, OCLN, CDH5* and *CLDN5*; N=3 separate differentiations; error bars are Mean +/- SD; one-Way ANOVA (the WT data were previously reported in Chapter 3)

4.4.2 Immunocytochemistry

hiPSC-BMEC were assessed for positivity of key BMEC makers, occludin, GLUT-1, VE-Cadherin and claudin-5 in immunocytochemistry. COL4A2^{G702D} and both isogenic controls (**Figure 4.10**) and COL4A1^{G755R} clone 4 and 5 (**Figure 4.10**), are positive for key markers.
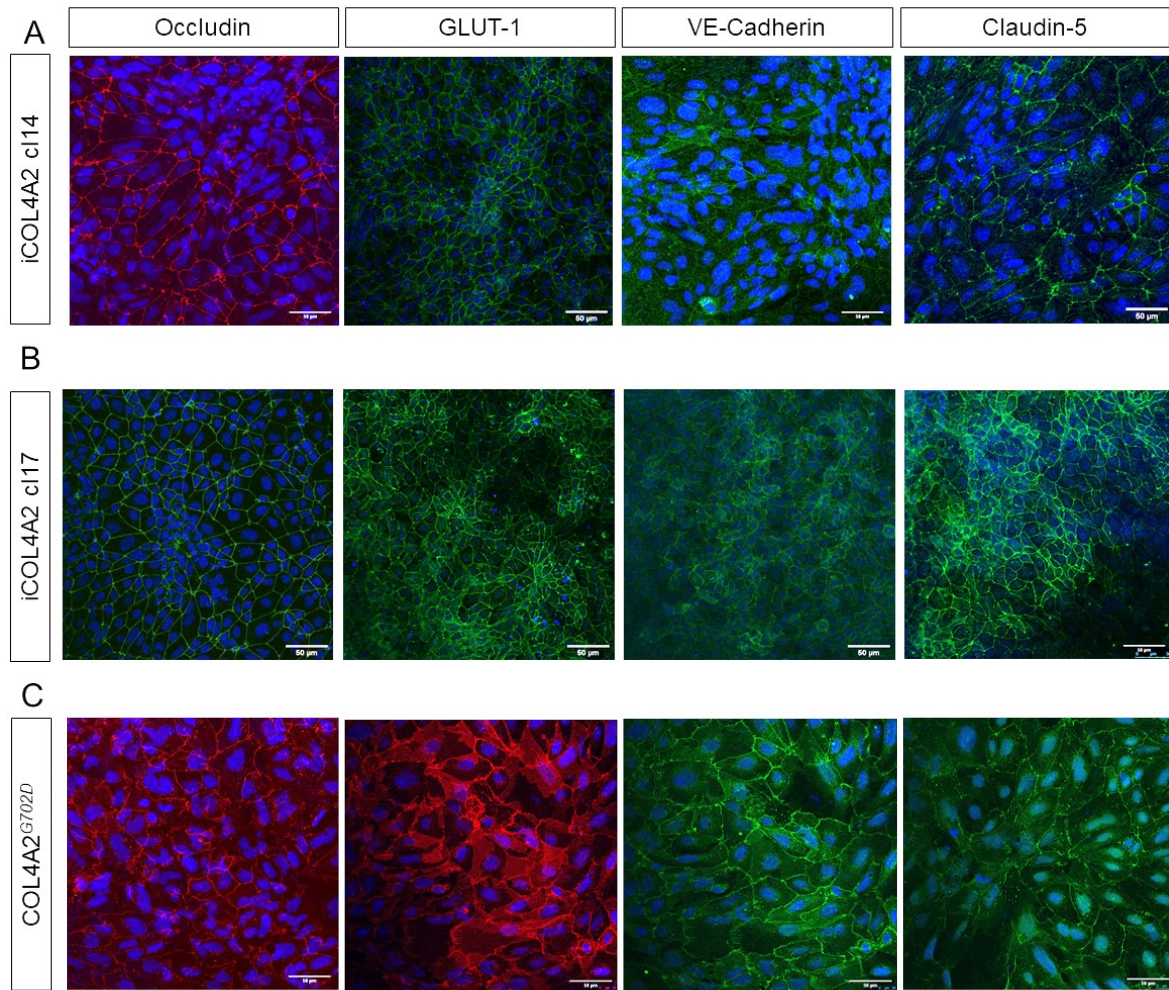
Figure 4.10 Immunocytochemistry for BMEC markers in iCOL4A2 and COL4A2^{G702D}:
(A) iCOL4A2 cl14, **(B)** iCOL4A2 cl17 and **(C)** COL4A2^{G702D}; scale bar is 50µm.
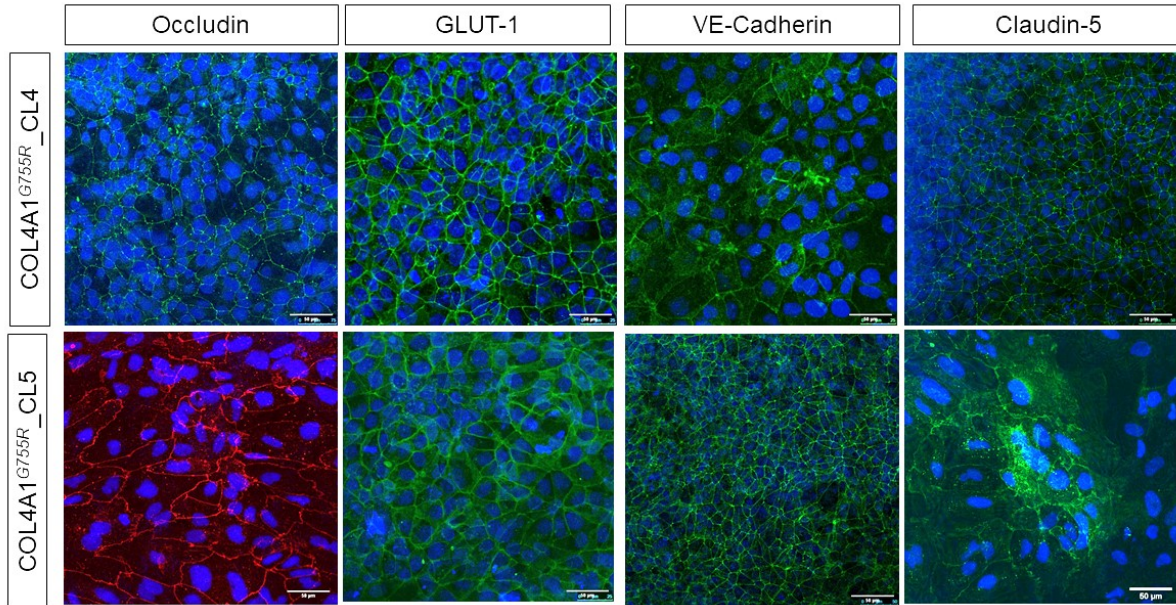
Figure 4.11 Immunocytochemistry for BMEC markers in COL4A1^{G755R}: COL4A1^{G755R} clone 4 and 5; scale bar is 50µm.

4.4.3 LDL-uptake

All lines including COL4A1^{G755R} (**Figure 4.12A**) and COL4A2^{G702D} and isogenic controls (**Figure 4.12B**) are able to uptake LDL. The representative images display different uptake, so this should be repeated with multiple images of each line, in order to quantify the mean fluorescence intensity.
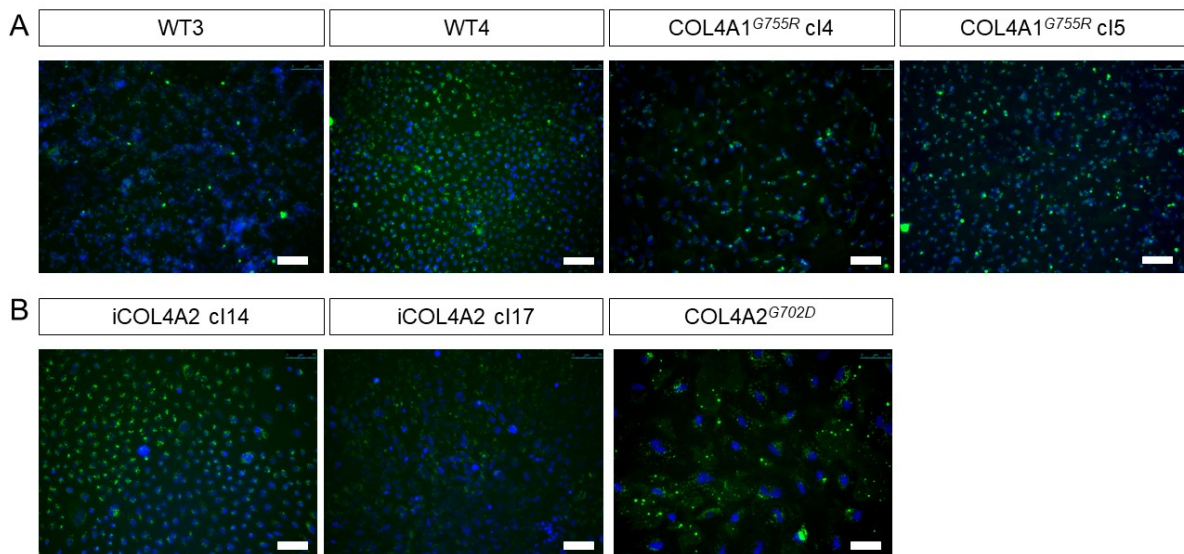
Figure 4.12 LDL-uptake in WTs, COL4A1^{G755R}, iCOL4A2 and COL4A2^{G702D}: (A) COL4A1^{G755R}_cl4, COL4A1^{G755R}_cl5 and **(B)** COL4A2 and isogenic controls; scale bar is 75µm. (WTs are reproduced from chapter 3 for comparison

4.4.4 Tube Formation

WT1 and COL4A1^{G702D} BMEC are able to form tubular networks (**Figure 4.13**). In comparison to COL4A2 isogenic 14, COL4A2^{G702D} form tubular networks on treatment with VEGF, but display less propensity without VEGF (**Figure 4.14B**). WT3, WT4 and COL4A1^{G755R}_cl5 are able to undergo tube formation, within 72 hrs, in the presence or absence of VEGF (**Figure 4.14A**).
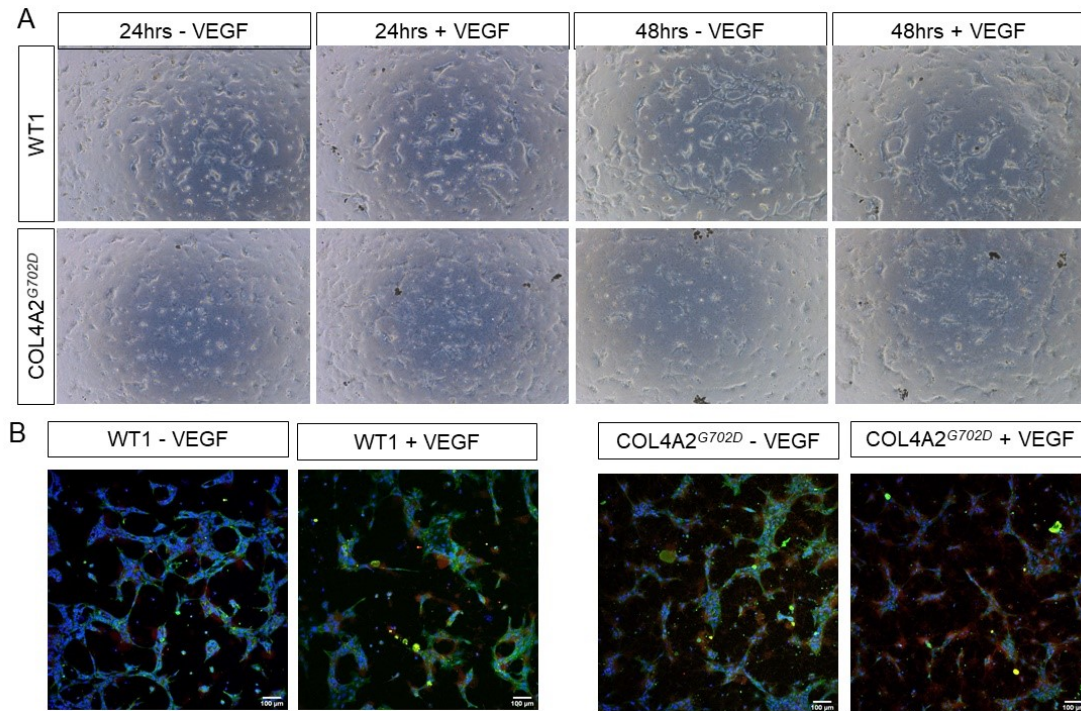
Figure 4.13 Tube formation of WT1 and COL4A2^{G702D} hiPSC-BMEC: (A) Phase Contrast Images (4x objective) and **(B)** immunocytochemistry after 72hrs, for occludin (red), VE-Cadherin (green) co-stained with DAPI; Scale bar is 100µm.
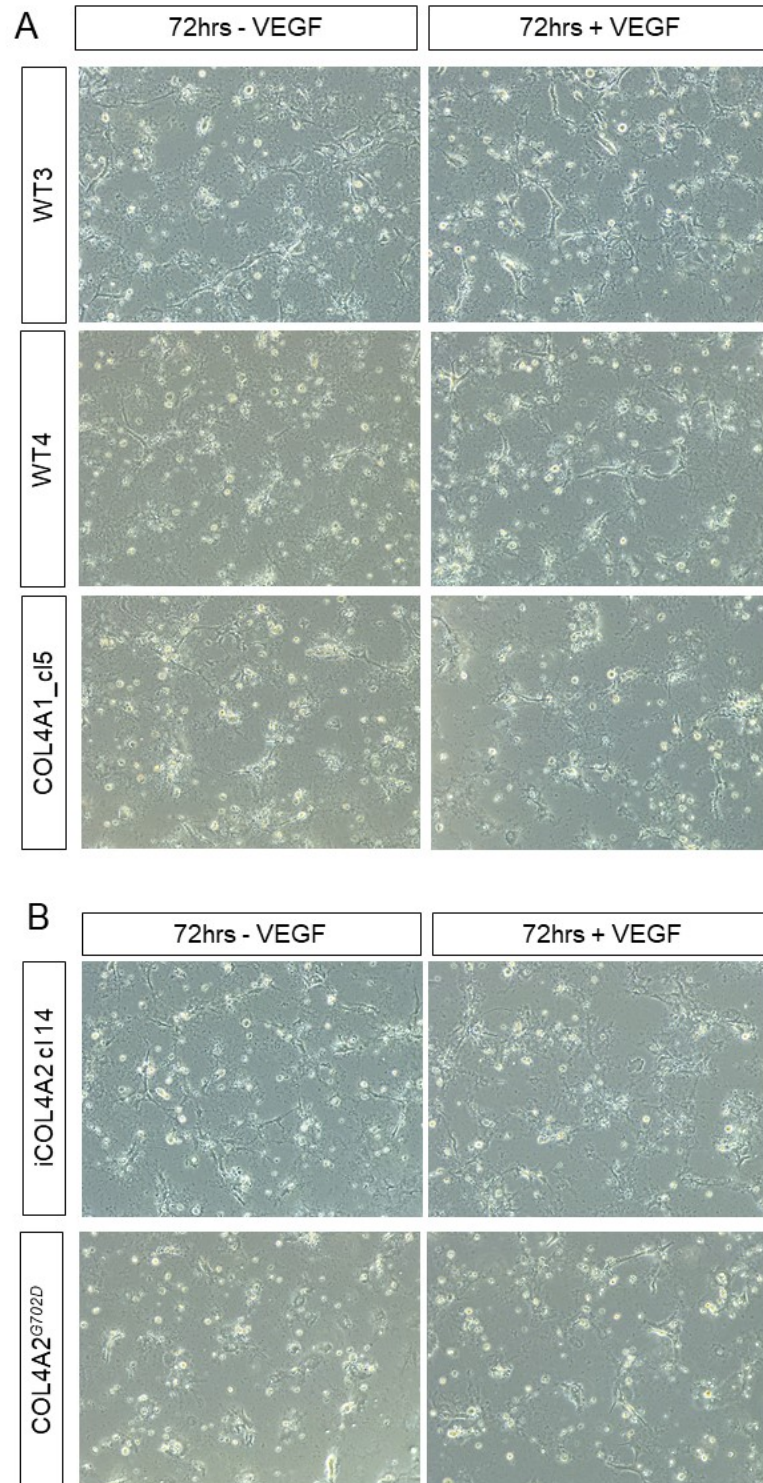
Figure 4.14 Tube formation for WTs, COL4A1^{G755R}, iCOL4A2 and COL4A2^{G702D}: Tube formation with and without VEGF after 72hrs, for **(A)** WT3, WT4 and COL4A1^{G755R}_cl5 and **(B)** iCOL4A2 cl14 and COL4A2^{G702D}. Images are 4x objective.

4.4.5 hiPSC-BMEC display barrier properties

hiPSC-BMEC functional capacity was assessed with optimised barrier assays reported in Chapter 3.

TEER

COL4A1^{G755R}_cl4 and cl5 are able to achieve TEER values of over 600Ωxcm^2 in two separate experiments (**Figure 4.15A**). COL4A1^{G755R}_cl4 TEER peaks at 2515Ωxcm^2 (**Figure 4.15A**) and COL4A1^{G755R}_cl5 TEER peaks at 962Ωxcm^2 (**Figure 4.15B**).

Notably, the pattern differs to that seen in WTs, in which characteristically, values peak at day 2 or 3, before declining. For example, the peak value of 2515Ωxcm^2 for COL4A1^{G755R}_cl4 occurs at day 5.
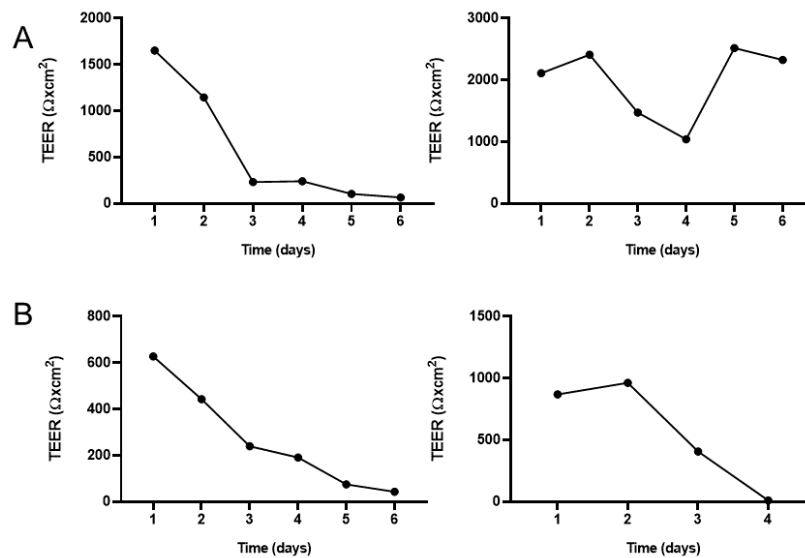
Figure 4.15 TEER of COL4A1^{G755R}: **(A)** COL4A1^{G755R} _cl4 and **(B)** COL4A1^{G755R} _cl5. Each graph indicates a separate biological replicate

COL4A2^{G702D} TEER is highly variably across three separate experiments, in which peak values range from 89Ωxcm^2 to 3586Ωxcm^2 (**Figure 4.16C**). In two differentiations of the CRISPR-corrected isogenic control iCOL4A2 cl14, TEER reaches 4116Ωxcm^2 and 3167Ωxcm^2 respectively (**Figure 4.16A**), cl17 peaks at 390Ωxcm^2 (**Figure 4.16B**), however, this is only one experiment.
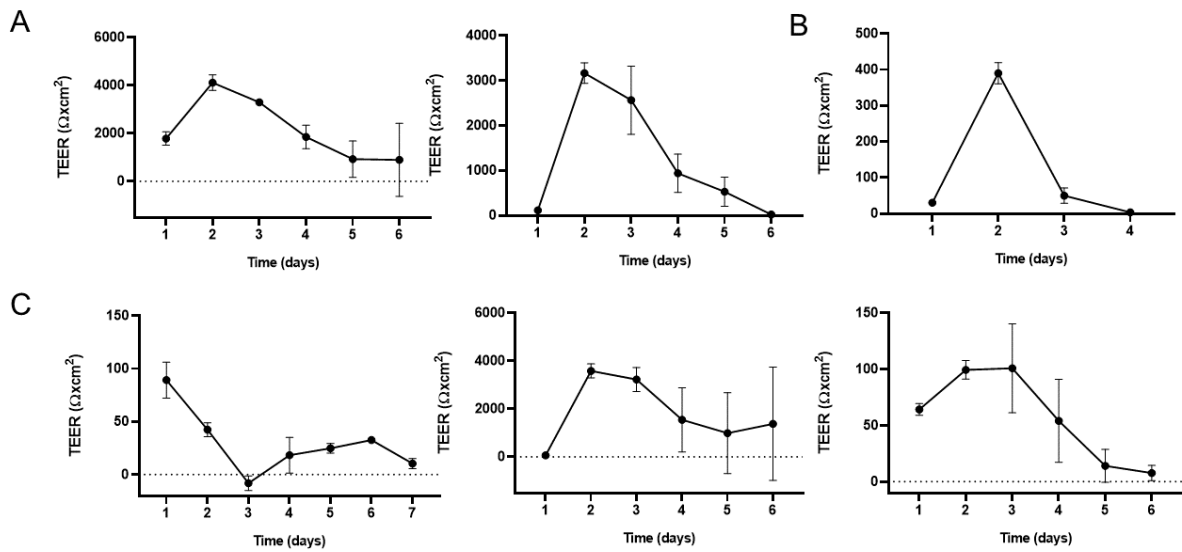
Figure 4.16 TEER of iCOL4A2 and COL4A2^{G702D}: **(A)** iCOL4A2^{G702D} cl14 **(B)** iCOL4A2^{G702D} cl17 and **(C)** COL4A2^{G702D}. Each graph indicates a separate biological replicate and error bars are of separate Transwells® from the same experiment (2-4 Transwells®).

Fluorescence: FITC-Dextran and NaFl

COL4A2^{G702D} BMEC display only 2.5% passage of 40kD FITC-Dextran passage (**Figure 4.17B**) and less than 18.8% % of 4kD FITC-Dextran (**Figure 4.17C**).
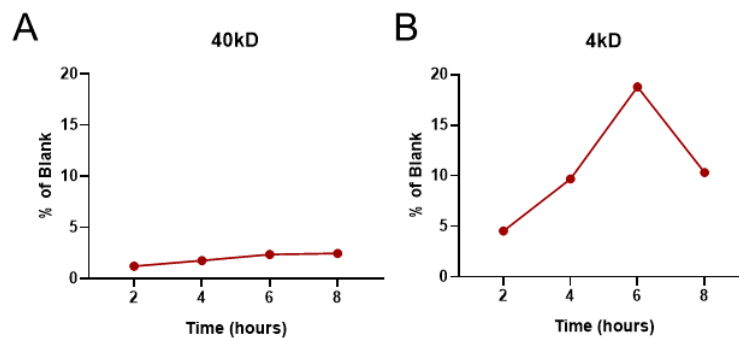
Figure 4.17 Barrier properties with FITC-Dextran for COL4A2^{G702D}: **(A)** COL4A2^{G702D} 40kD FITC-Dextran (n=2), **(B)** COL4A2^{G702D} 4kD FITC-Dextran (n=1)

Like the variation seen between TEER experiments, in three experiments, COL4A2^{G702D} BMEC are able to prevent between 88.6 and 98.7% of NaFl from passing across the monolayer (maximum values of 11.4%, 1.3% and 5.8% respectively, **Figure 4.18B**). Similarly, in two experiments of iCOL4A2 cl14 maximum values reach 1.4% and 6.0% respectively (**Figure 4.18A**).

Therefore, when averaged across the 2-8hr time course, there is a non-significant trend of increasing passage of NaFl in COL4A2^{G702D} relative to isogenic 14 (mean 4.2% and 2.4%, respectively; **Figure 4.18C**), although large standard deviation is observed. TEER was recorded immediately prior to NaFl, to ensure comparable values between different samples of that differentiation. This variation results from differences between separate differentiations.
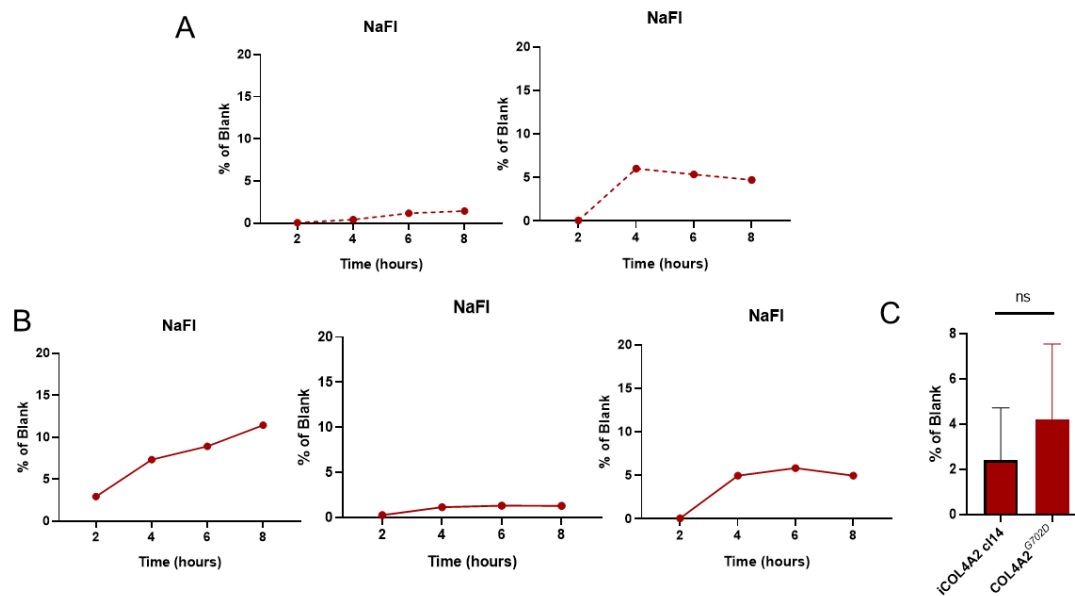
Figure 4.18 Barrier properties with NaFl for iCOL4A2 and COL4A2^{G702D}: (A) iCOL4A2 cl14 NaFl (n=2) **(B)** COL4A2^{G702D} NaFl (n=3) **(E)** mean % of blank over 2-8hours; error bars are mean +/- SD; blank is 100%.

4.6 Characterising the disease phenotype of COL4A1^{G755R} and COL4A2^{G702D} hiPSC-BMEC

Following these characterisation experiments to determine hiPSC from disease lines are able to produce functional BMEC, phenotypic differences between WTs, COL4A1^{G755R}, COL4A2^{G702D} and isogenic controls were explored.

4.6.1 COL4A1^{G755R} and COL4A2^{G702D} hiPSC-BMEC do not display proliferation differences compared to controls

On observation, COL4A2^{G702D} BMEC displayed low cell confluency on sub-culture after matrix selection, taking longer to reach confluency than WT lines. Hence, proliferation was assessed, by quantifying the percentage of Ki67+ cells relative to DAPI+. There is a non-significant trend of reduced proliferation in COL4A2^{G702D} relative to iCOL4A2 cl14 (14.9% 24.1% respectively; **Figure 4.18**).
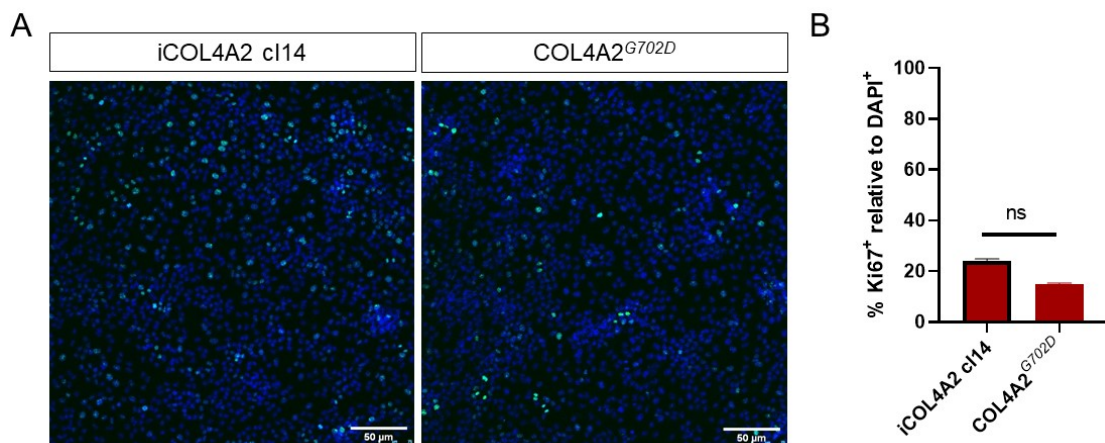
Figure 4.18 Ki67 assay for iCOL4A2 and COL4A2^{G702D}: (A) immunocytochemistry of Ki67 and **(B)** % Ki67 positive cells relative to DAPI positive. 4 images per well were quantified, n=2, mean +/-SD, images are representative; scale bar is 50µm.

Similarly, there is no significant difference between WT4 and COL4A1^{G755R}_cl4 and COL4A1^{G755R}_cl5 (**Figure 4.19**), but some inter-clonal difference is observed, with cl5 displaying higher proliferation than WT4 and cl4 displaying less (71.8% and 45.3% respectively; **Figure 4.19B**).
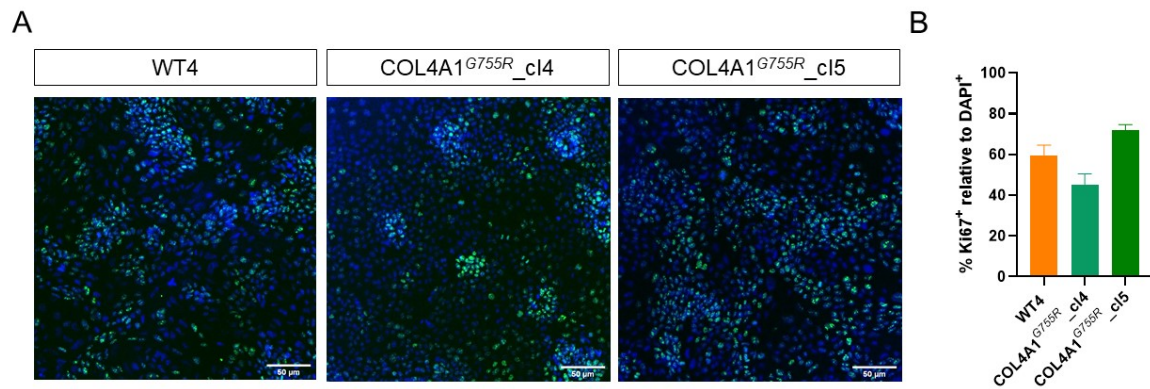
Figure 4.19 Ki67 assay for WT4 and COL4A1^{G755R}**: (A)** Immunocytochemistry of Ki67 and **(B)** % Ki67 positive cells relative to DAPI positive. 3-4 images per well were quantified, n=1, mean +/-SD, images are representative; scale bar is 50um.

To further investigate any potential differences in proliferation, mRNA expression for key proliferation genes, *TP53* (P53), *CDKN1A* (P21) and *CCND1* (Cyclin D1) was conducted. There is no observable difference between COL4A2^{G702D} and its two isogenic controls (**Figure 4.20A**). There is trend of increased *CDKN1A* in COL4A1^{G755R}_cl4 and cl5 relative to WT3 and WT4 (**Figure 4.20B**). With no apparent phenotype, further avenues were explored in order to identify disease relevant differences.
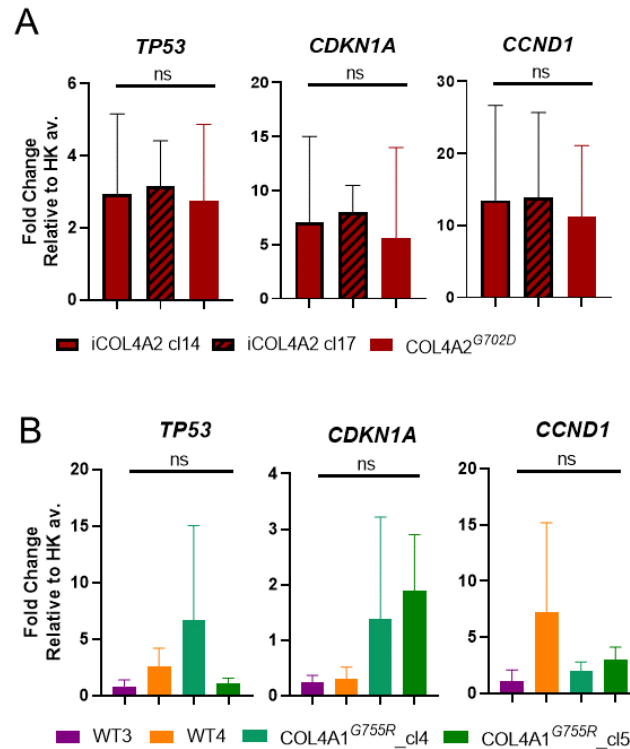
Figure 4.20 qRT-PCR for proliferation markers: (A) COL4A2^{G702D} and isogenic controls and **(B)** COL4A1^{G755R} and WTs, relative to housekeeping average (GAPDH and PBGD), n=3, error bars are mean +/- SD

4.6.2 COL4A1/2 hiPSC-BMEC display impaired R123 efflux transport

As introduced in chapter 3, the R123 assay is used as an indicator of P-gp function, using the inhibitor CsA[307]. As before, data are reported as the ratio of +CsA/-CsA whereby a value >1.0, where fluorescence is higher in the inhibited sample relative to the uninhibited, is the expected result for functional P-gp efflux transport, as demonstrated by WT lines in Chapter 3. A value equal to 1.0 represents no difference between inhibited and uninhibited samples and a value <1.0 indicates impaired efflux transport, whereby there is more fluorescence in the uninhibited sample.

The R123 ratio of COL4A2^{G702D} is significantly lower (p=0.0131) than COL4A2 isogenic clone 14 (**Figure 4.21A**). This suggests that there is lower accumulation and/or impaired efflux in the uninhibited sample of COL4A2^{G702D} when compared to the control. COL4A1^{G755R}_cl4 and COL4A1^{G755R}_cl5 also display the same trend (**Figure 4.21B**), with significant reduction in the ratio between WT3 and COL4A1_cl5 (P=0.0472).
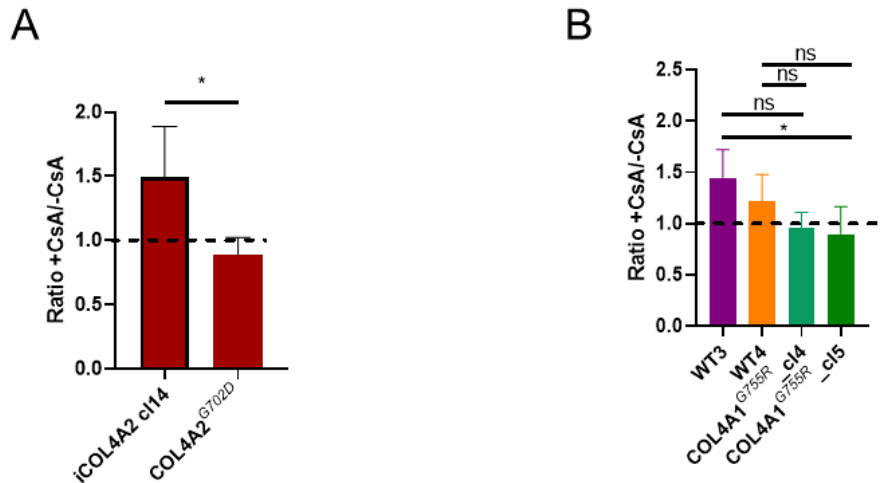
Figure 4.21 R123 assay ratio +CsA/-CsA for iCOL4A2, COL4A2^{G702D}, WTs and COL4A1^{G755R}: (A) iCOL4A2 cl14 n=4, COL4A2^{G702D} n=5 **(B)** WT3 n=6, WT4 n=4, COL4A1^{G755R}_cl4 n=3 and COL4A1_cl5 n=3, error bars are +/-SD

To determine if this could be as a result of reduced gene expression, qRT-PCR was performed for P-gp (encoded by the *ABCB1* gene). Whilst there are no significant reductions and large error is observed, there is a trend for decreased *ABCB1* in COL4A2^{G702D} (**Figure 4.22A**) and COL4A1^{G755R} clones, compared to one WT4, but not WT3 (**Figure 4.22B**). Given there is no significant difference at the mRNA level, it could be that translation of the protein is affected, or its localisation. It has been previously reported that P-gp stored at the nuclear envelope and trafficked to the membrane in response to a stimulus such as inflammation[364].
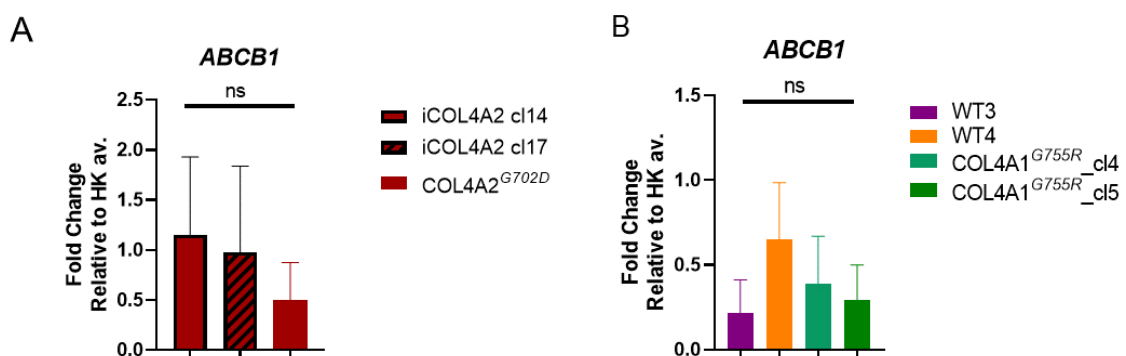
Figure 4.22 qRT-PCR for *ABCB1*: (A) COL4A2^{G702D} and **(B)** COL4A1^{G755R} and WTs, relative to relative to housekeeping average (GAPDH and PBGD), n=3, error bars are mean +/- SD

4.6.3 COL4A1/2 hiPSC-BMEC display tight junction abnormalities

BBB breakdown, arising from tight junction disruption has been implicated in SVD[156], with occludin levels increased in the blood of patients following ischaemic stroke [174]. Based on

this, an assessment of the distribution of occludin and claudin-5 at the tight junctions was performed.

Multiple fields of view were acquired to quantify changes in hiPSC-BMEC tight junctions (occludin and claudin-5) between mutant and WT/isogenic controls, using FIJI (ImageJ). The percentage of discontinuous junctions refers to the number of cells containing at least one discontinuous junction (**Figure 4.23A**), relative to DAPI-positive cells. Cell area was also quantified (**Figure 4.23B**), taking 5 cells per image (25 cells total). For claudin-5, the corrected total cell fluorescence (CTCF), relative to DAPI, was also calculated from 5 cells per field of view, totalling 25 cells (**Figure 4.23C**).
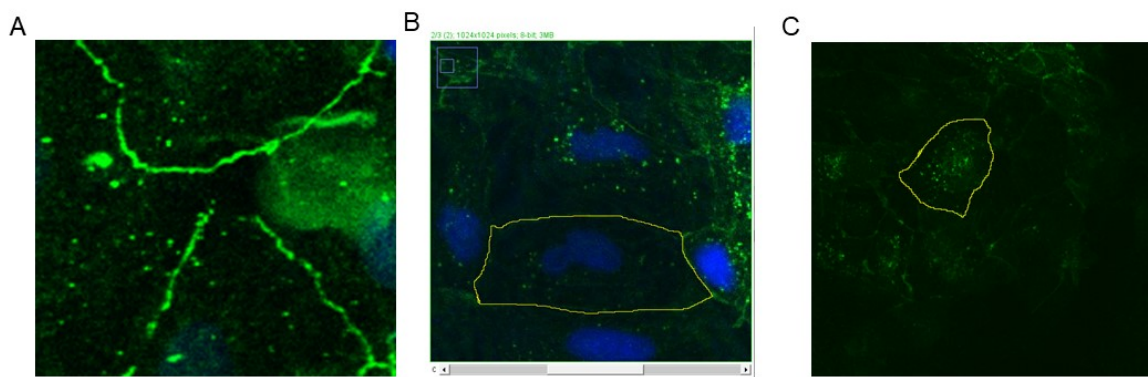
Figure 4.23 Parameters for tight junction quantification: (A) discontinuous junctions, **(B)** cell area and **(C)** corrected total cell fluorescence (CTCF).

There are no significant differences in mean fluorescence across the COL4A1 clones and WT lines (**Figure 4.24B**). However, there is a trend of increasing percentage of discontinuous junctions in COL4A1^{G755R}_cl5 relative to WT3 and 4 (**Figure 4.24A-C**). The same trend is also observed in mean cell area (**Figure 4.24D**). COL4A2^{G702D} hiPSC-BMEC (**Figure 4.25A**) display increased mean fluorescence (**Figure 4.25B**), a higher percentage of discontinuous junctions than iCOL4A2 cl14 (**Figure 4.25C**) and a reduced mean cell area (**Figure 4.25D**).
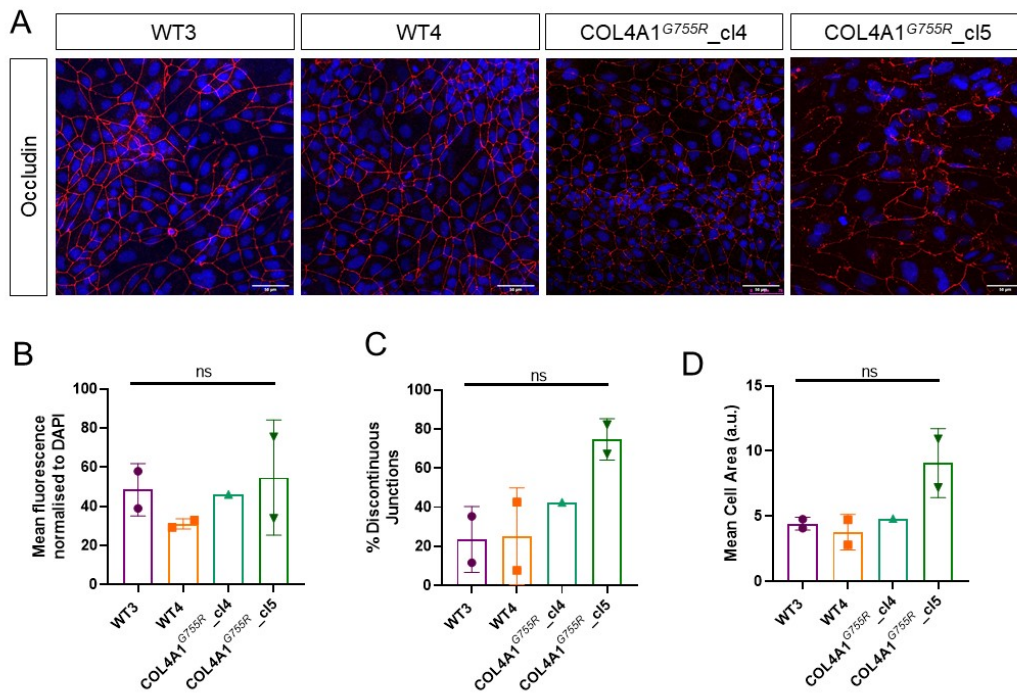
Figure 4.24 Immunocytochemistry and quantification for occludin in WTs and COL4A1^{G755R}**: (A)** immunocytochemistry **(B)** mean fluorescence intensity relative to number of DAPI-positive nuclei **(C)** percentage of discontinuous junctions **(D)** mean cell area; 3-5 fields of view from the same well were quantified for B and C; for D, 5 cells per image were quantified; scale bar is 50µm. WT3, WT4 and COL4A1_cl5 n=2, COL4A1_cl4 n=2.
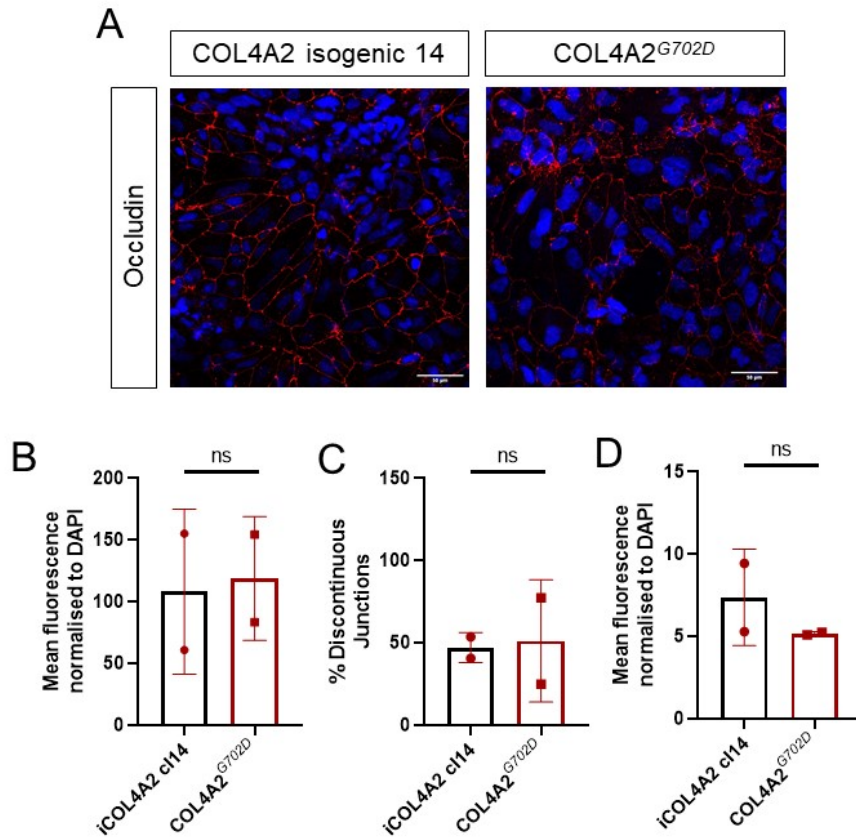
Figure 4.25 Immunocytochemistry and quantification for occludin in iCOL4A2 and COL4A2^{G702D}: occludin **(A)** immunocytochemistry **(B)** Mean fluorescence intensity relative to number of DAPI-positive nuclei **(C)** percentage of discontinuous junctions **(D)** mean cell area. 5 fields of view from the same well were quantified for B and C; for D, 5 cells per image were quantified, scale bar is 50µm, n=2.

claudin-5 mean fluorescence (quantified across the whole image) is increased in COL4A1^{G755R}_cl5 relative to WT3 and WT4 (**Figure 4.26B**). When using CTCF, which is calculated by outlining 5 separate cells in each field of view, this trend remains (CTCF; **Figure 4.26C**). However, even with this method, it is not possible to distinguish between intracellular and surface expression differences. The cell size heterogeneity visible in the representative images (**Figure 4.26A**), results in large error in mean cell area (**Figure 4.26D**). There is a reduction in claudin-5 mean fluorescence in COL4A2^{G702D} relative to the isogenic control (**Figure 4.27A,B**). CTCF is highly variable between multiple fields of the same well and when quantified displays larger standard deviation (**Figure 4.27C**). The same is also true for mean cell area, which shows a trend of decreased area in COL4A2^{G702D} (**Figure 4.27D**).
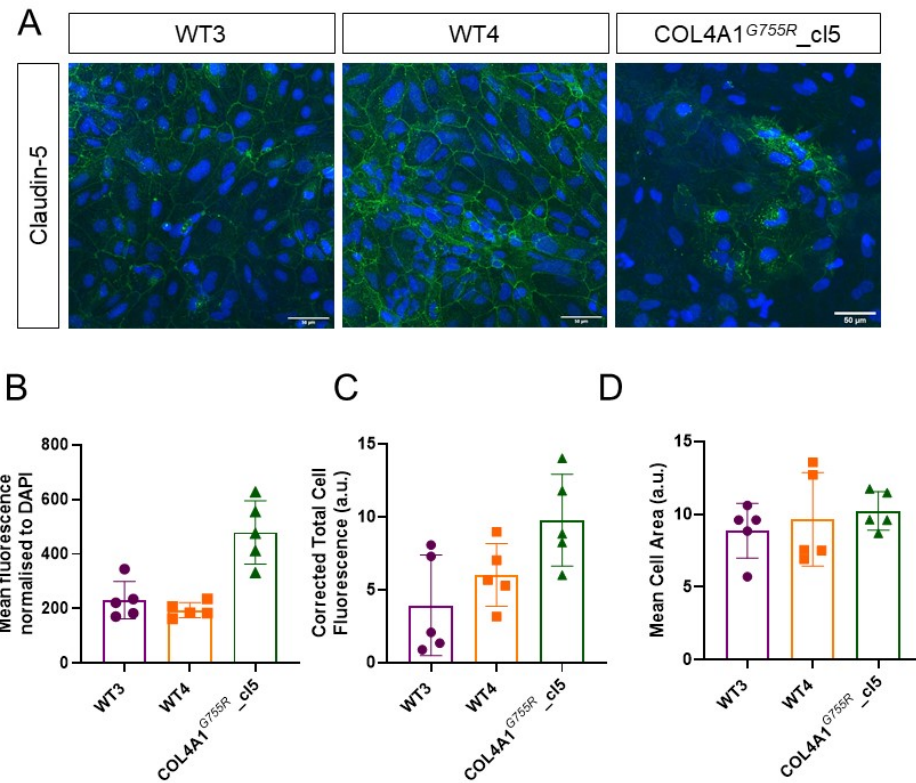
Figure 4.26 Immunocytochemistry and quantification for claudin-5 in WTs and COL4A1^{G755R}**: (A)** immunocytochemistry **(B)** mean fluorescence intensity relative to number of DAPI-positive nuclei **(C)** CTCF **(D)** mean cell area; 5 fields of view from the same well were quantified for B and C, for D, 5 cells per image were quantified, scale bar is 50μm, n=1, error bars are technical quintuplets.
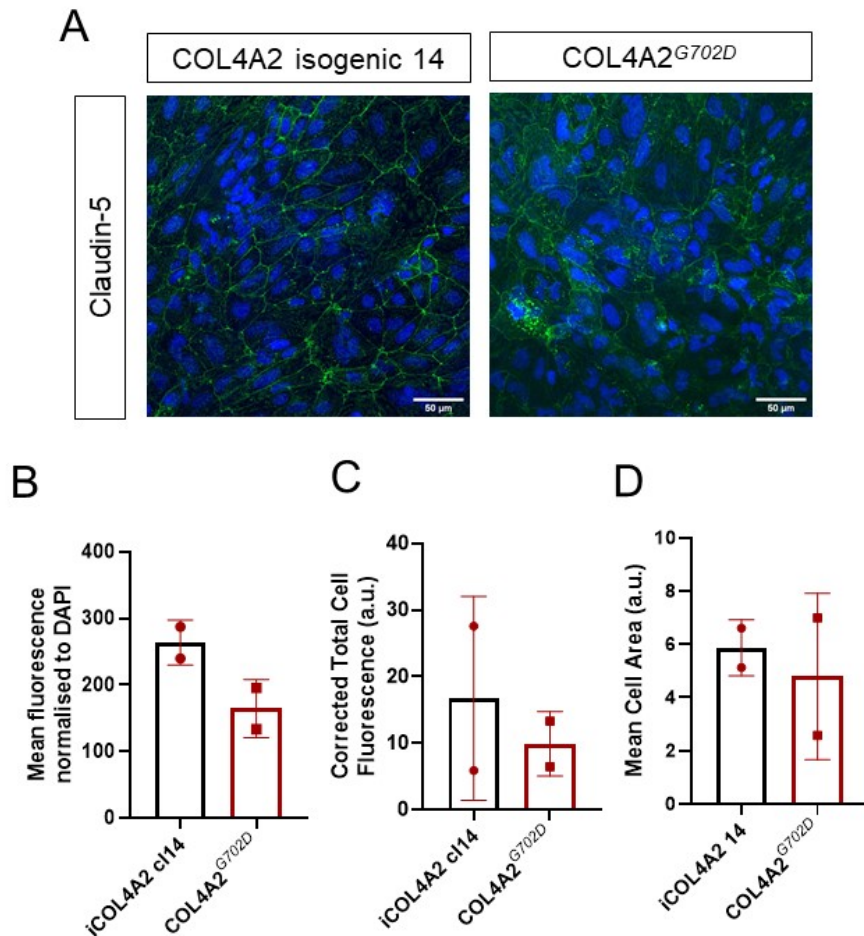
Figure 4.27 Immunocytochemistry and quantification for claudin-5 in iCOL4A2 and COL4A2^{G702D}**: (A)** immunocytochemistry **(B)** mean fluorescence intensity relative to number of DAPI-positive nuclei **(C)** CTCF **(D)** mean cell area; 5 fields of view from the same well were quantified for B and C, for D, 5 cells per image were quantified, scale bar is 50µm, n=2.

Western blot for BMEC markers

To follow up these findings in immunocytochemistry (**Figures 4.24-27**), western blot analysis was performed to better quantify any changes in total protein. The western blot demonstrates a reduction of claudin-5 in COL4A2^{G702D} relative to iCOL4A2 cl14 (**Figure 4.28A,B**), which is consistent with the immunocytochemistry (**Figure 4.27**); however, occludin is unchanged (**Figure 4.28A,B**).

Conversely, occludin is reduced in COL4A1^{G755R}_cl5 relative to WT3 and 4 (**Figure 4.28C,D**). However, there is discrepancy between the WTs, especially apparent in claudin-5, where it appears claudin-5 is increased in COL4A1^{G755R}_cl5 relative to WT4, but not WT3

(**Figure 4.28C,D**). Immunocytochemistry suggests claudin-5 is indeed increased (**Figure 4.26B**).
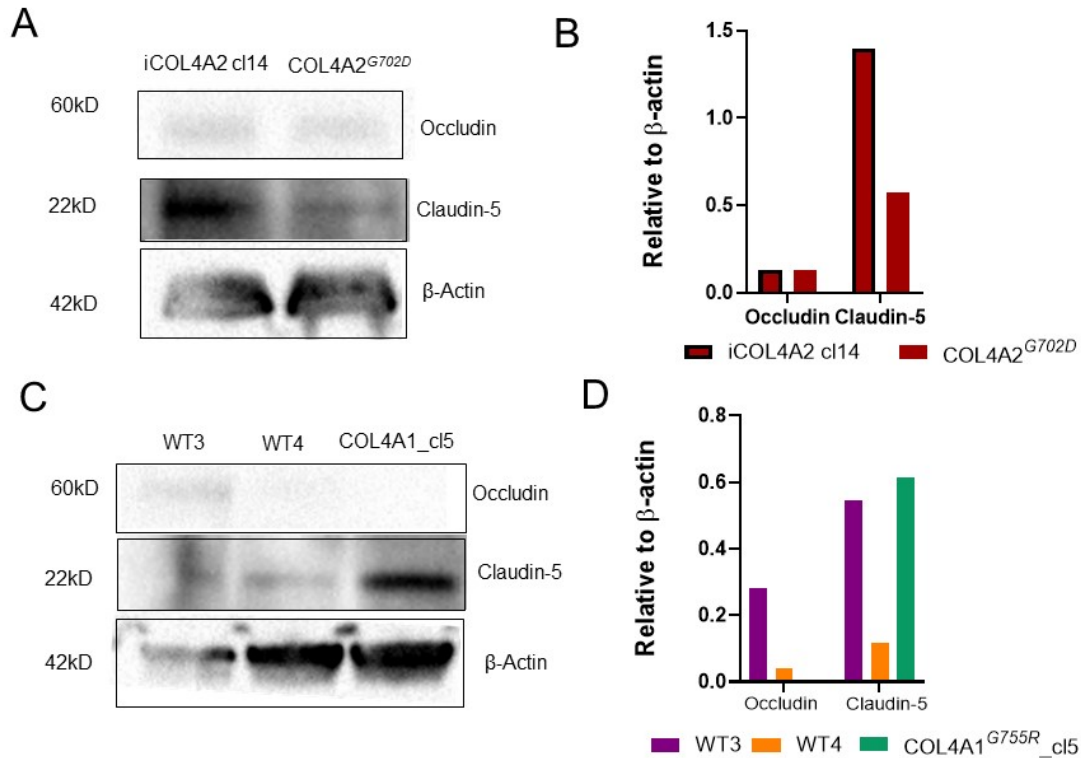
Figure 4.28 Western Blot for occludin, claudin-5 and housekeeping β-actin in hiPSC-BMEC: (A) COL4A2^{G702D} and iCOL4A2 cl14 and **(B)** relative quantification, **(C)** COL4A1^{G755R} and WTs and **(D)** relative quantification, n=1.

qRT-PCR for BMEC markers

Tight junction differences in occludin and claudin-5 observed with immunocytochemistry (**Figures 4.24-27**) and western blot (**Figure 4.28**) could relate to alterations in protein translation or mRNA transcription. Previous reports in ischaemic models, showed that claudin-5 expression was altered through the action of Caveloin-1[365,366] and VE-Cadherin expression was increased[366,367].

Therefore, qRT-PCR mRNA expression was assessed to determine any transcriptional differences that could explain these findings. Previously, (**Figures 4.8 and 4.9**), BMEC markers were quantified as ΔΔCt, with BMEC expression relative to the hiPSC line from which the BMEC were derived, to determine differentiation capability. Here, data is

presented compared only to housekeeping genes (GAPDH and PBGD), to remove any potential variation introduced by inherent differences in hiPSC line Ct values for these markers.

Overall, there are no clear trends in occludin or claudin-5 (**Figure 4.29**). VE-Cadherin (*CDH5*) is significantly increased (P<0.0001) in WT3 relative to WT4, COL4A1^{G755R}_cl4 cl5 (**Figure 4.29A**) but a trend of reduced expression of *CDH5* is apparent in COL4A2^{G702D} relative to isogenic controls (**Figure 4.29B**).
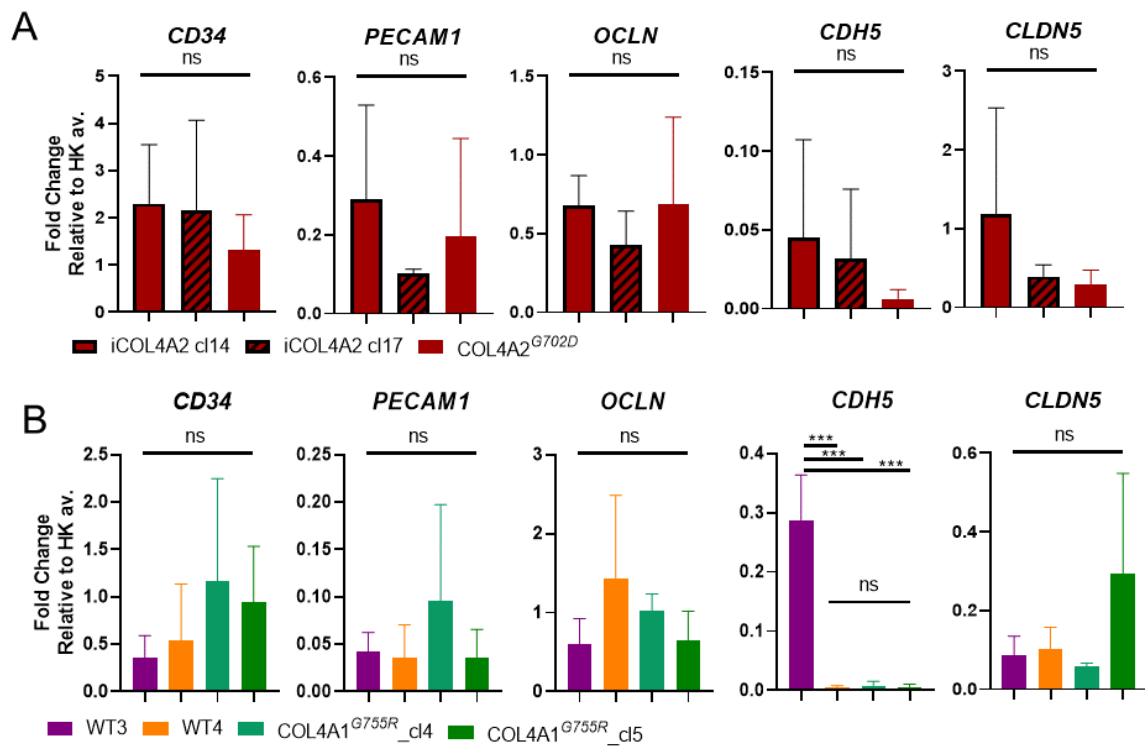
Figure 4.29 qRT-PCR for BMEC markers relative to HK: (A) COL4A2^{G702D} and isogenic controls **(B)** COL4A1^{G755R} and WTs, relative to relative to housekeeping average (*GAPDH* and *PBGD*), n=3, error bars are mean +/- SD

4.6.4 Collagen IV is reduced in COL4A2^{G702D} hiPSC-BMEC

Since tight junction assembly, maintenance and BBB integrity are inextricably linked to the extracellular matrix and given the mutations in this study are in COL4A1/2, gene expression and protein deposition of collagen IV were assessed.

Transcriptional changes in hiPSC-BMEC relative to housekeeping genes, in either α-chain were investigated with qRT-PCR. There is no difference between COL4A1 and COL4A2 expression in COL4A2^{G702D} relative to either isogenic control (**Figure 4.30A**). There is a non-significant trend of increased COL4A2 in COL4A1^{G755R}_cl4 and cl5 compared to both WT lines (**Figure 4.30B**).
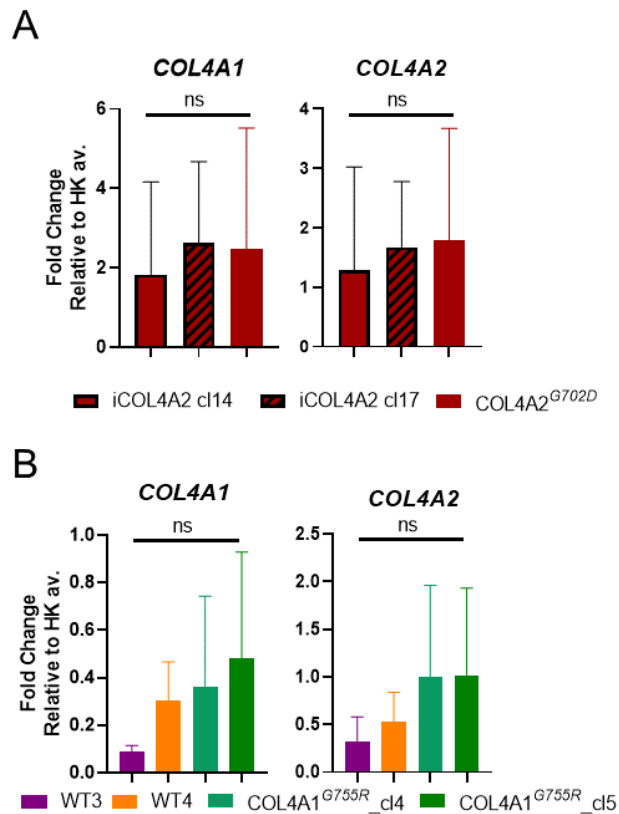
Figure 4.30 qRT-PCR for *COL4A1* and *COL4A2*: (A) COL4A2^{G702D} and isogenic controls and **(B)** COL4A1^{G755R} and WTs, relative to relative to housekeeping average (GAPDH and PBGD), n=3, error bars are mean +/- SD

Immunocytochemistry

Since mRNA expression is only indicative of transcriptional levels, an antibody recognising total collagen IV (i.e. non-specific to sub-chains), was used to determine protein levels by immunocytochemistry. Collagen IV is reduced in COL4A2^{G702D} relative to WT1 (**Figure 4.31**). But when compared to iCOL4A2, no differences were observed (**Figure 4.32**). COL4A1^{G755R} display decreased collagen IV compared to WT3, but not WT4 (**Figure 4.33**).
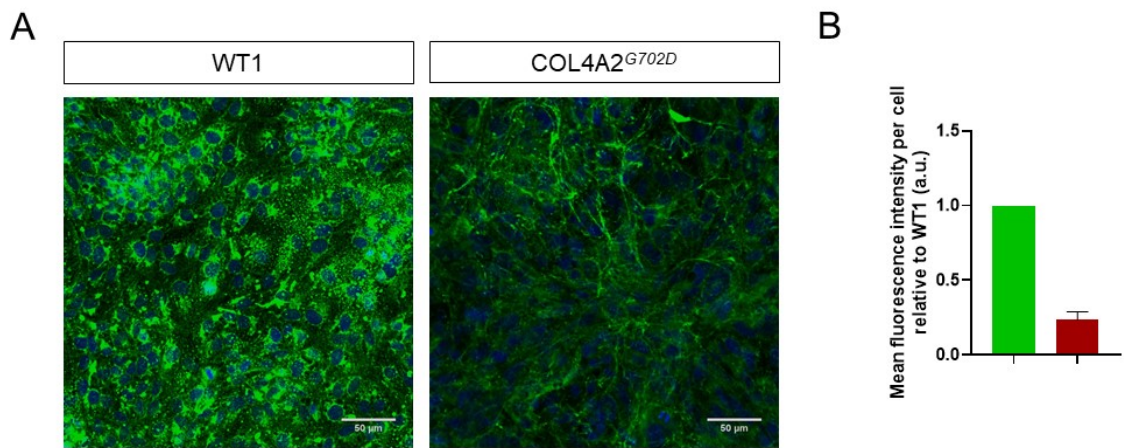
Figure 4.31 Collagen IV immunocytochemistry in WT1 and COL4A2^{G702D}: (A) Immunocytochemistry and **(B)** quantification, images are representative, scale bar is 50μm, n=1
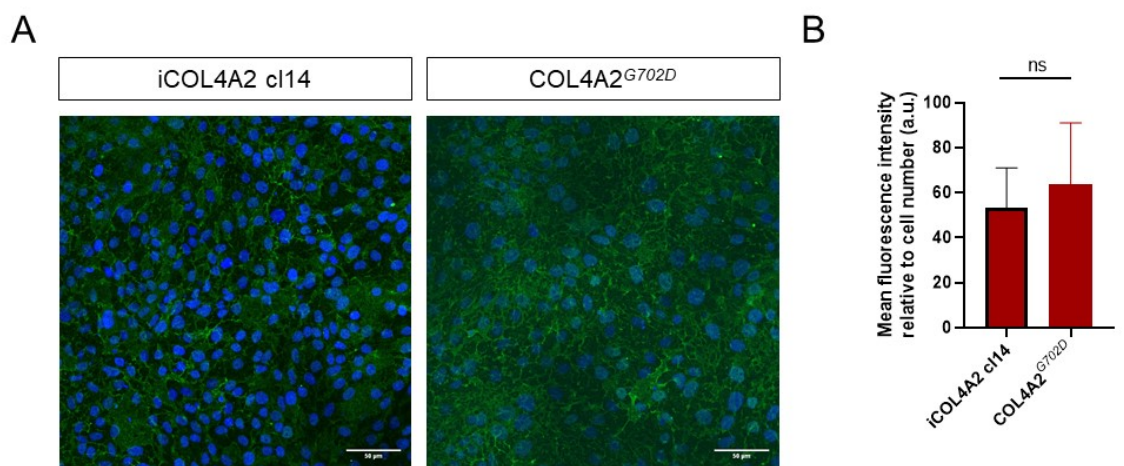
Figure 4.32 Collagen IV immunocytochemistry in iCOL4A2 cl14 and COL4A2^{G702D}: (A) Immunocytochemistry and **(B)** quantification, images are representative, scale bar is 50μm, n=3, error bars are mean +/- SD
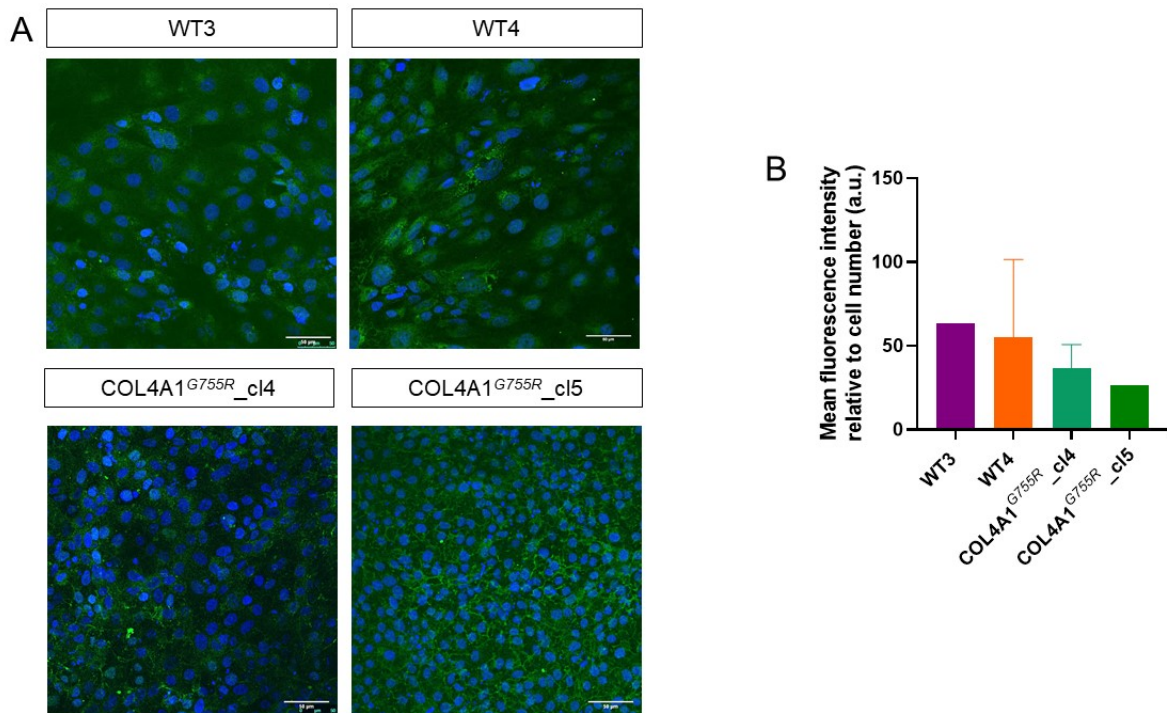
Figure 4.33 Collagen IV immunocytochemistry in WTs and COL4A1^{G755R}: (A)
Immunocytochemistry **(B)** quantification, WT3 and COL4A1_cl5 n=1, WT4 and COL4A1_cl4
n=2, error bars are mean +/- SD

4.7 Altered MMPs as a potential mechanism in COL4A1/2 SVD

So far, results have shown tight junction and collagen IV abnormalities. It is currently difficult
to discriminate if there is less deposition of collagen IV or the total protein level is reduced.
We hypothesis that degradation of collagen IV could play a role, since MMPs have been
shown to be involved with blood-brain barrier breakdown [155,156] and are able to degrade tight
junctions [171,172]. Notably, occludin has been reported as a target of MMP2 and 9[175,176] and
reductions in occludin have been associated with an increase in MMP14[177]. Therefore,
MMPs were investigated as a potential mechanism since they play a key role in extracellular
matrix remodelling.

4.7.1 qRT-PCR reveals COL4A1/2 mutation-specific differences in MMPs

Some MMPs that play a key role in stroke[173] and SVD-induced VCI[155] (MMP1,2,9 and 14)
were assessed using qRT-PCR. There is a non-significant trend of increased *MMP9* in
COL4A2^{G702D} relative to isogenic controls (**Figure 4.34A**). This trend is also observed in

COL4A1^{G755R} relative to WTs (**Figure 4.34B**). Moreover, *MMP2* and, more moderately, *MMP14* is increased in COL4A1^{G755R} but this is not consistent with COL4A2^{G702D}.
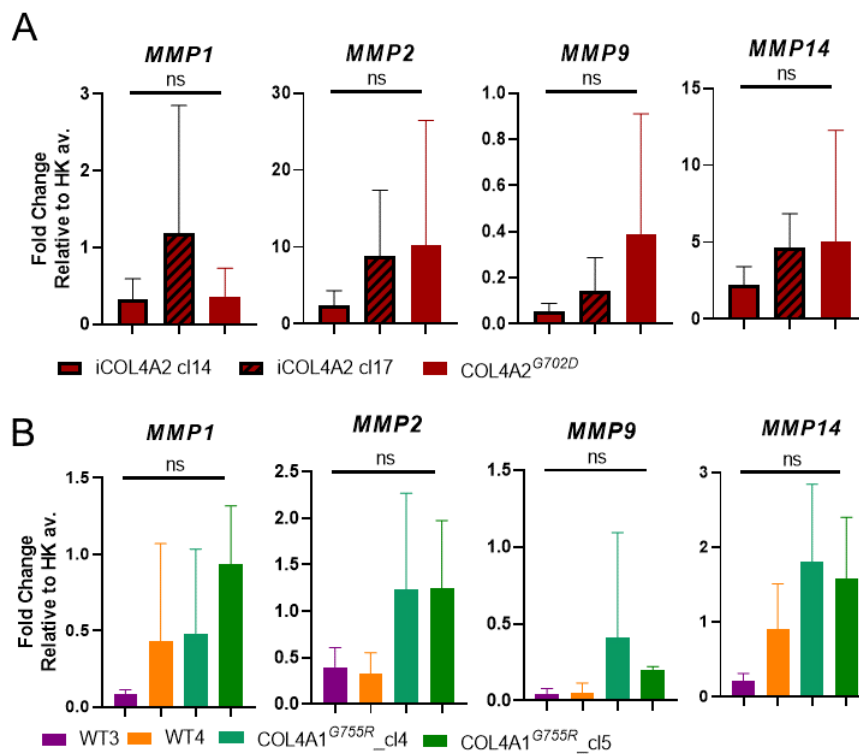
Figure 4.34 qRT-PCR for MMPs: (A) COL4A2^{G702D} and isogenic controls and **(B)** COL4A1^{G755R} and WTs, relative to relative to housekeeping average (GAPDH and PBGD), n=3, error bars are mean +/- SD

TIMPs, which function in conjunction with MMPs to alter the extracellular matrix, were also assessed with qRT-PCR. Here, there are no observable trends in COL4A2^{G702D} relative to isogenic controls (**Figure 4.35A**). In the case of COL4A1^{G755R}, cl4 and cl5 display increased TIMP2 and TIMP3 mRNA expression (**Figure 4.35B**). Interestingly, TIMP2, which is a key regulator of MMP2[368], is also elevated (**Figure 4.34B**).
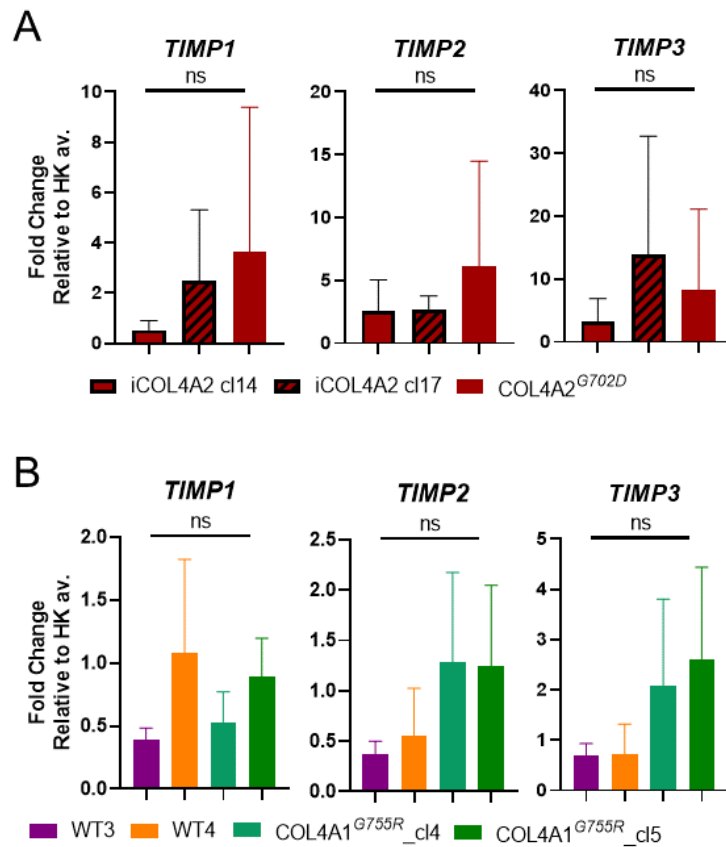
Figure 4.35 qRT-PCR for TIMPs: (A) COL4A2^{G702D} and isogenic controls and **(B)** COL4A1^{G755R} and WTs, relative to relative to housekeeping average (GAPDH and PBGD), n=3, error bars are mean +/- SD

4.7.2 MMP antibody array reveals increased MMP9 in COL4A2^{G702D}

Since mRNA levels are only indicative of protein changes, an antibody array with multiple targets (MMP1,2,3,8,9,10,13 and TIMP1,2,4) was used to assess MMP levels in WT1 and COL4A2^{G702D} hiPSC-BMEC. MMP9 is 2.8-fold higher in COL4A2^{G702D} relative to WT1 (**Figure 4.36**). This is consistent with mRNA expression in which MMP9 is increased in COL4A2^{G702D} relative to isogenic controls, although is only suggestive, not indicative of protein activity (**Figure 4.34A**). However, protein analysis with the isogenic controls would be required to confirm this association.
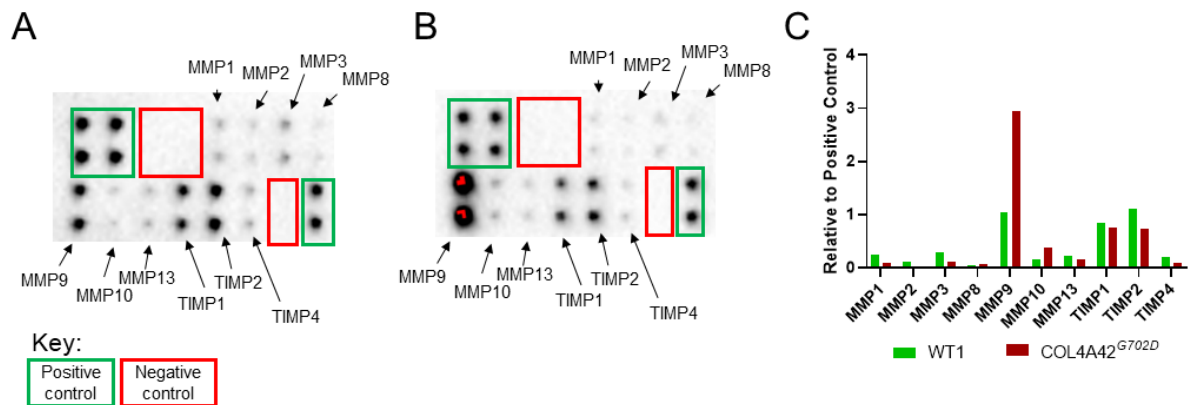
Figure 4.36 MMP antibody array: (A) WT1 BMEC and **(B)** COL4A2^{G702D} BMEC, **(C)** relative quantification, 10 second exposure (performed with Dominika Krzyzanska)

4.7.3 Western blot

A western blot for MMP14 was performed to verify MMP14 levels seen increased in COL4A1^{G755R} by qRT-PCR (**Figure 4.31**). MMP14 is increased in COL4A2^{G702D} relative to isogenic 14 (**Figure 4.37A,B**). However, MMP14 was not increased in COL4A1^{G755R}_cl5 relative to WTs (**Figure 4.37C,D**).
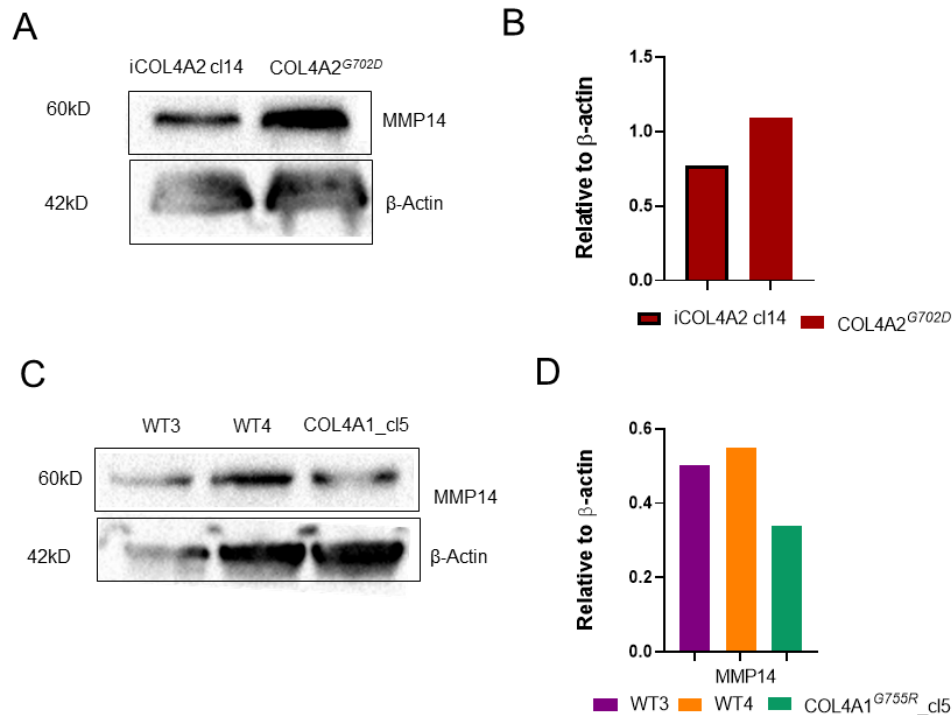
Figure 4.37 Western blot for MMP14 and housekeeping β-actin in hiPSC-BMEC: (A)
COL4A2^{G702D} and isogenic 14 and **(B)** relative quantification **(C)** COL4A1^{G755R} and WT and
(D) relative quantification; n=1. The blot is the same as that used for Figure 4.28, and has
been blotted for additional proteins.

4.8 Inhibition of MMPs increases BMEC marker expression

MMPs have been shown to be raised at RNA and protein level with COL4A1^{G755R} and
COL4A2^{G702D} hiPSC-BMEC. Two different strategies were taken to assess the effect of
inhibition of MMPs on tight junction levels.

4.8.1 Doxycycline pan-inhibition of MMPs

The tetracycline antibiotic Doxycycline, acts as a pan-inhibitor of MMPs[187]. It elicits its
inhibitory function by binding to MMPs and changing how they interact with their targets[369].
Its potential therapeutic benefit has been explored in the context of skeletal muscle injury[166],
traumatic brain injury[188] and improving outcomes in the SHRSP model[187].

hiPSC-BMEC sub-cultured onto collagen IV and fibronectin were treated for 4 days with 5µM
Doxycycline. qRT-PCR was performed for specific BMEC markers (**Figure 4.38**). mRNA of
OCLN was increased in all three lines upon treatment with Doxycycline (**Figure 4.38**)
relative to the control (untreated samples) and *CLDN5* was increased in COL4A1_cl4 and
cl5 but not WT3.
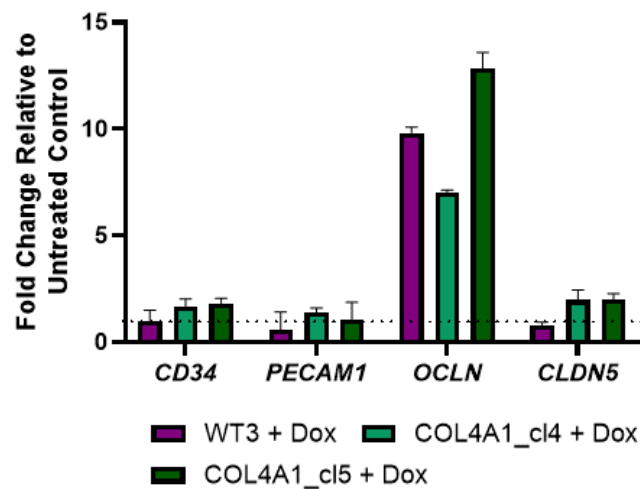
Figure 4.38 qRT-PCR following four days of treatment with 5µM of Doxycycline: qRT-PCR for *CD34*, *PECAM1*, *OCLN* and *CLDN5;* the dashed line depicts fold change of 1.0 (e.g. no change from the untreated sample) n-1; error bars are technical triplicates

Although an increase in *OCLN* was observed in the treated sample, large cell death was observed, limiting the cell lysate yield for western blot. Hence, the concentration of Doxycycline was reduced to 2.5µM. qRT-PCR revealed an increase in *CLDN5* in WT4 and COL4A1_cl5 (**Figure 4.39A**). Interestingly, there was no increase in *OCLN* compared to treatment with 5µM Doxycycline, suggesting this could be a dose-dependent response.

In COL4A2^{G702D} and iCOL4A2 cl14, *PECAM1* is increased greatly in COL4A2^{G702D} compared to the isogenic (**Figure 4.39B**). *PECAM1* was previously shown to be raised in COL4A2^{G702D} compared to iCOL4A2 cl4 and cl17 (**Figure 4.9**), suggesting it could play a role in the disease process. Along with this, there are changes to all other markers, *CD34*, *OCLN*, *CDH5* and *CLDN5* (**Figure 4.39B**).

Since transcription of Stromelysin (MMP3) has been shown to be affected by Doxycycline treatment[369,370], qRT-PCR was also performed on a panel of MMPs and TIMPs. In WT4 and COL4A1_cl4 and cl5, MMPs overall were decreased (less than 1.0-fold change from the untreated sample; **Figure 4.39C**). However, in iCOL4A2 cl14, MMP1, MMP2 and MMP14 were all increased upon Doxycycline treatment (**Figure 4.39D**). This suggests that alternate mechanisms could be involved in the different mutations. However, all qRT-PCR experiments were performed once so would need to be repeated to confirm these findings.

Cell lysate of Doxycycline treated and untreated samples was analysed with western blot (**Figure 4.39E and F**). In concordance with the mRNA expression, claudin-5 protein level was increased in all lines upon treatment with Doxycycline **(Figure 4.39E)**.
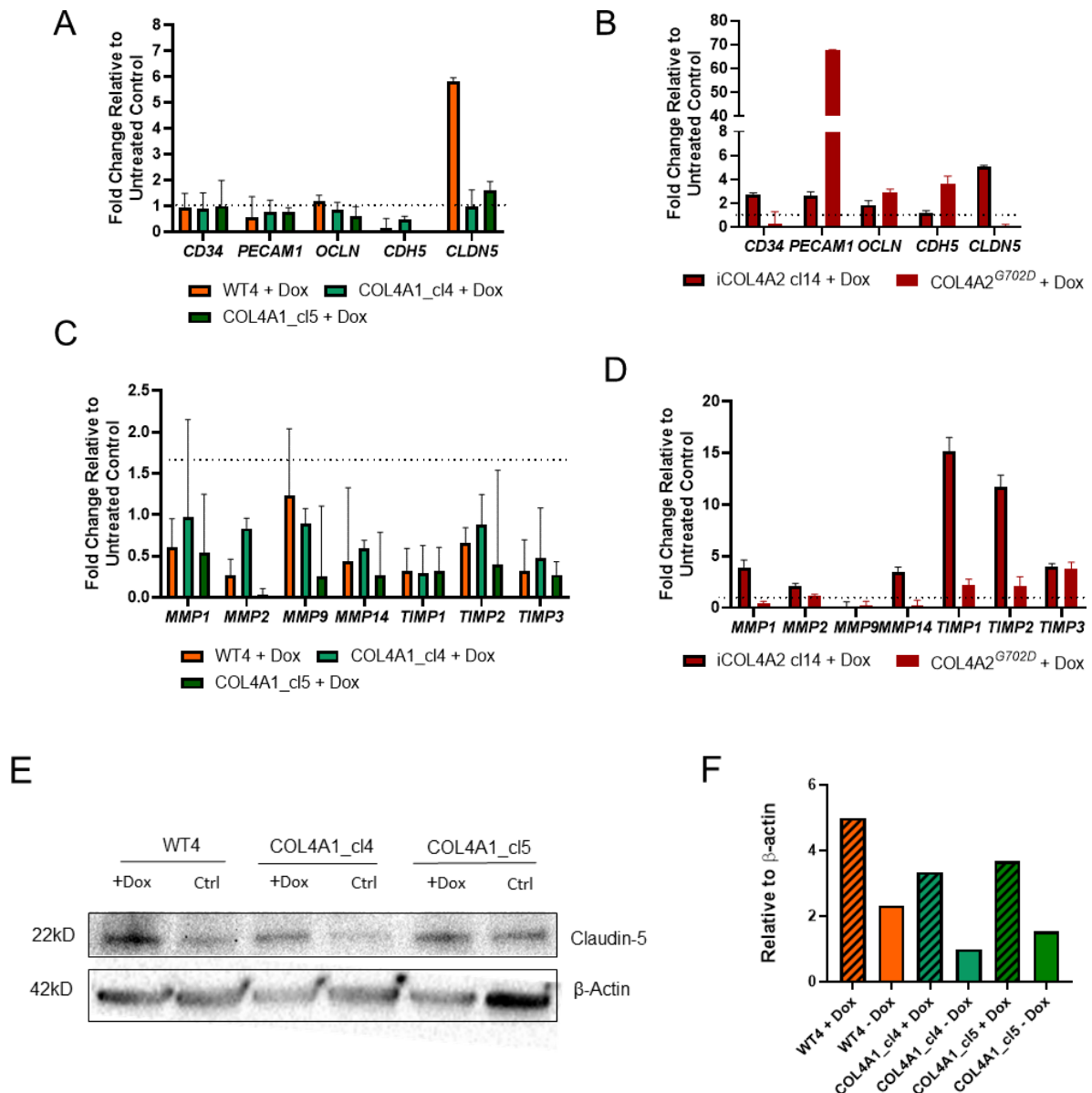
Figure 4.39 Treatment of hiPSC-BMEC for four days with 2.5µM of Doxycycline: qRT-PCR for BMEC markers in **(A)** COL4A1^{G755R} and WT **(B)** COL4A2^{G702D} and isogenic; qRT-PCR for MMPs in **(C)** COL4A1^{G755R} and WT **(D)** COL4A2^{G702D} and isogenic; (the dashed line depicts fold change of 1.0 (e.g. no change from untreated), error bars are technical triplicates **(E)** western blot for claudin-5 and β-Actin in COL4A1^{G755R} and WT and **(F)** quantification of (E) relative to β-Actin, n=1

4.8.2 siRNA-mediated gene silencing of MMP14 in COL4A2^{G702D}

Caution must be taken with the use of global treatments such as Doxycycline, given that the action of MMPs is finely balanced between beneficial and detrimental effects[189]. Hence, a more targeted approach was sought.

MMP14 was chosen because it is increased in COL4A2^{G702D} compared to iCOL4A2_cl14 (**Figure 4.37**). Previously in our group, 40nM MMP14 siRNA was shown to reduce the mRNA expression of MMP14 in hiPSC-BMEC (Dominika Krzyzanska, *Unpublished*). This was repeated with siRNA gene silencing of MMP14 in COL4A2^{G702D} and the isogenic control iCOL4A2_cl14. A concentration of 40nm siRNA elicited minimal knockdown of the RNA level of MMP14, compared to scrambled siRNA in both COL4A2^{G702D} and iCOL4A2_cl14 (**Figure 4.40**).
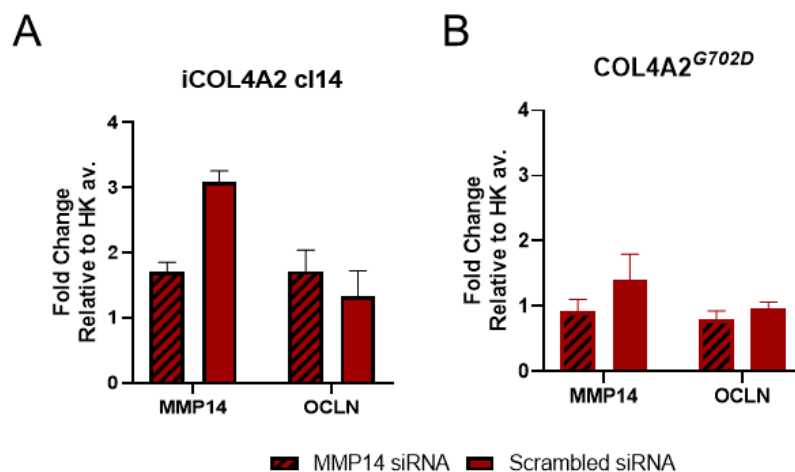
Figure 4.40 qRT-PCR following single a 24hr treatment with 40nm siRNA for MMP14 or scrambled (control): qRT-PCR for *MMP14* and *OCLN* in **(A)** iCOL4A2 cl14 and **(B)** COL4A2^{G702D}, n=1, error bars are technical triplicates

Since there was little cell death, the concentration was increased to 100nm for both MMP14 and scrambled siRNA. For western blot, hiPSC-BMEC were transfected twice with siRNA and collected after 72hrs. Western blot showed there was no reduction in MMP14 on treatment with MMP14 siRNA compared to scrambled siRNA in both the iCOL4A2 cl14 and COL4A2^{G702D} samples, compared to the scrambled control (**Figure 4.41**). Although, there

was an increase in occludin and claudin-5 upon MMP14 siRNA treatment. However, the experiment would need to be repeated to confirm these findings.
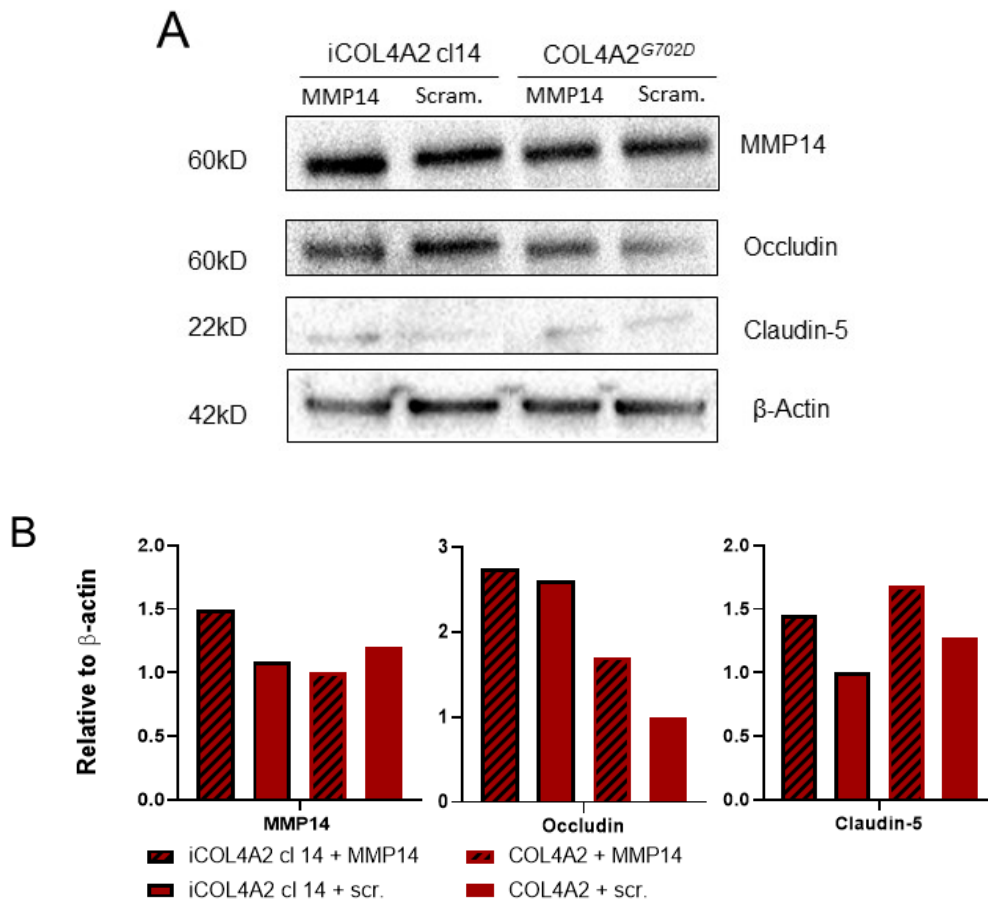
Figure 4.41 Western blot following of two treatments with 100nm siRNA for MMP14 or scrambled (control): Western blot for MMP14, occludin and claudin-5 in iCOL4A2_cl14 and COL4A2^{G702D} **(A)** and quantification **(B),** n=1

Since no reduction in MMP14 protein was observed following siRNA treatment, the timing of siRNA treatment should be explored, by transfecting immediately post sub-culture, or even during the single cell suspension phase prior to plating.

4.8 Preliminary characterisation of iCOL4A1 hiPSC-BMEC

Moving forward, WT lines should be replaced with the newly generated iCOL4A1 clones. To determine the capacity of isogenic clone 6 (iCOL4A1_cl6) to differentiate, a single BMEC differentiation was performed with iCOL4A1_cl6 in parallel with the line from which it was

derived (COL4A1_cl4), as described previously. Both lines were able to differentiate in BMEC positive by immunocytochemistry for VE-Cadherin, GLUT-1, occludin and claudin-5 (**Figure 4.42A**). By qRT-PCR, iCOL4A1_cl6 displayed higher maker expression than COL4A1_cl4 (**Figure 4.42B**). A comparable pattern was observed in TEER, although iCOL4A1_cl6 displayed higher TEER for a longer duration than COL4A1_cl4 (**Figure 4.42C**). Lastly, NaFl leakage was greater in COL4A1_cl4 than in iCOL41_cl6 throughout the time course (**Figure 4.42D**) and at the end point where a greater % of the bank value was observed in COL4A1_cl4 than the isogenic (**Figure 4.42E**).
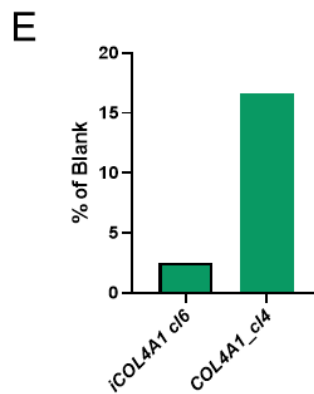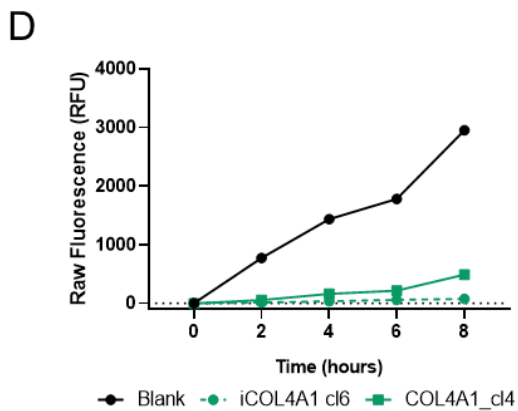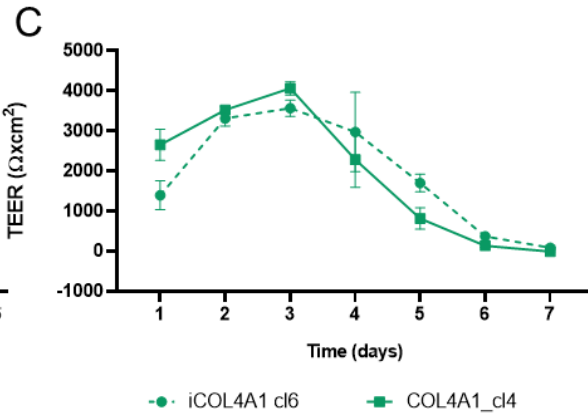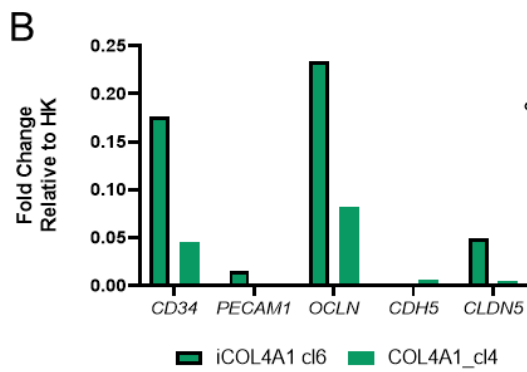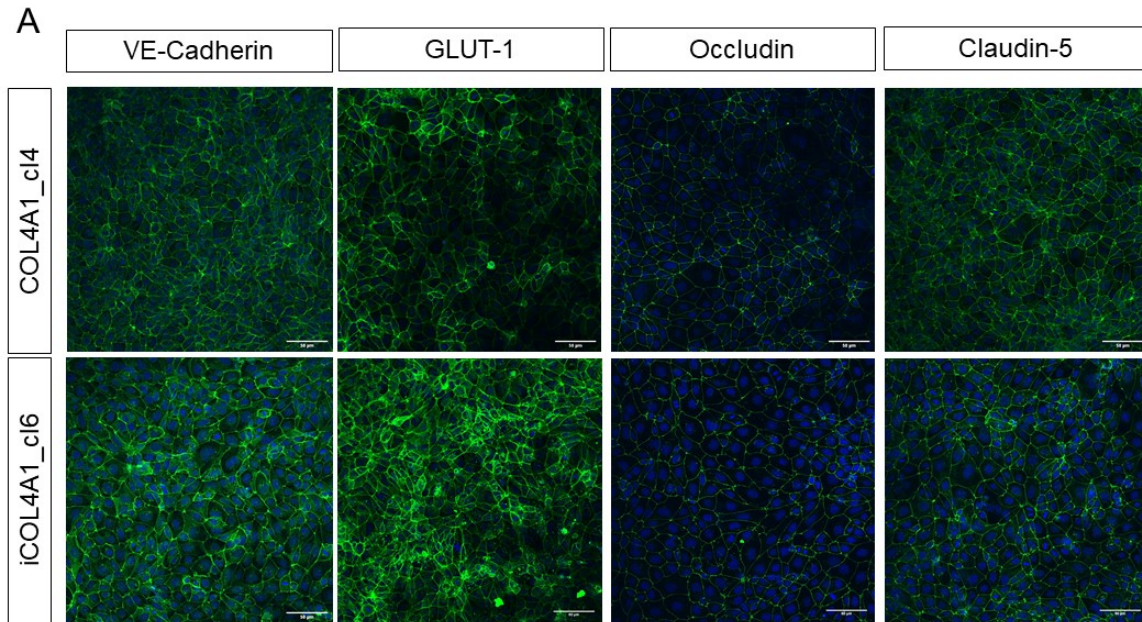
Figure 4.42 Characterisation of iCOL4A1 hiPSC-BMEC: isogenic clone 6 hiPSC-BMEC differentiation in parallel with COL4A1_cl4 **(A)** immunocytochemistry, scale bar is 50µm **(B)** qRT-PCR for BMEC markers relative to HK (*GAPDH*) **(C)** TEER **(D)** NaFl time course and **(E)** as a % of the blank at 8 hours.

4.9 Chapter summary

To summarise, this chapter has demonstrated that COL4A2^{G702D} and COL4A1^{G755R} hiPSC are able to differentiate into functional BMEC. Phenotypic abnormalities have been identified between COL4A1/2 and control hiPSC-BMEC. Firstly, the R123 efflux assay established impaired function in COL4A1/2 BMEC, indicative of altered function. In patients this could result in infiltration of small molecules across the BBB, which are not removed by P-gp efflux.

Secondly, tight junction defects, shown by increased percentage of discontinuous occludin junctions and mis-localisation of claudin-5 and reduced collagen IV, pointed towards a role for MMPs in COL4A1/2 SVD pathophysiology. This is relevant to SVD patients, in which MMPs are elevated[155]. Aberrations in mRNA expression and protein level of MMPs have been identified, with different MMPs possibly playing a role in COL4A1 (MMP2 and 9) and COL4A2 (MMP9 and 14). These findings bear relevance to previous findings in wider cerebrovascular disease for MMP2,9 and 14[175,177].

Doxycycline pan-inhibition showed an increase in claudin-5 in western blot compared to the untreated control. qRT-PCR also showed an increase in occludin in WT and COL4A1^{G755R}. This suggests interfering with MMP function can have a positive effect on tight junction proteins. However, MMP14 siRNA showed minimal reduction of MMP14 at the mRNA level and little or no reduction at the protein level. Therefore, further investigation is needed to identify the key MMP propagating the disease phenotype and to pinpoint an appropriate method of inhibition.

Overall, this chapter has demonstrated disease-relevant findings that could advance our understanding of COL4A1/2 SVD.

Chapter 5: Triple co-culture *in vitro* BBB model development

5.1 Aims of this chapter

This chapter describes the differentiation of hiPSC into astrocytes and the use of the these, along with MC, to generate a triple co-culture BBB model. For hiPSC-astrocyte production, an intermediate NSC population was generated using an adapted protocol[286], before utilising an astrocyte medium[336] to direct NSCs into astrocytes. The NSC protocol has a high failure rate, evident in the inability to generate NSCs across multiple WT lines. hiPSC-astrocytes were then combined with hiPSC-BMEC (Chapter 3) into a double co-culture. In addition, hiPSC-MC (provided by Dr Alex Granata) were used to generate a triple co-culture *in vitro* BBB model. The building of the BBB model began in a commercially available Transwell® system. Following initial experiments with WT lines, COL4A1/2 hiPSC-BMEC were combined into a co-culture model with MC originating from the same lines; hiPSC-astrocytes were not able to be generated from any disease lines.

In order to generate a more physiologically relevant model, shear stress was introduced, followed by pilot experiments of a microfluidic BBB-on-a-chip (in conjugation with Dr Yan Yan Shery Yuang and Dr Magda Gerigk, Engineering Department, University of Cambridge).

5.2 Differentiation of hiPSCs to astrocytes, through a neural stem cell intermediate

Astrocytes are known to play a key role in BBB formation and maintenance[101] and have been shown by others to increase barrier properties of hiPSC-BMEC *in vitro* [77]. Here, using two WT lines, hiPSCs were first differentiated to NSCs as an adherent monolayer, before further differentiation into astrocytes.

5.2.1 Differentiation of hiPSC into NSC

An existing protocol[286] was modified to its current form (Ben Newman, *unpublished*) and used to differentiate two WT (WT1 and WT2) lines into NSC (**Figure 1**). The NSC protocol has a high failure rate, since NSCs were not able to be generated from WT3 and WT4 lines.
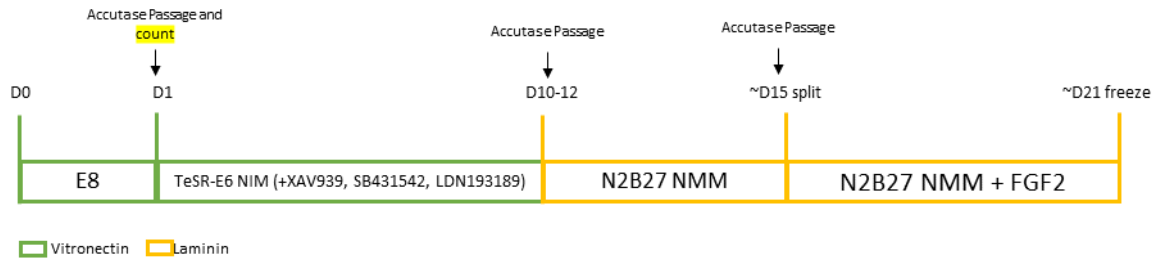
Figure 5.1 Protocol for hiPSC to NSC differentiation: Cells are plated in E8 media on Vitronectin before being treated for 10-12 days with NIM, before plating onto Laminin in NMM.

WT1 NSC are positive to PAX6 and NESTIN (**Figure 5.2A**) by immunocytochemistry as well as across two differentiations in qRT-PCR (**Figure 5.2B**), but WT2 NSC have reduced NESTIN (*NES*) expression (0.47-fold of hiPSC) compared to WT1 (18.8-fold). In WT1 NSC, some residual hiPSC remain, as can be seen at high magnification (**Figure 5.2A**), suggesting that the population is heterogenous.
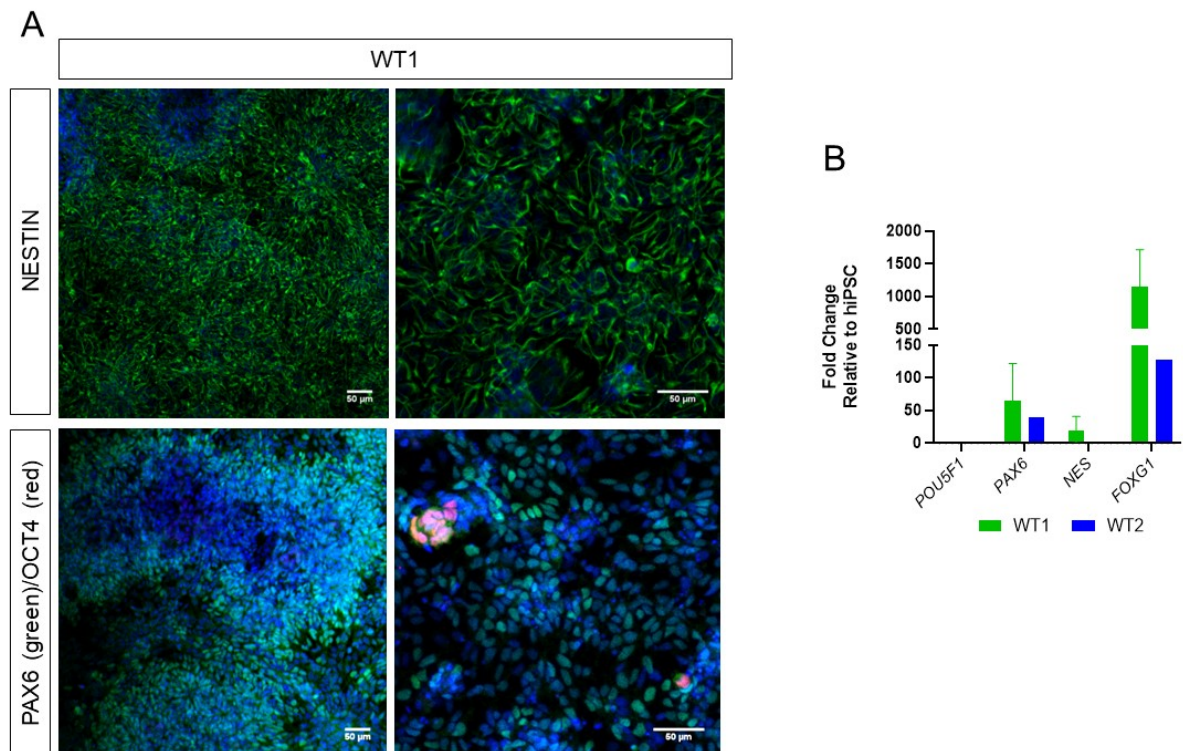
Figure 5.2 WT1 NSC Immunocytochemistry: (A) Nestin and PAX6/OCT3/4, **(B)** qPCR for pluripotency marker *POU5F1* (OCT3/4), NSC markers *PAX6*, *NES* (Nestin) and *FOXG1* for WT1 (n=2 differentiations) and WT1 (n=1 differentiation). Scale bar is 50µm.

5.2.3 Differentiation of NSC into Astrocytes

WT1 and WT2 NSCs were further differentiated into astrocytes[336] by serial passaging in media containing specific cytokines (CNTF, BMP4 and FGF-2; **Figure 5.3**).
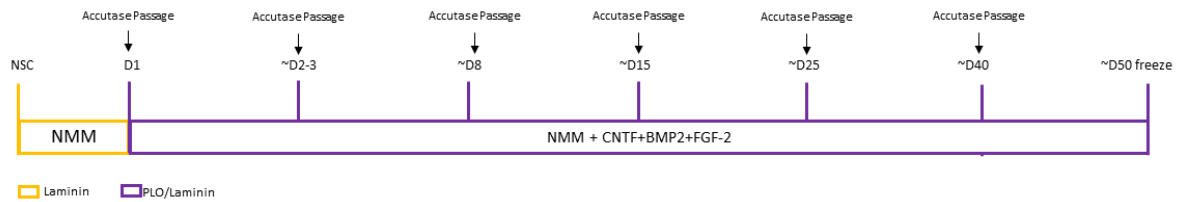
Figure 5.3 Differentiation of NSC into Astrocytes: cells are plated into NMM on Laminin before splitting to single cells and seeding onto PLO/Laminin in astrocyte media.

NSC markers PAX6 and FOXG1 reduce immediately after one passage in astrocyte media (**Figure 5.4**). NESTIN does not show the same immediate reduction and fluctuates across the astrocyte passages, suggesting this is not a pure homogenous culture of astrocytes, but contains mixed neural cells.
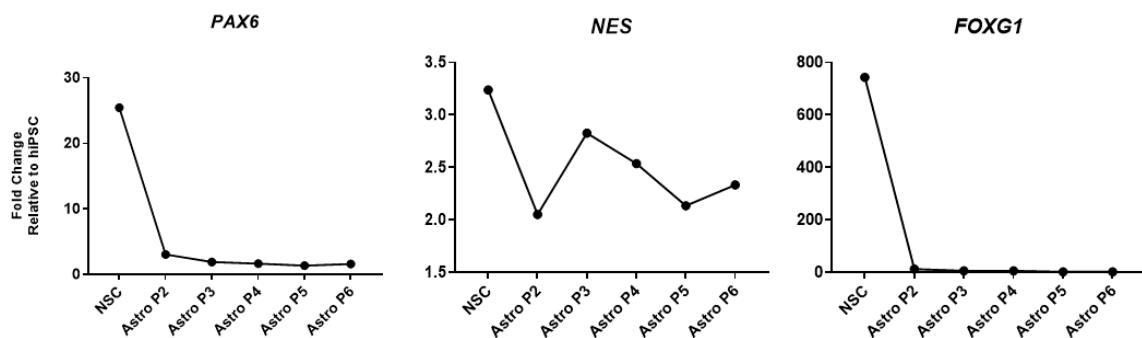
Figure 5.4 qRT-PCR time-course of NSC markers: qRT-PCR for *PAX6*, *NES* and *FOXG1*, abbreviation, P=passage, n=1 differentiation.

Astrocytes are positive for GFAP at P2 (**Figure 5.5A**) and continue to express it through to P6 as they undergo a morphological change with increasing cell size and longer processes. GFAP and CHD5 astrocyte markers show minimal increase overall by qRT-PCR from NSC to P6 Astrocytes, which could suggest that maturity is not reached in these cells (GFAP changes from 3.044-fold in NSCs, to 3.54-fold at P6 of Astrocyte culture; **Figure 5.5B**). In keeping with this, at P2, cells are positive for the neuronal marker βIII Tubulin (**Figure 5.5C**) which also suggests this is a heterogeneous culture of neural and glial cells.
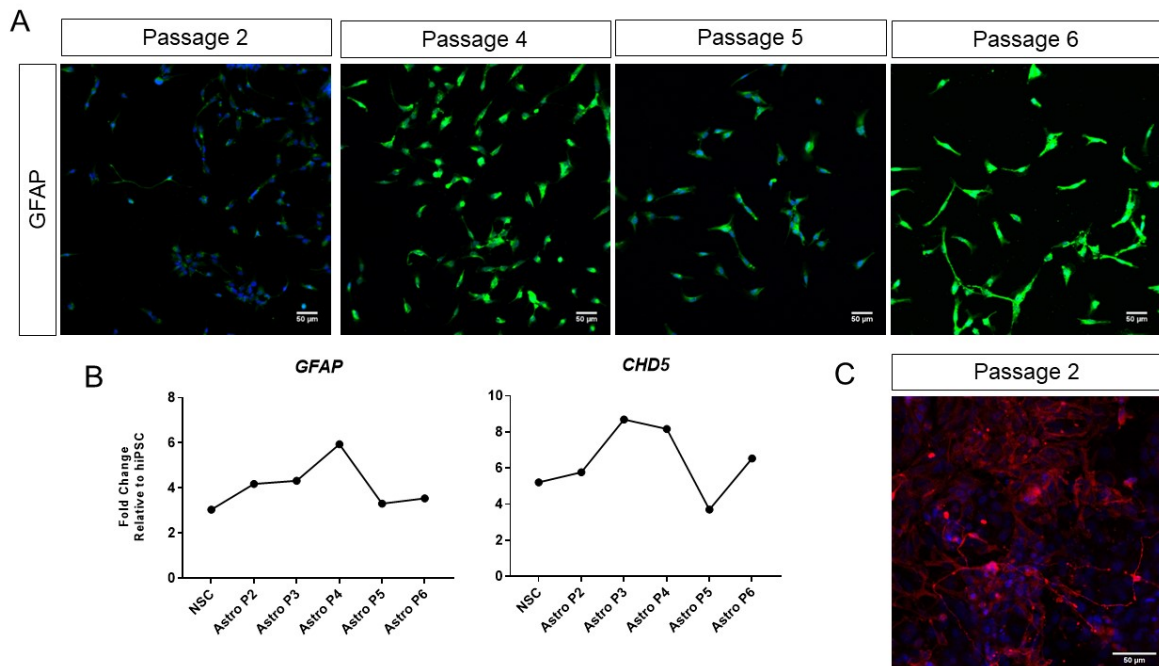
Figure 5.5 Characterisation of astrocytes over a time course: (A) Immunocytochemistry time-course of GFAP, WT1, n=1 differentiation **(B)** qPCR time-course of astrocyte markers, abbreviation, P=passage, n=1 differentiation, **(C)** βIII Tubulin at passage 2, scale bar is 50μm.

End-stage P6 Astrocytes are positive to GFAP, βIII Tubulin and NSC marker NESTIN, by immunocytochemistry (**Figure 5.6A**). WT1 and WT2 astrocytes show high variation by qRT-PCR for NSC makers such as PAX6 and FOXG1 (**Figure 5.6B**). All astrocyte markers are increased, relative to hiPSC, although there is high variation between WT1 and WT2, especially for CHD5 and SLC1A2 (**Figure 5.6C**).
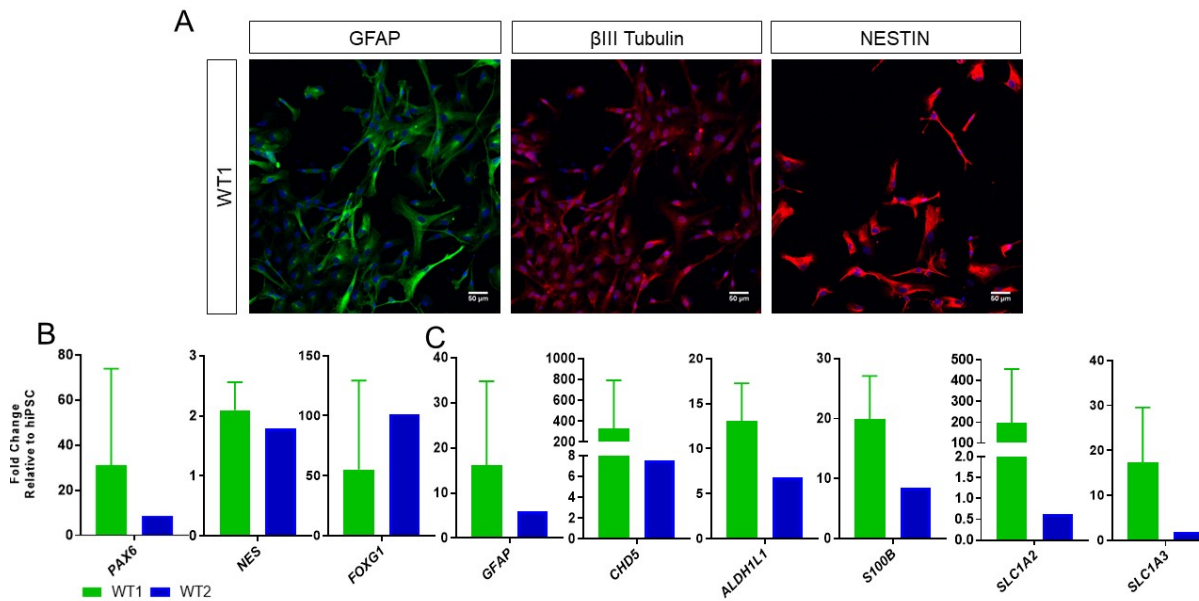
Figure 5.6 Characterisation of hiPSC-Astrocytes at passage 6: WT1 Astrocytes **(A)** immunocytochemistry and qRT-PCR for **(B)** NSC and **(C)** astrocyte markers, n=1, scale bar is 50µm.

5.3 Co-culture development in a Transwell®

hiPSC-mural cells (MC; provided by Dr Alex Granata) were differentiated using a modified neural-crest smooth muscle cell protocol[287,346,347] but display a pericyte-like phenotype, hence they are referred to as MC. hiPSC-MC and/or differentiated hiPSC-astrocytes were combined with BMEC, into a serious of co-culture models, building on previous examples of Transwell® systems in the literature[306,313].

5.3.1 BMEC and Astrocyte co-culture

Astrocytic end feet contacting on BMEC promote barrier properties[101], with previous reports of rat astrocytes increasing hiPSC-BMEC TEER[307]. Moreover, primary astrocyte-conditioned media has been shown to increase electrical resistance of bovine BMEC *in vitro*[371], suggesting astrocytes provided paracellular signals to BMEC. Therefore, hiPSC-astrocytes were added in co-culture with BMEC.

Initially, BMEC were co-cultured with astrocytes, in the bottom of the well, which were physically distant from BMEC on the apical side of the Transwell® (**Figure 5.7A**). Initial experiments demonstrated TEER of WT1 BMEC increased to 1614Ωxcm^2 by day 4 with astrocytes present, compared to 953Ωxcm^2 for BMEC alone (**Figure 5.7B**). Although, co-culture only offered marginally increased barrier properties for 3 days.
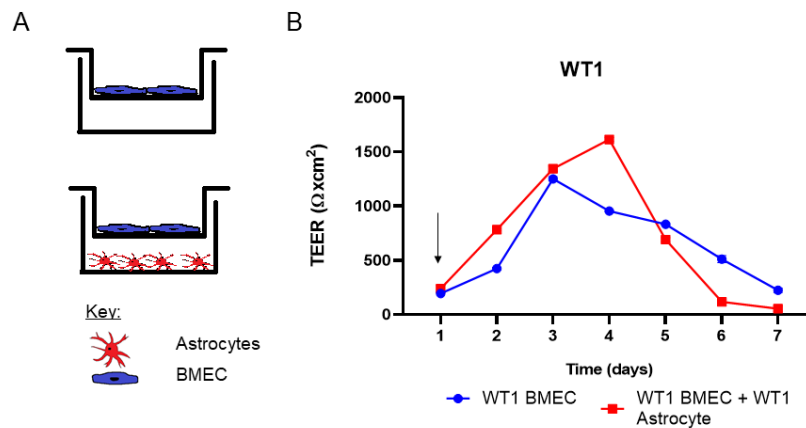
Figure 5.7 WT1 hiPSC-BMEC and astrocyte co-culture: (A) Co-culture set-up with WT1 BMEC and astrocytes **(B)** corresponding TEER**,** n=1, arrow indicates start of co-culture.

In a separate experiment with WT2 BMEC (**Figure 5.8A**), TEER was seen to increase over time (**Figure 5.8B**), up to $3134\Omega xcm^2$, compared to a peak of $2025\Omega xcm^2$ for BMEC alone. However, despite the high TEER value at the point of lysis on day 10, BMEC markers did not increase and *OCLN* (occludin) decreased on co-culture with astrocytes compared to BMEC alone (**Figure 5.8C**). Given that Astrocytes are physically distant from BMEC, the elicited response on co-culture TEER (**Figure 5.8B**), is a paracellular response, in keeping with reports in the literature[371].
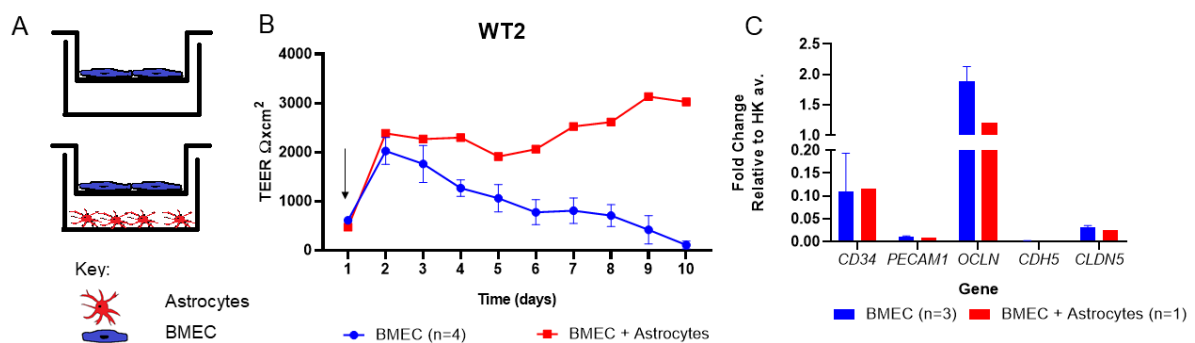
Figure 5.8 WT2 hiPSC-BMEC and astrocyte co-culture: (A) Co-culture set-up with WT2 BMEC and astrocytes **(B)** corresponding TEER, arrow indicates start of co-culture and **(C)** qRT-PCR of **B,** n=1.

5.3.2 BMEC and MC co-culture

Another key cell type that plays a role in the neurovascular unit are pericytes[372], which promote maintenance of the BBB. *In vitro* experiments with hiPSC-BMEC have suggested

that pericytes increase TEER more than astocytes[77], although others report little effect of pericytes[353]. Moreover, in an *in vitro* model of ischaemic stroke, pericytes responded by migrating away from BMEC, possibly as a beneficial role to assist vascular remodelling[373,374].

Here, as hiPSC were differentiated using a modified neural-crest smooth muscle cell protocol[287,346,347] but display a pericyte-like phenotype, they are referred to as mural cells (MC). MC were used at different stages of the differentiation protocol (**Figure 1.12**)[346]. Cells in the 12-day PDGF-BB + TGF-β1 treatment phase are referred to as 'PT'. Between days 6 and 12 of PT, cells are consider phenotypically plastic and mRNA expression of *CNN1* increases (Dr Alex Granata, *Unpublished*) and by day 12 these cells are positive for *ACTA2*, *TALGN* and *MYOCD*[288] suggesting these cells are maturing. Following PT, cells are cultured in DMEM/F12 with 10% FBS. At this stage, the proliferation of MC increases and the mRNA level of *ACTA2*, *TALGN* and *CNN1* decreases[288]. Mature MC can be cultured long-term for up to 30 days in DMEM/F12 with 10% FBS.

Since MC are typically cultured on 0.1% gelatin[287,346,347], initial experiments were conducted with MC plated in the bottom of the well on gelatin (**Figure 5.9A**), and BMEC plated on the apical side of a Transwell® above.

WT4 BMEC TEER remains unchanged on co-culture with MC, although it plateaus around 440Ωxcm^2 by day 6 (**Figure 5.9B**), when BMEC were lysed for qRT-PCR analysis. Gene expression data (**Figure 5.9C**), suggest that co-culture with MC does not change *CD34* and *PECAM1* expression, compared to BMEC alone, although co-culture may increase *CLDN5*, but this would need to be repeated to confirm the trend.
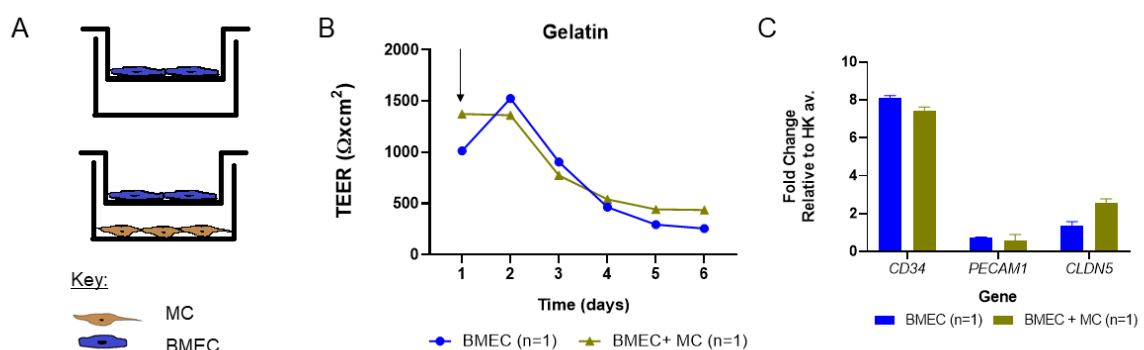
Figure 5.9 WT4 hiPSC-BMEC and MC co-culture: (A) co-culture setup **(B)** WT4 BMEC on 0.1% Gelatin, arrow indicates start of co-culture **(C)** qRT-PCR of **B**, n=1, error bars are technical triplicates

Following this, other matrices were tested, included fibronectin and laminin. Both fibronectin (**Figure 5.10B**) and laminin (**Figure 5.10C**) cultured MC, promote increased TEER compared to BMEC alone, with fibronectin sustaining higher TEER for days 2-6, compared to 2-4 with MC on laminin coating.
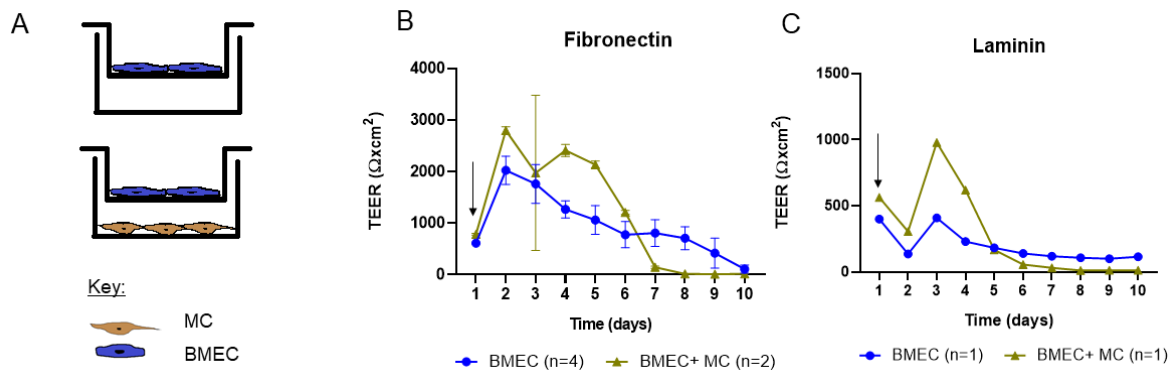
Figure 5.10 WT2 hiPSC-BMEC and MC co-culture: (A) Co-culture set-up with WT2 BMEC alone or with MC **(B)** WT2 with MC on fibronectin and **(C)** WT2 with MC on laminin, arrow indicates start of co-culture.

Also, in keeping with the MC differentiation protocol, cells were maintained in serum (10% FBS) for two to four weeks[287,346,347]. Since longevity of high TEER was not achieved with MC, compared to the one observed with astrocytes, earlier stage MC were used, since they are likely to be more plastic. Cells in the PT media stage, from day 6 onwards were used (PTd6).

PTd6 MC (**Figure 5.11**) had a similar, limited, effect on TEER of the mature cells in serum (**Figures 5.9 and 5.10**). In two separate differentiations of WT4 BMEC, MC co-culture TEER remained greater than BMEC alone for 3-4 days in total (**Figure 5.11B**).
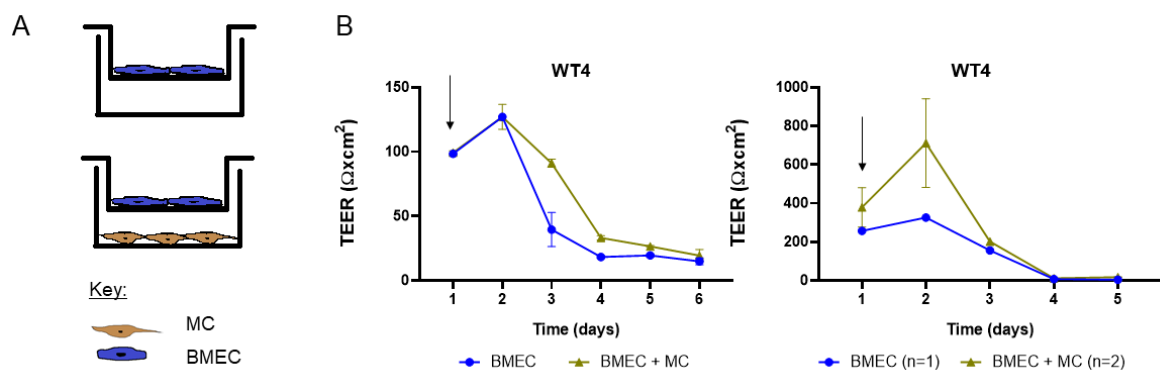
Figure 5.11 WT4 hiPSC-BMEC and MC co-culture: (A) co-culture set up and (**B**) WT4 BMEC with PTd6 MC (two separate experiments), arrow indicates start of co-culture.

5.3.3 BMEC, MC and astrocyte triple co-culture

Given the demonstrated separate effect of astrocytes and MC on BMEC TEER, different combinations of triple co-cultures were tested, in order to determine the optimal arrangement. Firstly, a simple setup was used, in which MC and astrocytes were plated together in the bottom of the well (**Figure 5.12A**). An initial experiment with WT2 BMEC demonstrated that MC co-culture did not increase TEER compared to BMEC alone, but triple co-culture with MC and astrocytes in the bottom of the well increased TEER for 3 days; a peak of 829Ωxcm^2 compared to 119Ωxcm^2 for BMEC + MC and 166Ωxcm^2 for BMEC alone (**Figure 5.12B**).
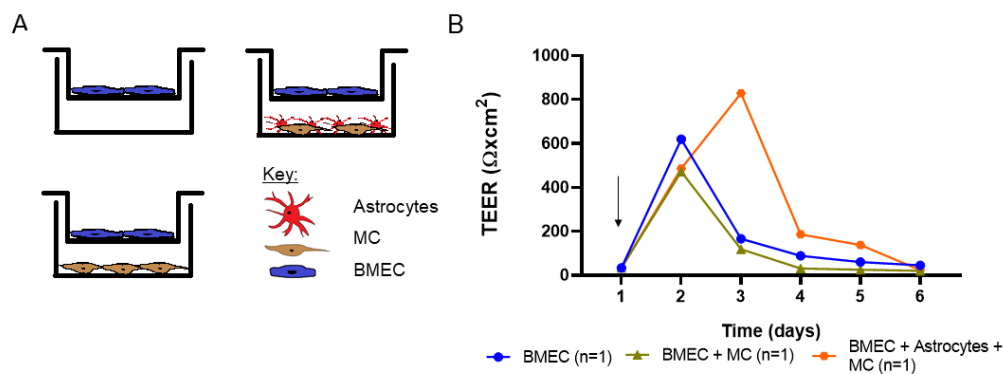
Figure 5.12 WT2 hiPSC-BMEC, astrocyte and MC co-culture: (A) co-culture setup **(B)** WT2 triple co-culture TEER, arrow indicates start of co-culture.

To determine if the triple co-culture more effective than astrocytes alone, a 4-way comparison model was conducted (**Figure 5.13A**). The TEER of BMEC alone peaked at 1052Ωxcm^2, but fell below 500Ωxcm^2 by day 3 (443Ωxcm^2; **Figure 5.13B**). Co-culture with MC peaked at 1050Ωxcm^2 and remained greater than BMEC alone for 6 days.

Strikingly, astrocyte co-culture initially peaked at 1393Ωxcm^2 before reducing until day 9, when resistance increased again to reach 2368Ωxcm^2 by the end of the experiment (**Figure 5.13B**), replicating the upward trend that was seen previously (**Figure 5.8B**). Interestingly, the triple co-culture arrangement maintained TEER across the 15-day time course of the experiment between 342Ωxcm^2 and 771Ωxcm^2; intermediary to values obtained in BMEC + astrocytes and BMEC + MC conditions. Thus, astrocytes in co-culture with MC do not show the same capacity to increase TEER as they do alone (**Figure 5.8B**). Analysis by qRT-PCR at the end of the experiment, revealed a similar trend, in which BMEC marker expression of *PECAM1* and *OCLN* was increased on co-culture with astrocytes but not in the triple co-culture (**Figure 5.13C**), whereas *CD34* reduced on co-culture. Astrocytes at the end of the

15-day experiment display positivity for astrocyte marker GFAP, but also neural marker βIII tubulin (**Figure 5.13D**), suggesting the population is a mixed pool of neural/glial cells, as previously seen with astrocytes not in co-culture (**Figure 5.6**).
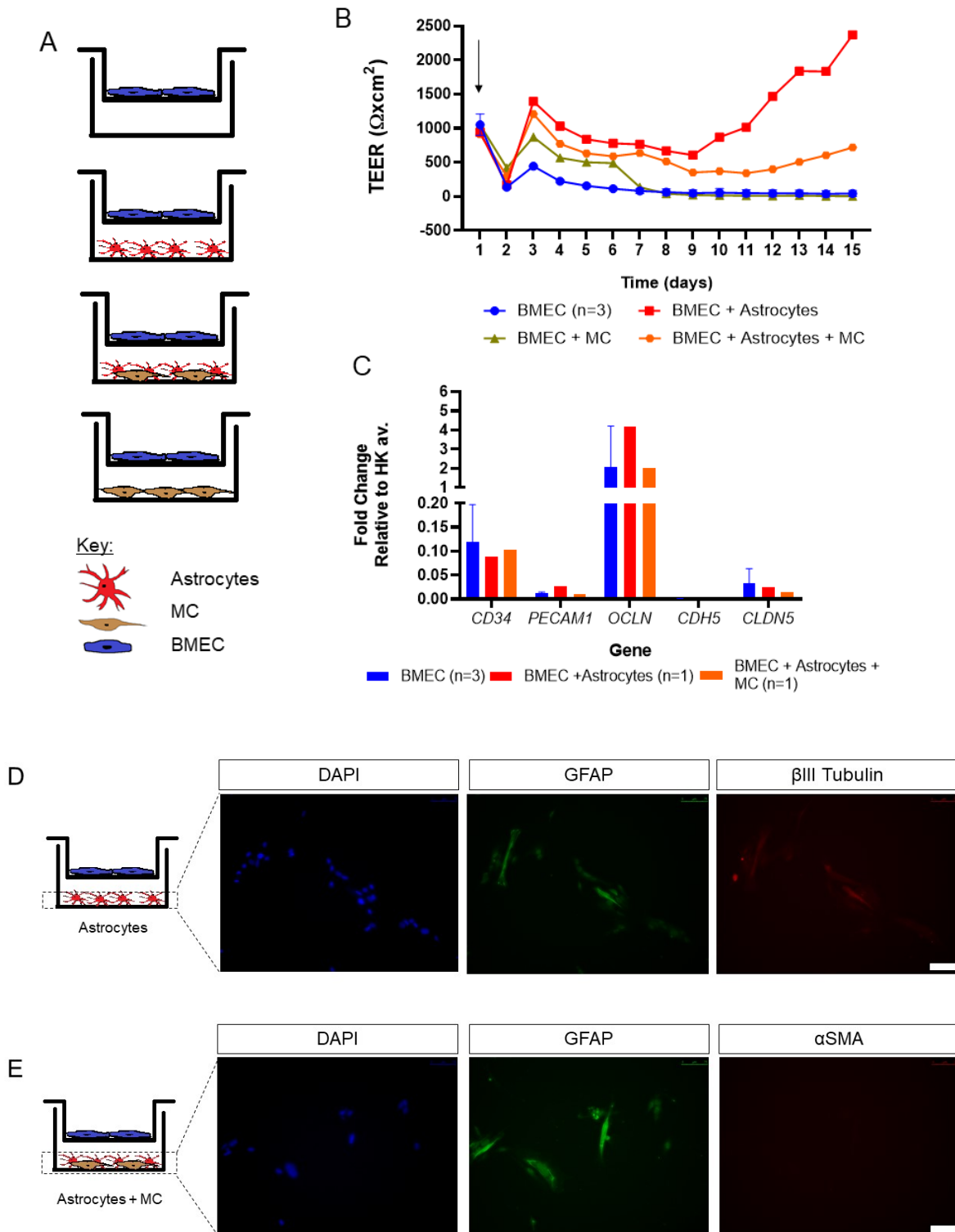
Figure 5.13 WT2 hiPSC-BMEC, astrocyte and MC co-culture: WT2 BMEC **(A)** co-culture set up **(B)** TEER co-culture arrow indicates start of co-culture and **(C)** qRT-PCR **(D)** double

co-culture astrocytes exposed to BMEC **(E)** astrocytes in separate co-culture; scale bar is 75µm.

In the mixed co-culture of MC and astrocytes, MC were lost by the end point, evident by a lack of αSMA stain (**Figure 13E**). In the triple co-culture (**Figure 13B**), cell death of MC could impair astrocyte growth, hence the TEER is lower than BMEC and astrocyte co-culture. Moreover, astrocytes and MC were cultured in astrocyte media on PLO-Laminin which likely favours astrocytes.

Therefore, to allow separate matrices for astrocytes and MC and following literature examples[65,375], MC were plated onto the basolateral side of the Transwell® before BMEC were added to the apical side (**Figure 5.14**). To do this, the Transwell® was inverted in the safety cabinet and a suspension of MC was placed onto the basolateral side of the Transwell® before leaving cells to attach for 1 hour, observing under the microscope at the conclusion of this incubation period. During this phase, the BMEC cell suspension was counted and then plated onto the apical side of the Transwell® as described previously. This double co-culture was incubated overnight before the Transwell® was removed and place over a well of astrocytes plated 1-2 days previously.
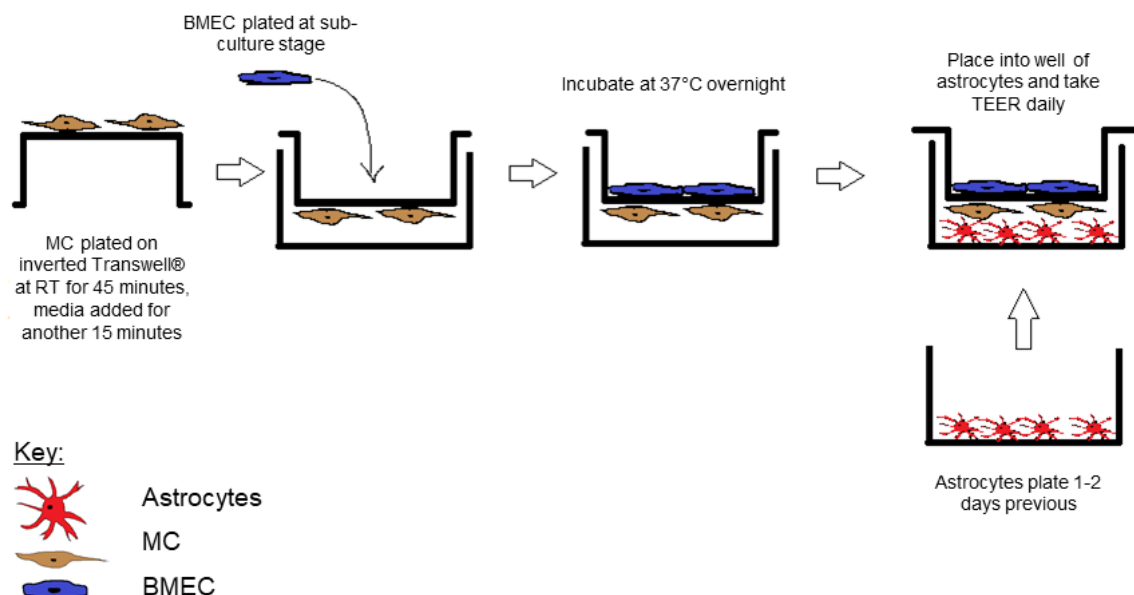
Figure 5.14 Plating strategy for triple co-culture

The triple co-culture plated in this way elicited peak TEER at day 2 of $2976\Omega xcm^2$ compared to $2025\Omega xcm^2$ BMEC alone and $1814\Omega xcm^2$ for BMEC + MC (**Figure 5.15B**). Compared to previous experiments, MC does not increase TEER compared to BMEC alone, in this case appearing to be detrimental. However, it is technically challenging to determine if MC are

indeed present on the underside of the Transwell® throughout the experiment. Although, here all qRT-PCR markers (*CD34*, *PECAM1*, *OCLN*, *CDH5* and *CLDN5*) increase in triple co-culture (**Figure 5.15C**). In the presence of MC on the basolateral side of the Transwell®, astrocytes remained positive for GFAP and βIII Tubulin (**Figure 5.15D**).

Even with low starting TEER, mixed WT triple co-culture elicits an increased TEER at day 2 ($214\Omega xcm^2$ compared to $63\Omega xcm^2$ for BMEC + MC and $5\Omega xcm^2$ for BMEC alone; **Figure 5.16B**). This also suggests a rapid <24hr response by BMEC to co-culture.
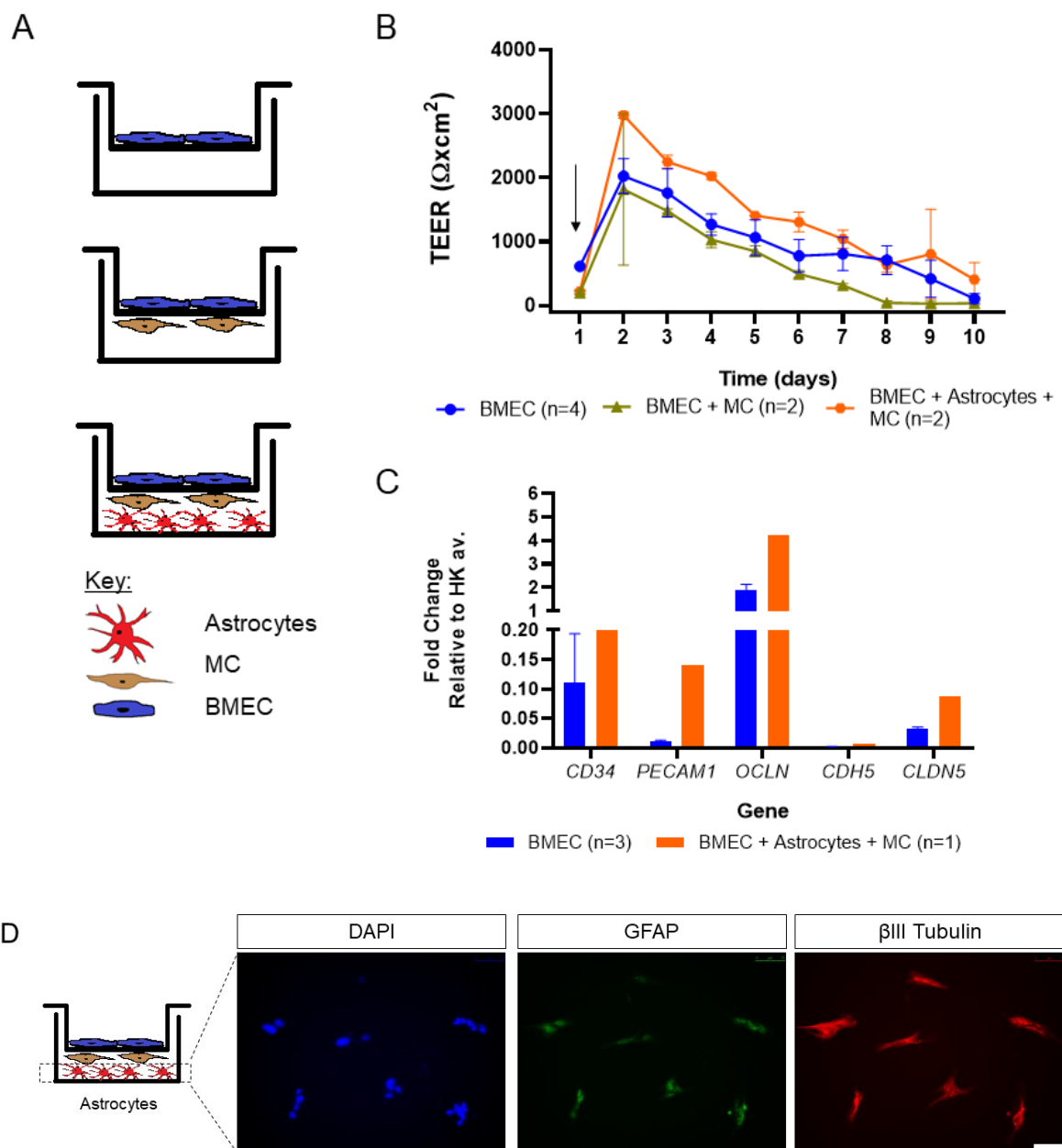
Figure 5.15 WT2 hiPSC-BMEC, astrocyte and MC co-culture: (A) co-culture set up **(B)** WT2 triple co-culture, arrow indicates start of co-culture **(C)** qRT-PCR for BMEC in mono-

and triple- culture **(D)** immunocytochemistry of astrocytes in triple co-culture, scale bar is 75μm.
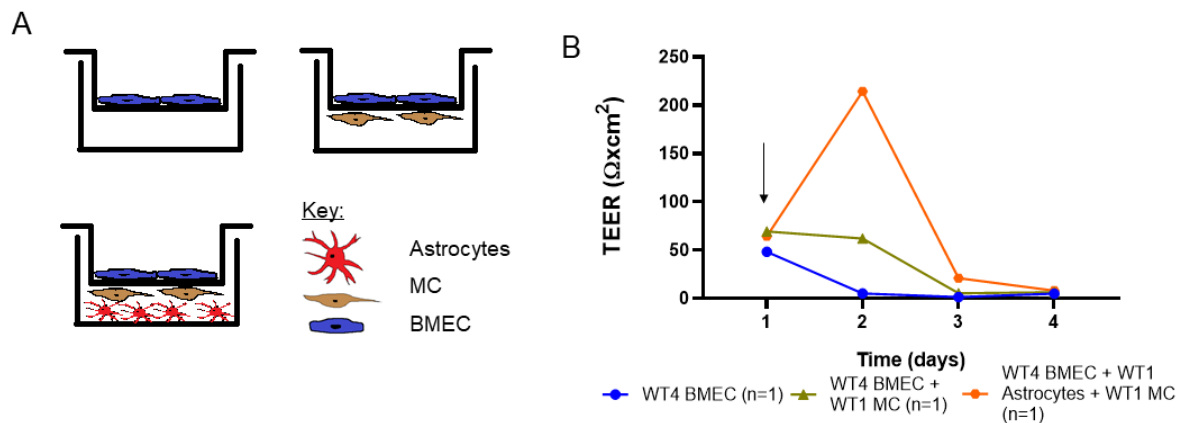
Figure 5.16 WT1 and WT4 hiPSC-BMEC, astrocyte and MC co-culture: (A) co-culture set up **(B)** mixed co-culture of WT4 BMEC and WT1 MC/astrocytes, arrow indicates start of co-culture.

Given the poor cell survival and lack of longevity, further consideration must be given to media and matrix coating, in order to increase survival. In both arrangements with MC, either in mixed co-culture with astrocytes in the bottom of the well, or on the basolateral side of the Transwell®, there is no confirmation the cells remain there after plating, with TEER and immunocytochemistry data suggesting they could be lost shortly after initiation of co-culture.

5.4 Co-culture of COL4A1/2 hiPSC-BMEC with hiPSC-MC

Following development of the Transwell® co-culture system with WT lines, COL4A1/2 BMEC were combined with MC (provided by Dr Alex Granata), into a co-culture set up with BMEC alone or with MC in the bottom of the well (**Figure 5.17A**). hiPSC-astrocytes could not be generated with either disease line, hence only MC were used.

In keeping with previous WT BMEC and MC co-culture, the addition of hiPSC-MC promotes limited short-term increase in TEER values in COL4A2^{G702D} and iCOL4A2 cl14 BMEC (**Figure 5.17B-D**). Even with low TEER (**Figure 5.17C,D**), the same trend and response to MC is observed. Moreover, COL4A2^{G702D} and the iCOL4A2 co-cultures behave similarly, suggesting that diseased MC do not have a negative effect on diseased BMEC. qRT-PCR samples were collected at day 5 and suggest an inverse relationship compared to TEER (**Figure 5.17E,F**). For example, TEER of COL4A2^{G702D} BMEC at day 5 was 30Ωxcm^2 and BMEC + SMC was 297Ωxcm^2, but qRT-PCR results suggest BMEC markers were decreased on co-culture. For the isogenic control, TEER was comparable between BMEC

$(57\Omega xcm^2)$ and BMEC + MC $(95\Omega xcm^2)$ but qRT-PCR values of samples collected from parallel wells (indicated by the dotted lines) on day 5 were either unchanged or, in the case of occludin (*OCLN*), increased (**Figure 5.17F**).
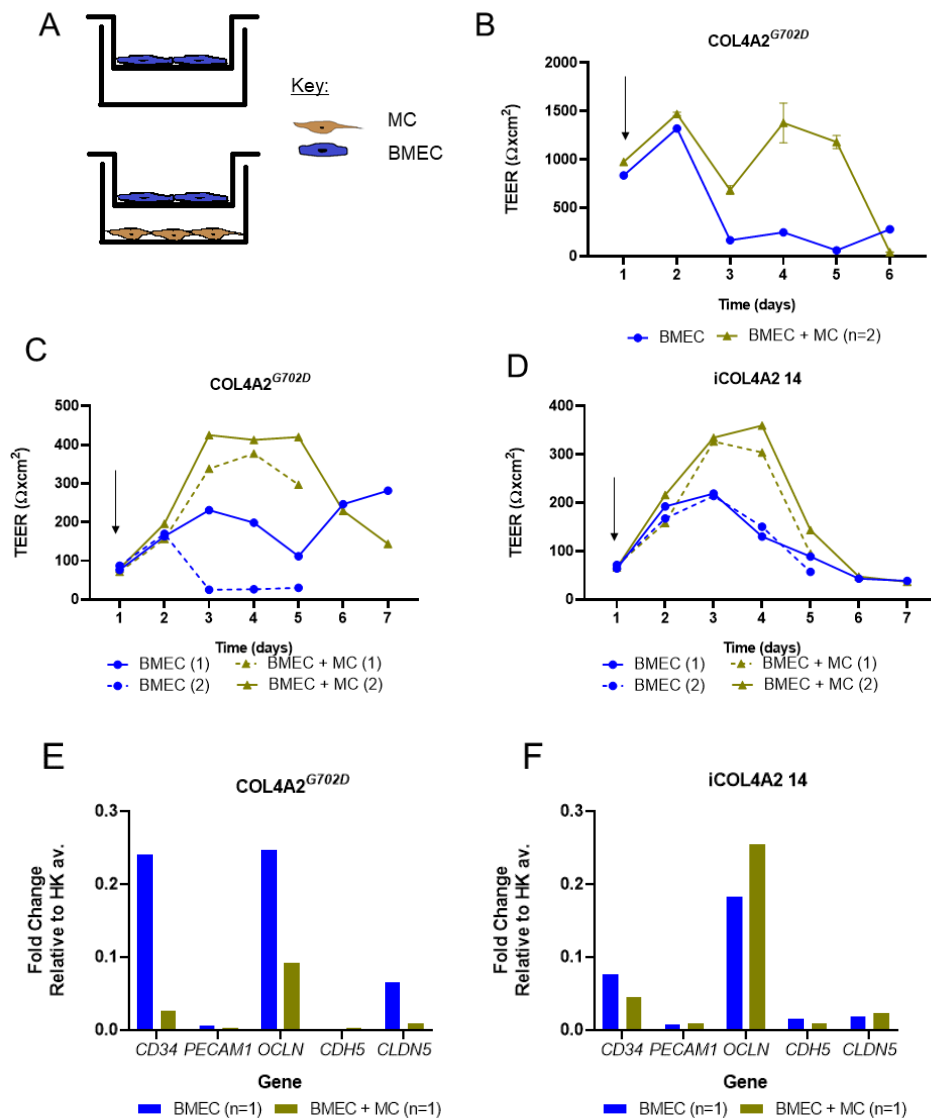
Figure 5.17 iCOL4A2 and COL4A2^{G702D} hiPSC-BMEC and MC co-culture: (A) co-culture setup **(B)** COL4A2 **(C)** COL4A2. and **(D)** iCOL4A2 cl14 dotted lines collected for qRT-PCR **(E)** qRT-PCR of **C** and **(F)** qRT-PCR of **D**, arrow indicates start of co-culture.

Conversely, MC co-culture does not notably increase TEER of COL4A1^{G755R}_cl4 or cl5 (**Figure 5.18B-D**), when co-culture begins on day 1 or day 3. However, qRT-PCR of COL4A1_cl5 + MC displays increased expression of *CD34*, *PECAM1*, *OCLN* and *CLDN5* compared to BMEC alone (**Figure 5.18E**). Co-culture experiments are summarised overall in **Table 5.1**, discussing the effect on TEER and qRT-PCR.
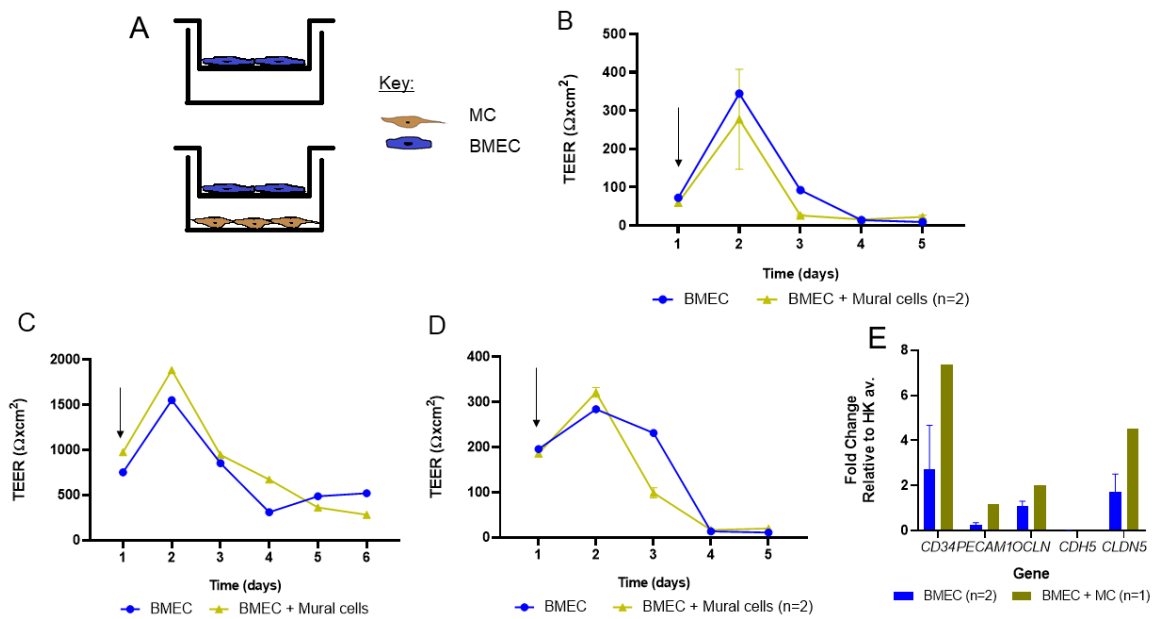
Figure 5.18 COL4A1^{G755R} hiPSC-BMEC and MC co-culture: (A) Co-culture set-up **(B)** COL4A1_cl4 and **(C)** COL4A1_cl5 experiment 1 **(D)** experiment 2 **(E)** qRT-PCR of **C**, arrow indicates start of co-culture.

MC contribution BMEC phenotype, which may have resulted in decreased TEER in response to paracellular release of MMPs from MC, was not observed. This led to the development of a more physiologically relevant model, in order to enhance the SVD phenotype in an *in vitro* setting and better understand the roles of different cell types. Currently lacking in the model are shear stress and cell-cell contact, key aspects of the BBB's function *in vivo*, thus, each of these aspects was addressed in turn.
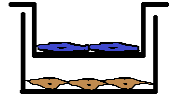
Experimental condition	Effect on TEER	Effect on mRNA of BMEC markers
BMEC + Astrocytes	Increase	Increase/Decrease
BMEC + MC	No change/limited increase over short period of 2-3 days	Increase/Decrease
BMEC + Astrocytes + MC Or:	Increase compared to BMEC alone but not more than BMEC+astrocytes	Increase/no change

Table 5.1 A summary of co-culture experiments and their effect on TEER and mRNA

5.5 Use of Quasi Vivo® to exert shear stress on a Transwell® model

Physiologically, BMEC are exposed to shear stress exerted by blood flow, which plays a role in the formation and maintenance of the BBB[376]. hiPSC-BMEC were exposed to shear stress artificially *in vitro* using a bespoke Quasi Vivo® system (**Figure 5.19**). The QV1100 (kindly provided by Kirkstall Ltd) was designed to be compatible with 24-well Costar Transwell® hanging inserts used in this work, since the commercially available QV600 is designed for 24-well standing inserts and QV500 is a shallow channel not designed for cell culture inserts.

There is little consensus within the literature regarding flow rate in human cerebral vessels, in particular small vessels, owing to the difficult nature of recording *in vivo*. In one report,

values of between 1.1mL/s and 3.4mL/s were recorded across different large vessels within the brain[377]. The supplier of Quasi Vivo®, Kirkstall Ltd, recommended 100µl/min as a starting point. Most *in vitro* experiments published with their setup use hepatocytes, with flow rates between 180-500µl/minute [378–380]. The pump was calibrated as reported in the Materials and Methods, to a flow rate of 100µl/minute.
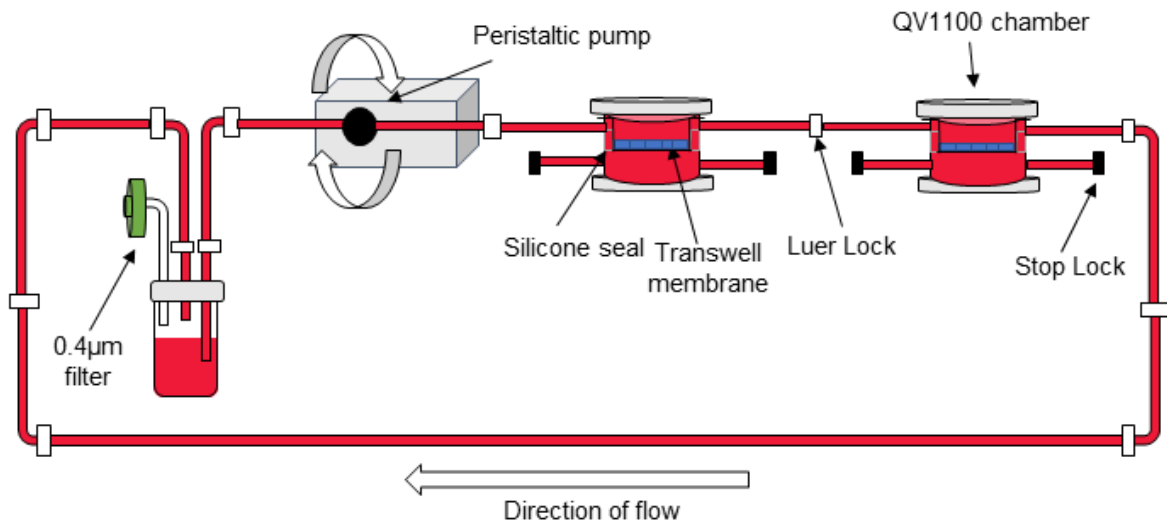
Figure 5.19 Example Quasi Vivo® set up with two chambers

Quasi Vivo® increases TEER of WT3 BMEC for 2 days, compared to BMEC in static conditions, with a peak value at day 2 of $215\Omega xcm^2$ compared to $121\Omega xcm^2$ under static conditions (**Figure 5.20A**). Interestingly, relative to housekeeping genes, BMEC markers reduced in cells exposed to flow compared to static (**Figure 5.20B**). Although, it is important to note that the qRT-PCR was performed at the endpoint, not at the peak TEER result. Overgrowth was seen in both cells exposed to shear stress (**Figure 5.20C**) and those that were not (**Figure 5.20D**). Cells began to peel at the edge of the Transwell® (**Figure 5.20E**) in the Quasi Vivo® which would explain the loss of TEER readings. Moreover, since the recording of TEER values relies on careful removal of the Transwell® from the Quasi Vivo®, it is possible that this could disturb the monolayer, affecting resistance readings.
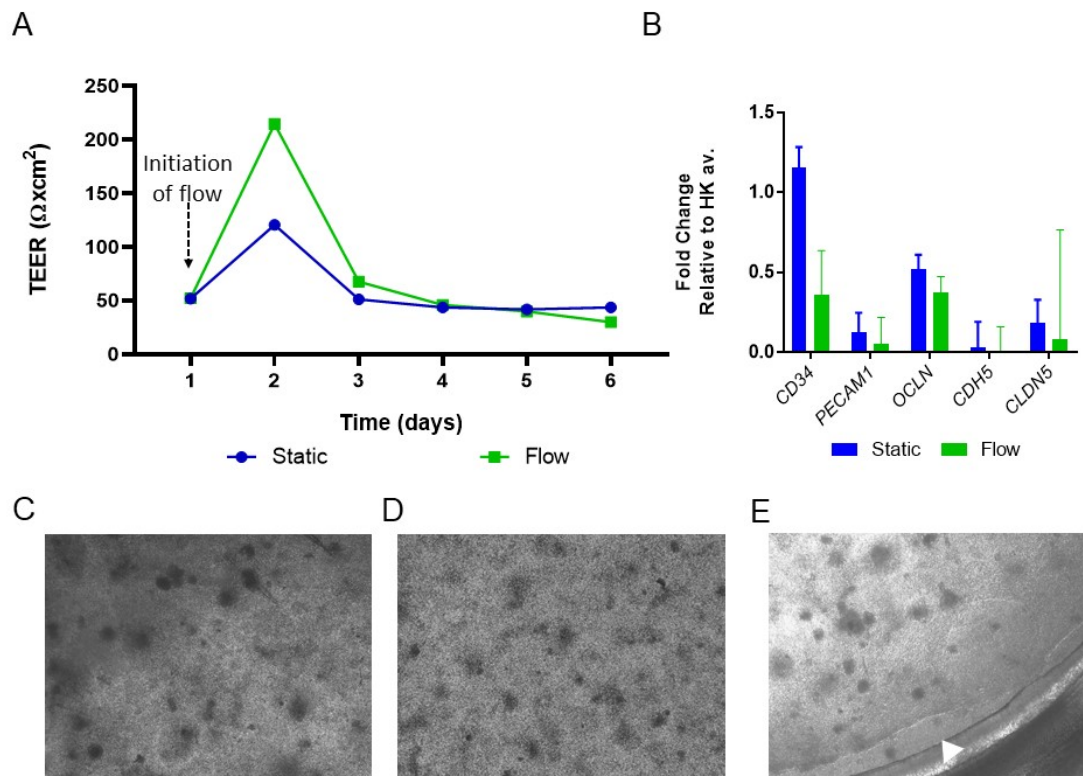
Figure 5.20 The effect of Quasi Vivo® flow on WT3 BMEC: (A) TEER, arrow indicates start of flow **(B)** qRT-PCR n=1; error bars are technical triplicates; phase contrast image of **(C)** cells exposed to shear stress **(D)** cells under static conditions **(E)** Transwell® edge, arrowhead indicates monolayer peeling; images are 5x objective

Following from efforts to exert stress upon BMEC in order to mature properties, focus was turned to another factor lacking in the model: cell-cell contact. Transwell® arrangements (**Figures 5.7-18**) do not allow for cell-cell contact between astrocytes in the bottom of the well and BMEC on the apical side of a Transwell® or with MC on the basolateral side, given that the pores are 0.4µm in size. Other groups have attempted to enable cell-cell contact in a Transwell® system with 3.0µm pores[375], but without demonstrating increased benefit beyond the paracellular effect of astrocytes shown in this work (**Figure 5.8**). Therefore, a new approach of a microfluidic organ-on-a-chip system was taken to generate a cell-cell contact model.

5.6 Microfluidic vessel-on-a-chip

Experiments were conducted with the help of Dr Magda Gerigk (Engineering Department, University of Cambridge), to adapt a previous model of cancer cell migration across a HUVEC barrier, mimicking the BBB[381]. Ultimately, this model could also enable the

incorporation of flow directly through the 3D BMEC vessel, to build a more robust and relevant method than the Quasi Vivo® and offer opportunity for further development.

5.6.1 hiPSC-BMEC attach and proliferate within the microfluidic chip

Utilising an existing design[381], a new plan was established, to incorporate hiPSC-BMEC rapid vessel formation in a 3D-printed channel, to interface with a collagen I gel, containing astrocytes and MC (**Figure 5.21**).
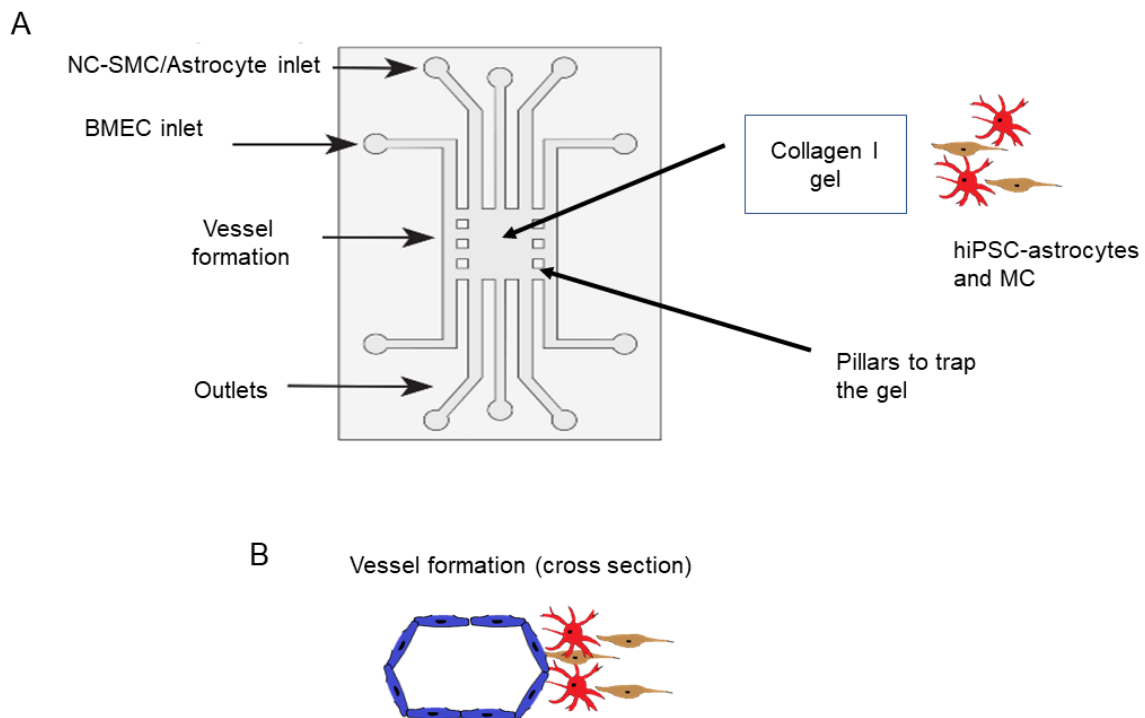
Figure 5.21 Microfluidic chip design: (A) device graphic (provided by Dr Magda Gerigk, adapted from[381]) and **(B)** cross-section of rapid vessel formation and cell-cell contact between pillars

As described in the Materials and Methods, collagen I gel was prepared and inserted into the chamber, before coating of the BMEC channel with collagen IV and incubation overnight at 37°C. hiPSC-BMEC were plated at the sub-culture stage directly into the BMEC inlet (**Figure 5.22A**). After 45 minutes at 37°C, the device was inverted and a second addition of hiPSC-BMEC was administered, to enable coverage of the entire channel, to allow 3D vessel formation.

Cells attached at the inlet (**Figure 5.22A**) and to a lesser extent in the curvature of the BMEC channel (**Figure 5.22B**), with greatest attachment seen at the collagen gel/BMEC channel interface (**Figure 5.22C**), although the areas between pillars trapped dead cells.
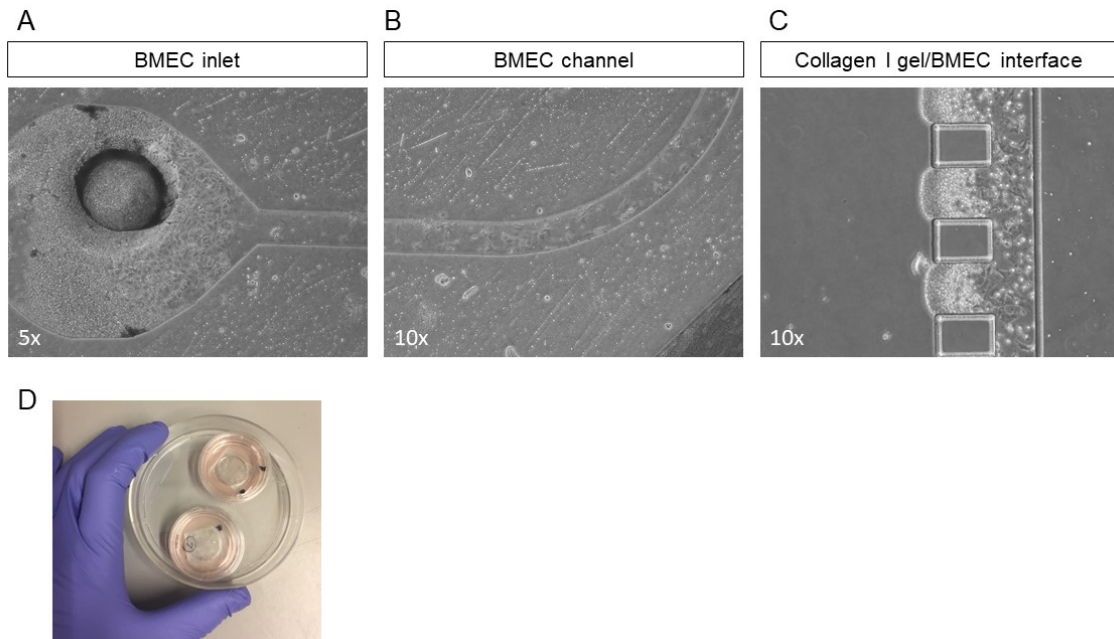
Figure 5.22 hiPSC-BMEC seeded in the microfluidic chip 1-day post-seeding: (A) BMEC inlet **(B)** BMEC channel **(C)** collagen I gel/BMEC interface **(D)** overall size of two microfluidic chips in 10cm dish

Immunocytochemistry reveals cells in the BMEC channel that are positive for VE-Cadherin and occludin (**Figure 5.23A**). Since in this particular device the collagen I gel failed to form, occludin/VE-Cadherin positive hiPSC-BMEC attached and proliferated throughout the gel trap area (**Figure 5.23B**), displaying expected morphology.
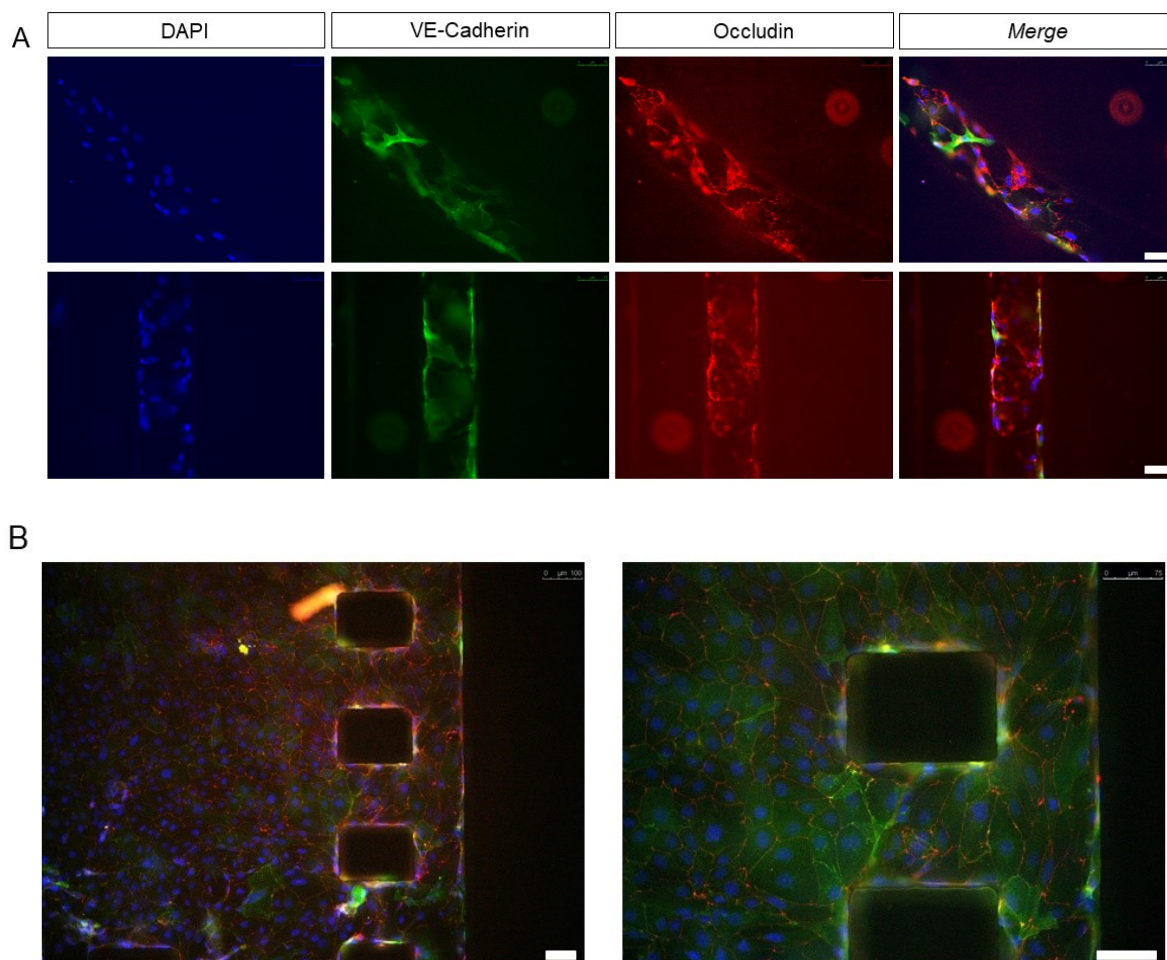
Figure 5.23 hiPSC-BMEC seeded in the microfluidic chip 4 days post-seeding:
immunocytochemistry of **(A)** BMEC channels and **(B)** gel trap and pillars; occludin (red), VE-Cadherin (green) and DAPI (blue), scale bar is 75um.

As demonstrated by immunocytochemistry analysis, collagen I gel failed to adhere to the gel trap pillars (**Figure 5.23B**). In addition, from experiments conducted so far, the collagen IV matrix does not always interface at the collagen I gel (**Figure 5.24A**) and the collagen I gel fails to adhere uniformly to the pillars (**Figure 5.24B**). On addition of cells, after 2-3 days, the monolayer began to peel at areas under higher stress, such as around the BMEC inlet (**Figure 5.24C**). Hence, further optimisation of the system is required. For example, modifying the concentration of collagen I, replacing with an alternate matrix protein, such as fibrin[382] or altering the number of cells seeded.
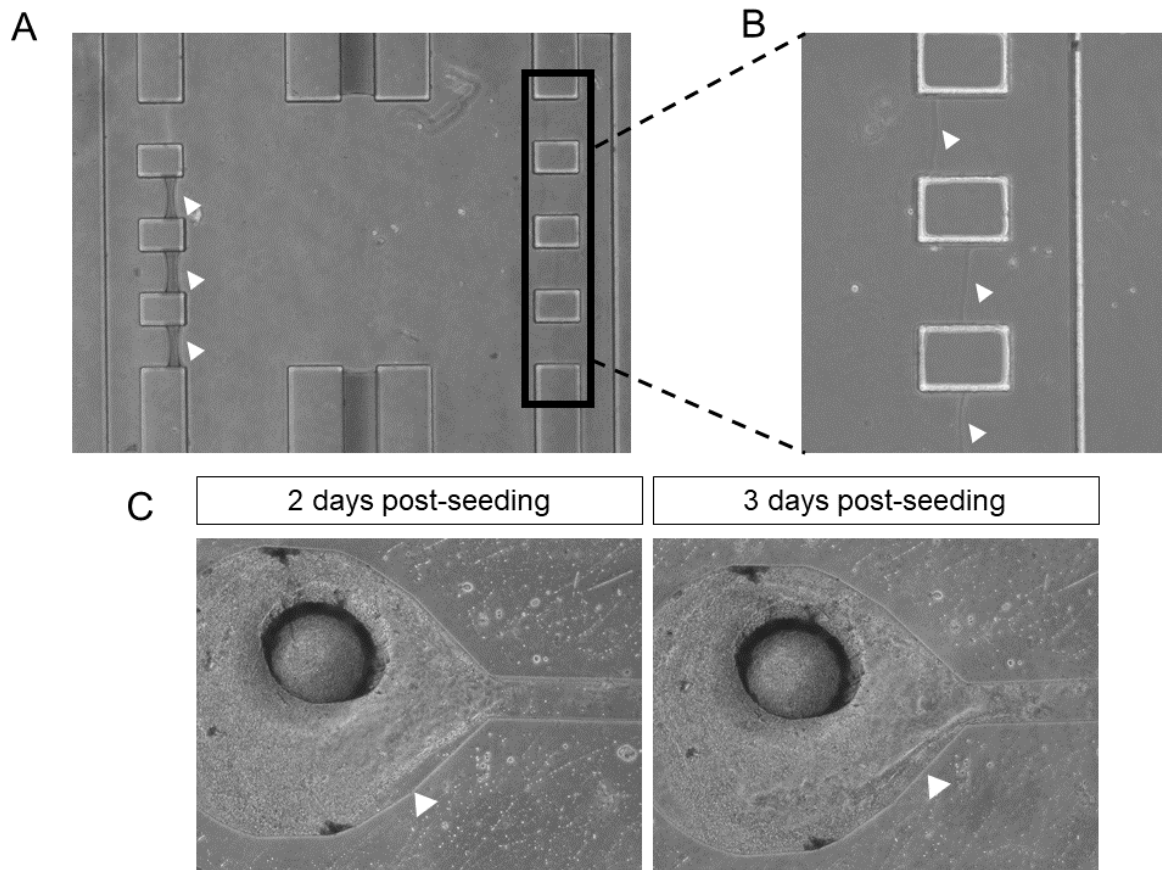
Figure 5.24 Microfluidic chip issues: (A) incomplete formation of gel and collagen IV interface, arrowheads indicate incomplete formation of collagen gel/collagen IV interface **(B)** misalignment of the gel and collagen IV interface, arrowheads indicate gel/collagen IV interface **(C)** peeling of hiPSC-BMEC away from the chamber after 2 and 3 days post-seeding

5.7 Chapter summary

This chapter has demonstrated the generation of WT hiPSC-Astrocytes and their combination, along with hiPSC-MC (provided by Dr Alex Granata) to create a triple co-culture *in vitro* model of the BBB.

The effect of co-culture on increased TEER, suggests a maturation of hiPSC-BMEC and response, often rapid, by BMEC to their surrounding environment and paracellular cues of co-cultured cells. There are conflicting reports in the literature for hiPSC-BMEC co-culture experiments, with the Lippmann group reporting that pericytes elicit higher TEER than a mixed neural/astrocyte population [77]; whereas the Shusta group report greater increase with astrocytes/neurons than with pericytes[353].

Overall, qRT-PCR results are inconsistent. More rigorous investigation, such as collecting samples through a time-course would determine if gene expression is the most appropriate outcome measure of co-culture effect on barrier properties. A quantification of tight junctions with immunocytochemistry, such as in Chapter 4, may be more suitable.

Furthermore, in this chapter, consideration was given to developing a more representative model of the *in vivo* BBB, with efforts to introduce flow and cell-cell contact. Ultimately, the microfluidic chip would enable both of these aspects, further enhancing the disease modelling capabilities beyond that reported in a Transwell® and allowing better understanding of the complex interplay of cells of the NVU in SVD.

Chapter 6: Discussion and Conclusion

6.1 Discussion

There are currently no disease-modifying treatments for SVD and little is known about the underlying mechanisms of the disease. Pre-clinical mouse models do not recapitulate all aspects of human disease[298,351], so there is a requirement for a human-relevant model of SVD. It has previously been suggested that matrisome malfunction plays an important role in SVD[129]. Moreover, BBB leakage, caused by tight junction disruption has been implicated in SVD[156].

Hence, the hypothesis of this thesis is that COL4A1/2 SVD pathophysiology is caused by NVU dysfunction, in turn leading to increased permeability of the BBB. To address this hypothesis, the first of the project research aims was to develop a physiologically relevant *in vitro* co-culture model of the BBB, with hiPSC. Using hiPSC means the model will be isogenic and patient-specific[352–354], providing relevance to human disease. The Transwell® model was chosen because of its simplicity, enabling interchangeable arrangements of BBB cell types and the ability to probe functional barrier properties more readily than mouse models or complex 3D systems[273]. The second aim was to use hiPSC-BMEC derived from COL4A1/2 patient lines to elucidate the disease-causing mechanism of COL4A1/2-SVD, resulting in impaired BBB structure and function. To address this, two patient lines were used, COL4A1^{G755R} and COL4A2^{G702D}.

6.1.1 Optimisation of the hiPSC-BMEC protocol

To explore the first aim, hiPSC-BMEC were initially generated from multiple control (WT) lines using an established BMEC protocol[77]. The qRT-PCR results displayed high variability both between differentiations of different WT hiPSC lines and between different differentiations of the same line. Variability between hiPSC differentiations is well known in the field of hiPSC research and highlights the difficulty in generating reliable and reproducible hiPSC disease models (comprehensively reviewed in[383]). The hiPSC-BMEC protocol from the Lippmann group[77] takes hiPSC through an undefined E6 stage, which is predicated on spontaneous differentiation in low growth factor medium. The intermediate population was believed to be NESTIN/PAX6+[307,313] and additional characterisation with qRT-PCR confirmed this (**Figure 3.3**). Next, different steps were taken to try to overcome the variability of the protocol.

To address the differentiation intra-variability, first of all, I investigated the method of cell plating at the sub-culture stage. The procedure of counting and plating cells of a known number at the sub-culture stage onto fibronectin/collagen IV was adopted, in line with other protocols[314]. To further improve the variability, which still persisted, I adopted fully-defined B-

27 to replace the human serum from platelet-poor plasma following documented batch-batch variation[311] . In this work, B-27 enabled comparable differentiation capacity to a parallel differentiation performed with human serum.

However, because the inter-line variability still remained, I assessed the effect of differing the seeding density between lines. This exposed proliferation differences between WT1 and WT2 hiPSC lines, with reduced expression of BMEC markers in WT2, potentially indicative of a reduced capacity to differentiate. Hence, new WT lines were introduced, to improve the reliability. Fully characterised, commercially available HIPSCI Consortium lines, with known normal karyotype confirmed with Array CGH, were adopted in subsequent experiments. This improved comparability between the WT lines, with qRT-PCR data of WT3 and WT4 hiPSC-BMEC in agreement.

Even after the reported optimisation, there is still an issue of lack of selection. Since the fibronectin/collagen IV matrix likely yields incomplete selection, there is a requirement to plate a large number of cells at the sub-culture stage to yield a monolayer, with high cell death observed. Collagen IV and fibronectin are choice matrices for other endothelial-like cells, meaning they may not be specific to BMEC. For example, fibronectin is commonly used for primary endothelial progenitor cells[384]. An alternative selection approach is magnetic associated cell sorting (MACS) using specific markers. Patsch *et al* demonstrated a pure population of hiPSC-Endothelial cells with MACS selection for CD144+ cells[385]. However, MACS selection has yet to be employed in hiPSC-BMEC protocols. With the potential of incomplete matrix selection being a contributing factor to end-stage heterogeneity; following a recent report[305], initial experiments were performed using the antibiotic puromycin as a selective agent. Preliminary results were promising, with comparable qRT-PCR results to those differentiated without puromycin and visible removal of hiPSC colony structures prior to sub-culture (**Figure 3.12**). However, further optimisation is still required for routine adoption of puromycin, especially in relation to seeding density post sub-culture.

In conclusion, the differentiation protocol has been substantially improved by introducing cell counting and B-27. This contributes to the field of hiPSC-BMEC differentiation by presenting a robust and reproducible alternative to current protocols[77,305,307,311,314] by combining together different approaches.

6.1.2 BBB functional studies: current methodology and limitations

Once the hiPSC-BMEC protocol was able to yield comparable mRNA expression levels of BMEC markers between different WT lines, these cells were thoroughly functionally tested. Cells plated on Transwell® membranes for functional experiments notably showed an

increase in qRT-PCR specific marker expression in BMEC compared to a 12-well plastic plate (**Figure 3.18**). This could be explained by the 5 times higher collagen IV/fibronectin coating on Transwells®, highlighting the contribution of the matrix to the phenotype of these cells. It could also be that this marked increase is the result of growth factor availability to both apical and basolateral sides of the monolayer. Alternatively, the Transwell® may have reduced stiffness compared to the plastic culture plates. Standard tissue culture plates have an Elastic Modulus of around 1.0×10^5-1.0×10^6 kPa[386] but the stiffness of the Transwell® membrane, despite not being reported by the manufacturer, might be less.

Characterisation was performed with a plethora of assays, in order to collectively demonstrate the efficacy of the hiPSC-BMEC. There are limitations for each individual assay, highlighting the need to use multiple methods[306]. For example TEER is affected by position of the electrode, temperature and media content[303,304]. A move towards un-biased approaches could improve the reliability of TEER and reduce the human error. For example, using the World Precision Instruments EndOhm (Cell Culture Cup Chamber), which takes voltage measurements evenly across the entire area, or the Axion Biosystems Maestro automated, self-contained and temperature-controlled system that acquires real-time measurements. Although TEER is an important and widely used measure of BMEC function, it could be replaced by thorough barrier tests using fluorescent compounds of known size.

However, in the case of fluorescent compound barrier tests (FITC-Dextran and NaFl), as the size of the compound decreases, the blank value also increases, since more fluorescent compound can pass through the 0.4µm pores of the Transwell®. This reduces the sensitivity when compared to the blank and saturation of fluorescence may be reached, limiting the sensitivity of the assay. In addition, molecular weight in KDa cannot be reliably equated to physical size or shape, as the folding of proteins can differ (reviewed in[387]), so it is difficult to compare to *in vivo* selectivity on this basis alone. Moreover, fluorescent compounds such as FITC-Dextran and NaFl do not necessarily share biochemical properties, such as charge and branching, with molecules that would typically be found in the blood[55].

Hence, active drug transport studies that utilise specific transporters on the membrane surface, would be better predictors for barrier function than TEER or passive diffusion between cells[305]. The uptake of these complex assays is limited in the field of BBB modelling and so far only one group has demonstrated *in vivo*-like drug transport with an *in vitro* model[305]. This is likely because of the cost and specialist experience required for mass spectrometry compared to the readily available permeability assays with fluorescent compounds such as FITC-Dextran or NaFl[306]. Hence, to negate the expense and specialist training required, the functional assessment of the BBB could be improved by performing

multiple assays as part of the standard characterisation, beyond simply TEER. For example, TEER, FITC-Dextran, NaFl, R123, tube formation and LDL-uptake all provide relevant readouts of different aspects of BBB function that collectively demonstrate the efficacy of hiPSC-BMEC.

To conclude, in this work, I have utilised multiple functional assays to probe the function of derived hiPSC-BMEC. However, further assays could be included such as a wound healing or migration assay and nitrous oxide release.

6.1.3 SVD disease modelling

To address the second aim, two lines with characteristic glycine mutations, one in COL4A1 and one in COL4A2 were utilised to model collagen IV SVD. Both mutations are located in the triple helical regions of the respective gene, COL4A1^{G755R} is in exon 30 and COL4A2^{G702D} is in exon 28. Gly-Xaa-Yaa repeats, of which the Glycine is substituted in both COL4A1^{G755R} and COL4A2^{G702D}, are imperative for the correct formation of the triple helix[202]. Neither COL4A1^{G755R} or COL4A2^{G702D} are located within integrin, fibronectin, laminin or other binding sites[264]. Therefore, protomer assembly could be affected by the location of these mutations within the triple helical region[196]. Surface plasmon resonance which has previously been used to demonstrate collagen IV chain assembly, could reveal the effect of the location of the specific mutations on formation of the tertiary structure[196].

COL4A1^{G755R} and COL4A2^{G702D} hiPSC were successfully differentiated into BMEC and characterised along with WTs. A number of phenotypic differences were observed between the control and diseased BMEC. The first of these relates to proteins that play a key role in BMEC structure, function and BBB maintenance[71]. COL4A1^{G755R} and COL4A2^{G702D} BMEC display discontinuous tight junction protein occludin compared to controls. In a previous report, occludin was shown to be increased in the blood of patients following ischaemic stroke[156,174]. This could be a downstream effect of discontinuous junctions seen in this *in vitro* setting. Another tight junction protein, claudin-5, accumulated intracellularly in COL4A1^{G755R} and to a lesser extent in COL4A2^{G702D}, demonstrated by increased CTCF compared to controls. Claudin-5 total protein was also reduced in COL4A2^{G702D} by western bot. claudin-5 contributes to BBB stabilisation, with mice deficient for claudin-5 demonstrating a loosened BBB[78]. Similarly, a previous report showed that siRNA knockdown of claudin-5 in cultured human BMEC results in an increase in permeability[388]. This miss-localisation could suggest less claudin-5 is translocated to the cell membrane. Alternatively, the accumulation of claudin-5 intracellularly could be consistent with a role for ER stress. ER stress has been suggested to contribute to COL4A1/2 SVD pathology, whereby collagen IV accumulates in the ER, leading to the unfolded protein response[46,262]. To explore this further,

immunocytochemistry to determine co-localisation of claudin-5 and collagen IV with a Golgi marker such as 58K protein[389] and ER stress markers such as BIP, ATF6 or EIF2[48] should be performed.

The key hypothesis of this work is that the matrisome is abnormal in COL4A1/2 SVD. Therefore MMPs, as regulators of the BM[145] appear as strong mechanistic candidates in SVD[155,156]. A reduction in collagen IV in COL4A2^{G702D} compared to WT1 was observed by immunocytochemistry, although, the reverse trend was seen when compared to the isogenic control. COL4A1^{G755R} displays decreased collagen IV compared to one WT (WT3, not WT4). However, the immunocytochemistry analysis performed in this work is not sufficient to distinguish between the different stages of collagen IV turnover: production, accumulation and degradation. Going forward, we have developed a new approach using flow cytometry that is able to differentiate between intracellular and extracellular collagen[390]. At the transcriptional level, there is a trend of increased *COL4A2* in COL4A1^{G755R}, but no changes in *COL4A1* or *COL4A2* expression in COL4A2^{G702D}.

These findings, along with the observed abnormal levels of tight junction proteins, also pointed to a potential role for MMPs. MMPs were shown to be elevated in COL4A1/2 hiPSC-BMEC. Specifically, MMP9 and MMP14 in COL4A2^{G702D} and MMP2 and MMP9 in COL4A1^{G755R}. MMP14 RNA expression was increased in COL4A1^{G755R} but there was no increase seen in the protein level by western blot. The MMP14 increase in COL4A2^{G702D} hiPSC-BMEC is in keeping with results in the original patient fibroblasts, in which supernatant from COL4A2^{G702D} fibroblasts had increased MMP14 (Dr Tom van Agtmael, *Unpublished*). These data are also in concordance with previous reports in cerebrovascular disease in which MMP2, MMP9[155] and MMP14[177] are raised. Of the inhibitors, TIMP2 and TIMP3 are non-significantly increased in COL4A1^{G755R} but there are no trends in COL4A2^{G702D}. Concurrent increase of both MMP2 and TIMP2 in COL4A1^{G755R} is intriguing, since TIMP2 inhibits MMP2[368]. TIMP2 also regulates MMP14, which in turn activates pro-MMP2[161–163], highlighting the complex interplay of MMPs and TIMPs in tissue homeostasis.

Although, it is important to remember that raised RNA and protein levels do not dictate increased MMP activity. Therefore, beyond simple gene and protein expression, gel zymography should be used to assess MMP activity. Also, more detailed studies of the temporal release of MMPs could be informative to determine causality versus consequence of elevated MMPs. It has previously been shown that following BBB opening induced by reperfusion, the initial raised level of MMP2 level could be reversed and precedes an irreversible increase in MMP9[156].

The discontinuous junctions of occludin in COL4A1^{G755R} is consistent with the literature, in which occludin is a reported target of MMP2 and MMP9[175,176], both of which are raised in COL4A1^{G755R} BMEC. Moreover, miss-localisation of claudin-5 and intracellular accumulation in COL4A1/2 BMEC when compared to controls could relate to the re-distribution away from the cytoskeleton in the presence of MMP2 and 9 that has previously been seen in ischaemic stroke[175].

MMPs could serve as a tractable target for therapy, an avenue that was explored with inhibition experiments. MMP inhibition with Doxycycline showed increased claudin-5 protein compared to the untreated sample. However, given that Doxycycline is a non-selective inhibitor of MMPs, a more target approach was sought. MMP14 was chosen because it was raised in COL4A2^{G702D} in western blot, compared to iCOL4A2 cl14. MMP14 gene silencing with siRNA did not reduce MMP14 at the protein level although occludin and claudin-5 were increased. Going forward, transfection of 100nm siRNA should be repeated, changing the time point of treatment. In this experiment, cells were treated 3-4 days after sub-culturing onto fibronectin/collagen IV. In the future, treating cells earlier, such as during or immediately after sub-culture, could enhance the gene silencing. Although, given that a promising result was observed with Doxycycline, which acts by inhibiting the activity of MMPs[369], an activity inhibitor compound could be tested instead of siRNA. For example, the inhibitor of MMP14 function, NSC405020[391], could be used in COL4A2^{G702D} and iCOL4A2 cl14 hiPSC-BMEC to assess MMP14 inhibition.

Future work should assess the effect of perturbing MMPs on their activity by using gel zymography. This is especially important in the context of Doxycycline treatment which is known to physically interact with MMPs, thus altering their activity on substrates, not exclusively the RNA or protein level[369,392,393]. Once identified, the inhibitor should be tested in functional studies, such as NaFI and TEER. In addition, tight junctions should be assessed with confocal microscopy, to determine if the COL4A1/2 phenotypic abnormalities can be resolved. Regardless, a greater understanding is needed to determine how to target MMPs specifically at the BBB, given they are present throughout the body[158]. This of particular importance when considering MMP modulation as a potential target for therapy.

Another key result in this work is the altered function of P-gp. Beside the well-understood role of tight junctions in preventing passage of unwanted substances into the brain, the efflux receptor, P-gp plays a very important part in extruding compounds into the bloodstream, thereby also reducing passage into the neural tissue[86]. For this reason, P-gp has garnered great attention for its role in drug resistant cancers, where it is reportedly elevated[88]. In the R123 assay, blocking P-gp with CsA results in an accumulation of R123 within the cell[307],

demonstrated with higher fluorescence than CsA negative samples. Hence, the ratio (of CsA inhibited and uninhibited samples) equal to 1.0 means that there is no difference between +CsA/-CsA samples. There is a significant reduction in this ratio, to 1.0 or less, between COL4A2^{G702D} and the iCOL4A2 cl14, and a significant difference between COL4A1^{G755R} _cl5 and one WT (WT3).

The work reported in this thesis is preliminary and the results are inconclusive. Many of the experiments have been performed less than three times and need further repetition. A potential next step would be to study ECM secreted by the cells, to better characterise the disease phenotype and investigate the BM defect that is proposed to be causal in these cells. Despite the results being inconclusive, this work may lead to more in-depth studies on mechanisms such as MMPs or P-gp. The following suggestions are potential mechanisms that could explain the results presented in this work but have not yet been tested. Preliminary studies should be conducted, to determine if this a potential avenue for future work.

There are several potential explanations for the abnormality observed in P-gp function. Firstly, altered BMEC surface structure, affecting exposure to R123, could mean that R123 is not passively taken up as readily in COL4A1/2 BMEC as it is in WT/isogenic controls. Electron microscopy could be used to determine the physical structure of diseased and WT BMEC monolayers. If true, this would describe an independent mechanism to perturbed P-gp efflux, since less R123 has been taken up into the cell. Alternatively, P-gp could be less expressed or not be correctly trafficked to the surface in COL4A1/2 BMEC, compared to controls. Indeed, qRT-PCR results showed a non-significant trend of reduced *ABCB1* (encoding P-gp) expression in COL4A2^{G702D} compared to the isogenic and COL4A1^{G755R} compared to WTs (**Figure 4.23**). My findings appear to contradict a previous study that reported an increase of P-gp in stroke[394,395]. However, this study was conducted in a rat model of middle cerebral artery occlusion, which is not representative of lacunar stroke. P-gp was also found to be reduced at the mRNA level in an Alzheimer's Disease hiPSC-BMEC model[396] but there was no difference reported in the R123 assay between diseased and control BMEC[396]. This suggests reduced mRNA expression of P-gp is not sufficient to explain an altered R123 result, such as the one reported here. In the future, the protein level of P-gp should be quantified by western blotting, to determine if this is reduced, in keeping with the mRNA expression. In addition to this, recycling of P-gp to the membrane should be explored by utilising immunocytochemistry or flow cytometry assays to compare P-gp levels in membrane permeabilised and non-permeabilised samples over a time-course.

Alternatively, abnormal P-gp and MMP levels could be explained by dysregulation of Cluster of differentiation 147 (CD-147; **Figure 6.1**). CD-147 (also known as EMMPRIN or Basigin) is a regulator of both P-gp and MMP expression[397,398]. CD-147 stimulates MMPs 1 and 2[399], which promotes vascular remodeling[400,401]. MMP9 in particular has been heavily associated with increased CD-147[401] in the context of cerebral ischaemia[402]. Moreover, CD-147 is increased on the surface of P-gp (MDR1) resistant cancer cells, with a concurrent increase of MMP1, MMP2 and MMP9, that can be attenuated by using an antibody to inhibit CD-147[403]. CD-147 deficient mice exhibit BBB leakage, suggesting it plays an important role in development and/or maintenance of the BBB[401,404].

Through the action of CD-147, the modulation by MMPs could be causal of tight junction defects (**Figure 6.1**) such as the miss-localisation of occludin and claudin-5. However, the increased BBB permeability could also be an indirect one. The loss of function of P-gp could lead to the accumulation of toxic compounds in BMEC, as reported in the global P-gp knockout mouse[89,90]. This could then cause endothelial cell dysfunction and eventual tight junction loss, rather than the MMP/P-gp complex eliciting a direct effect on the tight junctions. Alternatively, Caveolin-1 has been demonstrated to mediate the altered expression of claudin-5 in cerebral ischaemia[365,366], causing it to redistribute away from the cytoskeleton[175]. Caveolin-1 also binds P-gp and traffics it to the cell surface[364,405], suggesting a convergent mechanism on the localisation of membrane proteins.

Future work could include assessing the cell surface expression of CD-147 with immunocytochemistry. For example, a co-stain of MMP9 and CD-147, as reported previously[401] as well as the expression level with qRT-PCR and western blot could reveal if there are any differences between COL4A1/2 BMEC and controls. As a potential route to therapy, siRNA of CD-147 has previously been shown to reduced α-SMA in myofibroblasts during corneal tissue remodelling[406]. Moreover, inhibition of CD-147 has been revealed as therapeutic strategy in malignant melanoma[407]. However, P-gp is not the only efflux receptor on BMEC, so other receptors such as BCRP and MRP should also be assessed, to determine if there are any compensatory mechanisms.
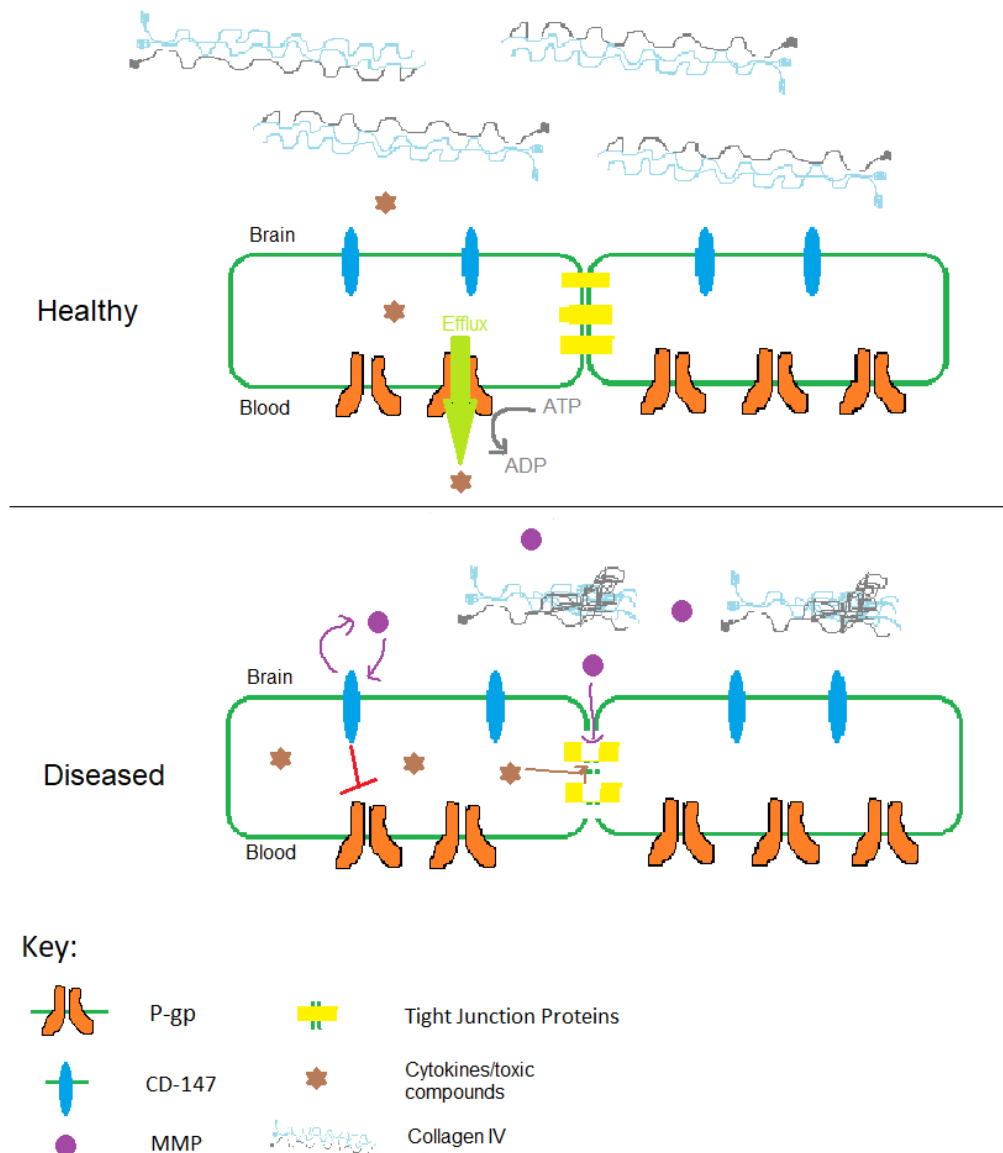
Figure 6.1 A mechanistic diagram showing CD-147 involvement in P-gp and MMPs in relation to BMEC dysfunction.

Caution must be heeded regarding the overinterpretation of the observed P-gp result, since the reduction of P-gp could be an *in vitro* artefact resulting from the lack of polarity in these cells. P-gp is located on the luminal side of BMEC *in vivo*[71,87] but the polarisation of *in vitro* hiPSC-BMEC is unknown. Hence, an alternative approach may be to implement a R123 assay in a Transwell® system, in the presence and absence of shear stress, to see if this exposure promotes a polarised response. Or, to treat control and diseased hiPSC-BMEC with puromycin, a P-gp substrate[359] to see if this increases P-gp functionality in the diseased or control BMEC, measurable with the R123 assay. Ultimately, to determine that this is not

simply an *in vitro* artefact, validation in a mouse model or SVD human brain tissue samples would be valuable.

To conclude, COL4A1/2 SVD is a complex disorder with many interacting mechanisms, of which causality is difficult to determine. In an effort to address this, I have developed a novel *in vitro* model using BMEC from COL4A1^{G755R} and COL4A2^{G702D} hiPSC that recapitulates aspects of collagen IV SVD pathology. The findings in this thesis have unraveled a role for MMPs and potentially P-gp, in the disease process of COL4A1/2 SVD. This contributes to the field of SVD research, complementing the existing work in collagen IV mouse models[271]. Taken together, these results could enable the identification of much-needed new treatments for SVD.

6.1.4 *in vitro* triple co-culture model of the BBB

To progress from the reductionist BMEC-only system towards a more physiological model, BMEC were combined with MC (provided by Dr Alex Granata). WT astrocytes were also generated and used in double and triple co-culture. A consistent result is the short-term increase in TEER that was observed with MC, regardless of the matrix on which they were cultured. Double co-culture of BMEC with astrocytes increased TEER more than MC. This contradicts a previous study whereby pericytes increased TEER more than astrocytes[77]. However, immortalised hCMEC/D3 display higher TEER on co-culture with primary human astrocytes than pericytes[408]. Another study has shown no influence on TEER of pericytes cultured in the bottom of the well to BMEC on the apical side[349]. These authors suggest competition for nutrients or differences in pericyte motility could play a role in BMEC/pericyte co-culture systems[349]. The variation within the double and triple co-culture experiments reported in this work, along with disagreement in the literature, suggests that the complex interplay of multiple cell types *in vitro* is not well understood. To progress from these models and to enhance our understanding of *in vitro* interactions, a method that enables cell-cell contact should be sought, since this is a key aspect that is lacking in many *in vitro* models.

The effect of co-culture on gene expression also remains unclear, with some triple co-culture experiments increasing BMEC marker expression and others, not. This could be because all qRT-PCR experiments were conducted at the end point, which may not represent the temporal aspect of mRNA expression and generally depicts the lowest peak in TEER value. Moreover, in some experiments, such as the MC and astrocyte co-culture, low survival of MC was seen, which could suggest a lack of cells to elicit a positive effect on marker expression or even a negative effect on the BMEC due to factors released from necrotic cells.

Of the co-culture disease modelling, COL4A2^{G702D} showed the same response to MC co-culture as the iCOL4A2 cl14 and WTs. Therefore, mis-matched co-culture of COL4A2^{G702D} and iCOL4A2 cl14 could help to determine if COL4A2^{G702D} BMEC have a detrimental effect on the isogenic and *vice versa*. Alternatively, MC could be cultured on top of the Transwell® and later removed with ammonium hydroxide[409]. The abundance of matrix proteins (reviewed in[410]) that are secreted by MC would be left behind. This would allow the addition of matched/mismatched BMEC, to determine if the ECM deposited by COL4A2^{G702D} MC is detrimental to the isogenic. Moreover, conditioned media experiments could be performed in the same manner, to determine if soluble factors released by healthy and diseased MC, such as MMPs, have a detrimental or beneficial effect on matched and mismatched BMEC.

In conclusion, I have generated an *in vitro* triple co-culture model that confirms the beneficial effect of astrocytes on the TEER of BMEC and the limited increase with MC. Importantly, the Transwell® results demonstrate the ability to readily interchange different cell types to perturb co-culture interactions.

6.2 Limitations and Future Work

There are some areas of this work that limit the interpretation of the results presented. As discussed above, the results of this thesis are inconclusive. In addition, there are also some specific aspects to be addressed. One such drawback is that there is only one clone of COL4A2^{G702D} hiPSC. Since so little is known about erasing the epigenetic landscape during reprogramming from fibroblasts to hiPSC, multiple clones must be used to account for impartial resetting of the epigenome[55,317]. Moreover, it is important to be reminded that this line originates from the asymptomatic father of an SVD patient with the same mutation. This could suggest that the wider genetic background and environmental exposure throughout life, both of which are unique to an individual, could play a role in the different clinical presentation of the father and son. Acquiring hiPSC from the patient (son), with 2-3 clones reprogrammed, would help to confirm the findings in this work. Alternatively, the COL4A2^{G702D} mutation could be introduced into two separate WT lines, such as the HIPSCI consortium lines used in this work, to demonstrate the causality of the mutation to the observed phenotype, regardless of the genetic background. Equally, using hiPSC from the father could help to uncover the phenotype given that the epigenetic or environmental changes present could have a protective or compensatory effect, compared to hiPSC from the patient.

Nonetheless, some aspects of the COL4A2^{G702D} hiPSC-BMEC phenotype could be intrinsic to the hiPSC line, not the mutation, given that the COL4A2^{G702D} isogenic clones (14 and 17) do not behave in the same way as the WT lines. For example, iCOL4A2 cl14 still displays a

high percentage of discontinuous junctions, even though it is reduced compared to COL4A2^{G702D}. WT3 and WT4 are around 20-25%, but iCOL4A2 cl14 is around 50%. Moreover, there could be an inherent problem of proliferation in this line, with low Ki67$^+$ cells in both COL4A2^{G702D} and iCOL4A2 cl14 of between 18-25%. Comparatively, WT4 is around 60%. Thus, additional studies with the newly generated COL4A1^{G755R} isogenic line will help to validate the phenotypic changes observed in COL4A2^{G702D}.

Moreover, this is a static 2D model that does not include any of the typical factors circulating in the cerebral vasculature. Hence, this work should progress to a cell-cell interaction model so that the complex interplay of BMEC, MC and astrocytes and their secreted factors can be appreciated in the context of collagen IV mutations. Alternatively, stimuli to promote the phenotype could be used. For example, using tumour necrosis factor α (TNFα), IL1α or IL1β insults may exacerbate the phenotypic results presented here of discontinuous junctions and increased MMPs.

A technical limitation prevented the differentiation of COL4A1^{G755R} and COL4A2^{G702D} hiPSC into astrocytes, meaning that a complete triple co-culture disease model could not be generated. The differentiation into NSC relies on cell-cell contact, with a dense monolayer maintained over 10-12 days[286], which could be compromised in COL4A1/2 hiPSC. However, preliminary experiments in this work suggest there is proliferation defect (shown by a lower percentage of Ki67+ cells) in COL4A2^{G702D} but not COL4A1^{G755R}. Moreover, only two out of four WT lines were successfully differentiated, so it is likely to be an issue with the protocol. Moving forward, the hiPSC-NSC protocol could be adapted to follow a similar premise as the hiPSC-BMEC protocol, using E6 media and Matrigel®, as previously reported[328]. Alternatively, the starting material could be changed from single cell seeding to the use of hiPSC colonies at 70-80% confluency, in order to preserve cell-cell attachment during the critical early stages of the differentiation.

The Transwell® model used in this work has limitations, namely that it is a static system with a porous membrane creating physically separated chambers[65]. To address these limitations, steps were taken to generate a more complex model by introducing cell-cell contact and shear stress. Shear stress of *in vitro* endothelial cells has been shown to increase tight junction proteins and efflux transporters, including P-gp[411]. The Quasi Vivo® system used in this work offers interchangeable options to apply flow to the apical and/or basolateral side of the Transwell® as well as to modulate the flow rate. Initial results suggested the cell monolayer began to peel from the edges of the Transwell® when exposed to flow, in concordance with reduced qRT-PCR of BMEC markers. Little is known about the *in vivo* flow rate in cerebral small vessels. Since peeling was seen at 100μl/min, the system should be

tested with lower flow rates, such as 50µl/min, which has been reported to maintain cell viability over 72hours of human primary brain endothelial cells[412]. The authors reported that primary BMEC could withstand 100µl/min, with the lower flow rate adopted to better suit the primary pericytes and astrocytes intended for co-culture. Therefore, the plating density of hiPSC-BMEC could also be optimised to enable long term monolayer maintenance.

Another parameter limiting this BBB model is cell-cell contact. It has been suggested that this could be achieved in a cell culture membrane system, such as a 3.0µm pore size Transwell®[375]. Although, the manufacturer (Corning®) also supply 5.0 and 8.0µm pore Transwells®, which could be tested to determine the pore size that allows contact, whilst preventing cell migration. Other vendors such as BRAND, NUNC™ and Millicell® also supply up to 8.0µm pore sizes for their cell culture inserts.

Ultimately, progressing to a 3D model such as an organ-on-a-chip system favourably enables miniaturisation, offering the ability to conduct high-throughput screening of small molecules. To address this, I utilised an existing BBB-on-a-chip model in collaboration with Dr Huang's group at the Department of Engineering in Cambridge. The PDMS device had a high failure rate of correct collagen I gel formation and coating of the outer channel before cell seeding, which requires further optimisation. To do this, the gel formation could be improved by exploring different concentrations of collagen I to modulate its consistency, or to utilise other compositions such as fibrin[382]. From a design perspective, the chip could be improved by creating larger spaces between the gel-trap pillars so that the collagen gel formation is not impeded.

Alternatively, another available system could be used in which MC, astrocytes and BMEC are embedded within the gel simultaneously, result in spontaneous vessel formation[382]. This may overcome the issue of gel formation being required prior to cell seeding, with the current system. On the other hand cells could be seeded in separate, adjoining channels, allowing gradual vessel formation[413] and negating the issue of embedded cells in ECM. A different approach could be to utilise a commercially available system such as the MIMETAS Organoplate®. Although, rigid patented systems such as these do not offer the flexibility to tailor to the specific needs of the experimental set up.

6.3 Conclusion

To conclude, there are three main outcomes that have been achieved in this doctoral thesis. Firstly, I have greatly improved the hiPSC-BMEC differentiation protocol by incorporating cell counting and B-27. Along with this, a multitude of functional tests have been employed cohesively to test the BBB properties of these cells. Secondly, I have combined hiPSC-BMEC with MC and astrocytes, generating an isogenic, triple co-culture Transwell® model.

Several different Transwell® arrangements have been explored, demonstrating the versatility of this system.

Finally, I have developed a novel model of collagen IV SVD using hiPSC-BMEC from COL4A1/2 patients which demonstrates, for the first time, that aspects of collagen IV SVD pathology can be replicated *in vitro.* Two distinct or potentially interacting mechanisms, centered on P-gp and MMPs, have been revealed as promising targets for further exploration, although the results are preliminary and inconclusive at the stage. Overall, the results presented here point to potential causative mechanisms in collagen IV SVD, a disease in which treatment and prognosis are currently limited.

References

1. Pantoni, L. Cerebral small vessel disease: from pathogenesis and clinical characteristics to therapeutic challenges. *www.thelancet.com/neurology Rev. Lancet Neurol* **9**, 689–701 (2010).

2. Li, Q. *et al.* Cerebral Small Vessel Disease. *Cell Transplantation* **27**, 1711–1722 (2018).

3. Wardlaw, J. M., Smith, C. & Dichgans, M. Mechanisms underlying sporadic cerebral small vessel disease : insights from neuroimaging. *Lancet Neurol.* **12**, 70060–7 (2013).

4. Petty, G. W. *et al.* Ischemic Stroke Subtypes. *Stroke* **31**, 1062–1068 (2000).

5. Gorelick, P. B. *et al.* Vascular contributions to cognitive impairment and dementia: A statement for healthcare professionals from the American Heart Association/American Stroke Association. *Stroke* **42**, 2672–2713 (2011).

6. Dichgans, M. & Zietemann, V. Prevention of vascular cognitive impairment. *Stroke* **43**, 3137–3146 (2012).

7. Wardlaw, J. M. *et al.* Lacunar stroke is associated with diffuse Blood-Brain barrier dysfunction. *Ann. Neurol.* **65**, 194–202 (2009).

8. De Laat, K. F. *et al.* Loss of white matter integrity is associated with gait disorders in cerebral small vessel disease. *Brain* **134**, 73–83 (2011).

9. Altmann-Schneider, I. *et al.* Cerebral microbleeds are predictive of mortality in the elderly. *Stroke* **42**, 638–644 (2011).

10. Debette, S. & Markus, H. S. The clinical importance of white matter hyperintensities on brain magnetic resonance imaging: Systematic review and meta-analysis. *BMJ (Online)* **341**, 288 (2010).

11. Müller, K., Courtois, G., Ursini, M. V. & Schwaninger, M. New Insight into the Pathogenesis of Cerebral Small-Vessel Diseases. *Stroke* **48**, 520–527 (2017).

12. Schmidtke, K. & Hüll, M. Cerebral small vessel disease: how does it progress? (2005). doi:10.1016/j.jns.2004.11.048

13. Groeschel, S., Chong, W. K., Surtees, R. & Hanefeld, F. Virchow-Robin spaces on magnetic resonance images: Normative data, their dilatation, and a review of the literature. *Neuroradiology* **48**, 745–754 (2006).

14. Wardlaw, J. M. *et al.* Neuroimaging standards for research into small vessel disease and its contribution to ageing and neurodegeneration. *Lancet. Neurol.* **12**, 822–38 (2013).

15. Franke, C. L., van Swieten, J. C. & van Gijn, J. Residual lesions on computed tomography after intracerebral hemorrhage. *Stroke* **22**, 1530–1533 (1991).

16. Bath, P. M. & Wardlaw, J. M. Pharmacological treatment and prevention of cerebral small vessel disease: A review of potential interventions. *Int. J. Stroke* **10**, 469–478 (2015).

17. Lakhan, S. E., Kirchgessner, A., Tepper, D. & Leonard, A. Matrix metalloproteinases and blood-brain barrier disruption in acute ischemic stroke. *Front. Neurol.* **4 APR**, (2013).

18. Smith, E. E. & Markus, H. S. New Treatment Approaches to Modify the Course of Cerebral Small Vessel Diseases. *Stroke* **51**, 38–46 (2020).

19. Wardlaw, J. M. *et al.* Neuroimaging standards for research into small vessel disease and its contribution to ageing and neurodegeneration. *The Lancet Neurology* **12**, 822–838 (2013).

20. Giau, V. Van, Bagyinszky, E., Youn, Y. C., An, S. S. A. & Kim, S. Y. Genetic factors of cerebral small vessel disease and their potential clinical outcome. *International Journal of Molecular Sciences* **20**, (2019).

21. Haffner, C., Malik, R. & Dichgans, M. Genetic factors in cerebral small vessel disease and their impact on stroke and dementia. *J. Cereb. Blood Flow Metab.* **36**, 158–171 (2016).

22. de Leeuw, F. E. *et al.* Prevalence of cerebral white matter lesions in elderly people: a population based magnetic resonance imaging study. The Rotterdam Scan Study. *J. Neurol. Neurosurg. Psychiatry* **70**, 9–14 (2001).

23. De Silva, T. M. & Faraci, F. M. Contributions of Aging to Cerebral Small Vessel Disease. *Annu. Rev. Physiol.* **82**, 275–295 (2020).

24. Kalaria, R. N., Hase, Y. & Ihara, M. The rise and rise of cerebral small vessel disease: Implications for vascular cognitive impairment and dementia. *Future Neurology* **14**, (2019).

25. McGlasson, S. *et al.* Rare variants of the 3'-5' DNA exonuclease TREX1 in early onset small vessel stroke. *Wellcome Open Res.* **2**, (2017).

26.   Rannikmae, K. *et al.* Common variation in COL4A1/COL4A2 is associated with sporadic cerebral small vessel disease. *Neurology* **84**, 918–926 (2015).

27.   Mishra, A. *et al.* Association of variants in HTRA1 and NOTCH3 with MRI-defined extremes of cerebral small vessel disease in older subjects. doi:10.1093/brain/awz024

28.   Prins, N. D. & Scheltens, P. White matter hyperintensities, cognitive impairment and dementia: An update. *Nature Reviews Neurology* **11**, 157–165 (2015).

29.   Heye, A. K. *et al.* Blood pressure and sodium: Association with MRI markers in cerebral small vessel disease. *J. Cereb. Blood Flow Metab.* **36**, 264–274 (2016).

30.   Staals, J., Makin, S. D. J., Doubal, F. N., Dennis, M. S. & Wardlaw, J. M. Stroke subtype, vascular risk factors, and total MRI brain small-vessel disease burden. *Neurology* **83**, 1228–1234 (2014).

31.   Goldstein, L. B. *et al.* Primary prevention of ischemic stroke. A guideline from the American Heart Association/American Stroke Association Stroke Council: Cosponsored by the Atherosclerotic Peripheral Vascular Disease Interdisciplinary Working Group; Cardiovascular Nursing Council; Clinical Cardiology Council; Nutrition, Physical Activity, and Metabolism Council. *Stroke* **37**, 1583–1633 (2006).

32.   Dichgans, M. Genetics of ischaemic stroke. *Lancet Neurology* **6**, 149–161 (2007).

33.   Arntz, R. M. *et al.* Accelerated development of cerebral small vessel disease in young stroke patients. *Neurology* **87**, 1212–1219 (2016).

34.   Tan, R. Y. Y. *et al.* How common are single gene mutations as a cause for lacunar stroke? A targeted gene panel study. (2019). doi:10.1212/WNL.0000000000008544

35.   Tikka, S. *et al.* CADASIL and CARASIL. (2014). doi:10.1111/bpa.12181

36.   Joutel, A. *et al.* Notch3 mutations in CADASIL, a hereditary adult-onset condition causing stroke and dementia. *Nature* **383**, 707–710 (1996).

37.   Chabriat, H., Joutel, A., Dichgans, M., Tournier-Lasserve, E. & Bousser, M.-G. CADASIL. *Lancet Neurol.* **8**, 643–653 (2009).

38.   Hara, K. *et al.* Association of HTRA1 Mutations and Familial Ischemic Cerebral Small-Vessel Disease. *N. Engl. J. Med.* **360**, 1729–1739 (2009).

39.   Bugiani, M. *et al.* Cathepsin A-related arteriopathy with strokes and leukoencephalopathy (CARASAL). *Neurology* **87**, 1777–1786 (2016).

40.   Richards, A. *et al.* C-terminal truncations in human 3′-5′ DNA exonuclease TREX1

cause autosomal dominant retinal vasculopathy with cerebral leukodystrophy. *Nat. Genet.* **39**, 1068–1070 (2007).

41. Marini, S., Anderson, C. D. & Rosand, J. Genetics of Cerebral Small Vessel Disease. *Stroke* **51**, 12–20 (2020).

42. French, C. R. *et al.* Mutation of FOXC and PITX induces cerebral small-vessel disease. *J. Clin. Invest.* **124**, 4877–4881 (2014).

43. Nishimura, D. Y. *et al.* A spectrum of FOXC1 mutations suggests gene dosage as a mechanism for developmental defects of the anterior chamber of the eye. *Am. J. Hum. Genet.* **68**, 364–372 (2001).

44. Clark, J. M. *et al.* MELAS: Clinical and pathologic correlations with MRI, xenon/CT, and MR spectroscopy. *Neurology* **46**, 223–7 (1996).

45. Rolfs, A. *et al.* Prevalence of Fabry disease in patients with cryptogenic stroke: A prospective study. *Lancet* **366**, 1794–1796 (2005).

46. Kuo, D. S., Labelle-Dumais, C. & Gould, D. B. COL4A1 and COL4A2 mutations and disease: Insights into pathogenic mechanisms and potential therapeutic targets. *Hum. Mol. Genet.* **21**, (2012).

47. Verbeek, E. *et al.* COL4A2 mutation associated with familial porencephaly and small-vessel disease. *Eur. J. Hum. Genet.* **20**, 844–851 (2012).

48. Murray, L. S. *et al.* Chemical chaperone treatment reduces intracellular accumulation of mutant collagen IV and ameliorates the cellular phenotype of a COL4A2 mutation that causes haemorrhagic stroke. *Hum. Mol. Genet.* **23**, 283–292 (2014).

49. Shi, Y. & Wardlaw, J. M. Update on cerebral small vessel disease: a dynamic whole-brain disease. *Bmj* **1**, 83–92 (2016).

50. Choi, J. C. Genetics of cerebral small vessel disease. *J. stroke* **17**, 7–16 (2015).

51. Joutel, A. & Faraci, F. M. Cerebral small vessel disease: insights and opportunities from mouse models of collagen IV-related small vessel disease and cerebral autosomal dominant arteriopathy with subcortical infarcts and leukoencephalopathy. *Stroke* **45**, 1215–21 (2014).

52. Farrall, A. J. & Wardlaw, J. M. Blood-brain barrier: Ageing and microvascular disease - systematic review and meta-analysis. *Neurobiology of Aging* **30**, 337–352 (2009).

53. Taheri, S. *et al.* Blood-brain barrier permeability abnormalities in vascular cognitive

impairment. *Stroke* **42**, 2158–2163 (2011).

54. Schreiber, S., Bueche, C. Z., Garz, C. & Braun, H. Blood brain barrier breakdown as the starting point of cerebral small vessel disease? - New insights from a rat model. *Exp. Transl. Stroke Med.* **5**, 4 (2013).

55. Bhalerao, A. *et al.* In vitro modeling of the neurovascular unit: Advances in the field. *Fluids and Barriers of the CNS* **17**, (2020).

56. Choi, J. W. & Moon, W. J. Gadolinium deposition in the brain: Current updates. *Korean Journal of Radiology* **20**, 134–147 (2019).

57. Wardlaw, J. M. *et al.* Blood-brain barrier failure as a core mechanism in cerebral small vessel disease and dementia: evidence from a cohort study. *Alzheimer's Dement.* **13**, 634–643 (2017).

58. Ratelade, J. *et al.* Severity of arterial defects in the retina correlates with the burden of intracerebral haemorrhage in COL4A1-related stroke. *J. Pathol.* **244**, 408–420 (2018).

59. De Silva, T. M. & Miller, A. A. Cerebral Small Vessel Disease: Targeting Oxidative Stress as a Novel Therapeutic Strategy? *Front. Pharmacol.* **7**, 61 (2016).

60. Carvey, P. M., Hendey, B. & Monahan, A. J. The blood-brain barrier in neurodegenerative disease: A rhetorical perspective. *Journal of Neurochemistry* **111**, 291–314 (2009).

61. Wardlaw, J. M. *et al.* Blood-brain barrier failure as a core mechanism in cerebral small vessel disease and dementia: evidence from a cohort study. *Alzheimer's Dement.* **13**, 634–643 (2017).

62. Saunders, N. R., Habgood, M. D., Møllgård, K. & Dziegielewska, K. M. The biological significance of brain barrier mechanisms: Help or hindrance in drug delivery to the central nervous system? *F1000Research* **5**, (2016).

63. Wolburg, H., Noell, S., Mack, A., Wolburg-Buchholz, K. & Fallier-Becker, P. Brain endothelial cells and the glio-vascular complex. *Cell and Tissue Research* **335**, 75–96 (2009).

64. Wolburg, H. & Lippoldt, A. *Tight junctions of the blood-brain barrier: Development, composition and regulation*.

65. Wong, A. D. *et al.* The blood-brain barrier: an engineering perspective. *Front. Neuroeng.* **6**, 1–22 (2013).

66.   Mae, M., Armulik, A. & Betsholtz, C. Getting to Know the Cast - Cellular Interactions and Signaling at the Neurovascular Unit. *Curr. Pharm. Des.* **17**, 2750–2754 (2012).

67.   Abbott, N. J. & Friedman, A. Overview and introduction: The blood-brain barrier in health and disease. *Epilepsia* **53**, 1–6 (2012).

68.   Abbott, N. J., Rönnbäck, L. & Hansson, E. Astrocyte-endothelial interactions at the blood-brain barrier. *Nature Reviews Neuroscience* **7**, 41–53 (2006).

69.   Pardridge, W. M. Blood-brain barrier drug targeting: the future of brain drug development. *Molecular interventions* **3**, 90 (2003).

70.   Luissint, A.-C., Artus, C., Glacial, F., Ganeshamoorthy, K. & Couraud, P.-O. *Tight junctions at the blood brain barrier: physiological architecture and disease-associated dysregulation*. *Fluids and Barriers of the CNS* **9**, (2012).

71.   Paolinelli, R., Corada, M., Orsenigo, F. & Dejana, E. The molecular basis of the blood brain barrier differentiation and maintenance. Is it still a mystery? *Pharmacological Research* **63**, 165–171 (2011).

72.   Benson, K., Cramer, S. & Galla, H. J. Impedance-based cell monitoring: Barrier properties and beyond. *Fluids and Barriers of the CNS* **10**, (2013).

73.   Srinivasan, B. *et al.* TEER Measurement Techniques for In Vitro Barrier Model Systems. *Journal of Laboratory Automation* **20**, 107–126 (2015).

74.   Butt, A. M., Jones, H. C. & Abbott, N. J. Electrical resistance across the blood-brain barrier in anaesthetized rats: a developmental study. *J. Physiol.* **429**, 47–62 (1990).

75.   Wilhelm, I. & Krizbai, I. A. In vitro models of the blood-brain barrier for the study of drug delivery to the brain. *Molecular Pharmaceutics* (2014). doi:10.1021/mp500046f

76.   Smith, Q. R. & Rapoport, S. I. Cerebrovascular permeability coefficients to sodium, potassium, and chloride. *J. Neurochem.* **46**, 1732–42 (1986).

77.   Hollmann, E. K. *et al.* Accelerated differentiation of human induced pluripotent stem cells to blood–brain barrier endothelial cells. *Fluids Barriers CNS* **14**, 9 (2017).

78.   Nitta, T. *et al.* Size-selective loosening of the blood-brain barrier in claudin-5-deficient mice. *J. Cell Biol.* **161**, 653–660 (2003).

79.   Abbott, N. J., Patabendige, A. A. K., Dolman, D. E. M., Yusof, S. R. & Begley, D. J. Structure and function of the blood-brain barrier. *Neurobiology of Disease* **37**, 13–25 (2010).

80. Wimmer, I. *et al.* PECAM-1 stabilizes blood-brain barrier integrity and favors paracellular T-cell diapedesis across the blood-brain barrier during neuroinflammation. *Front. Immunol.* **10**, 711 (2019).

81. DeLisser, H. M. *et al.* Involvement of endothelial PECAM-1/CD31 in angiogenesis. *Am. J. Pathol.* **151**, 671–677 (1997).

82. Simpson, I. A., Vannucci, S. J., DeJoseph, M. R. & Hawkins, R. A. Glucose Transporter Asymmetries in the Bovine Blood-Brain Barrier. *J. Biol. Chem.* **276**, 12725–12729 (2001).

83. Warren, M. S. *et al.* Comparative gene expression profiles of ABC transporters in brain microvessel endothelial cells and brain in five species including human. *Pharmacol. Res.* **59**, 404–413 (2009).

84. Chen, C. jie *et al.* Internal duplication and homology with bacterial transport proteins in the mdr1 (P-glycoprotein) gene from multidrug-resistant human cells. *Cell* **47**, 381–389 (1986).

85. Chaves, C., Shawahna, R., Jacob, A., Scherrmann, J.-M. & Declèves, X. Human ABC Transporters at blood-CNS Interfaces as Determinants of CNS Drug Penetration. *Curr. Pharm. Des.* **20**, 1450–1462 (2014).

86. Gomez-Zepeda, D., Taghi, M., Scherrmann, J. M., Decleves, X. & Menet, M. C. ABC transporters at the blood–brain interfaces, their study models, and drug delivery implications in gliomas. *Pharmaceutics* **12**, 20 (2020).

87. Cecchelli, R. *et al.* Modelling of the blood - Brain barrier in drug discovery and development. *Nature Reviews Drug Discovery* **6**, 650–661 (2007).

88. Gottesman, M. M., Fojo, T. & Bates, S. E. Multidrug resistance in cancer: Role of ATP-dependent transporters. *Nature Reviews Cancer* **2**, 48–58 (2002).

89. Schinkel, A. H. P-Glycoprotein, a gatekeeper in the blood-brain barrier. *Advanced Drug Delivery Reviews* **36**, 179–194 (1999).

90. Schinkel, A. H. *et al.* Disruption of the mouse mdr1a P-glycoprotein gene leads to a deficiency in the blood-brain barrier and to increased sensitivity to drugs. *Cell* **77**, 491–502 (1994).

91. Demars, K. M. *et al.* Spatiotemporal changes in p-glycoprotein levels in brain and peripheral tissues following ischemic stroke in rats. *J. Exp. Neurosci.* **11**, (2017).

92. Miller, D. S., Bauer, B. & Hartz, A. M. S. Modulation of P-glycoprotein at the blood-

brain barrier: Opportunities to improve central nervous system pharmacotherapy. *Pharmacological Reviews* **60**, 196–209 (2008).

93. Worzfeld, T. & Schwaninger, M. Apicobasal polarity of brain endothelial cells. *Journal of Cerebral Blood Flow and Metabolism* **36**, 340–362 (2016).

94. Cait, J. *et al.* Podocalyxin is required for maintaining blood–brain barrier function during acute inflammation. *Proc. Natl. Acad. Sci. U. S. A.* **116**, 4518–4527 (2019).

95. Kalaria, R. N. & Kroon, S. N. *Expression of leukocyte antigen CD34 by brain capillaries in Alzheimer's disease and neurologically normal subjects*. HActa. europathologtca ~* **84**, (Springer-Verlag, 1992).

96. Mitic, L. L., Van Itallie, C. M. & Anderson, J. M. Molecular physiology and pathophysiology of tight junctions I. Tight junction structure and function: Lessons from mutant animals and proteins. *American Journal of Physiology - Gastrointestinal and Liver Physiology* **279**, (2000).

97. Volterra, A. & Meldolesi, J. Astrocytes, from brain glue to communication elements: The revolution continues. *Nature Reviews Neuroscience* **6**, 626–640 (2005).

98. Oberheim, N. A. *et al.* Uniquely hominid features of adult human astrocytes. *J. Neurosci.* **29**, 3276–3287 (2009).

99. Cabezas, R. *et al.* Astrocytic modulation of blood brain barrier: Perspectives on Parkinson's disease. *Frontiers in Cellular Neuroscience* **8**, (2014).

100. Haseloff, R. F., Blasig, I. E., Bauer, H. C. & Bauer, H. In search of the astrocytic factor(s) modulating blood-brain barrier functions in brain capillary endothelial cells in vitro. *Cellular and Molecular Neurobiology* **25**, 25–39 (2005).

101. Alvarez, J. I., Katayama, T. & Prat, A. Glial influence on the blood brain barrier. *GLIA* **61**, 1939–1958 (2013).

102. Shalaby, F. *et al.* Failure of blood-island formation and vasculogenesis in Flk-1-deficient mice. *Nature* **376**, 62–66 (1995).

103. Spampinato, S. F., Bortolotto, V., Canonico, P. L., Sortino, M. A. & Grilli, M. Astrocyte-derived paracrine signals: Relevance for neurogenic niche regulation and blood-brain barrier integrity. *Front. Pharmacol.* **10**, 1346 (2019).

104. Tao-Cheng, J. H., Nagy, Z. & Brightman, M. W. Tight junctions of brain endothelium in vitro are enhanced by astroglia. *J. Neurosci.* **7**, 3293–3299 (1987).

105. Prat, A., Biernacki, K., Wosik, K. & Antel, J. P. Glial cell influence on the human blood-brain barrier. *Glia* **36**, 145–155 (2001).

106. Iadecola, C. Neurovascular regulation in the normal brain and in Alzheimer's disease. *Nature Reviews Neuroscience* **5**, 347–360 (2004).

107. Chandrasekaran, A., Avci, H. X., Leist, M., Kobolák, J. & Dinnyés, A. Astrocyte Differentiation of Human Pluripotent Stem Cells: New Tools for Neurological Disorder Research. *Front. Cell. Neurosci.* **10**, (2016).

108. Kuegler, P. Markers of murine embryonic and neural stem cells, neurons and astrocytes: reference points for developmental neurotoxicity testing. *ALTEX* **27**, 16–41 (2010).

109. Gee, J. R. & Keller, J. N. Astrocytes: Regulation of brain homeostasis via apolipoprotein E. *International Journal of Biochemistry and Cell Biology* **37**, 1145–1150 (2005).

110. Daneman, R., Zhou, L., Kebede, A. A. & Barres, B. A. Pericytes are required for blood-brain barrier integrity during embryogenesis. *Nature* **468**, 562–566 (2010).

111. Dalkara, T., Gursoy-Ozdemir, Y. & Yemisci, M. Brain microvascular pericytes in health and disease. *Acta Neuropathologica* **122**, 1–9 (2011).

112. Fernández-Klett, F., Offenhauser, N., Dirnagl, U., Priller, J. & Lindauer, U. Pericytes in capillaries are contractile in vivo, but arterioles mediate functional hyperemia in the mouse brain. *Proc. Natl. Acad. Sci. U. S. A.* **107**, 22290–22295 (2010).

113. Sweeney, M. D., Ayyadurai, S. & Zlokovic, B. V. Pericytes of the neurovascular unit: Key functions and signaling pathways. *Nature Neuroscience* **19**, 771–783 (2016).

114. Sims, D. E. The pericyte--a review. *Tissue Cell* **18**, 153–74 (1986).

115. Van Dijk, C. G. M. *et al.* The complex mural cell: Pericyte function in health and disease. *International Journal of Cardiology* **190**, 75–89 (2015).

116. Majesky, M. W. Developmental Basis of Vascular Smooth Muscle Diversity. *Arterioscler. Thromb. Vasc. Biol.* **27**, 1248–1258 (2007).

117. Etchevers, H. C., Dupin, E. & Le Douarin, N. M. The diverse neural crest: From embryology to human pathology. *Dev.* **146**, (2019).

118. Faal, T. *et al.* Induction of Mesoderm and Neural Crest-Derived Pericytes from Human Pluripotent Stem Cells to Study Blood-Brain Barrier Interactions. *Stem Cell Reports*

12, 451–460 (2019).

119. Peppiatt, C. M., Howarth, C., Mobbs, P. & Attwell, D. Bidirectional control of CNS capillary diameter by pericytes. *Nature* **443**, 700–704 (2006).

120. Armulik, A., Abramsson, A. & Betsholtz, C. Endothelial/pericyte interactions. *Circulation Research* **97**, 512–523 (2005).

121. Bell, R. D. *et al.* Pericytes Control Key Neurovascular Functions and Neuronal Phenotype in the Adult Brain and during Brain Aging. *Neuron* **68**, 409–427 (2010).

122. Armulik, A. *et al.* Pericytes regulate the blood-brain barrier. *Nature* **468**, 557–561 (2010).

123. Cho, H., Kozasa, T., Bondjers, C., Betsholtz, C. & Kehrl, J. H. Pericyte-specific expression of Rgs5: implications for PDGF and EDG receptor signaling during vascular maturation. *FASEB J.* **17**, 440–2 (2003).

124. Bondjers, C. *et al.* Microarray analysis of blood microvessels from PDGF-B and PDGF-Rβ mutant mice identifies novel markers for brain pericytes. *FASEB J.* **20**, 1703–1705 (2006).

125. Naba, A. *et al.* The Matrisome: In Silico Definition and In Vivo Characterization by Proteomics of Normal and Tumor Extracellular Matrices. *Mol. Cell. Proteomics* **11**, M111.014647 (2012).

126. Xu, L., Nirwane, A. & Yao, Y. Basement membrane and blood-brain barrier. *Stroke and Vascular Neurology* **4**, 78–82 (2019).

127. LeBleu, V. S., MacDonald, B. & Kalluri, R. Structure and Function of Basement Membranes. *Exp. Biol. Med.* **232**, 1121–1129 (2007).

128. Kalluri, R. Basement membranes: structure, assembly and role in tumour angiogenesis. *Nat. Rev. Cancer* **3**, 422–433 (2003).

129. Joutel, A., Haddad, I., Ratelade, J. & Nelson, M. T. Perturbations of the cerebrovascular matrisome: A convergent mechanism in small vessel disease of the brain? *J. Cereb. Blood Flow Metab.* **36**, 143–57 (2016).

130. Yurchenco, P. D. Basement membranes: Cell scaffoldings and signaling platforms. *Cold Spring Harb. Perspect. Biol.* **3**, 1–27 (2011).

131. Vracko, R. & Benditt, E. P. Capillary basal lamina thickening: Its relationship to endothelial cell death and replacement. *Journal of Cell Biology* **47**, 281–285 (1970).

132. Bonnans, C., Chou, J. & Werb, Z. Remodelling the extracellular matrix in development and disease. *Nature Reviews Molecular Cell Biology* **15**, 786–801 (2014).

133. Raghunathan, R., Sethi, M. K., Klein, J. A. & Zaia, J. Proteomics, glycomics, and glycoproteomics of matrisome molecules. *Mol. Cell. Proteomics* **18**, 2138–2148 (2019).

134. Hohenester, E. & Yurchenco, P. D. Laminins in basement membrane assembly. *Cell Adhesion and Migration* **7**, 56–63 (2013).

135. Breitkreutz, D., Koxholt, I., Thiemann, K. & Nischt, R. Skin basement membrane: The foundation of epidermal integrity - BM functions and diverse roles of bridging molecules nidogen and perlecan. *Biomed Res. Int.* **2013**, (2013).

136. Stratman, A. N., Malotte, K. M., Mahan, R. D., Davis, M. J. & Davis, G. E. Pericyte recruitment during vasculogenic tube assembly stimulates endothelial basement membrane matrix formation. *Blood* **114**, 5091–5101 (2009).

137. Verkman, A. S. Aquaporin water channels and endothelial cell function*. *J. Anat.* **200**, 617–627 (2002).

138. Freitas-Rodríguez, S., Folgueras, A. R. & López-Otín, C. The role of matrix metalloproteinases in aging: Tissue remodeling and beyond. *Biochimica et Biophysica Acta - Molecular Cell Research* **1864**, 2015–2025 (2017).

139. Frantz, C., Stewart, K. M. & Weaver, V. M. The extracellular matrix at a glance. *Journal of Cell Science* **123**, 4195–4200 (2010).

140. Horsburgh, K. *et al.* Small vessels, dementia and chronic diseases - molecular mechanisms and pathophysiology. *Clin. Sci.* **132**, 851–868 (2018).

141. Monet-Leprê Tre, M. *et al.* Abnormal recruitment of extracellular matrix proteins by excess Notch3 ECD : a new pathomechanism in CADASIL. *A J. Neurol.* doi:10.1093/brain/awt092

142. Beaufort, N. *et al.* Cerebral small vessel disease-related protease HtrA1 processes latent TGF-β binding protein 1 and facilitates TGF-β signaling. *Proc. Natl. Acad. Sci. U. S. A.* **111**, 16496–16501 (2014).

143. Ge, G. & Greenspan, D. S. BMP1 controls TGFβ1 activation via cleavage of latent TGFβ-binding protein. *J. Cell Biol.* **175**, 111–120 (2006).

144. Skarie, J. M. & Link, B. A. FoxC1 is essential for vascular basement membrane integrity and hyaloid vessel morphogenesis. *Investig. Ophthalmol. Vis. Sci.* **50**, 5026–

5034 (2009).

145.   Stamenkovic, I. Extracellular matrix remodelling: The role of matrix metalloproteinases. *Journal of Pathology* **200**, 448–464 (2003).

146.   Seo, S. *et al.* Forkhead box transcription factor FoxC1 preserves corneal transparency by regulating vascular growth. *Proc. Natl. Acad. Sci. U. S. A.* **109**, 2015–2020 (2012).

147.   Plaisier, E. *et al. COL4A1* Mutations and Hereditary Angiopathy, Nephropathy, Aneurysms, and Muscle Cramps. *N. Engl. J. Med.* **357**, 2687–2695 (2007).

148.   Craggs, L. J., Yamamoto, Y., Deramecourt, V. & Kalaria, R. N. Microvascular Pathology and Morphometrics of Sporadic and Hereditary Small Vessel Diseases of the Brain. doi:10.1111/bpa.12177

149.   Farkas, E. *et al.* Age-related microvascular degeneration in the human cerebral periventricular white matter. *Acta Neuropathol.* **111**, 150–157 (2006).

150.   Martinez-Lemus, L. A., Zhao, G., Galiñanes, E. L. & Boone, M. Inward remodeling of resistance arteries requires reactive oxygen species-dependent activation of matrix metalloproteinases. *Am. J. Physiol. - Hear. Circ. Physiol.* **300**, (2011).

151.   Lemarié, C. A., Tharaux, P. L. & Lehoux, S. Extracellular matrix alterations in hypertensive vascular remodeling. *Journal of Molecular and Cellular Cardiology* **48**, 433–439 (2010).

152.   Rannikmäe, K. *et al.* Common variation in COL4A1/COL4A2 is associated with sporadic cerebral small vessel disease. *Neurology* **84**, (2015).

153.   McCaffrey, G. & Davis, T. P. Physiology and pathophysiology of the blood-brain barrier: P-glycoprotein and occludin trafficking as therapeutic targets to optimize central nervous system drug delivery. *J. Investig. Med.* **60**, 1131–40 (2012).

154.   Wardlaw, J. M. *et al.* Blood-brain barrier failure as a core mechanism in cerebral small vessel disease and dementia: evidence from a cohort study. (2017). doi:10.1016/j.jalz.2016.09.006

155.   Candelario-Jalil, E. *et al.* Matrix metalloproteinases are associated with increased blood-brain barrier opening in vascular cognitive impairment. *Stroke* **42**, 1345–1350 (2011).

156.   Yang, Y. & Rosenberg, G. A. Blood-brain barrier breakdown in acute and chronic cerebrovascular disease. *Stroke* **42**, 3323–3328 (2011).

157. Arba, F. *et al.* Small Vessel Disease Is Associated with Tissue Inhibitor of Matrix Metalloproteinase-4 After Ischaemic Stroke. *Transl. Stroke Res.* **10**, 44–51 (2019).

158. Werb, Z. ECM and cell surface proteolysis: Regulating cellular ecology. *Cell* **91**, 439–442 (1997).

159. Matrisian, L. M. The matrix-degrading metalloproteinases. *BioEssays* **14**, 455–463 (1992).

160. Malemud, C. J. Matrix metalloproteinases (MMPs) in health and disease: An overview. *Frontiers in Bioscience* **11**, 1696–1701 (2006).

161. Têtu, B. *et al.* The influence of MMP-14, TIMP-2 and MMP-2 expression on breast cancer prognosis. *Breast Cancer Res.* **8**, R28 (2006).

162. Stetler-Stevenson+, W. G., Brown, P. D., Onisto, M., Levy, A. T. & Liotta, L. A. *Tissue Inhibitor of Metalloproteinases-2 (TIMP-2) mRNA Expression in Tumor Cell Lines and Human Tumor Tissues*. **265**,

163. Deryugina, E. I. *et al.* MT1-MMP initiates activation of pro-MMP-2 and integrin αvβ3 promotes maturation of MMP-2 in breast carcinoma cells. *Exp. Cell Res.* **263**, 209–223 (2001).

164. Xia, W. *et al.* Expression of catalytically active matrix metalloproteinase-1 in dermal fibroblasts induces collagen fragmentation and functional alterations that resemble aged human skin. *Aging Cell* **12**, 661–671 (2013).

165. Zeng, Z.-S., Cohen, A. M., José, J. & Guillem, G. *Loss of basement membrane type IV collagen is associated with increased expression of metalloproteinases 2 and 9 (MMP-2 and MMP-9) during human colorectal tumorigenesis*. *Carcinogenesis* **20**, (1999).

166. Roach, D. M. *et al.* Up-regulation of MMP-2 and MMP-9 leads to degradation of type IV collagen during skeletal muscle reperfusion injury; protection by the MMP inhibitor, doxycycline. *Eur. J. Vasc. Endovasc. Surg.* **23**, 260–269 (2002).

167. Itoh, Y., Parks, W. C. & Apte, S. Membrane-type matrix metalloproteinases: Their functions and regulations. (2015). doi:10.1016/j.matbio.2015.03.004

168. OKADA, Y. *et al.* Matrix metalloproteinase 2 from human rheumatoid synovial fibroblasts: Purification and activation of the precursor and enzymic properties. *Eur. J. Biochem.* **194**, 721–730 (1990).

169. Stracke, J. O. *et al.* Biochemical characterization of the catalytic domain of human

matrix metalloproteinase 19. Evidence for a role as a potent basement membrane degrading enzyme. *J. Biol. Chem.* **275**, 14809–14816 (2000).

170. Nagase, H., Visse, R. & Murphy, G. Structure and function of matrix metalloproteinases and TIMPs. *Cardiovascular Research* **69**, 562–573 (2006).

171. Gurney, K. J., Estrada, E. Y. & Rosenberg, G. A. Blood-brain barrier disruption by stromelysin-1 facilitates neutrophil infiltration in neuroinflammation. *Neurobiol. Dis.* **23**, 87–96 (2006).

172. Lakhan, S. E., Kirchgessner, A., Tepper, D. & Leonard, A. Matrix metalloproteinases and blood-brain barrier disruption in acute ischemic stroke. *Front. Neurol.* **4 APR**, (2013).

173. Mun-Bryce, S. & Rosenberg, G. A. Matrix metalloproteinases in cerebrovascular disease. *Journal of Cerebral Blood Flow and Metabolism* **18**, 1163–1172 (1998).

174. Pan, R. *et al.* Blood Occludin Level as a Potential Biomarker for Early Blood Brain Barrier Damage Following Ischemic Stroke. *Sci. Rep.* **7**, 40331 (2017).

175. Liu, J., Jin, X., Liu, K. J. & Liu, W. Matrix metalloproteinase-2-mediated occludin degradation and caveolin-1-mediated claudin-5 redistribution contribute to blood-brain barrier damage in early ischemic stroke stage. *J. Neurosci.* **32**, 3044–3057 (2012).

176. Clark, A. W., Krekoski, C. A., Bou, S. S., Chapman, K. R. & Edwards, D. R. Increased gelatinase A (MMP-2) and gelatinase B (MMP-9) activities in human brain after focal ischemia. *Neurosci. Lett.* **238**, 53–56 (1997).

177. Zhao, B. Q. *et al.* Role of matrix metalloproteinases in delayed cortical responses after stroke. *Nat. Med.* **12**, 441–445 (2006).

178. McColl, B. W., Rothwell, N. J. & Allan, S. M. Systemic inflammation alters the kinetics of cerebrovascular tight junction disruption after experimental stroke in mice. *J. Neurosci.* **28**, 9451–9462 (2008).

179. Lapchak, P. A., Chapman, D. F. & Zivin, J. A. Metalloproteinase inhibition reduces thrombolytic (tissue plasminogen activator)-induced hemorrhage after thromboembolic stroke. *Stroke* **31**, 3034–3040 (2000).

180. Wang, X. *et al.* Lipoprotein receptor-mediated induction of matrix metalloproteinase by tissue plasminogen activator. *Nat. Med.* **9**, 1313–1317 (2003).

181. Adibhatla, R. & Hatcher, J. Tissue Plasminogen Activator (tPA) and Matrix Metalloproteinases in the Pathogenesis of Stroke: Therapeutic Strategies. *CNS*

Neurol. Disord. - Drug Targets **7**, 243–253 (2008).

182. Planas, A. M., Solé, S. & Justicia, C. Expression and activation of matrix metalloproteinase-2 and -9 in rat brain after transient focal cerebral ischemia. *Neurobiol. Dis.* **8**, 834–846 (2001).

183. Gasche, Y. *et al.* Early appearance of activated matrix metalloproteinase-9 after focal cerebral ischemia in mice: A possible role in blood-brain barrier dysfunction. *J. Cereb. Blood Flow Metab.* **19**, 1020–1028 (1999).

184. Rosenberg, G. A., Estrada, E. Y. & Dencoff, J. E. Matrix metalloproteinases and TIMPs are associated with blood-brain barrier opening after reperfusion in rat brain. *Stroke* **29**, 2189–2195 (1998).

185. Cuadrado, E. *et al.* Vascular MMP-9/TIMP-2 and neuronal MMP-10 up-regulation in human brain after stroke: A combined laser microdissection and protein array study. *J. Proteome Res.* **8**, 3191–3197 (2009).

186. Fujimoto, M. *et al.* Tissue inhibitor of metalloproteinases protect blood-brain barrier disruption in focal cerebral ischemia. *J. Cereb. Blood Flow Metab.* **28**, 1674–1685 (2008).

187. Pires, P. W. *et al.* Doxycycline, a matrix metalloprotease inhibitor, reduces vascular remodeling and damage after cerebral ischemia in stroke-prone spontaneously hypertensive rats. *Am. J. Physiol. - Hear. Circ. Physiol.* **301**, H87 (2011).

188. Malek, A. *et al.* Doxycycline improves traumatic brain injury outcomes in a murine survival model. *J. Trauma Acute Care Surg.* (2020).

189. Winer, A., Adams, S. & Mignatti, P. Matrix metalloproteinase inhibitors in cancer therapy: Turning past failures into future successes. *Molecular Cancer Therapeutics* **17**, 1147–1155 (2018).

190. Horstmann, S., Kalb, P., Koziol, J., Gardner, H. & Wagner, S. Profiles of matrix metalloproteinases, their inhibitors, and laminin in stroke patients: Influence of different therapies. *Stroke* **34**, 2165–2170 (2003).

191. Montaner, J. *et al.* Matrix metalloproteinase-9 pretreatment level predicts intracranial hemorrhagic complications after thrombolysis in human stroke. *Circulation* **107**, 598–603 (2003).

192. Lanfranconi, S. & Markus, H. S. COL4A1 mutations as a monogenic cause of cerebral small vessel disease: A systematic review. *Stroke* **41**, (2010).

193. Haniel, A., Welge-Lussen, U., Kuhn, K. & Poschl, E. Identification and characterization of a novel transcriptional silencer in the human collagen type IV gene COL4A2. *J. Biol. Chem.* **270**, 11209–11215 (1995).

194. Jeanne, M. & Gould, D. B. Genotype-phenotype correlations in pathology caused by collagen type IV alpha 1 and 2 mutations. *Matrix Biol.* **57–58**, 29–44 (2017).

195. Borza, D. B. *et al.* The NC1 Domain of Collagen IV Encodes a Novel Network Composed of the α1, α2, α5, and α6 Chains in Smooth Muscle Basement Membranes. *J. Biol. Chem.* **276**, 28532–28540 (2001).

196. Khoshnoodi, J. *et al.* Mechanism of chain selection in the assembly of collagen IV: A prominent role for the α2 chain. *J. Biol. Chem.* **281**, 6058–6069 (2006).

197. Ishikawa, Y. & Bächinger, H. P. A molecular ensemble in the rER for procollagen maturation ☆. (2013). doi:10.1016/j.bbamcr.2013.04.008

198. Ries, A., Engel, J., Lustig, A. & Kuhn, K. The function of the NC1 domains in type IV collagen. *J. Biol. Chem.* **270**, 23790–23794 (1995).

199. Dixit, S. N. *et al.* Type IV Collagens: Isolation and Characterization of 7S Collagen from Human Kidney, Liver and Lung. *Top. Catal.* **1**, 549–556 (1981).

200. Labelle-Dumais, C. *et al.* COL4A1 mutations cause ocular dysgenesis, neuronal localization defects, and myopathy in mice and walker-warburg syndrome in humans. *PLoS Genet.* **7**, (2011).

201. Jeanne, M., Jorgensen, J. & Gould, D. B. Molecular and genetic analyses of collagen type IV mutant mouse models of spontaneous intracerebral hemorrhage identify mechanisms for stroke prevention. *Circulation* **131**, 1555–1565 (2015).

202. Khoshnoodi, J., Pedchenko, V. & Hudson, B. G. Mammalian collagen IV. *Microsc. Res. Tech.* **71**, 357–370 (2008).

203. Rødahl, E. *et al.* Variants of anterior segment dysgenesis and cerebral involvement in a large family with a novel COL4A1 mutation. *Am. J. Ophthalmol.* **155**, 946–953 (2013).

204. Trüeb, B., Gröbli, B., Spiess, M., Odermatt, B. F. & Winterhalter, K. H. Basement membrane (type IV) collagen is a heteropolymer. *J. Biol. Chem.* **257**, 5239–45 (1982).

205. de Vries, L. S. *et al.* COL4A1 mutation in two preterm siblings with antenatal onset of parenchymal hemorrhage. *Ann. Neurol.* **65**, 12–18 (2009).

206.   Corlobe, A. *et al.* COL4A1 Mutation Revealed by an Isolated Brain Hemorrhage. *Cerebrovasc. Dis.* **35**, 593–594 (2013).

207.   Labelle-Dumais, C. *et al.* COL4A1 Mutations Cause Neuromuscular Disease with Tissue-Specific Mechanistic Heterogeneity. *Am. J. Hum. Genet.* **104**, 847–860 (2019).

208.   Plaisier, E. *et al.* Novel COL4A1 mutations associated with HANAC syndrome: A role for the triple helical CB3[IV] domain. *Am. J. Med. Genet. Part A* **152 A**, 2550–2555 (2010).

209.   Alamowitch, S. *et al.* Cerebrovascular disease related to COL4A1 mutations in HANAC syndrome. *Neurology* **73**, 1873–1882 (2009).

210.   Chen, Z. *et al.* HANAC syndrome Col4a1 mutation causes neonate glomerular hyperpermeability and adult glomerulocystic kidney disease. *J. Am. Soc. Nephrol.* **27**, 1042–1054 (2016).

211.   Takenouchi, T. *et al.* Porencephaly in a fetus and HANAC in her father: Variable expression of COL4A1 mutation. *Am. J. Med. Genet. Part A* **167**, 156–158 (2015).

212.   Shah, S. *et al.* A dominantly inherited mutation in collagen IV A1 (COL4A1) causing childhood onset stroke without porencephaly. *Eur. J. Paediatr. Neurol.* (2010). doi:10.1016/j.ejpn.2009.04.010

213.   Lichtenbelt, K. D., Pistorius, L. R., De Tollenaer, S. M., Mancini, G. M. & De Vries, L. S. Prenatal genetic confirmation of a COL4A1 mutation presenting with sonographic fetal intracranial hemorrhage. *Ultrasound in Obstetrics and Gynecology* **39**, 726–727 (2012).

214.   Matsumoto, T. *et al.* Intracranial sonographic features demonstrating in utero development of hemorrhagic brain damage leading to schizencephaly-associated COL4A1 mutation. *J. Med. Ultrason.* **42**, 445–446 (2015).

215.   Zagaglia, S. *et al.* Neurologic phenotypes associated with COL4A1/2 mutations: Expanding the spectrum of disease. *Neurology* **91**, e2078–e2088 (2018).

216.   Yaramis, A. *et al.* COL4A1 -related autosomal recessive encephalopathy in 2 Turkish children. *Neurol. Genet.* **6**, (2020).

217.   Shah, S. *et al.* Childhood presentation of COL4A1 mutations. *Dev. Med. Child Neurol.* **54**, 569–574 (2012).

218.   Sato, Y. *et al.* Novel COL4A1 mutation in a fetus with early prenatal onset of schizencephaly. *Hum. Genome Var.* **5**, 1–4 (2018).

219. Hino-Fukuyo, N. *et al.* Dramatic response after functional hemispherectomy in a patient with epileptic encephalopathy carrying a de novo COL4A1 mutation. *Brain Dev.* **39**, 337–340 (2017).

220. Meuwissen, M. E. C. *et al.* The expanding phenotype of COL4A1 and COL4A2 mutations: Clinical data on 13 newly identified families and a review of the literature. *Genetics in Medicine* **17**, 843–853 (2015).

221. Lemmens, R. *et al.* Novel COL4A1 mutations cause cerebral small vessel disease by haploinsufficiency. *Hum. Mol. Genet.* **22**, 391–7 (2013).

222. Zhao, Y. Y., Duan, R. N., Ji, L., Liu, Q. J. & Yan, C. Z. Cervical Spinal Involvement in a Chinese Pedigree with Pontine Autosomal Dominant Microangiopathy and Leukoencephalopathy Caused by a 3′ Untranslated Region Mutation of COL4A1 Gene. *Stroke* **50**, 2307–2313 (2019).

223. Breedveld, G. *et al.* Novel mutations in three families confirm a major role of COL4A1 in hereditary porencephaly. *J. Med. Genet.* **43**, 490–5 (2006).

224. Weng, Y. C. *et al.* COL4A1 mutations in patients with sporadic late-onset intracerebral hemorrhage. *Ann. Neurol.* **71**, 470–477 (2012).

225. Giorgio, E. *et al.* Two families with novel missense mutations in COL4A1: When diagnosis can be missed. *J. Neurol. Sci.* **352**, 99–104 (2015).

226. Russo, A., Pinto, A. M., Lopergolo, D., Renieri, A. & Battisti, C. An Italian family carrying a new mutation in the COL4A1 gene. *Journal of the Neurological Sciences* **414**, 116815 (2020).

227. Gould, D. B. *et al.* Role of COL4A1 in Small-Vessel Disease and Hemorrhagic Stroke. *N. Engl. J. Med.* **354**, 1489–1496 (2006).

228. Vahedi, K. *et al.* Clinical and brain MRI follow-up study of a family with COL4A1 mutation. *Neurology* **69**, 1564–1568 (2007).

229. Livingston, J. *et al.* COL4A1 mutations associated with a characteristic pattern of intracranial calcification. *Neuropediatrics* **42**, 227–233 (2011).

230. Campo-Caballero, D. *et al.* COL4A1 Mutation as a Cause of Familial Recurrent Intracerebral Hemorrhage. *J. Stroke Cerebrovasc. Dis.* **29**, 104652 (2020).

231. Kinoshita, K. *et al.* De novo p.G696S mutation in COL4A1 causes intracranial calcification and late-onset cerebral hemorrhage: A case report and review of the literature COL4A1-associated vasculopathy. *Eur. J. Med. Genet.* **63**, (2020).

232. Smigiel, R. *et al.* Novel COL4A1 mutation in an infant with severe dysmorphic syndrome with schizencephaly, periventricular calcifications, and cataract resembling congenital infection. *Birth Defects Res. A. Clin. Mol. Teratol.* **106**, 304–307 (2016).

233. Sibon, I. *et al.* COL4A1 mutation in Axenfeld-Rieger anomaly with leukoencephalopathy and stroke. *Ann. Neurol.* **62**, 177–184 (2007).

234. Nandeesh, B. N. *et al.* Cerebral small vessel disease with hemorrhagic stroke related to COL4A1 mutation: A case report. *Neuropathology* **40**, 93–98 (2020).

235. Gould, D. B. *et al.* Mutations in Col4a1 Cause Perinatal Cerebral Hemorrhage and Porencephaly. *Science (80-.).* **308**, 1167–1171 (2005).

236. Aguglia, U. *et al.* Suggestive evidence for linkage to chromosome 13qter for autosomal dominant type 1 porencephaly. *Neurology* **62**, 1613–5 (2004).

237. Vermeulen, R. J. *et al.* Fetal origin of brain damage in 2 infants with a COL4A1 mutation: Fetal and neonatal MRI. *Neuropediatrics* **42**, 1–3 (2011).

238. Watanabe, J. *et al.* Malignant Hyperthermia and Cerebral Venous Sinus Thrombosis After Ventriculoperitoneal Shunt in Infant with Schizencephaly and COL4A1 Mutation. *World Neurosurg.* **127**, 446–450 (2019).

239. Durrani-Kolarik, S., Manickam, K. & Chen, B. COL4A1 Mutation in a Neonate With Intrauterine Stroke and Anterior Segment Dysgenesis. *Pediatr. Neurol.* **66**, 100–103 (2017).

240. Vahedi, K. *et al.* COL4A1 mutation in a patient with sporadic, recurrent intracerebral hemorrhage. *Stroke* **38**, 1461–1464 (2007).

241. Meuwissen, M. E. C. *et al.* Sporadic COL4A1 mutations with extensive prenatal porencephaly resembling hydranencephaly. *Neurology* **76**, 844–846 (2011).

242. Hatano, T. *et al.* Dystonia due to bilateral caudate hemorrhage associated with a COL4A1 mutation. *Parkinsonism and Related Disorders* **40**, 80–82 (2017).

243. Rim, J. H. *et al.* Efficient strategy for the molecular diagnosis of intractable early-onset epilepsy using targeted gene sequencing. *BMC Med. Genomics* **11**, 6 (2018).

244. Nau, S. *et al.* COL4A1 mutations in two infants with congenital cataracts and porencephaly: an ophthalmologic perspective. *J. AAPOS* **23**, 246–248 (2019).

245. Plancher, J. M. *et al.* Case of Small Vessel Disease Associated with COL4A1 Mutations following Trauma. *Case Rep. Neurol.* **7**, 142–147 (2015).

246. Abe, Y. *et al.* A severe pulmonary complication in a patient with COL4A1-related disorder: A case report. *Eur. J. Med. Genet.* **60**, 169–171 (2017).

247. Tomotaki, S. *et al.* Severe Hemolytic Jaundice in a Neonate with a Novel COL4A1 Mutation. *Pediatr. Neonatol.* **57**, 522–525 (2016).

248. Gould, D. B. *et al.* Mutations in Col4a1 Cause Perinatal Cerebral Hemorrhage and Porencephaly. *Science (80-.).* **308**, 1167–1171 (2005).

249. Van Der Knaap, M. S. *et al.* Neonatal porencephaly and adult stroke related to mutations in collagen IV A1. *Ann. Neurol.* **59**, 504–511 (2006).

250. Cavallin, M. *et al.* Further refinement of COL4A1 and COL4A2 related cortical malformations. *Eur. J. Med. Genet.* **61**, 765–772 (2018).

251. Niwa, T. *et al.* Intracranial hemorrhage and tortuosity of veins detected on susceptibility-weighted imaging of a child with a type IV collagen α1 mutation and schizencephaly. *Magn. Reson. Med. Sci.* **14**, 223–226 (2015).

252. Yoneda, Y. *et al.* Phenotypic spectrum of COL4A1 mutations: Porencephaly to schizencephaly. *Ann. Neurol.* **73**, 48–57 (2013).

253. Leung, M. *et al.* COL4A1 mutation in a pediatric patient presenting with post-ictal hemiparesis. *Can. J. Neurol. Sci.* **39**, 654–657 (2012).

254. Bilguvar, K. *et al.* COL4A1 Mutation in Preterm Intraventricular Hemorrhage. *J. Pediatr.* **155**, 743–745 (2009).

255. Han, X., Pang, Z., Wang, Z., Xu, S. & Lin, Y. A case of primary angiitis of the central nervous system presenting with diffuse cerebral microbleeds and recurrent intracranial hemorrhage. *Neurological Sciences* **40**, 417–419 (2019).

256. Kollmann, P., Peeters, A., Vanakker, O. & Sznajer, Y. 'De novo' Col4A2 mutation in a patient with migraine, leukoencephalopathy, and small carotid aneurysms. *Journal of Neurology* **263**, 2327–2329 (2016).

257. Ha, T. T. *et al.* A mutation in COL4A2 causes autosomal dominant porencephaly with cataracts. *Am. J. Med. Genet. Part A* **170**, 1059–1063 (2016).

258. Gunda, B. *et al.* COL4A2 mutation causing adult onset recurrent intracerebral hemorrhage and leukoencephalopathy. *J. Neurol.* **261**, 500–503 (2014).

259. Yoneda, Y. *et al.* De novo and inherited mutations in COL4A2, encoding the type IV collagen α2 chain cause porencephaly. *Am. J. Hum. Genet.* **90**, 86–90 (2012).

260. Ilinca, A. *et al.* Whole-Exome Sequencing in 22 Young Ischemic Stroke Patients with Familial Clustering of Stroke. *Stroke* **51**, 1056–1063 (2020).

261. Meuwissen, M. E. C. *et al.* The expanding phenotype of COL4A1 and COL4A2 mutations: clinical data on 13 newly identified families and a review of the literature. *Genet. Med.* **17**, (2015).

262. Jeanne, M. *et al.* COL4A2 Mutations Impair COL4A1 and COL4A2 Secretion and Cause Hemorrhagic Stroke. (2012). doi:10.1016/j.ajhg.2011.11.022

263. McGovern, M., Flanagan, O., Lynch, B., Lynch, S. A. & Allen, N. M. Novel *COL4A2* variant in a large pedigree: Consequences and dilemmas. *Clin. Genet.* **92**, 447–448 (2017).

264. Parkin, J. Des *et al.* Mapping structural landmarks, ligand binding sites, and missense mutations to the collagen IV heterotrimers predicts major functional domains, novel interactions, and variation in phenotypes in inherited diseases affecting basement membranes. *Human Mutation* **32**, 127–143 (2011).

265. Grosfeld, A. *et al.* Interaction of hydroxylated collagen IV with the von Hippel-Lindau tumor suppressor. *J. Biol. Chem.* **282**, 13264–13269 (2007).

266. Chen, Z. L. *et al.* Ablation of astrocytic laminin impairs vascular smooth muscle cell function and leads to hemorrhagic stroke. *J. Cell Biol.* **202**, 381–395 (2013).

267. Pöschl, E. *et al.* Collagen IV is essential for basement membrane stability but dispensable for initiation of its assembly during early development. *Development* **131**, 1619–28 (2004).

268. Shah, S. *et al.* A dominantly inherited mutation in collagen IV A1 (COL4A1) causing childhood onset stroke without porencephaly. *Eur. J. Paediatr. Neurol.* **14**, 182–187 (2010).

269. van Agtmael, T. *et al.* Col4a1 mutation in mice causes defects in vascular function and low blood pressure associated with reduced red blood cell volume. *Human Molecular Genetics* **19**, 1119–1128 (2010).

270. Favor, J. *et al.* Type IV procollagen missense mutations associated with defects of the eye, vascular stability, the brain, kidney function and embryonic or postnatal viability in the mouse, Mus musculus: An extension of the Col4a1 allelic series and the identification of the first two Col4a2 mutant alleles. *Genetics* **175**, 725–736 (2007).

271. Van Agtmael, T. *et al.* Dominant mutations of Col4a1 result in basement membrane

defects which lead to anterior segment dysgenesis and glomerulopathy. *Hum. Mol. Genet.* **14**, 3161–3168 (2005).

272. Hainsworth, A. H. & Markus, H. S. Do in vivo experimental models reflect human cerebral small vessel disease? A systematic review. *Journal of Cerebral Blood Flow and Metabolism* **28**, 1877–1891 (2008).

273. Naik, P. & Cucullo, L. In vitro blood-brain barrier models: Current and perspective technologies. *Journal of Pharmaceutical Sciences* **101**, 1337–1354 (2012).

274. Song, L. I. & Pachter, J. S. *Culture of murine brain microvascular endothelial Cells that maintain expression and cytoskeletal association of tight junction-associated proteins. In Vitro Cell. Dev. Biol.~Animal* **39**,

275. Begley, D. J. *et al.* Functional Expression of P-Glycoprotein in an Immortalised Cell Line of Rat Brain Endothelial Cells, RBE4. *J. Neurochem.* **67**, 988–995 (2002).

276. Ades, E. W. *et al.* HMEC-1: Establishment of an immortalized human microvascular endothelial cell line. *J. Invest. Dermatol.* **99**, 683–690 (1992).

277. Poller, B. *et al.* The human brain endothelial cell line hCMEC/D3 as a human blood-brain barrier model for drug transport studies. *J. Neurochem.* **107**, 1358–1368 (2008).

278. Adriani, G., Ma, D., Pavesi, A., Kamm, R. D. & Goh, E. L. K. A 3D neurovascular microfluidic model consisting of neurons, astrocytes and cerebral endothelial cells as a blood-brain barrier. *Lab Chip* **17**, 448–459 (2017).

279. Dewi, B. E., Takasaki, T. & Kurane, I. In vitro assessment of human endothelial cell permeability: Effects of inflammatory cytokines and dengue virus infection. *J. Virol. Methods* **121**, 171–180 (2004).

280. Takahashi, K. & Yamanaka, S. Induction of Pluripotent Stem Cells from Mouse Embryonic and Adult Fibroblast Cultures by Defined Factors. *Cell* **126**, 663–676 (2006).

281. Takahashi, K. *et al.* Induction of Pluripotent Stem Cells from Adult Human Fibroblasts by Defined Factors. *Cell* **131**, 861–872 (2007).

282. González, F., Boué, S. & Belmonte, J. C. I. Methods for making induced pluripotent stem cells: Reprogramming à la carte. *Nature Reviews Genetics* **12**, 231–242 (2011).

283. Ban, H. *et al.* Efficient generation of transgene-free human induced pluripotent stem cells (iPSCs) by temperature-sensitive Sendai virus vectors. *Proc. Natl. Acad. Sci. U. S. A.* **108**, 14234–14239 (2011).

284. Ananiev, G., Williams, E. C., Li, H. & Chang, Q. Isogenic Pairs of Wild Type and Mutant Induced Pluripotent Stem Cell (iPSC) Lines from Rett Syndrome Patients as In Vitro Disease Model. *PLoS One* **6**, e25255 (2011).

285. Chamberlain, S. J. Disease modelling using human iPSCs Introduction to iPSC Technology. *Hum. Mol. Genet.* **25**, (2016).

286. Shi, Y., Kirwan, P. & Livesey, F. J. Directed differentiation of human pluripotent stem cells to cerebral cortex neurons and neural networks. *Nat. Protoc.* **7**, 1836–1846 (2012).

287. Serrano, F. *et al.* A Novel Human Pluripotent Stem Cell-Derived Neural Crest Model of Treacher Collins Syndrome Shows Defects in Cell Death and Migration. *Stem Cells Dev* . **28**, (2019).

288. Granata, A. *et al.* An iPSC-derived vascular model of Marfan syndrome identifies key mediators of smooth muscle cell death. *Nat. Genet.* **49**, 97–109 (2016).

289. Ling, C. *et al.* Modeling CADASIL vascular pathologies with patient-derived induced pluripotent stem cells. *Protein Cell* (2019). doi:10.1007/s13238-019-0608-1

290. Kelleher, J. *et al.* Patient-Specific iPSC Model of a Genetic Vascular Dementia Syndrome Reveals Failure of Mural Cells to Stabilize Capillary Structures. *Stem Cell Reports* **13**, 817–831 (2019).

291. Lim, R. G. *et al.* Huntington's Disease iPSC-Derived Brain Microvascular Endothelial Cells Reveal WNT-Mediated Angiogenic and Blood-Brain Barrier Deficits. *Cell Rep.* **19**, 1365–1377 (2017).

292. Slanzi, A., Iannoto, G., Rossi, B., Zenaro, E. & Constantin, G. In vitro Models of Neurodegenerative Diseases. *Frontiers in Cell and Developmental Biology* **8**, 328 (2020).

293. Groveman, B. R. *et al.* Sporadic Creutzfeldt-Jakob disease prion infection of human cerebral organoids. *Acta Neuropathol. Commun.* **7**, 12 (2019).

294. Matamoros-Angles, A. *et al.* iPS Cell Cultures from a Gerstmann-Sträussler-Scheinker Patient with the Y218N PRNP Mutation Recapitulate tau Pathology. *Mol. Neurobiol.* **55**, 3033–3048 (2018).

295. Cucullo, L. *et al.* Immortalized Human Brain Endothelial Cells and Flow-Based Vascular Modeling: A Marriage of Convenience for Rational Neurovascular Studies. *J. Cereb. Blood Flow Metab.* **28**, 312–328 (2008).

296. Toh, Y. C. *et al.* A novel 3D mammalian cell perfusion-culture system in microfluidic channels. *Lab Chip* **7**, 302–309 (2007).

297. Bergmann, S. *et al.* Blood–brain-barrier organoids for investigating the permeability of CNS therapeutics. *Nat. Protoc.* **13**, 2827–2843 (2018).

298. Bhalerao, A. *et al.* In vitro modeling of the neurovascular unit: advances in the field. *Fluids Barriers CNS* **17**, 22 (2020).

299. Pacitti, D., Privolizzi, R. & Bax, B. E. Organs to cells and cells to organoids: The evolution of In vitro central nervous system modelling. *Frontiers in Cellular Neuroscience* **13**, (2019).

300. Cho, C. F. *et al.* Blood-brain-barrier spheroids as an in vitro screening platform for brain-penetrating agents. *Nat. Commun.* **8**, (2017).

301. Urich, E. *et al.* Multicellular self-assembled spheroidal model of the blood brain barrier. *Sci. Rep.* **3**, 1500 (2013).

302. Pham, M. T. *et al.* Generation of human vascularized brain organoids. *Neuroreport* **29**, 588–593 (2018).

303. Odijk, M. *et al.* Measuring direct current trans-epithelial electrical resistance in organ-on-a-chip microsystems. *Lab Chip* **15**, 745–752 (2015).

304. Moya, M. L. *et al.* A Reconfigurable In Vitro Model for Studying the Blood–Brain Barrier. *Ann. Biomed. Eng.* **48**, 780–793 (2020).

305. Le Roux, G. *et al.* Proof-of-Concept Study of Drug Brain Permeability Between in Vivo Human Brain and an in Vitro iPSCs-Human Blood-Brain Barrier Model. *Sci. Rep.* **9**, (2019).

306. Helms, H. C. *et al.* In vitro models of the blood–brain barrier: An overview of commonly used brain endothelial cell culture models and guidelines for their use. *J. Cereb. Blood Flow Metab.* **36**, 862–890 (2016).

307. Lippmann, E. S. *et al.* Human Blood-Brain Barrier Endothelial Cells Derived from Pluripotent Stem Cells. *Nat. Biotechnol.* **30**, 2014 (2012).

308. Rosa, S. *et al.* Functional characterization of iPSC-derived arterial- and venous-like endothelial cells. *Sci. Rep.* **9**, (2019).

309. Praça, C. *et al.* Derivation of Brain Capillary-like Endothelial Cells from Human Pluripotent Stem Cell-Derived Endothelial Progenitor Cells. *Stem Cell Reports* **13**,

599–611 (2019).

310. Lian, X. *et al.* Efficient Differentiation of Human Pluripotent Stem Cells to Endothelial Progenitors via Small-Molecule Activation of WNT Signaling. *Stem Cell Reports* **3**, 804–816 (2014).

311. Neal, E. H. *et al.* A Simplified, Fully Defined Differentiation Scheme for Producing Blood-Brain Barrier Endothelial Cells from Human iPSCs. (2019). doi:10.1016/j.stemcr.2019.05.008

312. Robertson, C., Tran, D. D. & George, S. C. Concise review: maturation phases of human pluripotent stem cell-derived cardiomyocytes. *Stem Cells* **31**, 829–37 (2013).

313. Lippmann, E. S., Al-Ahmad, A., Azarin, S. M., Palecek, S. P. & Shusta, E. V. A retinoic acid-enhanced, multicellular human blood-brain barrier model derived from stem cell sources. *Sci. Rep.* **4**, 4160 (2015).

314. Stebbins, M. J. *et al.* Differentiation and characterization of human pluripotent stem cell-derived brain microvascular endothelial cells. *Methods* **101**, (2016).

315. Qian, T. *et al.* Directed differentiation of human pluripotent stem cells to blood-brain barrier endothelial cells. *Sci. Adv.* **3**, (2017).

316. Paik, D. T. *et al.* Large-scale single-cell RNA-seq reveals molecular signatures of heterogeneous populations of human induced pluripotent stem cell-derived endothelial cells. *Circ. Res.* **123**, 443–450 (2018).

317. Bagchi, S. *et al.* <p>In-vitro blood-brain barrier models for drug screening and permeation studies: an overview</p>. *Drug Des. Devel. Ther.* **Volume 13**, 3591–3605 (2019).

318. Kim, K. *et al.* Donor cell type can influence the epigenome and differentiation potential of human induced pluripotent stem cells. *Nat. Biotechnol.* **29**, 1117–1119 (2011).

319. Temple, S. The development of neural stem cells. *Nature* **414**, 112–117 (2001).

320. Martínez-Cerdeño, V. & Noctor, S. C. Neural progenitor cell terminology. *Frontiers in Neuroanatomy* **12**, 104 (2018).

321. Dibajnia, P. & Morshead, C. M. Role of neural precursor cells in promoting repair following stroke. *Acta Pharmacologica Sinica* **34**, 78–90 (2013).

322. Asami, M. *et al.* The role of Pax6 in regulating the orientation and mode of cell division of progenitors in the mouse cerebral cortex. *Development* **138**, 5067–5078 (2011).

323. Ellis, P. *et al.* SOX2, a Persistent Marker for Multipotential Neural Stem Cells Derived from Embryonic Stem Cells, the Embryo or the Adult. *Dev. Neurosci.* **26**, 148–165 (2004).

324. Dang, S. M., Kyba, M., Perlingeiro, R., Daley, G. Q. & Zandstra, P. W. Efficiency of embryoid body formation and hematopoietic development from embryonic stem cells in different culture systems. *Biotechnol. Bioeng.* **78**, 442–453 (2002).

325. Chandrasekaran, A. *et al.* Comparison of 2D and 3D neural induction methods for the generation of neural progenitor cells from human induced pluripotent stem cells. *Stem Cell Res.* **25**, 139–151 (2017).

326. Zhang, S. C., Wernig, M., Duncan, I. D., Brüstle, O. & Thomson, J. A. In vitro differentiation of transplantable neural precursors from human embryonic stem cells. *Nat. Biotechnol.* **19**, 1129–1133 (2001).

327. Surmacz, B., Fox, H., Gutteridge, A., Lubitz, S. & Whiting, P. Directing Differentiation of Human Embryonic Stem Cells Toward Anterior Neural Ectoderm Using Small Molecules. *Stem Cells* **30**, 1875–1884 (2012).

328. Lippmann, E. S., Estevez-Silva, M. C. & Ashton, R. S. Defined Human Pluripotent Stem Cell Culture Enables Highly Efficient Neuroepithelium Derivation Without Small Molecule Inhibitors. *Stem Cells* **32**, 1032–1042 (2014).

329. Tchieu, J. *et al.* A Modular Platform for Differentiation of Human PSCs into All Major Ectodermal Lineages. *Cell Stem Cell* **21**, 399-410.e7 (2017).

330. Yan, Y. *et al.* Efficient and Rapid Derivation of Primitive Neural Stem Cells and Generation of Brain Subtype Neurons From Human Pluripotent Stem Cells. *Stem Cells Transl. Med.* **2**, 862–870 (2013).

331. Bradley, R. A. *et al.* Regionally specified human pluripotent stem cell-derived astrocytes exhibit different molecular signatures and functional properties. *Dev.* **146**, (2019).

332. Wilson, P. G. & Stice, S. S. Development and Differentiation of Neural Rosettes Derived From Human Embryonic Stem Cells. (2006).

333. Yan, Y. *et al.* Efficient and Rapid Derivation of Primitive Neural Stem Cells and Generation of Brain Subtype Neurons From Human Pluripotent Stem Cells. *Stem Cells Transl. Med.* **2**, 862–870 (2013).

334. Kriegstein, A. & Alvarez-Buylla, A. The Glial Nature of Embryonic and Adult Neural

Stem Cells. *Annu. Rev. Neurosci.* **32**, 149–184 (2009).

335. Walker, T., Huang, J. & Young, K. Neural Stem and Progenitor Cells in Nervous System Function and Therapy. *Stem Cells Int.* **2016**, (2016).

336. Shaltouki, A., Peng, J., Liu, Q., Rao, M. S. & Zeng, X. Efficient generation of astrocytes from human pluripotent stem cells in defined conditions. *Stem Cells* **31**, 941–952 (2013).

337. Swistowski, A. *et al.* Xeno-Free Defined Conditions for Culture of Human Embryonic Stem Cells, Neural Stem Cells and Dopaminergic Neurons Derived from Them. *PLoS One* **4**, e6233 (2009).

338. TCW, J. *et al.* An Efficient Platform for Astrocyte Differentiation from Human Induced Pluripotent Stem Cells. *Stem Cell Reports* **9**, 600–614 (2017).

339. Lundin, A. *et al.* hiPS-Derived Astroglia Model Show Temporal Transcriptomic Profile Related to Human Neural Development and Glia Competence Acquisition of a Maturing Astrocytic Identity. *Adv. Biosyst.* **4**, (2020).

340. Cochrane, A. *et al.* Advanced in vitro models of vascular biology: Human induced pluripotent stem cells and organ-on-chip technology. *Advanced Drug Delivery Reviews* **140**, 68–77 (2019).

341. Stemple, D. L. & Anderson, D. J. Isolation of a stem cell for neurons and glia from the mammalian neural crest. *Cell* **71**, 973–985 (1992).

342. Chin, C. J. *et al.* Transcriptionally and Functionally Distinct Mesenchymal Subpopulations Are Generated from Human Pluripotent Stem Cells. *Stem Cell Reports* **10**, 436–446 (2018).

343. Kumar, A. *et al.* Specification and Diversification of Pericytes and Smooth Muscle Cells from Mesenchymoangioblasts. *Cell Rep.* **19**, 1902–1916 (2017).

344. Kusuma, S. *et al.* Self-organized vascular networks from human pluripotent stem cells in a synthetic matrix. *Proc. Natl. Acad. Sci. U. S. A.* **110**, 12601–12606 (2013).

345. Stebbins, M. J. *et al.* Human pluripotent stem cell–derived brain pericyte–like cells induce blood-brain barrier properties. *Sci. Adv.* **5**, eaau7375 (2019).

346. Cheung, C., Bernardo, A. S., Pedersen, R. A. & Sinha, S. Directed differentiation of embryonic origin–specific vascular smooth muscle subtypes from human pluripotent stem cells. *Nat. Protoc.* **9**, 929–938 (2014).

347. Cheung, C., Bernardo, A. S., Trotter, M. W. B. & Pedersen, R. A. Generation of human vascular smooth muscle subtypes provides insight into embryological origin-dependent disease susceptibility. **30**, 165–173 (2012).

348. Evseenko, D. *et al.* Mapping the first stages of mesoderm commitment during differentiation of human embryonic stem cells. doi:10.1073/pnas.1002077107

349. Jamieson, J. J., Linville, R. M., Ding, Y. Y., Gerecht, S. & Searson, P. C. Role of iPSC-derived pericytes on barrier function of iPSC-derived brain microvascular endothelial cells in 2D and 3D. *Fluids Barriers CNS* **16**, (2019).

350. Orlova, V. V. *et al.* Functionality of endothelial cells and pericytes from human pluripotent stem cells demonstrated in cultured vascular plexus and zebrafish xenografts. *Arterioscler. Thromb. Vasc. Biol.* **34**, 177–186 (2014).

351. Bart van der Worp, H. *et al.* Can animal models of disease reliably inform human studies? *PLoS Med.* **7**, 1–8 (2010).

352. Patel, R., Page, S. & Al-Ahmad, A. J. Isogenic blood-brain barrier models based on patient-derived stem cells display inter-individual differences in cell maturation and functionality. *J. Neurochem.* **142**, 74–88 (2017).

353. Canfield, S. G. *et al.* An isogenic blood-brain barrier model comprising brain endothelial cells, astrocytes, and neurons derived from human induced pluripotent stem cells. *J. Neurochem.* **140**, 874–888 (2017).

354. Motallebnejad, P., Thomas, A., Swisher, S. L. & Azarin, S. M. An isogenic hiPSC-derived BBB-on-a-chip. *Biomicrofluidics* **13**, (2019).

355. Rashid, S. T. *et al.* Modeling inherited metabolic disorders of the liver using human induced pluripotent stem cells. *J. Clin. Invest.* **120**, 3127–3136 (2010).

356. Yusa, K. *et al.* Targeted gene correction of α1-antitrypsin deficiency in induced pluripotent stem cells. *Nature* **478**, 391–394 (2011).

357. Bertulli, C. *et al.* Image-Assisted Microvessel-on-a-Chip Platform for Studying Cancer Cell Transendothelial Migration Dynamics. *Sci. Rep.* **8**, (2018).

358. Ran, F. A. *et al.* Genome engineering using the CRISPR-Cas9 system. *Nat. Protoc.* **8**, 2281–2308 (2013).

359. Bourgeois, S., Gruol, D. J., Newby, R. F. & Rajah, F. M. Expression of an mdr gene is associated with a new form of resistance to dexamethasone-induced apoptosis. *Mol. Endocrinol.* **7**, 840–851 (1993).

360. Smith, E. B. & Staples, E. M. *INTIMAL AND MEDIAL PLASMA PROTEIN CONCENTRATIONS AND ENDOTHELIAL FUNCTION*.

361. Voyta, J. C., Via, D. P., Butterfield, C. E. & Zetter, B. R. *Identification and Isolation of Endothelial Cells Based on Their Increased Uptake of Acetylated-Low Density Lipoprotein*.

362. Saeki, T., Uedas, K., Tanigawarat, Y., Horit, R. & Komano, T. *Human P-glycoprotein Transports Cyclosporin A and FK506**. **268**,

363. Brinkman, E. K. *et al.* Easy quantification of template-directed CRISPR/Cas9 editing. *Nucleic Acids Res.* **46**, e58 (2018).

364. Tome, M. E. *et al.* P-glycoprotein traffics from the nucleus to the plasma membrane in rat brain endothelium during inflammatory pain. *J. Cereb. Blood Flow Metab.* **36**, 1913–1928 (2016).

365. Stamatovic, S. M., Keep, R. F., Wang, M. M., Jankovic, I. & Andjelkovic, A. V. Caveolae-mediated internalization of occludin and claudin-5 during CCL2-induced tight junction remodeling in brain endothelial cells. *J. Biol. Chem.* **284**, 19053–19056 (2009).

366. Abdullahi, W., Tripathi, D. & Ronaldson, P. T. Blood-brain barrier dysfunction in ischemic stroke: Targeting tight junctions and transporters for vascular protection. *Am. J. Physiol. - Cell Physiol.* **315**, C343–C356 (2018).

367. Nakano-Doi, A., Sakuma, R., Matsuyama, T. & Nakagomi, T. Ischemic stroke activates the VE-cadherin promoter and increases VE-cadherin expression in adult mice. *Histol. Histopathol.* **33**, 507–521 (2018).

368. Bernardo, M. M. & Fridman, R. TIMP-2 (tissue inhibitor of metalloproteinase-2) regulates MMP-2 (matrix metalloproteinase-2) activity in the extracellular environment after pro-MMP-2 activation by MT1 (membrane type 1)-MMP. *Biochem. J.* **374**, 739–745 (2003).

369. Castro, M. M., Tanus-Santos, J. E. & Gerlach, R. F. Matrix metalloproteinases: Targets for doxycycline to prevent the vascular alterations of hypertension. *Pharmacol. Res.* **64**, 567–572 (2011).

370. Jonat, C., Chung, F. Z. & Baragi, V. M. Transcriptional down regulation of stromelysin by tetracycline. *J. Cell. Biochem.* **60**, 341–347 (1996).

371. Neuhaus, J., Risau, W. & Wolburg, H. Induction of Blood-Brain Barrier Characteristics

in Bovine Brain Endothelial Cells by Rat Astroglial Cells in Transfilter Coculture. *Ann. N. Y. Acad. Sci.* **633**, 578–580 (1991).

372. Armulik, A. *et al.* Pericytes regulate the blood–brain barrier. *Nature* **468**, 557–561 (2010).

373. Liu, S., Agalliu, D., Yu, C. & Fisher, M. The Role of Pericytes in Blood-Brain Barrier Function and Stroke. *Curr. Pharm. Des.* **18**, 3653–3662 (2012).

374. Virgintino, D. *et al.* An intimate interplay between precocious, migrating pericytes and endothelial cells governs human fetal brain angiogenesis. *Angiogenesis* **10**, 35–45 (2007).

375. Stone, N. L., England, T. J. & O'Sullivan, S. E. A novel transwell blood brain barrier model using primary human cells. *Front. Cell. Neurosci.* **13**, (2019).

376. Stanness, K. A. *et al. Morphological and functional characterization of an in vitro blood-brain barrier model. Brain Research* **771**, (1997).

377. Bouillot., P. *et al.* 3D phase contrast MRI: Partial volume correction for robust blood flow quantification in small intracranial vessels. *Magn. Reson. Med.* **79**, 129–140 (2018).

378. Vinci, B. *et al.* In vitro liver model using microfabricated scaffolds in a modular bioreactor. *Biotechnol. J.* **5**, 232–241 (2010).

379. Mazzei, D., Guzzardi, M. A., Giusti, S. & Ahluwalia, A. A low shear stress modular bioreactor for connected cell culture under high flow rates. *Biotechnol. Bioeng.* **106**, 127–137 (2010).

380. Rashidi, H., Alhaque, S., Szkolnicka, D., Flint, O. & Hay, D. C. Fluid shear stress modulation of hepatocyte-like cell function. *Arch. Toxicol.* **90**, 1757–1761 (2016).

381. Bertulli, C. *et al.* Image-Assisted Microvessel-on-a-Chip Platform for Studying Cancer Cell Transendothelial Migration Dynamics. *Sci. Rep.* **8**, 1–14 (2018).

382. Campisi, M. *et al.* 3D self-organized microvascular model of the human blood-brain barrier with endothelial cells, pericytes and astrocytes. *Biomaterials* **180**, 117–129 (2018).

383. Volpato, V. & Webber, C. Addressing variability in iPSC-derived models of human disease: Guidelines to promote reproducibility. *DMM Disease Models and Mechanisms* **13**, (2020).

384. Colombo, E., Calcaterra, F., Cappelletti, M., Mavilio, D. & Della Bella, S. Comparison of Fibronectin and Collagen in Supporting the Isolation and Expansion of Endothelial Progenitor Cells from Human Adult Peripheral Blood. *PLoS One* **8**, (2013).

385. Patsch, C. *et al.* Generation of vascular endothelial and smooth muscle cells from human pluripotent stem cells. *Nat. Cell Biol.* **17**, 994–1003 (2015).

386. Skardal, A., Mack, D., Atala, A. & Sokern, S. Substrate elasticity controls cell proliferation, surface marker expression and motile phenotype in amniotic fluid-derived stem cells. *J. Mech. Behav. Biomed. Mater.* **17**, 307–316 (2013).

387. Erickson, H. P. Size and shape of protein molecules at the nanometer level determined by sedimentation, gel filtration, and electron microscopy. *Biological Procedures Online* **11**, 32–51 (2009).

388. Luissint, A.-C. *et al.* Guanine nucleotide-binding protein Gαi2: a new partner of claudin-5 that regulates tight junction integrity in human brain endothelial cells. *J. Cereb. Blood Flow Metab.* **32**, 860–73 (2012).

389. Bloom, G. & Brashear, T. A. *A Novel 58-,kDa Protein Associates with the Golgi Apparatus and Microtubules*. **264**, (1989).

390. Kim, J. *et al.* Flow cytometry analysis: A quantitative method for collagen VI deficiency screening. *Neuromuscul. Disord.* **22**, 139–148 (2012).

391. Remacle, A. G. *et al.* Novel MT1-MMP small-molecule inhibitors based on insights into hemopexin domain function in tumor growth. *Cancer Res.* **72**, 2339–2349 (2012).

392. Golub, L. M. *et al.* Tetracyclines inhibit tissue collagenase activity. *J. Periodontal Res.* **19**, 651–655 (1984).

393. Golub, L. M. *et al.* Tetracyclines inhibit connective tissue breakdown by multiple non-antimicrobial mechanisms. *Advances in dental research* **12**, 12–26 (1998).

394. Qosa, H., Miller, D. S., Pasinelli, P. & Trotti, D. Regulation of ABC efflux transporters at blood-brain barrier in health and neurological disorders. *Brain Research* **1628**, 298–316 (2015).

395. Cen, J. *et al.* Alteration in P-glycoprotein at the blood-brain barrier in the early period of MCAO in rats. *J. Pharm. Pharmacol.* **65**, 665–672 (2013).

396. Oikari, L. E. *et al.* Altered Brain Endothelial Cell Phenotype from a Familial Alzheimer Mutation and Its Potential Implications for Amyloid Clearance and Drug Delivery. *Stem Cell Reports* **14**, 924–939 (2020).

397. Ding, S. *et al.* Cross-talk between signalling pathways and the multidrug resistant protein MDR-1. *Br. J. Cancer* **85**, 1175–1184 (2001).

398. Pokharel, D., Roseblade, A., Oenarto, V., Lu, J. & Bebawy, M. Proteins regulating the intercellular transfer and function of P-glycoprotein in multidrug-resistant cancer. *Ecancermedicalscience* **11**, (2017).

399. Gabison, E. E., Hoang-Xuan, T., Mauviel, A. & Menashi, S. EMMPRIN/CD147, an MMP modulator in cancer, development and tissue repair. *Biochimie* **87**, 361–368 (2005).

400. Tang, Y., Kesavan, P., Nakada, M. T. & Yan, L. *Tumor-Stroma Interaction: Positive Feedback Regulation of Extracellular Matrix Metalloproteinase Inducer (EMMPRIN) Expression and Matrix Metalloproteinase-Dependent Generation of Soluble EMMPRIN.* (2004).

401. Li, H., Wei, M., Li, S., Zhou, Z. & Xu, D. Increased CD147 and MMP-9 expression in the normal rat brain after gamma irradiation. (2012). doi:10.1093/jrr/rrs072

402. Burggraf, D. *et al.* Matrix metalloproteinase induction by EMMPRIN in experimental focal cerebral ischemia. *Eur. J. Neurosci.* **22**, 273–277 (2005).

403. Yang, J.-M. *et al. Overexpression of Extracellular Matrix Metalloproteinase Inducer in Multidrug Resistant Cancer Cells.* (2003).

404. Igakura, T. *et al. Roles of Basigin, a Member of the Immunoglobulin Superfamily, in Behavior as to an Irritating Odor, Lymphocyte Response, and Blood-Brain Barrier.* **224**, (1996).

405. Barakat, S. *et al.* Modulation of p-glycoprotein function by caveolin-1 phosphorylation. *J. Neurochem.* **101**, 1–8 (2007).

406. Huet, E. *et al.* Extracellular matrix metalloproteinase inducer/CD147 promotes myofibroblast differentiation by inducing α-smooth muscle actin expression and collagen gel contraction: implications in tissue remodeling. *FASEB J.* **22**, 1144–1154 (2008).

407. Hu, X. *et al.* Repressing CD147 is a novel therapeutic strategy for malignant melanoma. *Oncotarget* **8**, 25806–25813 (2017).

408. Maherally, Z. *et al.* Real-time acquisition of transendothelial electrical resistance in an all-human, in vitro, 3-dimensional, blood–brain barrier model exemplifies tight-junction integrity. *FASEB J.* **32**, (2018).

409. Hellewell, A. L., Rosini, S. & Adams, J. C. A rapid, scalable method for the isolation, functional study, and analysis of cell-derived extracellular matrix. *J. Vis. Exp.* **2017**, (2017).

410. Johnson, J. L. Matrix metalloproteinases: Influence on smooth muscle cells and atherosclerotic plaque stability. *Expert Review of Cardiovascular Therapy* **5**, 265–282 (2007).

411. Cucullo, L., Hossain, M., Puvenna, V., Marchi, N. & Janigro, D. The role of shear stress in Blood-Brain Barrier endothelial physiology. *BMC Neurosci.* **12**, 40 (2011).

412. Miranda-Azpiazu, P., Panagiotou, S., Jose, G. & Saha, S. A novel dynamic multicellular co-culture system for studying individual blood-brain barrier cell types in brain diseases and cytotoxicity testing. *Sci. Rep.* **8**, 1–10 (2018).

413. Bang, S. *et al.* A Low Permeability Microfluidic Blood-Brain Barrier Platform with Direct Contact between Perfusable Vascular Network and Astrocytes. *Sci. Rep.* **7**, (2017).

Chapter 7: Appendix

Supplementary Figures

7.1 hiPSC Morphology
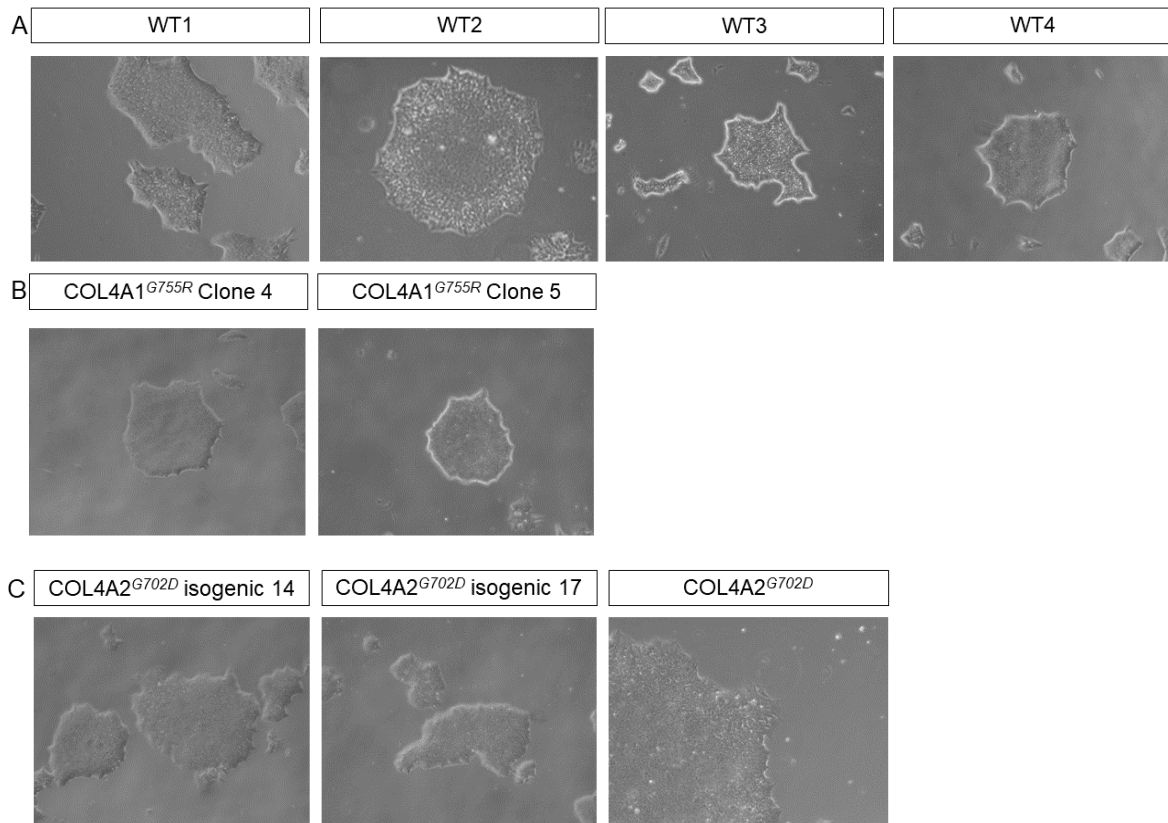
Figure 7.1 hiPSC morphology: brightfield images with 5x objective **(A)** WT, **(B)** COL4A1_cl4 and _cl5 and **(C)** COL4A2 isogenics and COL4A2^{G702D}.
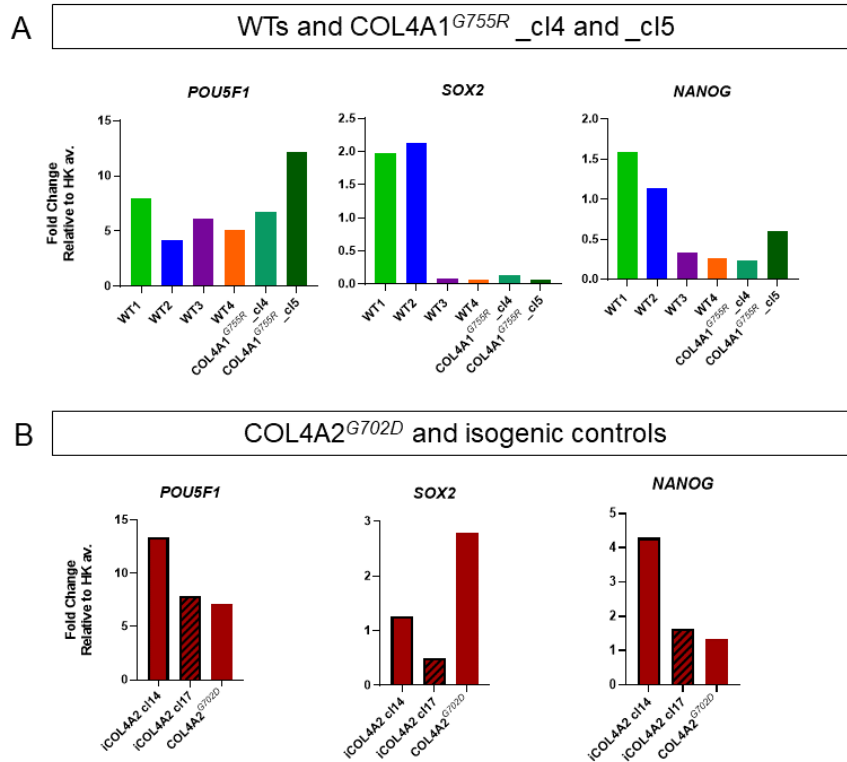
7.2 hiPSC Pluripotency markers

qRT-PCR

Figure 7.2 qRT-PCR for pluripotency markers in hiPSC lines: *POU5F1, SOX2, NANOG* relative to the housekeeping average for **(A)** WTs and COL4A1^{G755R} and **(B)** iCOL4A2 cl14, cl17 and COL4A2^{G702D} (Some of the raw data was provided by Krushangi Patel)

Immunocytochemistry
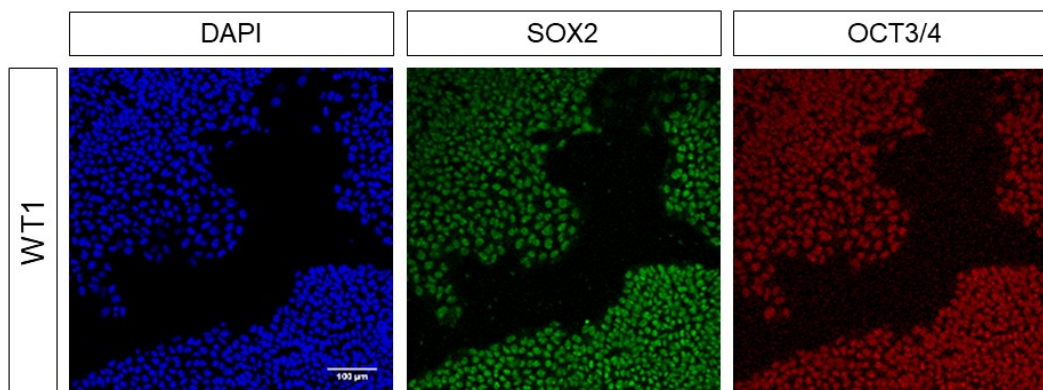
Figure 7.3 WT1 hiPSC pluripotency immunocytochemistry: SOX2 and OCT3/4 ; scale bar is 100µm
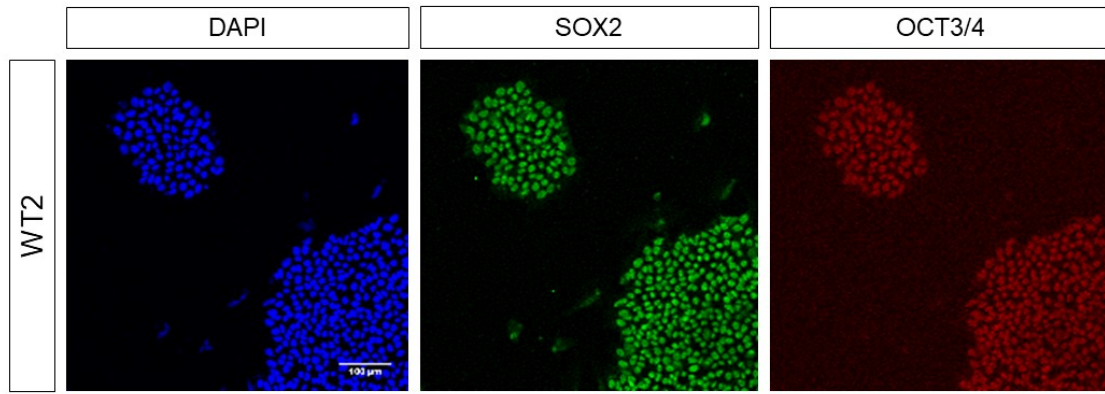
Figure 7.4 WT2 hiPSC pluripotency immunocytochemistry: SOX2 and OCT3/4; scale bar is 100µm
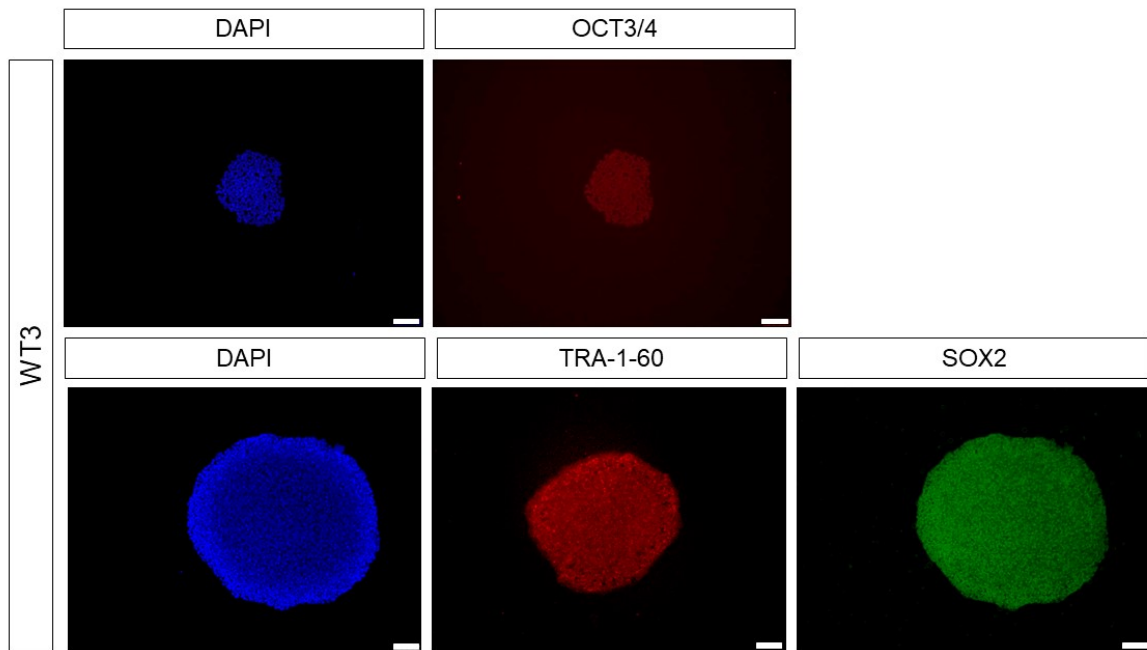
Figure 7.5 WT3 hiPSC pluripotency immunocytochemistry: SOX2, TRA-1-60 and OCT3/4; scale bar is 100µm (Performed by Krushangi Patel)
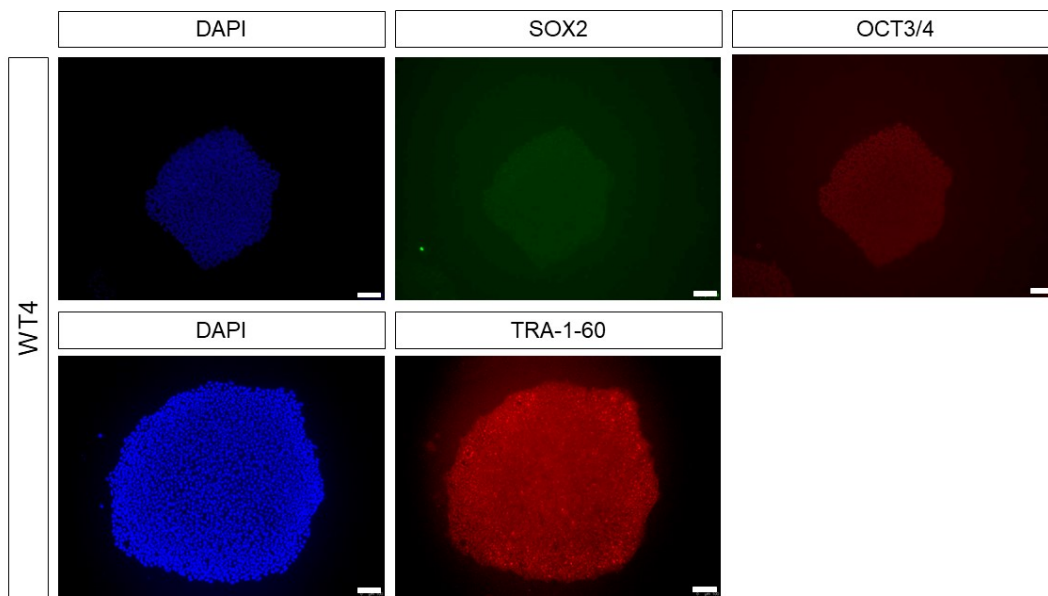
Figure 7.6 WT4 hiPSC pluripotency immunocytochemistry: SOX2, TRA-1-60 and OCT3/4; scale bar is 100µm (Performed by Krushangi Patel)
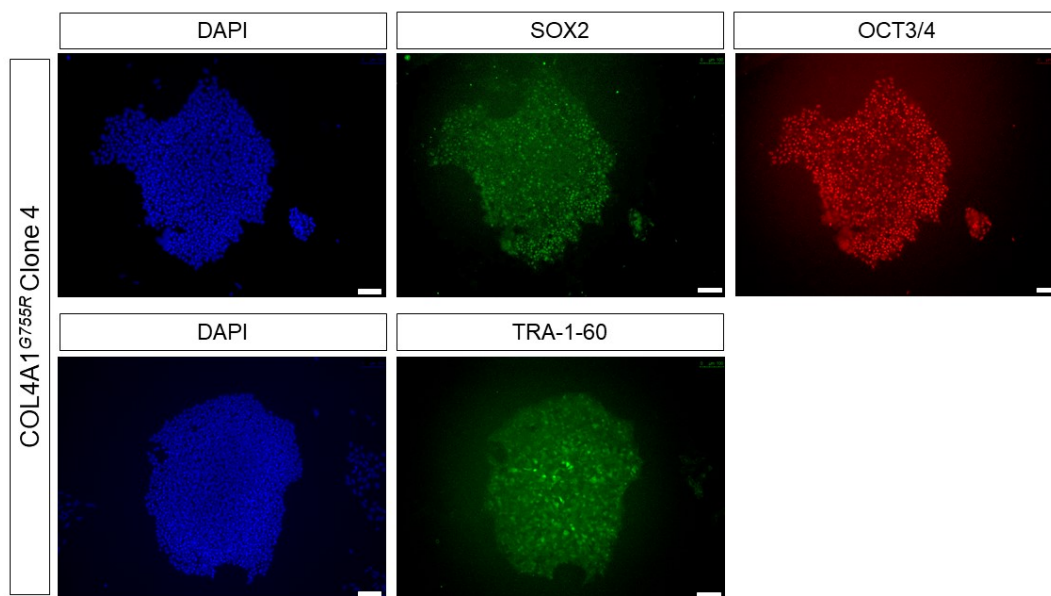

Figure 7.7 COL4A1^{G755R}_cl4 hiPSC pluripotency immunocytochemistry: Immunocytochemistry for SOX2, TRA-1-60 and OCT3/4; scale bar is 100µm
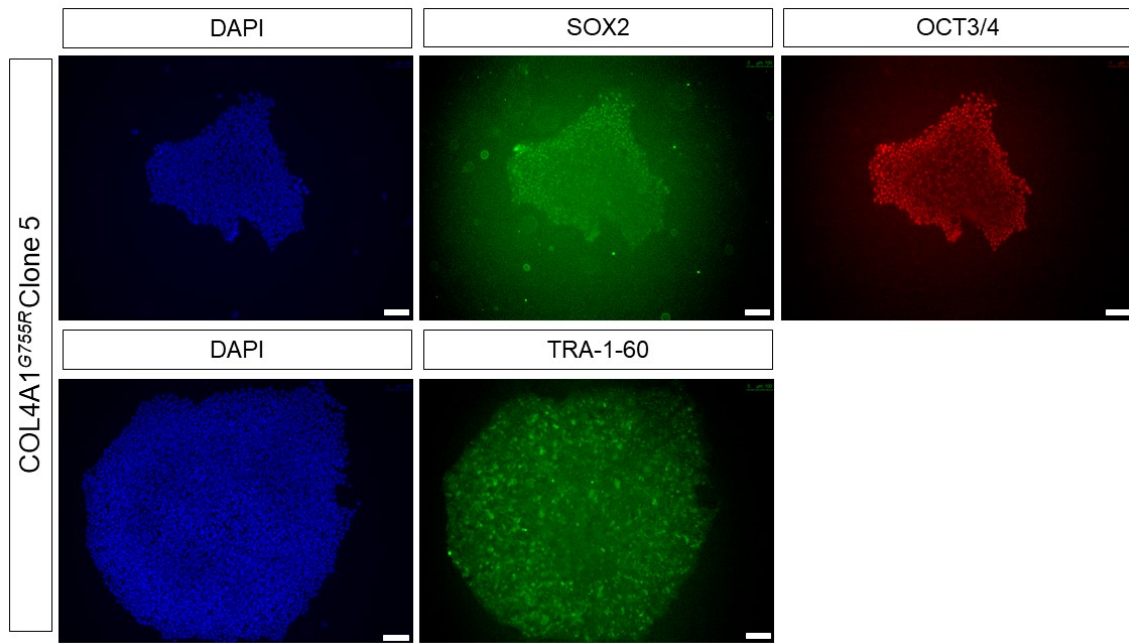
Figure 7.8 COL4A1^{G755R}_cl4 hiPSC pluripotency immunocytochemistry: SOX2, TRA-1-60 and OCT3/4; scale bar is 100µm
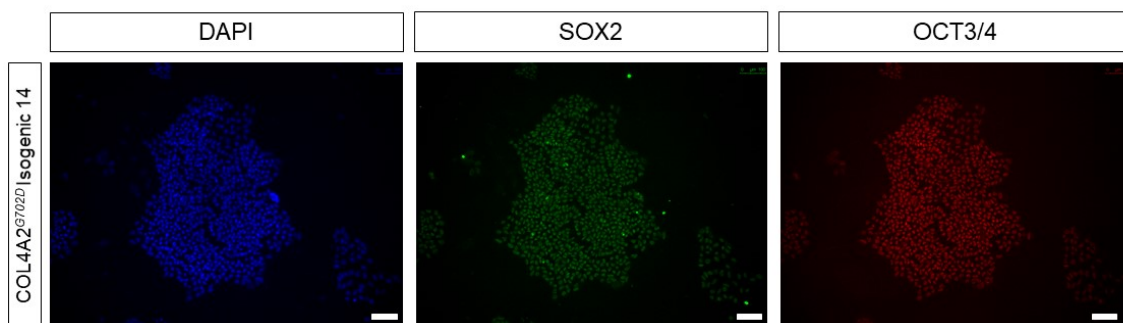

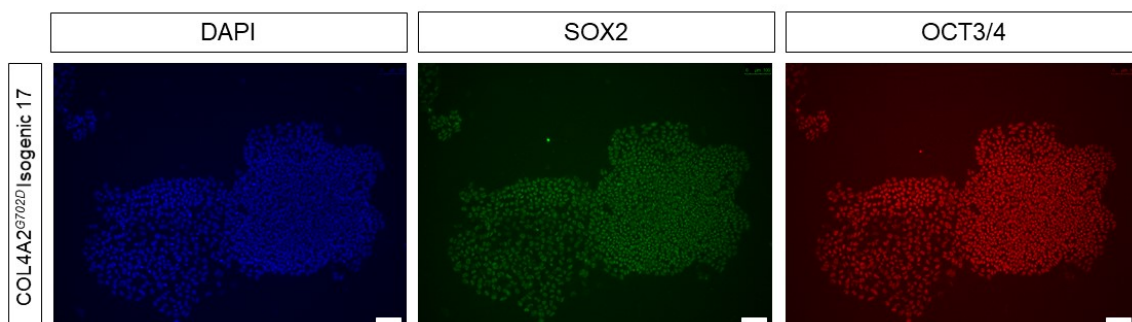**Figure 7.9 iCOL4A2 cl14 hiPSC pluripotency immunocytochemistry:** SOX2 and OCT3/4; scale bar is 100µm

Figure 7.10 iCOL4A2 cl17 hiPSC pluripotency immunocytochemistry: SOX2 and OCT3/4; scale bar is 100µm
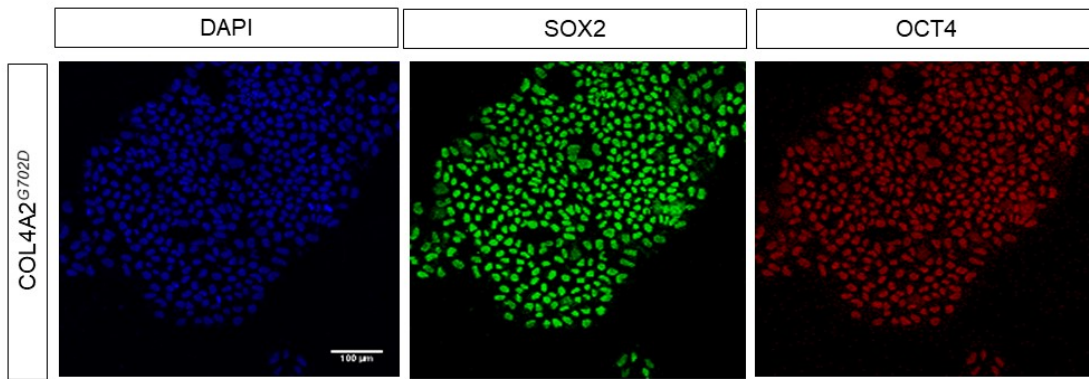
Figure 7.11 COL4A2^{G702D} hiPSC pluripotency immunocytochemistry: SOX2 and OCT3/4; scale bar is 100µm

7.3 hiPSC three germ layer differentiation

Figure 7.12 Three germ layer differentiation of WT3 hiPSC: endoderm (GATA-4), mesoderm (Brachyury) and ectoderm (PAX6), scale bar is 250µm (Performed by Krushangi Patel)
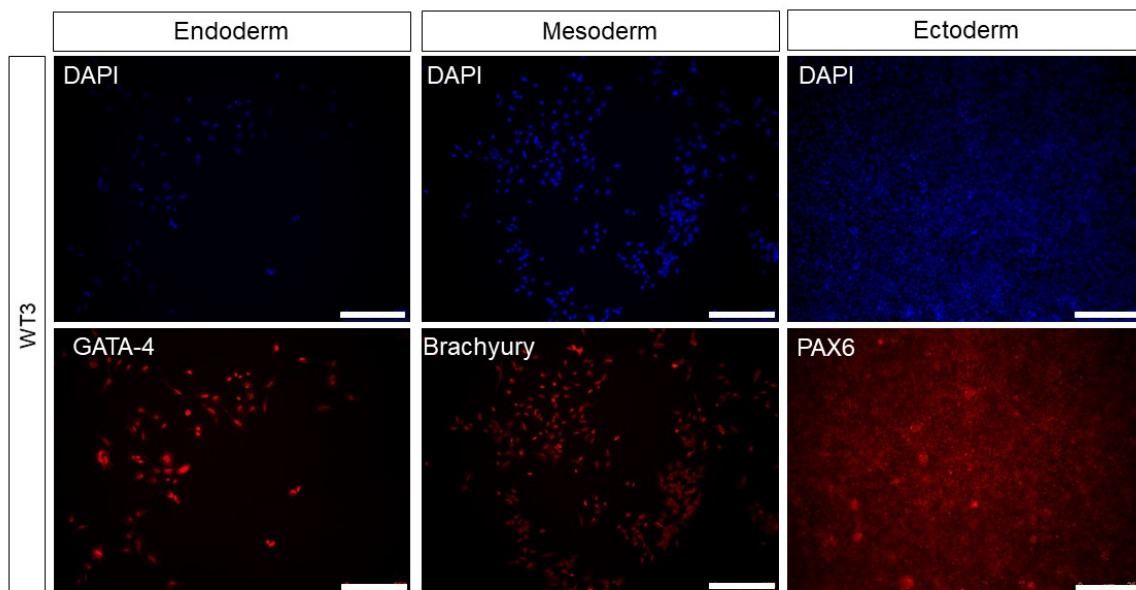
Figure 7.13 Three germ layer differentiation of WT4 hiPSC: endoderm (GATA-4), mesoderm (Brachyury) and ectoderm (PAX6), scale bar is 250μm (Performed by Krushangi Patel)
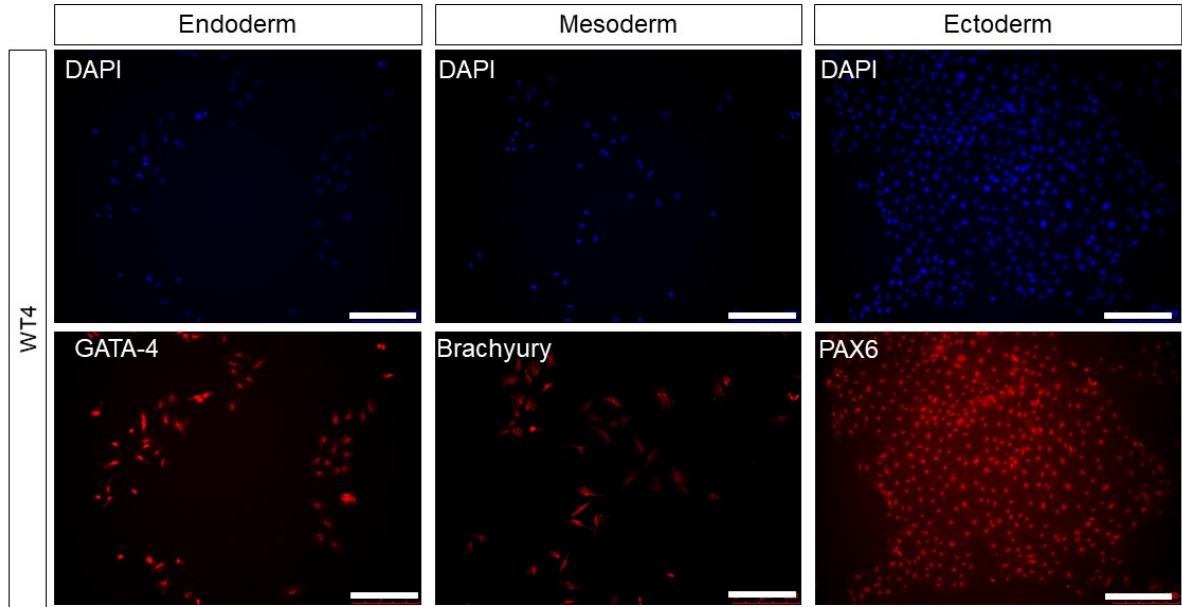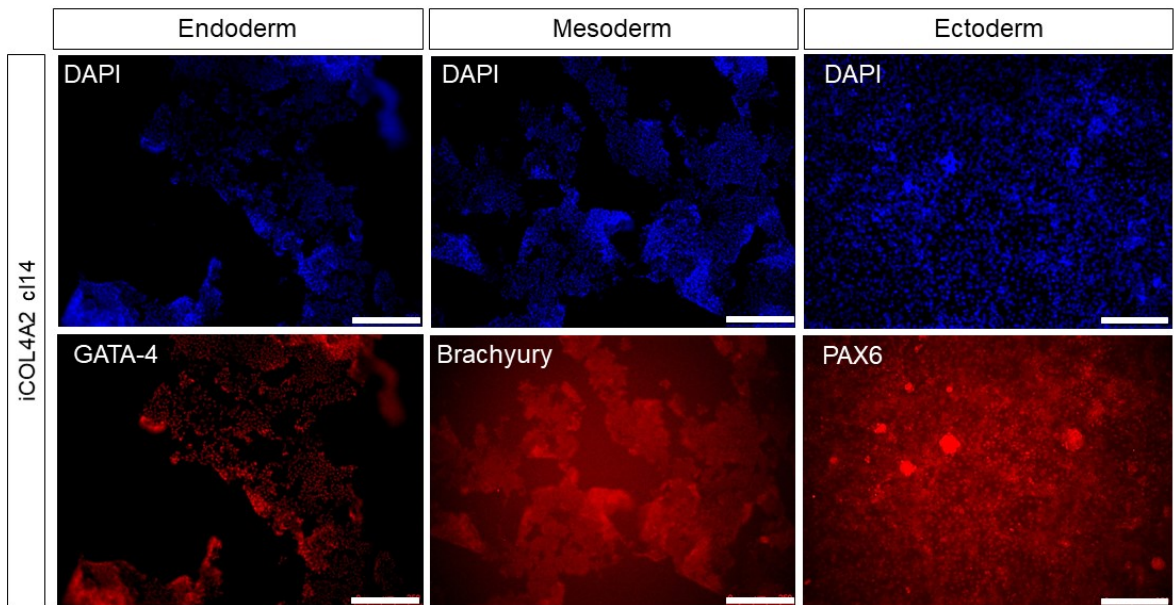

Figure 7.14 Three germ layer differentiation of iCOL4A2 cl14 hiPSC: endoderm (GATA-4), mesoderm (Brachyury) and ectoderm (PAX6), scale bar is 250μm (Performed by Krushangi Patel)

Figure 7.15 Three germ layer differentiation of iCOL4A2 cl17 hiPSC: endoderm (GATA-4), mesoderm (Brachyury) and ectoderm (PAX6), scale bar is 250µm (Performed by Krushangi Patel)

Figure 7.16 Three germ layer differentiation of iCOL4A1 cl6 hiPSC: endoderm (GATA-4), mesoderm (Brachyury) and ectoderm (PAX6), scale bar is 250µm (Performed by Krushangi Patel)
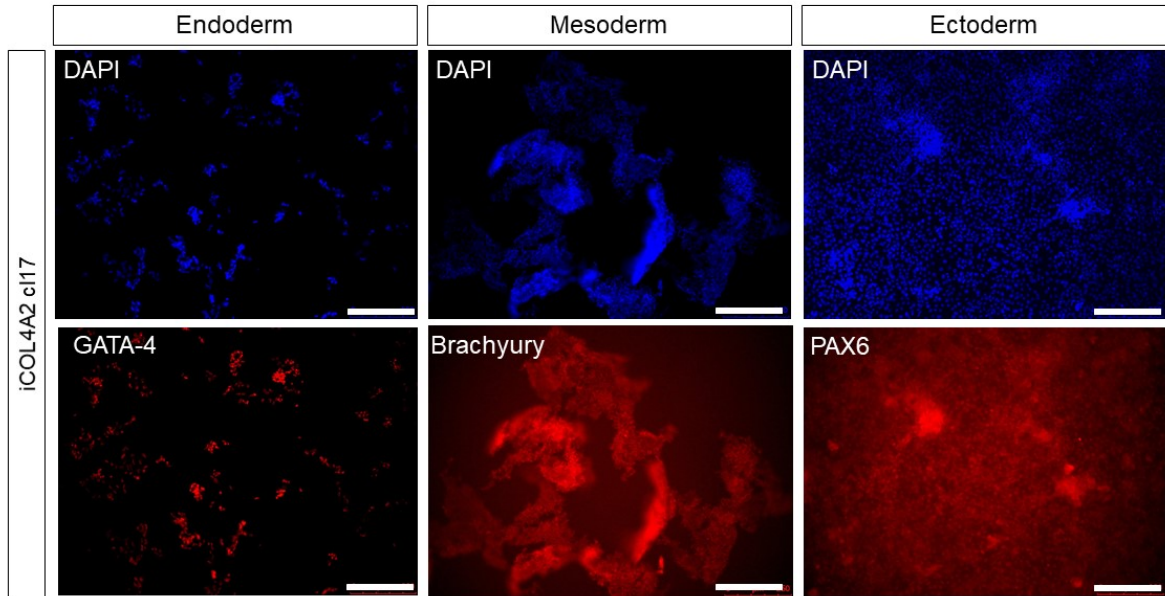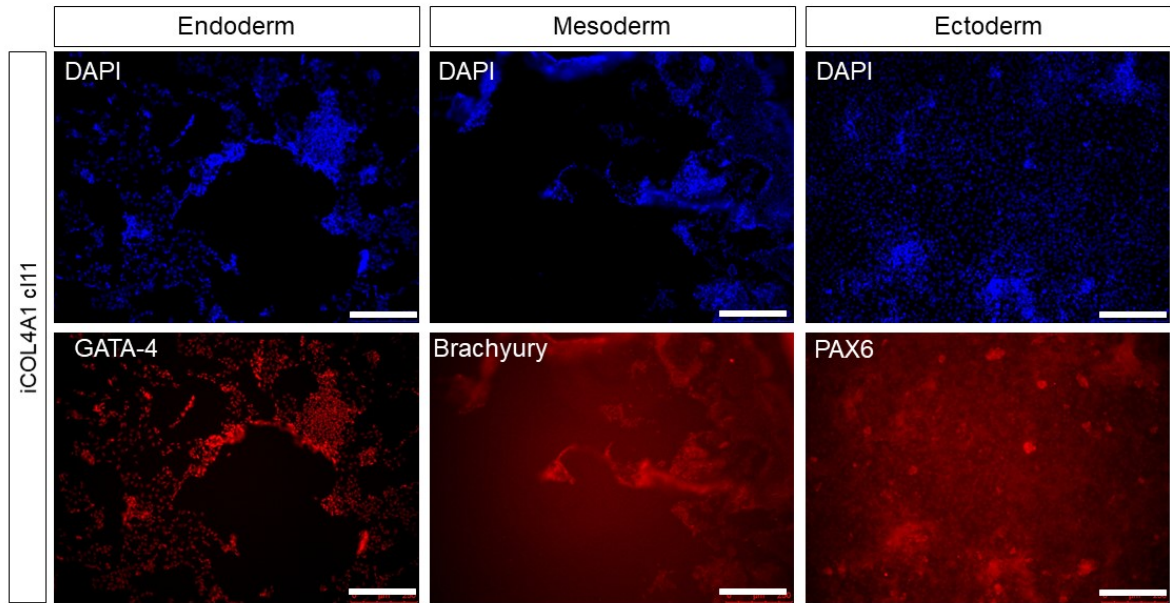
Figure 7.17 Three germ layer differentiation of iCOL4A1 cl11 hiPSC: endoderm (GATA-4), mesoderm (Brachyury) and ectoderm (PAX6), scale bar is 250µm (Performed by Krushangi Patel)
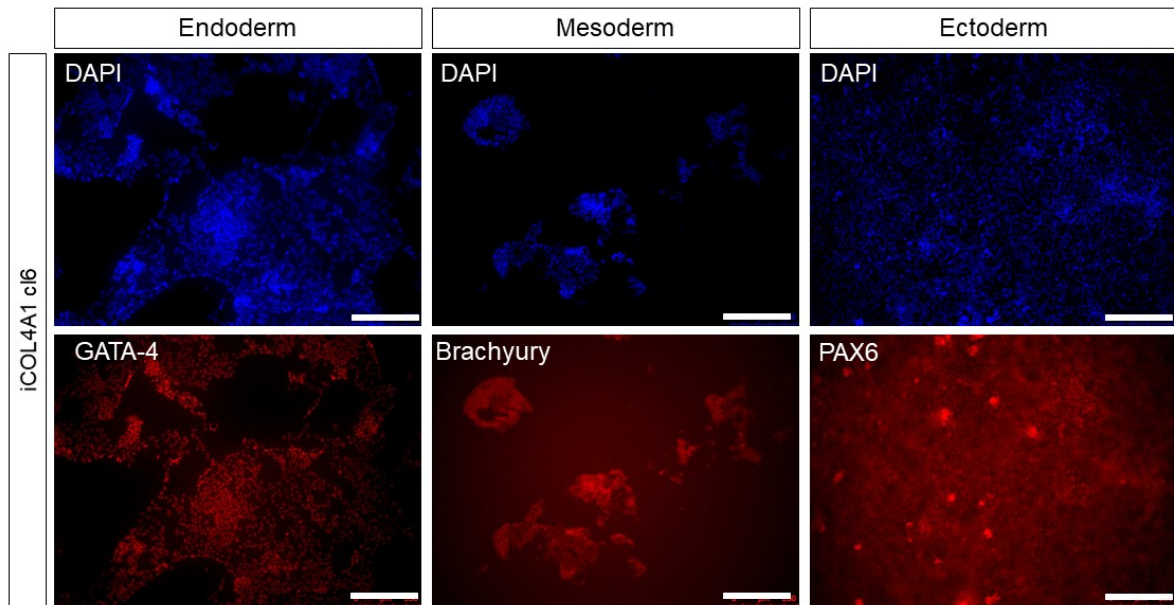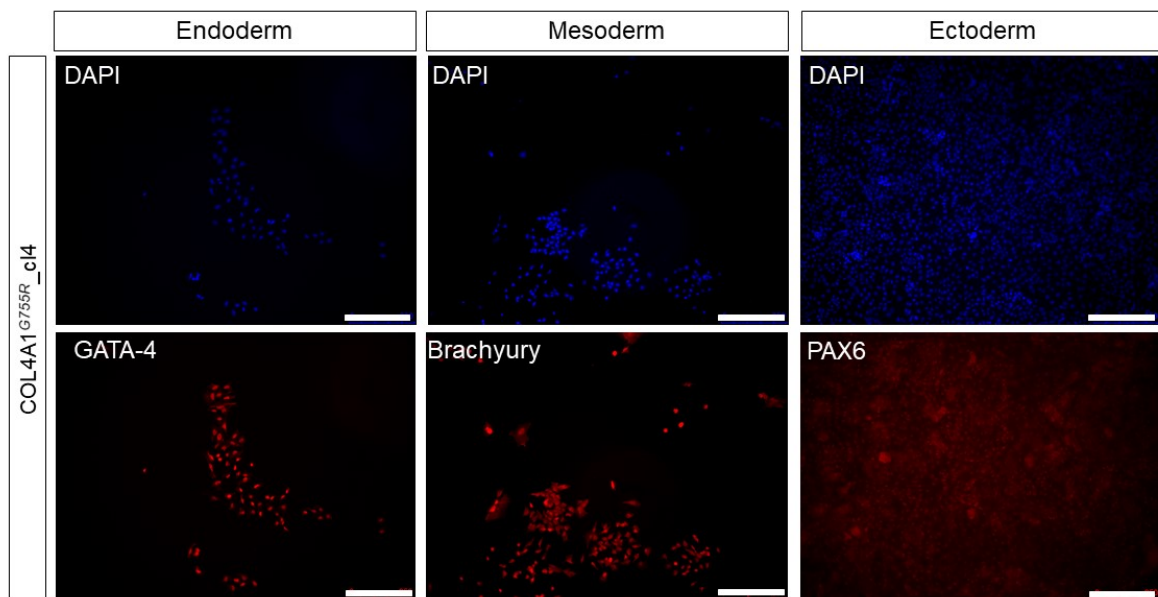

Figure 7.18 Three germ layer differentiation of COL4A1^{G755R}_cl4 hiPSC: endoderm (GATA-4), mesoderm (Brachyury) and ectoderm (PAX6), scale bar is 250µm (Performed by Krushangi Patel)

Figure 7.19 Three germ layer differentiation of COL4A1^{G755R}_cl5 hiPSC: endoderm (GATA-4), mesoderm (Brachyury) and ectoderm (PAX6), scale bar is 250µm (Performed by Krushangi Patel)
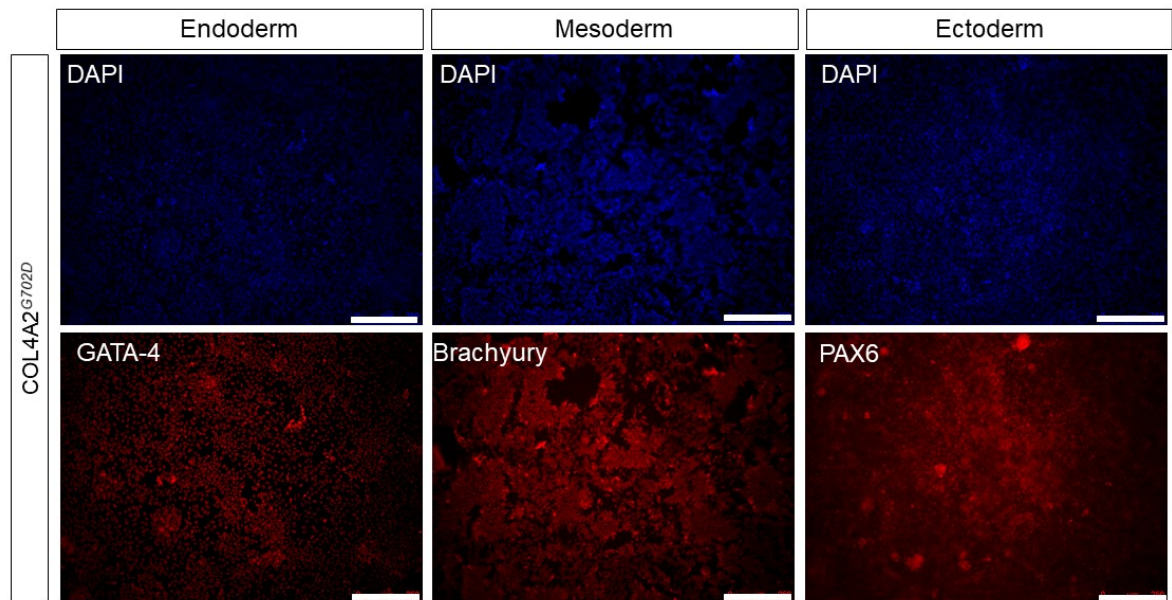
Figure 7.20 Three germ layer differentiation of COL4A2^{G702D} hiPSC: endoderm (GATA-4), mesoderm (Brachyury) and ectoderm (PAX6), scale bar is 250µm (Performed by Krushangi Patel)
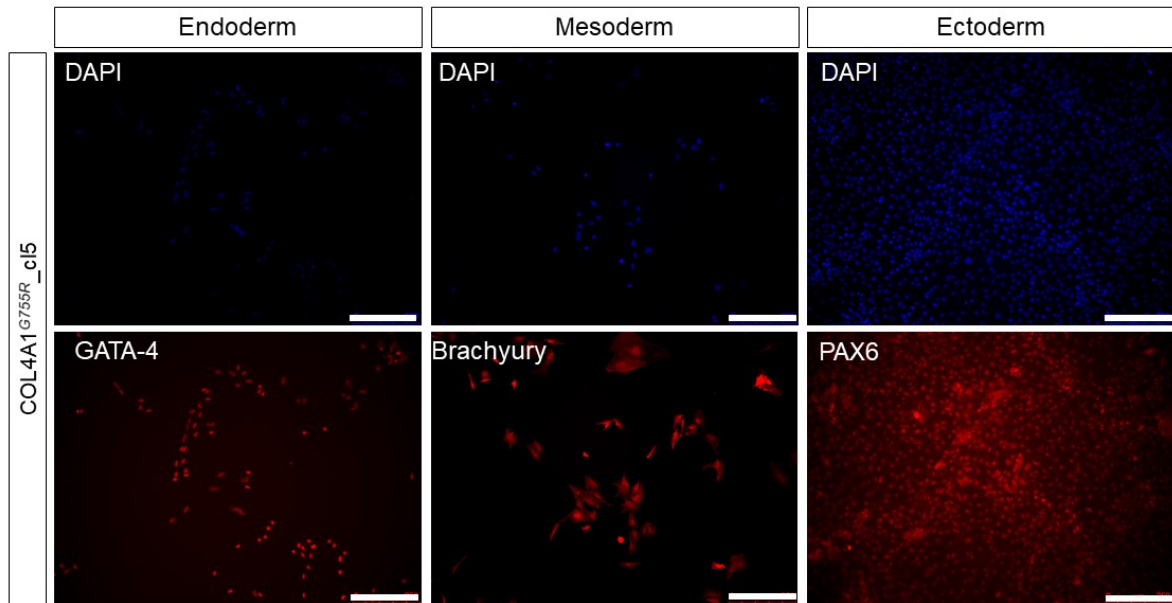
Primers, sequences and antibodies

7.4 Genomic PCR Amplification primers

Table 7.1 PCR primers

Gene/Mutation	Forward sequence 5'-3'	Reverse sequence 5'-3'
RELA (positive control)	TTCTAGGGAGCAGGTCCTGACT	TCCTTTCCTACAAGCTCGTGGG
COL4A1^{G755R} primer 1	GGGATTTTCAGGGAGAGCCT	AGCACATCCTGTCCTCGAAA
COL4A1^{G755R} primer 2	GCTTGAAAAGGGTTGAGCAG	GCATGCTTTTGGGAACAGAT
COL4A2^{G702D}	TCCAGTCCGTAAACAGGATTT	CAGCTTCTACAAAGTGGAAGATAATAG

7.5 Genomic sequencing primers

Table 7.2 sequencing primers

Gene/Mutation	Forward sequence 5'-3'
RELA (positive control)	AGTACAGAGGCCCAGACATCCAA
COL4A1^{G755R}	GCTTGAAAAGGGTTGAGCAG
COL4A2^{G702D}	TCCAGTCCGTAAACAGGATTT

7.6 Guide RNA oligonucleotide sequences

Table 7.3 gRNA sequences

Gene/Mutation and gRNA	gRNA
RELA (positive control)	GAUCUCCACAUAGGGGCCAG
COL4A1 ^{G755R} gRNA 2	CGGCATTCCTGGCACACCCA
COL4A1 ^{G755R} gRNA 3	CCGGCATTCCTGGCACACCC
COL4A2 ^{G702D}	CGAAGCCUGGGAUUCCUCGG

7.7 Donor DNA sequences

Table 7.4 Donor DNA sequences

Gene Mutation and gRNA	Forward sequence 5'-3'	Reverse sequence 5'-3'
COL4A1 *G755R* gRNA 2 and 3 **Corrected base** **mutated PAM**	G*A*C*TCAAAGGTTTGCCAGGTCTTCCCGGCATTCCTGGCACACCCGGAGAGAAGGGGAGCATTGGGGTACCAGGCGTTCCTGGAGAAC*A*T*G	C*A*T*GTTCTCCAGGAACGCCTGGTACCCCAATGCTCCCCTTCTCTCCGGGTGTGCCAGGAATGCCGGGAAGACCTGGCAAACCTTTGA*G*T*C
COL4A2 *G702D* **Corrected base** **mutated PAM**	G*C*C*TGATGTGGTTTGTGGTTTATTTGGTTATTTAGGTGCCAAAGGTCTCCGAGGAATCCCAGGCTTCGCAGGAGCTGATGGAGGAC*C*A*G	C*T*G*GTCCTCCATCAGCTCCTGCGAAGCCTGGGATTCCTCGGAGACCTTTGGCACCTAAATAACCAAATAAACCACAAACCACATCA*G*G*C

246

7.8 Primer sequences for qRT-PCR

Table 7.5 qRT-PCR primers

Gene Target	Forward Sequence 5'-3'	Reverse Sequence 5'-3'
GAPDH	AACAGCCTCAAGATCATCAGC	GGATGATGTTCTGGAGAGCC
HMBS (PBGD)	GGAGCCATGTCTGGTAACGG	CCACGCGAATCACTCTCATCT
POU5F1 (OCT4)	AGGGCAAGCGATCAAGCA	GGAAAGGGACCGAGGAGTA
SOX2	ATGCACCGCTACGACGTGA	CTTTTGCACCCCTCCCATTT
NANOG	ACTAACATGAGTGTGGATCC	TCATCTTCACACGTCTTTCAG
PECAM1	CAGGCGCCGGGAGAAGTGAC	CGTCCAGTCCGGCAGGCTCT
CD34	CACAGGAGAAAGGCTGGGCGA	TGGCCGTTTCTGGAGGTGGC
OCLN	GGAGTGAACCCAACTGCTCA	CTCCTGGGGATCCACAACAC
CDH5	GGTCAAACTGCCCATACTTG	CGCAATAGACAAGGACATAACAC
CLDN5	CAGTACCGCAGGAAGAGGAG	ATCCCATGGCAAACAGAGAG
ABCB1	AAGACCAAACCAGCCACAAC	GCACAACTTCTCCATCAGCA
PAX6	CTTTGCTTGGGAAATCCGAG	AGCCAGGTTGCGAAGAACTC
FOXG1	AGGAGGGCGAGAAGAAGA	TCACGAAGCACTTGTTGAGG
NES	TTCCCCAGAATCCTCTCCTT	AGTCGGACATTGCCCTACAC
COL4A2	TAAAGAGGAGCGCGACAGAT	CTGTTGCCTTGCTGTCCTTT
COL4A1	GATCTGTTGGTGGAATGGGC	ATCTCCCTTTTCACCTCGCA
GFAP	GAGGAAAGGGGACAGGAAAG	GGAAGGAAGGAAGGATCAGG
CHD5	CTCTGGGAGTGAGTGGAAGC	CCTGAGGATGATGGGAAAGA
S100B	CCTCTACCCCCGTGGAGTTA	TGATGTGCACAGCCTCAGAG
ALDH1L1	GTGTGTGCAAGCTCCAGTTG	ATGGTCCCGGGTCCAAATTC
SLC1A2	GATGGGGAAGGCTTGAGCTT	GATGACTGTCGTGCATTCGC
SLC1A3	ACACGGAAAAACCCTTGGGT	GTGCGTTTGGTCTTTGGGAC
MMP1	CTGGCCACAACTGCCAAATG	CTGTCCCTGAACAGCCCAGTACTTA
MMP2	TCTCCTGACATTGACCTTGGC	CAAGGTGCTGGCTGAGTAGATC
MMP9	TTGACAGCGACAAGAAGTGG	GCCATTCACGTCGTCCTTAT
MMP14	CAGAGAAGGCACACAAACGA	CACTGGTGAGACAGGCTTGA
TIMP1	CCTTCTGCAATTCCGACCTC	GTATCCGCAGACACTCTCCA
TIMP2	CACCCAGAAGAAGAGCCTGA	TCTCTTGATGCAGGCGAAGA
TIMP3	GTCGCGTCTATGATGGCAAG	AAGCAAGGCAGGTAGTAGCA
TP53	TGGCCATCTACAAGCAGTCA	GGTACAGTCAGAGCCAACCT
CDKN1A	CATGTGGACCTGTCACTGT	AGACTAAGGCAGAAGATGTAGAGCG
CCND1	CCCGCACGATTTCATTGAAC	AGGGCGGATTGGAAATGAA

CNN1	GTCCACCCTCCTGGCTTT	AAACTTGTTGGTGCCCATCT
P75	ACAAGACCTCATAGCCAGCAC	CTGTTGGCTCCTTGCTTGTTC
MCAM	AAGACCAAGATCCACAGCGA	TGGTTGTGTTGGAGTCTGGT
CSPG4 (NG2)	TTCCAGCTGAGCATGTCTGA	TCCTCCCGATCTGAAACCAC
PDGFRB	GCTTAAATCCACAGCCCGCA	AGGTAGTCCACCAGGTCTC

7.9 Primary antibodies for Immunocytochemistry

Table 7.6 Primary antibodies for immunocytochemistry

Target	Species	Supplier	Catalogue number
OCT3/4	Mouse	Santa Cruz	SC-5279
SOX2	Mouse	Abcam	sc-21705
TRA-1-60	Rabbit	R&D Systems	AF2018-SP
GATA-4	Mouse	Santa Cruz	sc-25310
Brachyury	Mouse	Santa Cruz	sc-166962
PAX6	Rabbit	BioLegend	PRB-278P
NESTIN	Rabbit	Abcam	ab105389
GFAP	Rabbit	Agilent Technologies	Z033429-2
βIII Tubulin	Mouse	R&D Systems	MAB1195
occludin	Mouse	Thermo Fisher	331500
PECAM-1 (CD31)	Mouse	Thermo Fisher	14-0311-81
VE-Cadherin	Goat	R&D Systems	AF938
claudin-5 pre-conjugated AF488	Mouse	Thermo Fisher	352588
GLUT-1	Mouse	Thermo Fisher	MA5--11315
P-glycoprotein (MDR1)	Rabbit	Abcam	ab129450
P75	Rabbit	Abcam	ab8874
Smooth Muscle Actin	Mouse	Agilent	M085101-2
SM22	Rabbit	Abcam	ab14106
Calponin	Mouse	Sigma-Aldrich	C-2687
NG2	Rabbit	Sigma-Aldrich	AB5320
PDGF receptor beta	Rabbit	Cell Signaling	3169P
Collagen IV	Rabbit	Abcam	ab6586
Collagen I	Goat	Sigma-Aldrich	AB758
Ki67	Rabbit	Cell Signalling	9129

7.10 Secondary Antibodies for Immunocytochemistry

Table 7.7 Secondary antibodies for immunocytochemistry

Target	Species	Supplier	Catalogue number
Alexa Fluor 488 Anti-Mouse	Chicken	Thermo Fisher	A21200
Alexa Fluor 568 Anti-Mouse	Donkey	Thermo Fisher	A10037
Alexa Fluor 488 Anti-Goat	Donkey	Thermo Fisher	A11055
Alexa Fluor 488 Anti-Goat	Rabbit	Thermo Fisher	A11078
Alexa Fluor 568 Anti-Rabbit	Donkey	Thermo Fisher	A10042
DAPI	N/A	Sigma-Aldrich	D9542
Hoechst	N/A	Thermo Fisher	62249

7.11 Primary Antibodies for Western Blot

Table 7.8 Primary antibodies for western blot

Target	Species	Supplier	Catalogue number
β-Actin	Mouse	Sigma-Aldrich	A1978
MMP14	Rabbit	Abcam	ab51074
occludin	Mouse	Thermo Fisher	331500
claudin-5	Rabbit	Abcam	Ab15106

7.12 Secondary Antibodies for Western Blot

Table 7.9 Secondary antibodies for western blot

Target	Species	Supplier	Catalogue number
Anti-Mouse IgG HRP	Goat	Insight Biotechnology	04-18-06
Anti-Rabbit IgG HRP	Goat	Insight Biotechnology	04-15-06

7.13 Antibodies for Flow Cytometry

Table 7.10 Antibodies for flow cytometry

Target	Species	Supplier	Catalogue number
claudin-5 pre-conjugated AF488	Mouse	Thermo Fisher	352588
CD144 (VE-cadherin) APC-conjugated	Mouse	Thermo Fisher	17-1441-80
IgG1 Isotype Control FITC-conjugated	Mouse	Thermo Fisher	GM4992
IgG1kappa Isotype Control APC-conjugated	Mouse	R&D Systems	IC002A